Control and Dynamics of Few-Body Systems at Ultracold Temperatures

by

Seth T. Rittenhouse

B.S., Western Washington University, 2002

M.S. (Mathematics), Western Washington University, 2003

A thesis submitted to the

Faculty of the Graduate School of the

University of Colorado in partial fulfillment

of the requirements for the degree of

Doctor of Philosophy

Department of Physics

2009

This thesis entitled:
Control and Dynamics of Few-Body Systems at Ultracold Temperatures
written by Seth T. Rittenhouse
has been approved for the Department of Physics

Chris H. Greene

John L. Bohn

Date

The final copy of this thesis has been examined by the signatories, and we find that both the content and the form meet acceptable presentation standards of scholarly work in the above mentioned discipline.

Rittenhouse, Seth T. (Ph.D., Physics)

Control and Dynamics of Few-Body Systems at Ultracold Temperatures

Thesis directed by Prof. Chris H. Greene

The role of few-body physics in ultracold gases has become increasingly important. For instance, knowledge of two-body scattering has allowed tuning of the two-body interaction strength through a Fano-Feshbach resonance in both Bose and Fermi gases. A detailed understanding of three-body scattering provides information on the trap loss processes which can determine the lifetime of a gas. It can also be used to explore basic few-body behavior. The description of a gas of bosonic dimers relies on understanding the four-body dimer-dimer scattering process. This dissertation concerns two related concepts, the behavior of N-fermion systems with tunable two-body interactions and controllable few-body systems and their impact on ultracold gases. Both fall under the overarching area of controlled few-body physics in many-body systems.

The N-fermion system is described in using the basic methods of hyperspherical coordinates. This approach provides an intuitive picture of the qualitative behavior of a degenerate Fermi gas by finding an effective one-dimensional potential that predicts the ground state energy and the RMS size of the gas in fair agreement with other theoretical techniques. This study also provides an important initial connection between the techniques of few-body physics and many-body systems. By extending the method to multi-component gases, I also predict a dynamic instability in three- and four-component Fermi gases that is now within the range of experimental exploration.

In the second part of this dissertation, I explore three- and four-body problems with s-wave interactions. By applying a new method based on the Lippmann-Schwinger equation to the three-body problem, I develop scattering potentials for an arbitrary three-body system with zero-range pseudo-potential interactions. By extending this

approach to multi-channel interactions, a new class of three-body quasi-bound states is predicted, creating true three-body Fano-Feshbach resonances. I also approximately find the four-fermion hyperradial scattering potential. These potentials are then used to find the zero-energy s-wave dimer-dimer scattering length to and accuracy larger than previous calculations. By exploring the dimer-dimer scattering potential, the full universal, energy-dependent, dimer-dimer scattering length is found, including the inelastic processes of dimer dissociation and relaxation.

Dedication

To my family, thank you for your continuous support.

Acknowledgements

First I would like to thank my advisor, Chris H. Greene. His guidance and example over the last four years has taught me what it means to be a physicist. I would also like to thank the people that I have gotten the pleasure of working with directly over the last years; Jose D'Incao for many hours discussing Efimov physics; Nirav Mehta for his helpful insight into scattering; Mike Cavagnero for guidance, encouragement and insight into hyperspherical coordinates; Doerte Blume for help in deciphering Monte-Carlo methods and their connections to the hyperspherical world; and Javier von Stecher for Hartree-Fock calculations and the use of his four-boson potentials.

The Greene, Zach Walters, Dan Haxton, Jia Wang, Josh Dunn, Roman Curik, Jason Pawlowski and Stefano Tonzani, have been a tremendous help in countless hours of discussion on all topics in AMO physics. Brandon Peden took on the task of editing this thesis and correcting the grammar, for which I and anyone else reading this must perenially be grateful. Everyone on the theory floor in JILA have always been supportive over the last four years. Thanks also to Evan Salim, Alan Bristow, Mike Martin and Mike Thorpe for their experimental insight. Thanks to Jim Shepard for humoring my various crazy ideas, and introducing me to COLSYS, a new toy I plan on using for a long time to come.

Thanks to Brad Johnson and Sebatian Schreiber for my first research experience. I would especially like to thank Alexa Halford for keeping me sane, and my friends Rick Karnesky and Brent Bailey. Last, but certainly not least, I would like to thank Pam

Leland for unfailing administrative support.

This work was suppoted by funding from the National Science Foundation. Computational support was provided by the W. M. Keck foundation.

Contents

Chapter

Tables

Table

Figures

Figure

Chapter 1

Introduction

Since the experimental realization of the first atomic Bose-Einstein condensates in 1995 [9, 10, 11] and later the first degenerate gas of fermionic atoms [12, 13, 14, 15, 16, 17], the field of ultracold gases has seen an explosion of experimental capabilities and theoretical interest, becoming a veritable playground of new and interesting quantum phenomena. Microscopic, few-body interactions in these systems plays a central role [18, 19, 20, 21, 22, 23]. For instance, under the influence of a of a Fano-Feshbach resonance, the s-wave interaction strength in an ultra-cold atomic gas can be tuned from weak to strong and attractive to repulsive. Further, few-body correlations can play an important role in determining experimental observables in such systems [23, 24, 25]. With the large variety of knobs to turn in these systems, they provide a perfect environment for exploring fundamental quantum mechanics as well as probing new physical phenomena. Further understanding of the few-body interactions can lead also to an understanding of the loss processes, such as the scaling of three-body recombination with the strength of the interaction [26, 27, 28, 29], that govern the lifetimes of ultracold gases.

As a result of this versatility, the majority of this dissertation is focused on the few-body control and dynamics present in ultra-cold atomic gases. This is not to say that the methods introduced here are exclusively applicable to this exciting field. Hyperspherical coordinates have a long history of use in several areas of theoretical physics ranging from nuclear physics [30, 31, 32, 5, 33] to atomic structure [34, 35, 36, 37, 38, 39] and

fundamental few-body scattering [40, 41].

Hyperspherical methods starts with a single concept, that of the hyperradius. As the name suggests, the hyperradius is the extension of the concept of the radius of a sphere beyond three dimensions. Generally, is proportional to the square root of the sum of the squares of all of the coordinates in a d dimensional Cartesian space, i.e.

$$R \propto \sqrt{\sum_{i=1}^{d} x_i^2}. \tag{1.1}$$

All the remaining $d-1$ degrees of freedom are then encapsulated in a set of hyperangles, denoted by Ω. In the cases considered in this thesis, the hyperradius can be considered as a coordinate describing the RMS radius of N-bodies. In this context, it is clear that such a coordinate is useful. For instance, if one wanted to describe some inelastic three-body process, for example $A + B + C \rightarrow AB + C$ where A, B, and C are three particles and AB is a bound state between particles A and B, this can be described as a system coming in from large hyperradius (where A, B and C are all far from each other) on one potential curve and leaving at large hyperradius (where the distance between AB and C is large) on another. Further, if one considers an adiabatic approach in which the hyperradius is fixed and the Hamiltonian is diagonalized in the remaining hyperangular degrees of freedom, all the continuum behavior of the systems is encapsulated in the hyperradius [36, 42, 43]. As with most adiabatic treatments, the hyperspherical method is a "divide and conquer" idea. By finding the eigenfunctions and eigenvalues of a system at fixed hyperradius, a set of 1D coupled potentials can be developed, and all of our normal Schrödinger quantum mechanics intuition can be brought to bear upon the resulting system.

1.1 The many-fermion problem

The many fermion problem with tunable s-wave interactions has generated a great deal of interest over the years. The two-body physics of the Fano-Feshbach resonance

is crucial in this system for understanding the control of the s-wave scattering length, a. By using such a resonance the mean-field interaction strength can be tuned through a wide range of values ranging from weakly attractive ($a < 0$) to weakly repulsive ($a > 0$). It was suggested by Leggett in 1980 [20] and later others [44, 21, 22] that this system provides a unique opportunity to study the crossover behavior between BCS type superfluidity, caused by momentum correlated pairs of fermions, to a Bose-Einstein condensate (BEC) of diatomic molecules. Interestingly, this connection between two different types of superfluidity was predicted to happen smoothly, without a phase change in between. Since these predictions, the experimental realization of this crossover has been achieved [12, 13, 14, 15, 16, 17], and theoretical descriptions of the strongly interacting regime abound, from quantum Monte Carlo treatments [45, 24] to extensions of the BCS wave function into the unitarity regime [46, 47, 48, 49]. Recently, in the original work of Tan [50, 51, 52] and others [53, 54, 55], a full description of the ultracold Fermi gas has been found in terms of a single quantity, the so called contact parameter. Despite the intense effort directed at this system, a complete description has yet to be achieved.

Understanding the BEC side of the resonance requires knowledge of the dimer-dimer scattering length. Initially, this was found in the first Born approximation [56, 21] and through mean field theory [56, 21] to be $a_{dd} \approx 2a$, and later by Pieri and Strinati, through a diagrammatic approach, to be $a_{dd} \approx 0.73a$ [57]. It wasn't until a complete solution to the four-fermion problem was extracted in 2004 by Petrov, Salomon and Shlyapnikov [23, 6] that the actual dimer-dimer scattering length, in large a limit, was found, $a_{dd} = 0.60(2)a$. Through correlated Gaussian methods, von Stecher, Blume and Greene [58, 8] were able to refine this prediction and extract the effective range correction. In a basic sense, the four-fermion problem represents the simplest system that could exhibit the physics of the crossover problem.

1.2 Three-body physics and the Efimov effect

While basic few body physics is necessary for understanding the behavior of ultracold many body systems, there is still considerable interest in the behavior of pure few-body dynamics. One area that is of considerable current interest is in the famous Efimov effect first predicted in 1970 by Vitaly Efimov [59, 32]. Efimov studies a three boson system with short-range two-body interactions in which each two-body system is infinitesimally away from forming a bound state; that is, the s-wave scattering length is infinite. Under these conditions, he found that the three-body system could form an infinite number of weakly bound trimer states with geometrically spaced binding energies. The qualitative understanding of this effect is natural, in retrospect. If the two-body sub-system is barely unable to form a bound state, it is natural to think that the extra attraction from the third particle is enough to push the system over the top. Quantitatively, Efimov and later others, found that this effect is described by a simple wave function in the hyperspherical representation [60, 26, 27].

The result on resonance can easily be extended to all scattering lengths when a is much greater than the range of the two-body interaction. It was later predicted that Efimov states should be observable through resonances in the three-body recombination rate for negative scattering lengths [26, 61]. In 2006 the first strong experimental evidence of such a resonance was observed in an ultra-cold gas of ^{133}Cs by Kraemer et. al. [62]. Unfortunately, only a single resonance has been seen to date. To confirm this as an Efimov resonance, the characteristic geometric scaling of at least two resonances must be seen. The resonance observed in [62] could be caused by a d-wave resonance in the scattering cross section [63] or possibly by a three-body Fano-Feshbach resonance attached to an excited three-body scattering threshold [29]. More recently, a resonance in the atom-dimer relaxation rate has been seen observed [64], which might be another indication of the presence of an Efimov state at positive scattering length. Predictions

focusing on the four-body loss rate [65] have recently given another handle on characterizing an Efimov resonance. The experimental realization of these predictions is still ongoing.

1.3 Dissertation structure

In Chapter 2 of this dissertation I give a brief introduction to hyperspherical coordinates with examples of possible parameterizations of the hyperangles. The parameterization method used is common and described thoroughly in Refs. [5, 66]. I also introduce the idea of the generalized angular momentum, or hyperangular momentum, and give it explicitly in terms of the hyperangles. These results are then used to analyze N non-interacting particles in an isotropic oscillator, the results of which give a useful example of the utility of hyperspherical coordinates.

Chapter 3 applies the results of Chapter 2 to generate a variational wavefunction, called the K-harmonic, for the two-component degenerate Fermi gas. This method is an extension of existing studies in Bose-Einstein condensates [67, 68]. Within this approximation, it is shown that zero-range Fermi pseudo-potential interactions predict an unphysical collapse behavior that is not seen in experiment or more complete quantum Monte Carlo studies of the system. I then show that this collapse can be averted through the use of a density dependent interaction. These results are extended to allow for multiple spin components.

In Chapter 4 the K-harmonic method is extended to allow for anisotropic trapping potentials by breaking the hyperspherical coordinates into a hypervectorial parameterization. This method is shown to reproduce the ground state energy and RMS radius of the gas predicted in Chapter 3. By performing a normal mode analysis the low energy excitation frequencies are extracted. These frequencies disagree both qualitatively and quantitatively with those observed experimentally, and disagree with predictions in the unitarity regime, $a \to -\infty$, from other theoretical methods. While this result is

disheartening, the methods presented are an initial step for further studies proposed in the chapter.

Chapter 5 departs from the variational treatments in the previous chapters and introduces the adiabatic hyperspherical representation. The hyperangular Green's functions is derived here for an arbitrary number of dimensions and applied to the three-body problem with regularized zero-range interactions. The resulting transcendental equation can be used to find the adiabatic potentials for an arbitrary three-body system in which the scattering lengths between particles is greater than the range of the interactions. Combined with the general form of the non-adiabatic corrections, three-body scattering at low temperatures becomes an intuitive process. These very general results are applied to the case of the lowest three hyperfine components of ^{6}Li. The Green's function method for three interacting particles is then extended to allow for multi-channel two-body interactions for identical bosons. By creating a resonance at an excited two-body scattering threshold, I predict a new series of Efimov states that are attached to an excited three-body scattering threshold, and embedded in the three-body continuum. These states can be interpreted as true three-body Fano Feshbach resonances.

Chapter 6 examines the four-fermion problem with positive s-wave scattering lengths. By utilizing a unique variational, non-orthogonal basis set, the hyperradial potential curves and their non-adiabatic corrections are found. These potentials are then used to analyze elastic and inelastic dimer-dimer scattering in the large scattering length regime. By describing dimer-dimer scattering through a complex, energy dependent scattering length, both elastic scattering and inelastic dimer breakup are analyzed. The results of this study are shown to compare favorably with existing theoretical predictions and extend beyond their range of validity. I then develop a new analysis based on Fermi's golden rule for describing the process of dimer-dimer relaxation, the results of which compare well with experimentally observed relaxation rates.

Chapter 7 provides a brief summary of the results of this dissertation and discusses

some future avenues of inquiry.

Chapter 2

Hyperspherical Coordinates

Strictly speaking an overview of hyperspherical coordinates is not really needed for this thesis, as there are many excellent existing works on the subject (see for instance [30, 31, 66, 5, 38, 67]). This section is included here for completeness, also some of the ideas and derivations will be useful in later chapters. To begin, consider a d dimensional Cartesian space whose coordinate axes are given by $\{x_i\}_{i=1}^{d}$. For the majority of this thesis these coordinates can be considered to be the components of a set of Jacobi vectors or the components of a set of trap centered vectors, but for now I will proceed with a more abstract approach. The basic concept of the hyperradius was introduced in the previous chapter. I define it explicitly here as

$$R^2 = \sum_{i=1}^{d} x_i^2. \tag{2.1}$$

While this definition will be used here, often a mass scaling will be inserted. For instance in a trap centered system of equal mass atoms an extra factor of $1/N$, where N is the number of atoms, will be used to simplify the interpretation of the hyperradius. For the purposes of this section, though, this definition will be adequate. With Eq. 2.1, the d dimensional Laplacian can be rewritten in terms of the hyperradius [66, 5]:

$$\nabla^2 = \sum_{i=1}^{d} \frac{\partial^2}{\partial x_i^2} = \frac{1}{R^{d-1}} \frac{\partial}{\partial R} R^{d-1} \frac{\partial}{\partial R} - \frac{\mathbf{\Lambda}^2}{R^2}. \tag{2.2}$$

In this equation $\mathbf{\Lambda}$ is called the hyperangular momentum, or grand angular momentum operator, the square of which is given by

$$\mathbf{\Lambda}^2 = \sum_{i>j} -|\Lambda_{ij}|^2 , \tag{2.3}$$
$$\Lambda_{ij} = x_i \frac{\partial}{\partial x_j} - x_j \frac{\partial}{\partial x_i}.$$

Already the d dimensional Laplacian has a rather pleasing form reminiscent of its 3D counterpart. In fact if d is taken to 3, Eq. (8) reduces exactly to the three dimensional Laplacian in spherical coordinates, and $\mathbf{\Lambda}$ becomes merely the normal spatial angular momentum operator. To proceed from here a way of defining the remaining $d-1$ degrees of freedom in terms of angles is needed.

2.1 Defining the hyperangles: Delve's coordinates

Unfortunately, or possibly fortuitously depending on your view point, there is no unique way to define the hyperangles in a given system. Here I will use a simple, standardized method of defining them used by many others [34, 38, 67, 5, 1, 2] in the form of the so called Delve's coordinates [30, 31]. I will begin by examining a well known example of hyperspherical coordinates, that of normal spherical polar coordinates. Clearly these coordinates can be used to describe the relative motion of 2 particles in 3 dimensions or the position of a single particle in a trap-centered coordinate system, but it can also be used in less obvious ways. For instance, spherical polar angles may be used to describe the relative motion of 4 particles in 1 dimension.

The components of a three dimensional vector, $\vec{r}$, can be written in terms of a radius and two angles as

$$x = r\cos\phi\sin\theta, \tag{2.4}$$
$$y = r\sin\phi\sin\theta, \tag{2.5}$$
$$z = r\cos\theta. \tag{2.6}$$

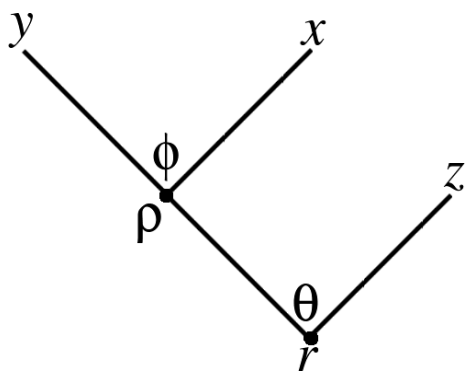

Figure 2.1: The tree that gives the standard spherical coordinates for a 3 dimensional system is shown.

This parameterization can be represented in a simple tree structure shown in Fig. 2.1. The end points of the tree represent each component of the vector $\vec{r}$, and each node in the tree is represents an angle. Also associated with each node is a sub radius. For the lowest node the "subradius" is merely the total length of the vector, r. For the upper node the subradius is merely the cylindrical radius $\rho = \sqrt{x^2 + y^2}$. Using the tree structure from Fig. 2.1, a set of rules can be developed for extracting the parameterization of Eqs. 2.4, 2.5, and 2.6. Starting at the bottom node with total radius, r, move up through the tree to the desired coordinate. For each move through the tree, if you move to the left (right) from a node multiply by the sine (cosine) of the angle associated with that node. Continue until you reach the Cartesian component.

This procedure can be generalized readily from three to d dimensions. Start by building a tree with d free ends and $d-1$ nodes, associate an angle with each node and follow the above rules. Using the tree structure, starting at the bottom node with total hyperradius, R, move up through the tree to the desired coordinate. If you move to the left (right) from a node, multiply by the sine (cosine) of the angle associated with that node. Continue until you have reach the desired Cartesian component. A specific tree for d dimensions is shown in Fig. 2.2. Following the rules this tree gives the hyperangular representation

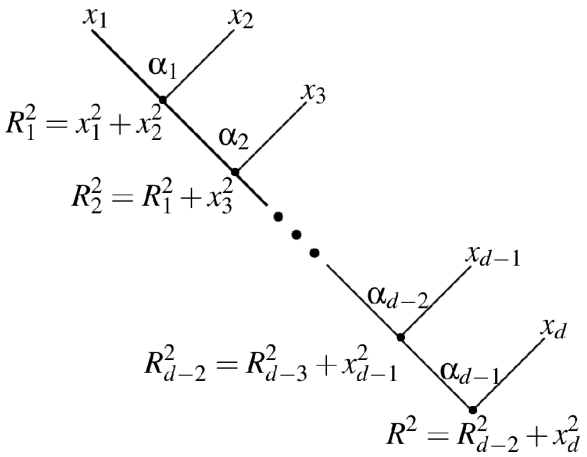

Figure 2.2: The canonical tree that gives a hyperangular parameterization for a d dimensional system is shown.

$$x_n = R\cos\alpha_{n-1}\prod_{j=n}^{d-1}\sin\alpha_j, \tag{2.7}$$

$$0 \le \alpha_j \le \pi,\ j = 2, ..., d-1$$

$$0 \le \alpha_1 \le 2\pi$$

where $\cos\alpha_0 \equiv 1$ and $\prod_{j=d}^{d-1}\sin\alpha_j \equiv 1$. This can also be written as

$$\tan\alpha_n = \frac{\sqrt{\sum_{j=1}^{n} x_j^2}}{x_{n+1}}, \tag{2.8}$$

$$n = 1, 2, 3, ..., d-1.$$

This hyperspherical tree has been dubbed the canonical tree [66, 5] as it is simple to construct and very easy to add more dimensions to.

To avoid double counting, the range that the hyperangles take on is restricted depending on how many free branches are attached to the node corresponding to a given angle. If the node has two free branches, then the angle takes on the full range 0 to 2π. If the node has one free branch attached, the angle goes from 0 to π. If the node has no free branches attached to it, the associated angle goes from 0 to $\pi/2$. Following these

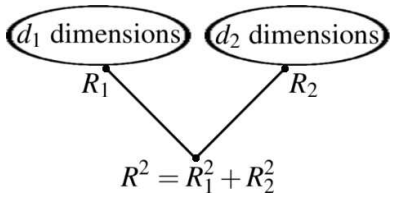

Figure 2.3: The tree structure used to correlate two subspaces to a single hyperradius.

rules for the canonical tree gives the ranges of the angles α_i,

$$0 \leq \alpha_1 \leq 2\pi,$$

$$0 \leq \alpha_i \leq \pi, i = 2, ..., d-1.$$

Another slightly more abstract way of considering this construction is to start by breaking the d dimensional space into two subspaces of dimension d_1 and d_2, and assuming that these two subspaces are already described by two sets of sub-hyperspherical coordinates, (R_1, Ω_1) and (R_2, Ω_2). With these assumptions all that remains is to correlate the sub-hyperradii. This is done by following the type of procedure described above using the tree structure shown in Fig. 2.3,

$$R_1 = R \sin\alpha, \tag{2.9}$$

$$R_2 = R \cos\alpha,$$

where α is now the final hyperangle in the system. Using this procedure recursively, one can define the hyperangles in the subspaces until the only remaining subspaces are the individual Cartesian components of the total d dimensional space. The concept of dividing the total space up into subspaces will prove very useful in later chapters.

As a final example of hyperangular parameterizations, I introduce a parameterization for N 3-dimensional vectors $\{\vec{\rho}_i\}_{i=1}^N$. One could break each vector up into its individual components and use the canonical parameterization from Eq. 2.7, but this removes much of the spatial physical intuition that one could bring to bear, such as the

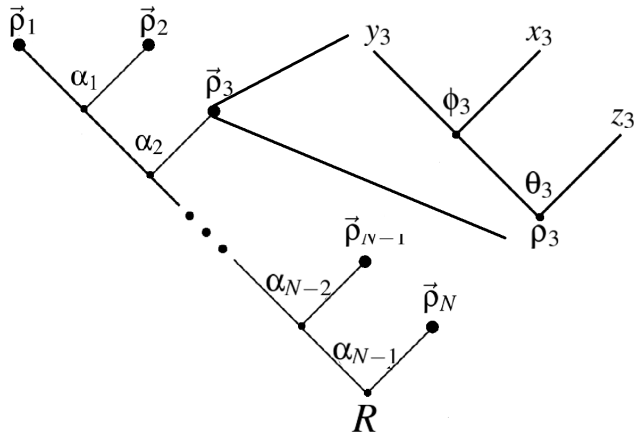

Figure 2.4: The tree structure used to parameterize the hyperangles for N three dimensional vectors is shown. Note that the dot at the end of each branch in the tree on the left stands for a spherical polar tree.

individual spatial angular momentum corresponding to each vector. Instead one can use a variation on the canonical tree shown in Fig. 2.4. On first glance, this tree might seem the same as the canonical tree shown in Fig. 2.2. In this case, though, the large dot at the end of each branch represents the spherical polar sub-tree of the form shown in Fig. 2.1 for each vector $\vec{\rho}_i$. Using this tree structure and following the rules outlined above, $2N$ of the $3N-1$ hyperangles are given by the normal spherical polar angles for each vector, $(\theta_1, \phi_1, \theta_2, \phi_2, ..., \theta_N, \phi_N)$. The remaining $N-1$ hyperangles are given by

$$\begin{aligned} \tan\alpha_i &= \frac{\sqrt{\sum_{j=1}^{i}\rho_j^2}}{\rho_{i+1}}, \\ 0 \leq \alpha_i &\leq \frac{\pi}{2}, \\ i &= 1, 2, 3, ..., N-1. \end{aligned} \tag{2.10}$$

where ρ_i is the length of the ith vector. It will be shown in the next section that this parameterization is useful when spatial angular momentum plays a role in the problem of interest. For completeness, following the rules laid out in Appendix A, the hyperangular

volume element that results from this parameterization is given by

$$d\Omega = \left(\prod_{i=1}^{N} d\omega_i\right)\left(\prod_{j=1}^{N-1} \cos^2\alpha_j \sin^{3j-1}\alpha_j\right)$$

where ω_i is the normal spherical polar differential volume for $\vec{\rho}_i$.

2.2 Hyperangular momentum and hyperspherical harmonics

The hyperangular momentum operator in terms of hyperangular coordinates can be found by using the fact that each subset of Cartesian components is itself a Cartesian vector space. With that in mind, consider the hyperspherical tree given by Fig. 2.3. By writing the Laplacian for each subspace in terms of the sub-hyperradii R_1 and R_2 and the sub-hyperangular momentum operators $\mathbf{\Lambda}_1$ and $\mathbf{\Lambda}_2$ the total hyperangular momentum operator can be extracted [66]. It is

$$\begin{aligned}\mathbf{\Lambda}^2 = &\frac{-1}{\sin^{(d_1-1)/2}\alpha\cos^{(d_2-1)/2}\alpha}\frac{\partial^2}{\partial\alpha^2}\sin^{(d_1-1)/2}\alpha\cos^{(d_2-1)/2}\alpha \\ &+\frac{\mathbf{\Lambda}_1^2+(d_1-1)(d_1-3)/4}{\sin^2\alpha}+\frac{\mathbf{\Lambda}_2^2+(d_2-1)(d_2-3)/4}{\cos^2\alpha}-\frac{(d-1)(d-3)+1}{4}.\end{aligned} \tag{2.11}$$

where α is defined as in Eq. 2.9 and $\mathbf{\Lambda}_i$ is the sub-hyperangular momentum of the subspace of dimension d_i. If one of the subspaces corresponds to a single Cartesian component then the sub-hyperangular momentum for that space is zero, i.e. if $d_i = 1$ then $\mathbf{\Lambda}_i^2 = 0$. To find $\mathbf{\Lambda}_1^2$ ($\mathbf{\Lambda}_2^2$), ones needs only to apply Eq. 2.11 recursively to each subspace. In this way, there is a sub-hyperangular momentum operator associated with each node in any given hyperspherical tree.

It is useful to be able to diagonalize the hyperangular momentum operator. The eigenfunctions of $\mathbf{\Lambda}^2$ are detailed in several references (See Refs. [34, 38, 5] for example), and the method of constructing them is given in Appendix A. These functions, $Y_{\lambda\mu}(\Omega)$, are called hyperspherical harmonics. Their eigenvalue equation is

$$\mathbf{\Lambda}^2 Y_{\lambda\mu}(\Omega) = \lambda(\lambda+d-2)\,Y_{\lambda\mu}(\Omega), \tag{2.12}$$

where $\lambda = 0, 1, 2, ...$ is the hyperangular momentum quantum number. The index μ enumerates the degeneracy for each λ and can be thought of as the collection of sub-hyperangular momentum quantum numbers that result from a given tree. Hyperspherical harmonics are also constructed as to diagonalize the sub-hyperangular momenta of each node in a given hyperspherical tree, e.g.

$$\mathbf{\Lambda}_1^2 Y_{\lambda\mu}(\Omega) = \lambda_1 (\lambda_1 + d_1 - 2) Y_{\lambda\mu}(\Omega), \tag{2.13}$$

where $\lambda_1 = 0, 1, 2, ...$ is the sub-hyperangular momentum quantum number associated with Λ_1^2. The total hyperangular momentum quantum number λ is limited by the relation

$$\lambda = |\lambda_1| + |\lambda_2| + 2n, \tag{2.14}$$

where n is a non-negative integer. The absolute values in this case are there to allow for when either d_1 or d_2 are 2. In this special case the hyperangular momentum quantum number λ_i associated with the two dimensional subspace can be negative, as with the magnetic quantum number, m, in spherical polar coordinates. Equation 2.14 only applies if both d_1 and d_2 are greater than 1. If, for instance $d_2 = 1$, then the restriction takes on the form

$$\lambda = |\lambda_1| + n.$$

The behavior illustrated in Eq. 2.13 clearly demonstrates why the parameterization shown in Fig. 2.4 is useful. Each three dimensional spherical polar subtree will have a spatial angular momentum and z-projection associated with it, e.g.

$$l_i^2 Y_{\lambda\mu}(\Omega) = l_i (l_i + 1) Y_{\lambda\mu}(\Omega),$$

where l_i^2 is the square of the angular momentum operator for the ith vector. This property allows for addition of angular momentum in the normal way, through sums over magnetic quantum numbers and Clebsch-Gordan coefficients. Now that the hy-

perspherical harmonics are defined, it is useful to examine a simple example applying them.

2.2.1 N bodies in a trap

Here I examine a simple example that demonstrates the utility of hyperspherical coordinates, that of N particles of mass m in a spherically symmetric oscillator trap. This example can be found in Refs. [69, 1], but I show it here as the results will prove very useful. The Hamiltonian for this system is given by

$$H = \sum_{i=1}^{N} \left(-\frac{\hbar^2}{2m} \nabla_i^2 + \frac{1}{2} m\omega^2 r_i^2 \right), \tag{2.15}$$

where $\vec{r}_i$ is the position of the ith particle with respect to the trap center, and ∇_i^2 is the normal 3D Laplacian with respect to $\vec{r}_i$. This system is trivially solved by a product of single particle oscillator states whose radial behaviors are the solutions of the single particle Schrödinger equation,

$$\left(\frac{-\hbar^2}{2m} \left(\frac{d^2}{dr^2} - \frac{l\,(l+1)}{r^2} \right) + \frac{1}{2} m\omega^2 r^2 - E_{n\ell} \right) r f_{n\ell}\,(r) = 0. \tag{2.16}$$

The solution to this is well known and is given by

$$r f_{nl}\,(r) = A_{nl} \exp\left(-r^2/2\ell\right) \left(\frac{r}{\ell}\right)^{l+1} L_n^{l+1/2} \left(\frac{r^2}{\ell^2}\right), \tag{2.17}$$

with energy $E_{n\ell} = \hbar\omega\,(2n + l + 3/2)$, where $\ell = \sqrt{\hbar/m\omega}$ and n is the number of radial nodes in the wavefunction.

This problem can also be solved in terms of hyperspherical harmonics and their resulting hyperangular momentum quantum number λ. The hyperradius for this $3N$ dimensional system can be defined along the lines of Eq. 2.1 with an extra factor of $1/N$:

$$R^2 = \frac{1}{N} \sum_{i=1}^{N} r_i^2 \tag{2.18}$$

giving a clear interpretation of the hyperradius as the coordinate parameterizing the rms radius of the gas. For this treatment, the explicit form of the hyperangles will

not be needed; for completeness, though and to tie into the previous section, the full hyperangular parameterization is given, but it is clear that they may be defined using the parameterization described in the section 2.1.

Transformation of (2.15) into hyperspherical coordinates using Eqs. 2.18 and 2.2 yields a Schrödinger equation that separates into hyperradial and hyperangular pieces. The hyperangular solution is a hyperspherical harmonic that diagonalizes $\mathbf{\Lambda}^2$. After removing first derivative terms in the hyperradius, the resulting hyperradial Schrödinger equation is given by

$$\left(\frac{-\hbar^2}{2M}\left(\frac{d^2}{dR^2}-\frac{K\left(K+1\right)}{R^2}\right)+\frac{1}{2}M\omega^2R^2-E\right)R^{(3N-1)/2}F\left(R\right)=0, \tag{2.19}$$

where $K=\lambda+3\left(N-1\right)/2$ and $M=Nm$. Comparing this with Eq. 2.16 one can see that if the substitutions $l\rightarrow K$, $n\rightarrow\chi$, $m\rightarrow M$, $r\rightarrow R$ and $rf_{nl}\left(r\right)\rightarrow R^{(3N-1)/2}F_{\chi K}\left(R\right)$ are made, the single particle radial Schrödinger equation becomes the N particle hyperradial Schrödinger equation. With these replacements the hyperradial solution to Eq. 2.19 is evidently

$$R^{(3N-1)/2}F_{\chi K}\left(R\right)=A_{\chi K}\exp\left(-R^2/2\mathcal{L}\right)\left(\frac{R}{\mathcal{L}}\right)^{K+1}L_{\chi}^{K+1/2}\left(\frac{R^2}{\mathcal{L}^2}\right), \tag{2.20}$$

where $\mathcal{L}=\ell/\sqrt{N}$, and χ is the number of hyperradial nodes in the N body system. The total energy of the N-body system is then given by

$$E_{\chi K}=\hbar\omega\left(2\chi+K+\frac{3}{2}\right)=\hbar\omega\left(2\chi+\lambda+\frac{3N}{2}\right). \tag{2.21}$$

With this result comes a different understanding of hyperspherical harmonics. The non-interacting oscillator is separable in both the independent particle coordinates $\{\vec{r}_i\}_{i=1}^{N}$ and in hyperspherical coordinates $\{R,\Omega\}$. This yields a relationship between the hyperspherical quantum numbers χ and λ and the single particle quantum numbers n_i, the number of radial nodes for the ith particle, and l_i, the ith particle's angular momentum, i.e.

$$2\chi+\lambda=\sum_{i=1}^{N}\left(2n_i+l_i\right). \tag{2.22}$$

It should be noted that this does not mean that the independent particle solution and the hyperspherical solution are exactly same, only that the hyperspherical solution $R^{(3N-1)/2}G_{\chi K}(R)\,Y_{\lambda\mu}(\Omega)$ must be a linear combination of independent particle solutions of the same energy, i.e.

$$R^{(3N-1)/2}G_{\chi K}(R)\,Y_{\lambda\mu}(\Omega)=\sum_k a_k\left[\prod_{i=1}^{N} r_i f_{n_i^k l_i^k}(r_i)\,y_{l_i^k m_i^k}(\omega_i)\right], \tag{2.23}$$

where $y_{lm}(\omega)$ is a normal spherical harmonic of the spatial solid angle ω and $\left(n_i^k, l_i^k, m_i^k\right)$ are the quantum numbers associated with the ith particle in the kth state subject to Eq. 2.22.

Equation 2.23 leads to an alternative way of constructing hyperspherical harmonics through oscillator function. Timofeyuk [70, 71] and Fabre de le Ripelle [72, 73] have done just that by finding the linear combination of independent particle oscillator solutions that produce a hyperradially nodeless solution, $\chi=0$. It is also worth noting that the hyperradius R is invariant under any permutation of particle coordinates, meaning that any permutation symmetry in the system (e.g. bosonic or fermionic symmetry) must be contained in the hyperspherical harmonic.

By finding a linear combination of independent particle solutions that correspond to the ground state of the system subject to a specific permutational symmetry it can easily be shown [1] through Eqs. 2.22 and 2.23 that the N-body wavefunction must diagonalize the hyperangular momentum operator Λ^2 with eigenvalue

$$\lambda_{GS}=\sum_{i=1}^{N}\left(2n_i^{GS}+l_i^{GS}\right). \tag{2.24}$$

Here "GS" indicates that the given quantum numbers are associated with the ground state of the system. This relationship follows from expanding a ground state independent particle N-body wavefunction in terms of noninteracting hyperspherical wavefunctions:

$$\Psi_{GS}(\vec{r}_1,\vec{r}_2,...,\vec{r}_N,\sigma_1,\sigma_2,...,\sigma_N)=\sum_\nu c_\nu R^{(3N-1)/2}G_{\chi_\nu K_\nu}(R)\,Y_{\lambda_\nu\mu_\nu}(\Omega,\sigma_1,\sigma_2,...,\sigma_N).$$

Here I have incorporated the possibility of additional spin coordinates $(\sigma_1, \sigma_2, ..., \sigma_N)$ to allow for the possibility of multi-component Fermi gasses. I will further assume that the ground state in question consists only of linear combinations of permutations of the product of N single particle oscillator states with spin components. For instance in a Fermi gas this would be a standard Slater determinant state. The energy of this ground state is then given by

$$E_{GS} = \sum_{i=1}^{N} \hbar\omega \left(2n_i + l_i + \frac{3}{2}\right).$$

This combined with Eq. 2.22 gives the relation between the hyperspherical quantum numbers and the independent particle quantum numbers,

$$2\chi_\nu + \lambda_\nu = \sum_{i=1}^{N} (2n_i + l_i)$$

for each ν in the expansion. Now all of the ground state permutational symmetry is contained in the hyperangular function so if $R^{(3N-1)/2} G_{0K_\nu}(R)\, Y_{\lambda_\nu \mu_\nu}(\Omega, \sigma_1, \sigma_2, ..., \sigma_N)$ is considered, it will have the appropriate symmetry with an energy of

$$E = \sum_{i=1}^{N} \hbar\omega \left(2n_i + l_i + \frac{3}{2}\right) - 2\chi_\nu,$$

which is less than than the ground state energy, a contradiction unless $\chi_\nu = 0$. Thus Eq. 2.24 has been shown.

The hyperspherical harmonics,

$$Y_{\lambda_{GS}\mu}(\Omega, \sigma_1, \sigma_2, ..., \sigma_N) = \frac{\Psi_{GS}(\vec{r}_1, \vec{r}_2, ..., \vec{r}_N, \sigma_1, \sigma_2, ..., \sigma_N)}{R^{(3N-1)/2} G_{0K_{GS}}(R)}, \tag{2.25}$$

corresponding to the ground state eigenvalue, λ_{GS}, are called the K harmonics, a concept that will be used heavily in Chapter 3. It is useful to note that $Y_{\lambda_{GS}\mu}(\Omega, \sigma_1, \sigma_2, ..., \sigma_N)$ defined here is **independent** of the oscillator length ℓ, a fact that will be used in later sections. A derivation similar to the one shown here with the center of mass motion of the system removed can be found in Ref. [1].

Chapter 3

N Interacting Fermions in a Trap Under the K-Harmonic Approximation

The realization of the degenerate Fermi gas (DFG) in a dilute gas of fermionic atoms has triggered widespread interest in the nature of these systems. This achievement combined with the use of a Fano-Feshbach resonance allows for a quantum laboratory in which many quantum phenomena can be explored over a wide range of interaction strengths. This leads to a large array of complex behaviors including the discovery of highly correlated BCS-like pairing for effectively attractive interactions [13, 15, 16, 17, 14]. There are many theoretical studies of these systems ranging from quantum Monte Carlo techniques [45, 24] to extending the BCS pairing wavefunction into the strongly interacting regime [48, 46, 49, 74]. In this chapter I propose a simpler variational treatment of this highly complex system. The methods presented here cannot completely describe the full nature of the system. They do however represent an important bridge between many-body systems and the world of hyperspherical coordinates which are often associated with few-body techniques [34, 41, 40]. Many of the results of this chapter can be found in Refs. [1, 2].

The starting point of the K harmonic method describes the degenerate Fermi gas with a set of $3N-1$ hyperangular coordinates on the surface of a $3N$ dimensional hypersphere of hyperradius R, where N is the number of atoms in the system. This formulation is a variational treatment of the N-body problem in which the hyperangular

behavior of the system is approximated by that of the non-interacting degenerate Fermi gas presented in Section 2.2.1. At first glance this approach might seem non-intuitive, but it is natural to assume that, in a first approximation, the behavior of the gas will be determined by its overall spatial extent. This type of approach has been used in studying Bose-Einstein condensates [67, 68, 75] and it has also been applied to finite nuclei [5, 71]. The theoretical approach developed here shares some mathematical kinship with D-dimensional perturbation theory; for instance, the $N \to \infty$ and $D \to \infty$ limits both result in wavefunctions perfectly localized in the hyperradius. However, the goals and motivations of the K-harmonic method differ for the most part from those of Ref. [76, 77, 78].

The main goal of this chapter is to describe the motion of the gas in a **single** collective coordinate R, which describes the overall extent of the gas. The benefit of this strategy is that the behavior of the gas is reduced to a single one-dimensional **linear** Schrödinger equation with an effective hyperradial potential. The use of a real potential then lends itself to the intuitive understanding of normal Schrödinger quantum mechanics. This method also allows for the calculation of physical quantities such as the energy and rms radius of the ground state; these observables agree quantitatively with those computed using Hartree-Fock methods. The method also yields a visceral understanding of a low energy collective oscillation of the gas, i.e. a breathing mode.

This chapter is arranged as follows. In Section 3.1 the K-harmonic method is introduced in general. In Section 3.2 the method is applied to a system of fermions interacting through a bare zero-range potential. In Section 3.3 the results from the bare zero-range potential are presented and discussed. In Section 3.4, I apply the K-harmonic method to a density dependent zero-range interaction and present the results.

3.1 The K-harmonic approximation

In this chapter I consider a collection of N identical fermionic particles of mass m in a spherically symmetric oscillator trap with oscillator frequency ω, distributed equally between two internal spin substates. The method presented here is similar to that of Refs. [67, 68, 75] in which the K-harmonic method is applied to a Bose gas. This study expands the method to a fermionic system. The Hamiltonian that governs this system is given by

$$H = \frac{-\hbar^2}{2m}\sum_{i=1}^{N}\nabla_i^2 + \frac{1}{2}m\omega^2\sum_{i=1}^{N}r_i^2 + \sum_{i>j}U_{int}\left(\vec{r}_{ij}\right) \tag{3.1}$$

where $U_{int}\left(\vec{r}\right)$ is an arbitrary two-body interaction potential and $\vec{r}_{ij} = \vec{r}_i - \vec{r}_j$. Interaction terms involving three or more bodies are ignored. In general, the Schrödinger equation that comes from this Hamiltonian is very difficult to solve. The goal here is to simplify the system by describing its behavior in terms of a single collective coordinate, the hyperradius defined by Eq. 2.18. Using Eqs. 2.2 and 2.18 it is simple to write the Schrödinger equation in terms of the hyperradius and hyperangles as

$$\begin{aligned} 0 = \Bigg[\frac{-\hbar^2}{2M}\left(\frac{\partial^2}{\partial R^2} - \frac{\left(3N-3\right)\left(3N-1\right)}{4R^2} - \frac{\Lambda^2}{R^2}\right) \\ + \frac{1}{2}M\omega^2R^2 + \sum_{i>j}U_{int}\left(\vec{r}_{ij}\right) - E\Bigg] R^{(3N-1)/2}\Psi\left(R,\Omega\right) \end{aligned} \tag{3.2}$$

where $\Psi\left(R,\Omega\right)$ has been multiplied by $R^{(3N-1)/2}$ to remove first derivative terms in the hyperradius. Here Λ is the grand angular momentum operator defined in Eq. 2.3. The heart of the K-harmonic approximation lies in the variational ansatz that the wavefunction Ψ can be separated into a hyperradial function and a hyperangular function. The hyperangular function is then fixed to the behavior of a non-interacting degenerate Fermi gas, i.e.

$$\Psi\left(R,\Omega\right) = F\left(R\right)Y_{\lambda\mu}\left(\Omega,\sigma_1,\sigma_2,...,\sigma_N\right), \tag{3.3}$$

where $Y_{\lambda\mu}$ is the K-harmonic described by Eq. 2.25 as

$$Y_{\lambda\mu}(\Omega) = \frac{\sum_{P}(-1)^{p} P \prod_{i=1}^{N} f_{n_i l_i}(r_i)\, y_{l_i m_i}(\omega_i)\, \langle \sigma_i | m_{s_i} \rangle}{G_{0K}(R)}. \tag{3.4}$$

In this expression, $f_{n_i l_i}(r_i)$ is the radial solution to the independent particle harmonic oscillator for the ith particle given by

$$r f_{nl}(r) = N_{n\ell} \exp\left(-r^2/2\ell^2\right) (r/\ell)^{l+1} L_n^{l+1/2}\left[(r/\ell)^2\right],$$

where $L_n^{\alpha}(r)$ is an associated Laguerre polynomial with $\ell = \sqrt{\hbar/m\omega}$. $y_{l_i m_i}(\omega_i)$ is an ordinary 3D spherical harmonic with ω_i the spatial solid angle for the ith particle and $|m_{s_i}\rangle$ is a spin ket that will allow for two spin species of atoms, $|\uparrow\rangle$ and $|\downarrow\rangle$. The sum in Eq. 3.4 runs over all possible permutations P of the N spatial and spin coordinates in the product wavefunction. The spin coordinates in $Y_{\lambda\mu}(\Omega, \sigma_1, \sigma_2, ..., \sigma_N)$ have been dropped for notational simplicity. The numerator on the right hand side of Eq. 3.4 corresponds to the ground state of the Fermi gas in which each particle successively fills a single particle state.

To utilize the trial wavefunction, Eq. 3.3, the expectation value $\langle Y_{\lambda\mu} | H | Y_{\lambda\mu} \rangle$ is taken, where the integration is over all hyperangles and spin coordinates at a fixed hyperradius. This approach gives a new effective linear 1D Schrödinger equation $H_{eff} R^{(3N-1)/2} F(R) = E R^{(3N-1)/2} F(R)$ in terms of an effective Hamiltonian H_{eff} given by

$$H_{eff} = \frac{-\hbar^2}{2M}\frac{d^2}{dR^2} + V_{eff}(R), \tag{3.5}$$

$$V_{eff}(R) = \frac{\hbar^2 K(K+1)}{2MR^2} + \frac{1}{2}M\omega^2 R^2 + \sum_{i>j}\langle Y_{\lambda\mu} | U_{int}(\vec{r}_{ij}) | Y_{\lambda\mu} \rangle. \tag{3.6}$$

where $V_{eff}(R)$ is an effective hyperradial potential. As in Eq. 2.19, here $K = \lambda + 3(N-1)/2$ and λ is given by Eq. 2.24. In the following sections I develop methods for evaluating the interaction expectation values for various two body interactions, and analyze the resulting effective potentials in the hyperradius.

It will later prove convenient to rescale this effective Hamiltonian in terms of non-interacting quantities to avoid divergences in the large N limit:

$$E = E_{NI} E' \tag{3.7}$$
$$R = \sqrt{\langle R^2 \rangle_{NI}} R',$$

which introduces the dimensionless variables of energy (E') and hyperradius (R'). Here the non-interacting energy E_{NI} and average hyperradius squared $\langle R^2 \rangle_{NI}$ are given explicitly by

$$E_{NI} = \left(\lambda + \frac{3N}{2}\right) \hbar\omega$$
$$\langle R^2 \rangle_{NI} = \left(\frac{\lambda}{N} + \frac{3}{2}\right) \ell^2.$$

Under this rescaling the effective hyperradial Schrödinger equation becomes

$$\left(\frac{-1}{2m^*}\frac{\partial^2}{\partial R'^2} + \frac{V_{eff}(R')}{E_{NI}} - E'\right) R'^{(3N-1)/2} F(R') = 0 \tag{3.8}$$

where $m^* = m E_{NI} N \langle R^2 \rangle_{NI} / \hbar^2$, and $V_{eff}(R')$ is the effective hyperradial potential in Eq. 3.6 evaluated at the rescaled hyperradius.

3.2 Bare zero-range s-wave interactions

The first two-body interaction considered here will be that of the well-known Fermi pseudo-potential [79],

$$U_{int}(\vec{r}) = \frac{4\pi\hbar^2 a}{2\mu_{2B}} \delta^{(3)}(\vec{r}) \tag{3.9}$$

where a is the s-wave scattering length, $\mu_{2B} = m/2$ is the two body reduced mass, and $\delta^{(3)}(\vec{r})$ is the Dirac δ-function. Normally a regularization factor of $\frac{\partial}{\partial r} r$ appears after the δ-function, but when considering a variational wave function whose derivative is regular at $r \to 0$ the regularization disappears, i.e. $\lim_{r\to 0} \frac{\partial}{\partial r} r\psi(r) = \lim_{r\to 0} \left[r\frac{\partial}{\partial r}\psi(r) + \psi(r)\right] = \psi(0)$. The use of zero-range contact interactions to model real interactions in atomic

systems has a long history [79]. The interest in these interaction models arises from the simplifications that can be made to the theory of complex systems [80, 81, 82].

Degenerate ground states cause some complications for this formulation. In this thesis these are avoided by restricting the system to the non-degenerate ground states that correspond to filled energy shells of the oscillator, i.e. "magic numbers" of particles. With moderate extensions the degeneracies can be taken into account by creating an interaction matrix, but the magic number restriction should still give a good description of the general behavior of systems with large numbers of atoms. The total number of atoms and the hyperangular momentum quantum number λ are most conveniently expressed in terms of the number n of single particle orbital energies filled:

$$N = \frac{n\left(n+1\right)\left(n+2\right)}{3} \tag{3.10a}$$

$$\lambda = \frac{\left(n-1\right)n\left(n+1\right)\left(n+2\right)}{4} \tag{3.10b}$$

$$k_f^0 = \sqrt{\frac{2m\omega}{\hbar}\left(n+\frac{1}{2}\right)}, \tag{3.10c}$$

where k_f^0 is the peak non-interacting Fermi wave number. In the limit where $N \gg 1$, λ and k_f^0 can be expressed in terms of the total number of particles N as

$$\lambda \to \frac{\left(3N\right)^{4/3}}{4}, \tag{3.11a}$$

$$k_f^0 \to \sqrt{\frac{2m\omega}{\hbar}\left(3N\right)^{1/3}}. \tag{3.11b}$$

I next calculate the interaction matrix element by combining 3.11a with $Y_{\lambda\mu}\left(\Omega\right)$ from 3.4

$$U_{eff}\left(R\right)\frac{4\pi\hbar^2 a}{2\mu_{2B}}\sum_{i>j}\left\langle Y_{\lambda\mu}\left|\delta^3\left(\vec{r}\right)\right|Y_{\lambda\mu}\right\rangle.$$

Since $Y_{\lambda\mu}\left(\Omega\right)$ is antisymmetric under particle exchange we may do a coordinate transposition in the sum, $\vec{r}_i \to \vec{r}_2$ and $\vec{r}_j \to \vec{r}_1$. Each transposition pulls out a negative sign

from Φ_λ and we are left with

$$\begin{aligned} U_{eff}(R) &= \frac{4\pi\hbar^2 a}{2\mu_{2B}} \sum_{i>j} \left\langle Y_{\lambda\mu} \left| \delta^3(\vec{r}_{12}) \right| Y_{\lambda\mu} \right\rangle \\ &= \frac{4\pi\hbar^2 a}{2\mu_{2B}} \frac{N(N-1)}{2} \left\langle Y_{\lambda\mu} \left| \delta^3(\vec{r}_{12}) \right| Y_{\lambda\mu} \right\rangle . \end{aligned}$$

To calculate $\left\langle Y_{\lambda\mu} \left| \delta^3(\vec{r}_{12}) \right| Y_{\lambda\mu} \right\rangle$ it is useful to start with a more general interaction. We assume that the interaction term in the total N body Hamiltonian is such that at a fixed hyperradius, $U_{int}(\vec{r}_{ij})$ is separable into a hyperradial function times a hyperangular integral, i.e.

$$U_{int}(\vec{r}_{ij}) \equiv V_{ij_R}(R) V_{ij_\Omega}(\Omega) . \tag{3.12}$$

From properties of the δ-function and Eq. 2.10 it is easy to see that the $U_{int}(\vec{r}) = \frac{4\pi\hbar^2 a}{2\mu_{2B}} \delta^3(\vec{r})$ fits this criterion. While $V_{ij_\Omega}(\Omega)$ might have some very complex form, it will be seen shortly that only the form of $V_{ij_R}(R)$ and $U_{int}(\vec{r}_{ij})$ will matter. This means that the hyperradial behavior of $U_{eff}(R)$ will be entirely determined by $V_{12_R}(R)$, i.e.

$$U_{eff}(R) = \frac{N(N-1)}{2} \left\langle Y_{\lambda\mu} \left| U_{int}(\vec{r}_{12}) \right| Y_{\lambda\mu} \right\rangle = \zeta \frac{N(N-1)}{2} V_{12_R}(R) , \tag{3.13}$$

where $\zeta = \left\langle Y_{\lambda\mu} \left| V_\Omega(\Omega) \right| Y_{\lambda\mu} \right\rangle$. To find ζ, the definition $Y_{\lambda\mu}(\Omega)$ from Eq. 3.4 is used, then $R^{3N-1} G_{0K}(R)^2$ is multiplied on both sides. Integrating over R and using Eq. 3.12 to replace $V_{12_R}(R) V_{12_\Omega}(\Omega)$ gives a simple equation that may be solved for ζ.

$$\frac{N(N-1)}{2} \zeta\alpha = \beta, \tag{3.14a}$$

$$\alpha = \int R^{3N-1} G_{0K}(R)^2 V_{12_R}(R) \, dR, \tag{3.14b}$$

$$\begin{aligned} \beta = & \frac{N(N-1)}{2} \int \left[\prod_{j=1}^{N} d^3 r_j \right] \sum_{P_1} (-1)^{p_1} P_1 \prod_{i=1}^{N} f_{n_i l_i}(r_i) \, y_{l_i m_i}(\omega_i) \left\langle \sigma_i | m_{s_i} \right\rangle , \\ & \times U_{int}(\vec{r}_{12}) \sum_{P_2} (-1)^{p_2} P_2 \prod_{i=1}^{N} f_{n_i l_i}(r_i) \, y_{l_i m_i}(\omega_i) \left\langle \sigma_i | m_{s_i} \right\rangle , \end{aligned} \tag{3.14c}$$

where I have used the fact that $R^{3N-1} dR d\Omega \propto \prod_{j=1}^{N} d^3 r_j$ [66]. The integral in β is a diagonal, determinantal matrix element and may be drastically simplified by using the

orthogonality of the single particle basis functions (for details see [83], §6-1):

$$\begin{aligned}\beta =& \frac{1}{2}\sum_{i,j=1}^{N}\int d^3r_1 d^3r_2 \\ &\times \left[\psi_i^*\left(\vec{r}_1\right)\psi_j^*\left(\vec{r}_2\right)U_{int}\left(\vec{r}_{12}\right)\psi_i\left(\vec{r}_1\right)\psi_j\left(\vec{r}_2\right)\right. \\ &\left. - \delta_{m_{s_i}m_{s_j}}\psi_i^*\left(\vec{r}_2\right)\psi_j^*\left(\vec{r}_1\right)U_{int}\left(\vec{r}_{12}\right)\psi_i\left(\vec{r}_1\right)\psi_j\left(\vec{r}_2\right)\right],\end{aligned} \tag{3.15}$$

where the sum runs over every independent particle state in the ground state wavefunction $\psi_i\left(\vec{r}\right)$. At this point it is convenient to specify $U_{int}\left(\vec{r}\right)$ as the pseudo-potential, Eq. 3.9. The pseudo-potential gives $V_{R_{12}}\left(R\right) = 1/R^3$, and using the definition of $G_{0K}\left(R\right)$ in Eq. 2.20 this yields

$$\alpha = \frac{\Gamma\left(\lambda + \frac{3\left(N-1\right)}{2}\right)}{\mathcal{L}^3\Gamma\left(\lambda + \frac{3N}{2}\right)}.$$

Substituting the pseudo-potential into Eq. 3.15 simplifies the sum considerably as

$$\beta = \frac{4\pi\hbar^2 a}{2\mu_{2B}}\int d^3r \sum_{\nu=1}^{N_1}\left|\psi_\nu\left(\vec{r}\right)\right|^2\sum_{\mu=1}^{N_2}\left|\psi_\mu\left(\vec{r}\right)\right|^2, \tag{3.16}$$

where the sum over ν (μ) is over all N_1 (N_2) of the spatial states occupied by particles in spin state 1 (2). In the case considered here, $N_1 = N_2 = N/2$, but it is clear how this can be generalized to polarized gases. Putting everything together with Eq. 3.5 yields an effective Schrödinger equation in the hyperradius:

$$\begin{aligned}ER^{(3N-1)/2}F\left(R\right) &= \left[\frac{-\hbar^2}{2M}\frac{d^2}{dR^2} + V_{eff}\left(R\right)\right]R^{(3N-1)/2}F\left(R\right), \\ V_{eff}\left(R\right) &= \frac{\hbar^2 K\left(K+1\right)}{2MR^2} + \frac{1}{2}M\omega^2R^2 + \frac{4\pi\hbar^2 a}{2\mu_{2B}}\frac{C_N}{N^{3/2}R^3},\end{aligned} \tag{3.17}$$

where

$$C_N = \frac{\ell^3\Gamma\left(\lambda + \frac{3N}{2}\right)\int d^3r \sum_{\nu=1}^{N/2}\left|\psi_\nu\left(\vec{r}\right)\right|^2\sum_{\mu=1}^{N/2}\left|\psi_\mu\left(\vec{r}\right)\right|^2}{\Gamma\left(\lambda + \frac{3\left(N-1\right)}{2}\right)}. \tag{3.18}$$

There are some interesting things to note about the effective potential V_{eff}. For $N = 1$, $C_N = 0$, $K = l$ and the effective Schrödinger equation become the Schrödinger

equation of a single particle in a trap. Note that the form of V_{eff} is very similar to the effective potential found for bosons by the authors of Ref. [67]. What may be surprising is the extra term of $3(N-1)/2$ contained in K. The kinetic energy term in V_{eff} is controlled by the hyperangular momentum, which in turn reflects the total nodal structure of the N-fermion wavefunction. This added piece of effective hyperangular momentum summarizes the energy cost of confining N fermions in the trap.

The large N behavior of C_N can be found by realizing that ψ_v in Eq. 3.16 is a non-interacting independent particle oscillator state, and the sum of $|\psi_\nu|^2$ over ν is the density of a single component,

$$\rho^{(1)}(\vec{r}) = \sum_{\nu=1}^{N/2} |\psi_\nu(\vec{r})|^2 . \tag{3.19}$$

In the limit $N \to \infty$, the Thomas-Fermi approximation [84], which should become exact for non-interacting oscillator states in the large N limit, gives

$$\rho^{(\chi)}(\vec{r}) = \frac{1}{6\pi^2}\left(\frac{2m\mu_\chi}{\hbar^2}\right)^{3/2}\left(1-\frac{m\omega^2 r^2}{2\mu_\chi}\right)^{3/2}, \tag{3.20}$$

$$N_{\chi_s} = \int d^3 r \rho(\vec{r}), \tag{3.21}$$

where $\rho^{(\chi)}(\vec{r})$ is the density for the χth component of the gas, and μ_χ is the non-interacting chemical potential set by the condition 3.21.Inserting this into Eq. 3.18 gives

$$C_N \to \sqrt{\frac{2}{3}}\frac{256}{315\pi^3}N^{3/2}\frac{\Gamma\left(\lambda+\frac{3N}{2}\right)}{\Gamma\left(\lambda+\frac{3(N-1)}{2}\right)}. \tag{3.22}$$

Inserting Eqs. 3.11a and 3.11b the leading order behavior in N can be extracted:

$$C_N \to \sqrt{\frac{2}{3}}\frac{32N^{7/2}}{35\pi^3}\left(1+\frac{0.049}{N^{2/3}}-\frac{0.277}{N^{4/3}}+...\right), \tag{3.23}$$

where the higher order terms in $1/N$ have been found by fitting the numerically calculated values of C_N. Table 3.1 gives $C_N/N^{7/2}$ calculated numerically for the several filled shells while Fig. 3.1 shows both the calculated values of $C_N/N^{7/2}$ for the first 100 filled shells and the values from the fit in Eq. 3.23 versus $1/N$.

n	N	λ	$C_N/N^{7/2}$
1	2	0	$\frac{1}{8\pi^2} \approx 0.0127$
2	8	6	0.0637
3	20	30	0.0251
4	40	90	0.0244
5	70	210	0.02435
...	...	...	...
15	1360	14280	0.0241
30	9920	215760	0.02409
100	343400	25497450	0.02408

Table 3.1: N, λ and $C_N/N^{7/2}$ for the several filled shells. We can see that $C_N/N^{7/2}$ quickly converges to the Thomas-Fermi limiting value of $32\sqrt{2/3}/35\pi^3 \approx 0.02408$ to several digits.

In both Table 3.1 and Fig. 3.1 the convergence to the large N behavior, $C_N \to \sqrt{2}32N^{7/2}/\left(\sqrt{3}35\pi^3\right) = 0.02408N^{7/2}$, can clearly be seen.

In the large N limit the effective potential in Eq. 3.8 can be written using Eqs. 3.11a, 3.11b and 3.17

$$\frac{V_{eff}\left(R'\right)}{E_{NI}} \to \frac{1}{2R'^2} + \frac{1}{2}R'^2 + \frac{\sigma k_f^0 a}{R'^3} \tag{3.24}$$

where $\sigma = 4096/2835\pi^2$. In the large N limit the effective mass m^* in the hyperradial derivative term in Eq. 3.8 becomes

$$m^* \to \frac{1}{16}\left(3N\right)^{8/3}. \tag{3.25}$$

For large numbers of particles, the second derivative term becomes negligible, a fact that will be useful in later sections. It can be noted that the only parameter that remains in the effective potential is the dimensionless quantity $k_f^0 a$.

The behavior of $V_{eff}\left(R'\right)$ versus R' is illustrated in Fig. 3.2 for various values of $k_f^0 a$. For $k_f^0 a = 0$ (solid curve), the non-interacting limit, the curve is exact, and the ground state solution is given by Eq. 2.20. For non-zero values of a, V_{eff} acquires an attractive ($k_f^0 a < 0$) or repulsive ($k_f^0 a > 0$) $1/R'^3$ contribution as indicated by the dot-dashed and dashed lines respectively. For $k_f^0 a < 0$ the DFG is metastable in a region

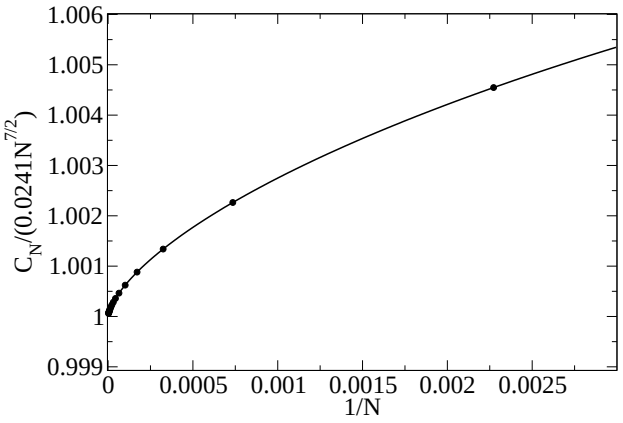

Figure 3.1: Values of C_N divided by the large N limit, $C_N \to 0.02408N^{7/2}$, versus $1/N$ are shown. The circles are the calculated value while the curve is the fit stated in Eq. 3.23. Figure from Ref. [1].

which has a repulsive barrier which it may tunnel through and emerges in the region of small R' where the interaction term is dominant. It should be noted, though, that small R' means the overall size of the gas is small. Thus the region of collapse corresponds to a very high density in the gas. In this region several of the assumptions made in this section can fall apart, most notably the assumption dealing with the validity of the two-body, zero-range potential [85]. For $k_f^0 a > 0$ the positive $1/R'^3$ serves to strengthen the repulsive barrier and pushes the gas further out.

3.3 Result for bare zero-range interactions

Examination of Eq. 3.24 shows that effectively attractive interactions ($a < 0$) and effectively repulsive interactions ($a > 0$) have qualitatively different behavior. With this in mind I will examine these two cases separately. With the effective hyperradial potential in hand, the hyperradial behavior of Eq. 3.3 can be variationally optimized by solving the effective Schrödinger Eq. 3.17. The results reported here are found by solving Eq. 3.17 for a fixed number of particles using the exact effective potential, but much of the intuition may be extracted from the large N limit potential in Eq. 3.24.

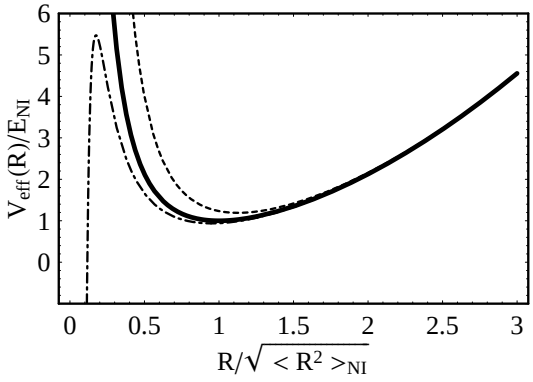

Figure 3.2: The dimensionless rescaled effective potential, V_{eff}/E_{NI} as a function of the rescaled hyperradius for $k_f^0 a = 0$ (solid), $k_f^0 a = 1.19$ (dashed) and $k_f^0 a = -0.40$. (dot-dash).

3.3.1 Repulsive interactions ($a > 0$)

For effective repulsive interaction the predicted energy from the K harmonic method is expected to deviate from experimental values, since the trial wavefunction does not allow any fermions to combine into molecular pairs as has been seen in experiments.[13, 15, 16, 17] This method only can describe the normal degenerate Fermi gas. The strong repulsive barrier for repulsive interactions shown in Fig. 3.2 arises as the gas pushes against itself which increases the energy and rms radius of the ground state. Figures 3.3 and 3.4 compare the ground state energy and average radius squared respectively of 240 trapped atoms, plotted as a function of $k_f^0 a$ with a Hartree-Fock (HF) calculation. The inset in Fig. 3.3 shows that the K harmonic energies are slightly above the HF energies; since both methods are variational upper bounds, we can conclude that the HF solution is a slightly better representation of the true solution to the full Schrödinger equation with δ-function interactions.

An added benefit of the K harmonic method is in providing an intuitively simple way to understand the energy of the lowest radial excitation of the gas, i.e. the breathing mode frequency. Figure 3.2 shows that as $k_f^0 a$ increases the repulsion increases the

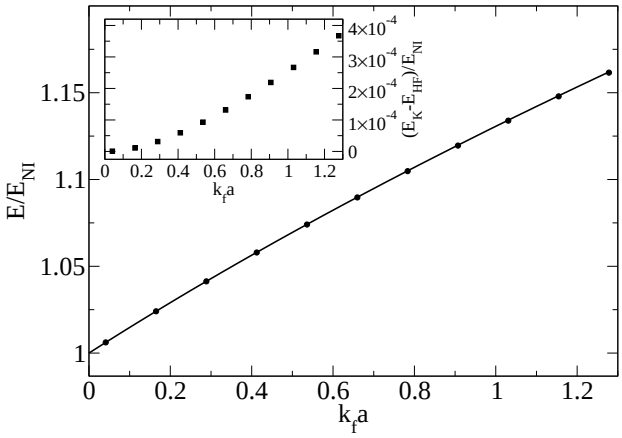

Figure 3.3: The ground state energy in units of the non-interacting energy versus $k_f^0 a$ for 240 atoms calculated using the K harmonic method (curve) and using Hartree-Fock (circles). Inset: the difference in the ground state energies predicted be the K harmonic (E_K) and Hartree-Fock (E_{HF}). Clearly the K harmonic energies are slightly higher than Hartree-Fock.

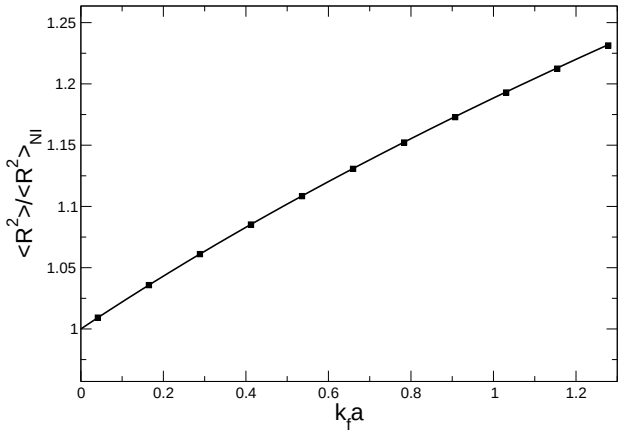

Figure 3.4: The ground state average squared radius of the gas atoms in units of the non-interacting rms squared radius is plotted versus $k_f^0 a$. The calculations considered 240 atoms in both the K harmonic method (curve) and Hartree-Fock (squares).

curvature at the local minimum, whereby stronger repulsion causes the breathing mode frequency to increase. Figure 3.5 compares the breathing mode frequency calculated using the K harmonic method to the sum rule prediction [86] based on HF orbitals,

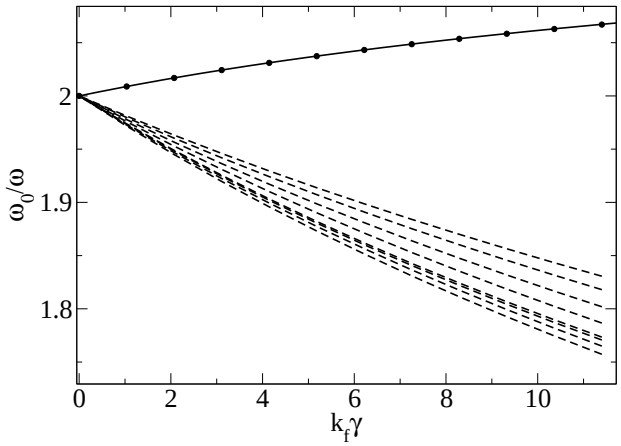

Figure 3.5: The lowest breathing mode excitation (ω_0) in units of the trap frequency is plotted versus $k_f^0 a$ for the K harmonic method (solid curve) and for the sum rule (circles). Also shown as dashed curves are the lowest eight radial excitation frequencies predicted in the HF approximation.

and also the lowest eight radial excitation frequencies predicted by Hartree-Fock. As anticipated, the K harmonic method and the sum rule method agree that the breathing mode frequency will increase with added repulsion. Interestingly both the K harmonic and sum rule methods disagree qualitatively with all eight of the lowest HF excitations. This difference is attributed to the fact that Hartree-Fock on its own can only describe **single particle** excitations while both the sum rule and the K harmonic methods describe **collective** excitations in which the entire gas oscillates coherently.

3.3.2 Attractive interactions ($a < 0$)

In this section the behavior of the gas under the influence of attractive s-wave interactions ($k_f^0 a < 0$) is examined. For attractive interactions the gas lives in a metastable region and can tunnel through the barrier shown in Fig. 3.2. Figure 3.6 shows the behavior of V_{eff} for several values of $k_f^0 a$. The location of the local minimum gets pulled down with stronger attraction as the gas pulls in on itself and deeper into the center of the trap. Further, as the strength of the interaction increases, the height of the barrier

decreases. In fact beyond a critical interaction strength a_c the interaction becomes so strong that it always dominates over the repulsive kinetic term. At this critical point the local extrema disappear entirely and the gas is free to fall into the inner "collapse" region. The value of a_c can be calculated approximately by finding the point where V_{eff} loses its local minimum and becomes entirely attractive. This critical interaction strength is given by

$$k_f^0 a_c = -\frac{189\pi^2}{1024}\frac{1}{5^{1/4}} \approx -1.22.$$

This is not exact as the gas will have some small zero point energy that will allow it to tunnel through or spill over the barrier before the minimum entirely disappears.

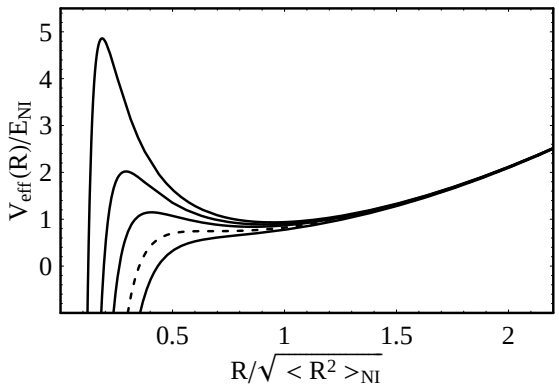

Figure 3.6: The dimensionless rescaled potential curve V_{eff}/E_{NI} is shown as a function of the rescaled hyperradius R' for several values of $k_f a$; $k_f a = k_f a_c$ (dashed), and from top to bottom $k_f a = -0.42, -0.66, -0.90, -1.53$ (all solid)

Just before the minimum disappears, its location is given by $R'_{\min} = 5^{-1/4}$, with an energy of $V_{eff}(R'_{\min}) = \sqrt{5}E_{NI}/3 \approx 0.75E_{NI}$. This means that if the gas, in actuality, is mechanically stable for all values of the two body scattering length, i.e. $a \to -\infty$, this approximation must be altered to include a renormalization cutoff in the strength of the δ-function such that $k_f^0 a > -1.22$ for all a. With this in mind, we begin to examine the behavior of the DFG for the allowed values of $k_f^0 a$.

Figures 3.7 and 3.8 show a comparison of the ground state energy and rms radius of the gas versus $k_f^0 a$ down to $k_f^0 a_c$ as calculated in the K harmonic and Hartree-Fock

methods. Again HF does just slightly better in energy, which we interpret as Hartree-Fock giving a slightly better representation of the actual ground state wavefunction. The energy difference becomes largest as the interaction strength approaches the critical value. This increase is due to the fact that Hartree-Fock predicts that collapse occurs slightly earlier with $k_f^0 a_c \approx -1.12$. As the interaction strength increases, the energy and rms radius of the gas decrease, and as $k_f^0 a$ approaches $k_f^0 a_c$ the overall size of the gas decreases sharply.

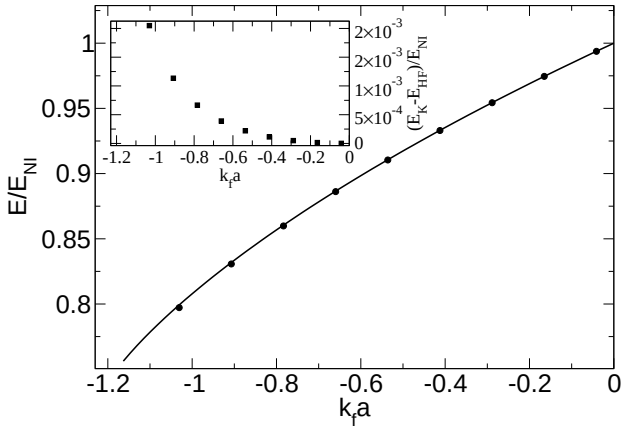

Figure 3.7: The ground state energy (in units of the non-interacting energy) versus $k_f^0 a$ for 240 atoms calculated using the K harmonic (curve) and Hartree-Fock (circles) methods. Inset: The difference in the ground state energies predicted by the K harmonic (E_K) and Hartree-Fock (E_{HF}). Clearly the K harmonic prediction is slightly higher.

While the local minimum present in V_{eff} only supports metastable states, and anything outside of the $\left|k_f^0 a\right| \ll 1$ regime is suspect, it is still informative to examine the behavior of the energy spectrum versus $k_f^0 a$, beginning with the breathing mode frequency. As the interaction strength becomes more negative Fig. 3.6 shows that the curvature about the local minimum in V_{eff} decreases. This "softening" of the hyperradial potential leads to a decrease in the breathing mode frequency in the outer well. Figure 3.9 shows the breathing mode vs. $k_f^0 a$ predicted by the K harmonic (curve) method and also using the sum rule with Hartree-Fock orbitals (circles). Also shown in

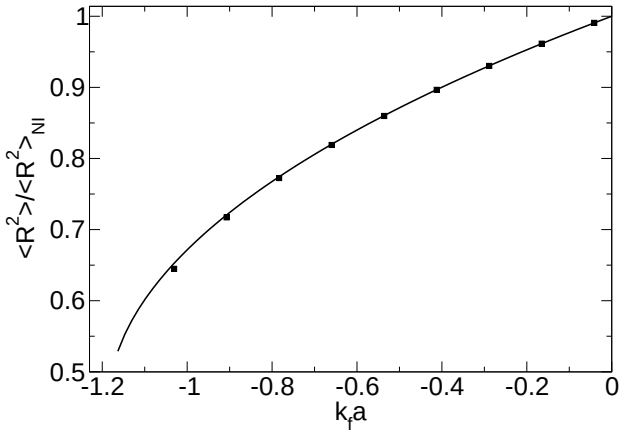

Figure 3.8: The average squared radius of the Fermi gas ground state in units of the non-interacting value is plotted versus $k_f^0 a$. The calculations are for 240 atoms in both the K harmonic method (curve) and Hartree-Fock (squares).

Fig. 3.9 are the lowest eight Hartree-Fock excitation frequencies for a filled shell of 240 atoms. Again, the K harmonic method agrees quite well with the sum rule, while both differ qualitatively from the HF prediction. The sharp decrease in the breathing mode frequency that occurs as $k_f^0 a \to k_f^0 a_c$ is a result of the excited mode "falling" over the barrier into the collapse region as the barrier is pulled down by the interaction.

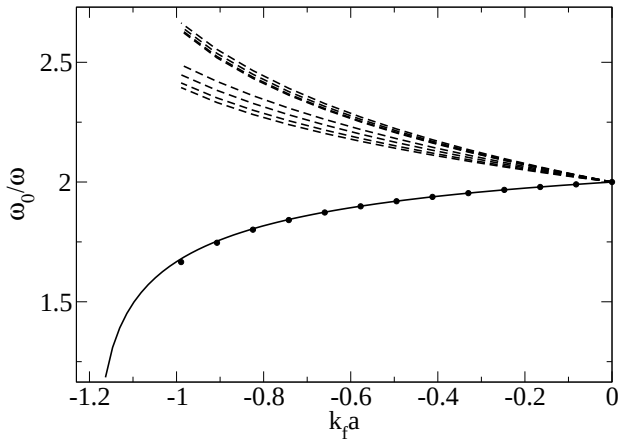

Figure 3.9: The frequency of the lowest energy radial transition in units of the trap frequency versus $k_f^0 a$ predicted by the K harmonic method (solid line) and by the sum rule (circles). Also shown are the lowest eight radial transitions predicted by Hartree-Fock.

Figure 3.10 displays some energy levels in the metastable region as functions of $k_f^0 a$ near $k_f^0 a_c$. Because of the singular nature of the $1/R^3$ behavior in the inner region, an inner repulsive $1/R^{12}$ barrier has been added to truncate the infinitely many nodes of the wavefunction in the inner region. The behavior of the wavefunction is not correct within this region anyway because recombination becomes dominant, and in any case the zero-range interaction is suspect beyond $\left|k_f^0 a\right| \sim 1$, and it must be renormalized.

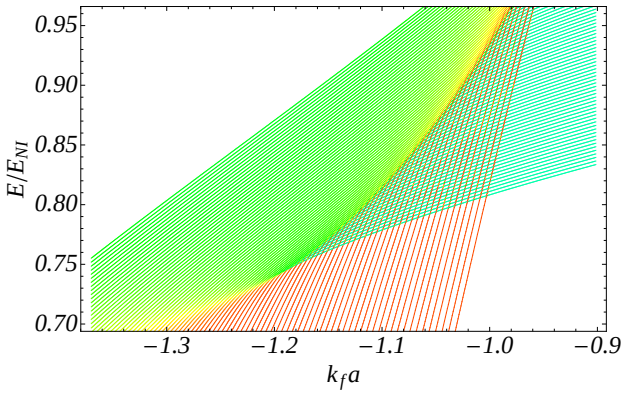

Figure 3.10: A portion of the energy spectrum vs $k_f^0 a$ close to the critical point $k_f^0 a = k_f^0 a_c$. Levels in the metastable region (cyan) decrease slowly while levels in the collapse region (red) decrease very quickly. Energy levels above the barrier in V_{eff} (green) live both in the collapse region and the metastable region.

Figure 3.10 shows three distinct types of energy level. Levels that are contained in the local minimum (shown in cyan) are decreasing, but not as quickly as the others; levels that are in the collapse region (shown in red) have a very steep slope as they are drawn further in toward $R = 0$; and energy levels that are above the barrier in V_{eff} (shown in green) have wavefunctions in both the collapse region and the local minimum. As $k_f^0 a$ decreases, the higher energy levels fall over the barrier into the collapse region earlier, until finally just before $k_f^0 a_c$ is reached the first excited metastable level falls below the "ground state". This corresponds to the breathing mode behavior seen in Fig. 3.9. Of course all of this applies only if there is no further hyperradial dependence of a. If the interaction becomes density dependent, a concept that will be explored in

section 3.4 and has been used in several other treatments [87, 3, 88, 2], a change in the hyperradius will change the density and thus change the effective scattering length, i.e. $a \to a(R)$.

3.3.3 The large N limit

This section deals with the degenerate Fermi gas in the large N limit. To do this, the fact that the $\partial^2/\partial R^2$ term in the effective Hamiltonian, the "hyperradial kinetic energy", becomes negligible can be exploited. In this limit the total energy of the system is merely given by $E = V_{eff}(R_{\min})$, as is the case in dimensional perturbation theory [89]. To find the ground state energy one must merely find the minimum (local minimum for $a < 0$) value of V_{eff}. Accordingly, we find the roots of $\dfrac{dV_{eff}}{dR'} = 0$. Using Eq. 3.24 we simplify this to

$$k_f^0 a = \frac{1}{3\sigma} R'_{\min}\left(R'^4_{\min} - 1\right), \tag{3.26}$$

where $R'_{\min}$ is the hyperradial value that minimizes V_{eff} and σ is defined in the same way as in Eq. 3.24. The solutions to Eq. 3.26 are illustrated graphically in Fig. 3.11; for any given $k_f^0 a$ only look for the value of $R'_{\min}$ that gives that value. The exact solution of Eq. 3.26 cannot be determined analytically for all values of $k_f^0 a$, but Fig. 3.11 shows that for $k_f^0 a > 0$ there is always only one positive, real $R'_{\min}$ that satisfies Eq. 3.26. This corresponds to the global minimum discussed for repulsive interactions. For $k_f^0 a < 0$ things are a bit more complicated. Figure 3.11 shows that for $k_f^0 a_c < k_f^0 a < 0$ there are two solutions to 3.26. The inner solution is a local maximum and corresponds to the peak of the barrier seen in Fig. 3.6; the outer solution corresponds to the local minimum where the DFG lives. The local minimum is the state of concern here as this will give the energy and hyperradial expectation values of the metastable Fermi gas. The value of $k_f^0 a$ where these two branches merge is the place where the local maximum merges with the local minimum, namely the critical value, $k_f^0 a_c$. There is no solution to 3.26

for $k_f^0 a < k_f^0 a_c$, and thus there is no region of stability. For $k_f^0 a = 0$, the non-interacting limit, there are two solutions, $R'_{\min} = 0$ and $R'_{\min} = 1$. The solution $R'_{\min} = 0$ must be discounted as there is a singularity in V_{eff} at $R = 0$. Thus in the non-interacting limit $R'_{\min} \to 1$ and $V_{eff}(R_{\min}) \to E_{NI}$, as should be expected.

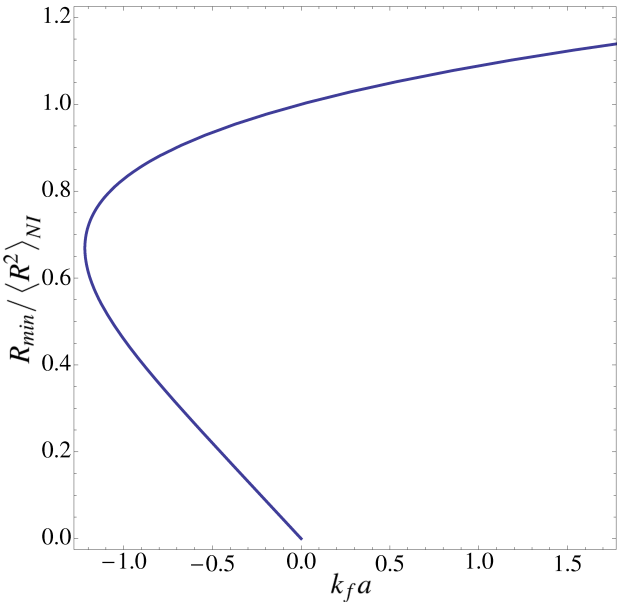

Figure 3.11: A plot of the location if the extrema in Eq./ 3.26 versus $k_f^0 a$ is shown. Examination of this plot tells us the behavior of $R'_{\min}$ for all allowed values of $k_f^0 a$ including the existence of the critical point $k_f^0 a_c$ located at the minimum of the plot where the maximum and minimum coincide.

Substitution of 3.26 into 3.24 gives the energy of the ground state in the large N limit, as a function of the size of the gas:

$$\frac{V_{eff}(R_{\min})}{E_{NI}} = \frac{1 + 5R'^4_{\min}}{6R'^2_{\min}}. \tag{3.27}$$

The solutions to Eq. 3.26 immediately give the ground state energy of the gas versus $k_f^0 a$. Fig. 3.12 shows the percentage difference of the ground state energy found by this minimization procedure and that of 240 particles found by solving Eq. 3.17.

Another result from 3.8 is the fact that in the large N limit the commutator $[H_{eff}, R] \to 0$. Thus for any operator that is solely a function of the hyperradius $\hat{O}(R)$

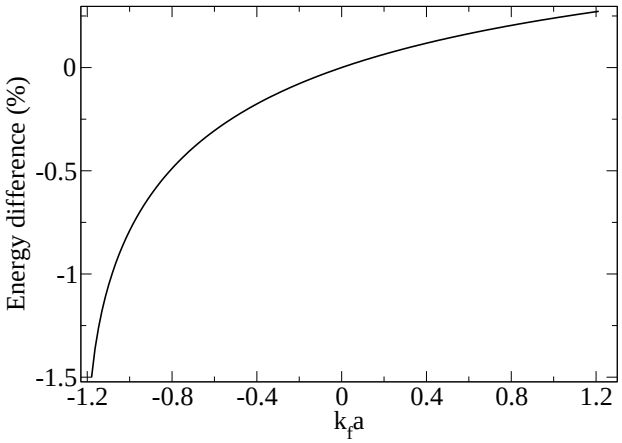

Figure 3.12: The percentage difference between the energy found by minimizing V_{eff} and the energy found by explicitly solving the hyperradial Schrödinger equation for 240 atoms is show as a function of $k_f^0 a$.

the ground state expectation value in the large N limit is given by the operator evaluated at $R'_{\min}$, i.e. $\left\langle \hat{O}\left(R'\right)\right\rangle = \hat{O}\left(R'_{\min}\right)$. This tells us that the large N limit wavefunction is given by $\left[R^{(3N-1)/2}G\left(R\right)\right]^2 = \delta\left(R - R_{\min}\right)$. This can be perturbed slightly by assuming a ground state hyperradial wavefunction approximated by a very narrow Gaussian centered at $R_{\min}$. The width of this Gaussian can be found by approximating V_{eff} about $R_{\min}$ as a harmonic oscillator with mass m^* and frequency ω_0. By comparing the oscillator potential with the second order Taylor series about $R_{\min}$ in V_{eff}, ω_0 can be found:

$$\omega_0 = \sqrt{\frac{1}{m^*}\frac{1}{E_{NI}}\left(\left.\frac{\partial^2 V_{eff}}{\partial R'^2}\right|_{R'=R'_{\min}}\right)}. \tag{3.28}$$

The breathing mode frequency is now simply ω_0. The frequency in Eq. 3.28 is in units of the non-interacting energy; to get back to conventional units, ω_0 must be multiplied by $E_{NI}/\hbar$. From Eq. 3.25, $m^* = mE_{NI}N\left\langle R^2\right\rangle_{NI}/\hbar^2$, and noting that $N\left\langle R^2\right\rangle_{NI} = \ell^2 E_{NI}/\hbar\omega$ yields

$$\omega_0^B = \sqrt{\frac{1}{E_{NI}}\left(\left.\frac{\partial^2 V_{eff}}{\partial R'^2}\right|_{R'=R'_{\min}}\right)}, \tag{3.29}$$

for ω_0^B, the breathing mode frequency in units of the trap frequency. Using Eq. 3.24

and substituting in Eq. 3.26 to evaluate at the minimum gives that

$$\omega_0^B = \sqrt{5 - \frac{1}{R'^4_{\rm min}}}. \tag{3.30}$$

Note that this is now dependent only on the value of $k_f^0 a$, i.e. for a fixed $k_f^0 a$ the predicted breathing mode frequency is **independent** of the number of atoms in the system in the large N limit.

Figure 3.13 shows the breathing mode frequency predicted by Eq. 3.30 versus $k_f^0 a$.

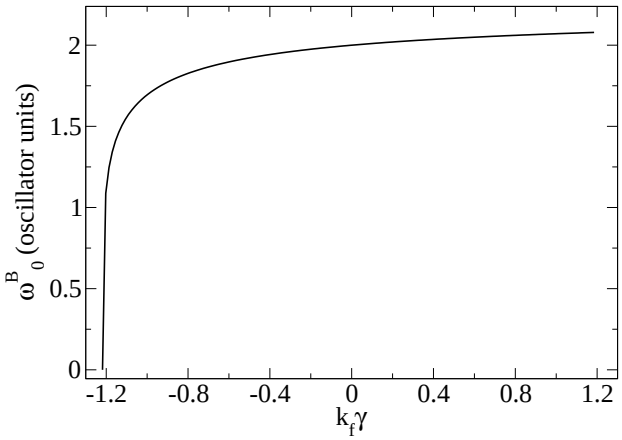

Figure 3.13: The breathing mode (in units of the oscillator frequency ω) in the large N limit versus $k_f^0 a$. Note that as $k_f^0 a \to k_f^0 a_c$ the frequency drops to zero as the local minimum disappears.

The same behavior can be seen in this plot as was seen in Fig. 3.9 where the breathing mode frequency dives to zero as $k_f^0 a \to k_f^0 a_c$.

3.4 Density dependent interactions

Unfortunately, in strongly-interacting or high-density systems, the overly singular nature of the δ-function often poses a problem [85]. Another problem is that dynamic instability arises when the non-regularized zero-range interaction is used variationally in a two component degenerate Fermi gas, as seen in the previous section, which is not

seen in experiment [1, 13, 15, 16, 17, 14]. One method of avoiding these problems is to use a density-dependent interaction. Refs. [3, 87, 2] do just that, introducing a density-dependent interaction strength for a zero-range interaction. In this section I apply the hyperspherical K-harmonic method to this type of interaction potential. The goal will be to evaluate the interaction potential matrix element in Eq. 3.6 to find the effective hyperradial potential $V_{eff}\left(R'\right)$.

3.4.1 Operator matrix elements in the $N \to \infty$ limit

Before specifying the exact interaction used here, a method for evaluating the more general interaction matrix elements must be found. In this section I develop a method for calculating hyperangular matrix elements of an operator in the large N limit, e.g.,

$$\tilde{O}\left(R'\right) = \int Y^*_{\lambda\mu}\left(\Omega\right) \hat{O}\left(R', \Omega\right) Y_{\lambda\mu}\left(\Omega\right) d\Omega. \tag{3.31}$$

Here $\hat{O}\left(R', \Omega\right)$ is a general operator that is a function of the rescaled hyperradius R' from Eq. 3.7 and the hyperangles Ω. Here $Y_{\lambda\mu}\left(\Omega\right) = Y_{\lambda\mu}\left(\Omega, \sigma_1, \sigma_2, ..., \sigma_N\right)$ is the K–harmonic, defined by Eq. 3.4, for N fermions distributed equally between two internal spin states. Again the spin coordinates $(\sigma_1, \sigma_2, ..., \sigma_N)$ have been suppressed for notational simplicity. To allow us to integrate over all of the $3N$ dimensions of the space, both sides of Eq. 3.31 are multiplied by a δ-function in the hyperradius and integrated over R':

$$\tilde{O}\left(R'_0\right) = \int \delta\left(R' - R'_0\right) Y^*_{\lambda\mu}\left(\Omega\right) \hat{O}\left(R', \Omega\right) Y_{\lambda\mu}\left(\Omega\right) d\Omega dR'. \tag{3.32}$$

A clever choice for the δ-function representation will aid in this calculation. To create the δ-function, consider the function

$$R'^{(3N-1)/2} G_N\left(R'\right) = A_N \left(\frac{\sqrt{N\left\langle R^2\right\rangle_{NI}} R'}{\ell R'_0}\right)^{\lambda+3N/2-1/2} \exp\left(-\frac{R'^2 N\left\langle R^2\right\rangle_{NI}}{2\ell^2 R'^2_0}\right), \tag{3.33}$$

where A_N is a normalization constant, and $\ell = \sqrt{\hbar/m\omega}$ is the oscillator length defined in Eq. 2.17. This should look very familiar, as it is the hyperradial solution for N non-interacting fermions in a symmetric oscillator from Eq. 2.20 with oscillator length $\ell R'_0$. It is easy to show that, in the limit where $N \to \infty$, Eq. 3.33 becomes

$$\lim_{N\to\infty} \left[R'^{(3N-1)/2} G_N\left(R'\right)\right]^2 = \delta\left(R' - R'_0\right).$$

Inserting this into Eq. 3.32 and playing slightly fast and loose with exchange of the order of the limit and the integral yields

$$\tilde{O}\left(R'_0\right) = \lim_{N\to\infty} \int \left[R'^{(3N-1)} G_N\left(R'\right)\right]^2 Y^*_{\lambda\mu}\left(\Omega\right) O\left(R', \Omega\right) Y_{\lambda\mu}\left(\Omega\right) d\Omega dR'.$$

Referring to Eq. 3.4 and remembering that the K-harmonic $Y_{\lambda\mu}\left(\Omega\right)$ is **independent** of the oscillator length scale, it follows that the wave function $G_N\left(R'\right)\Phi_\lambda\left(\Omega\right)$ is merely a Slater determinant of non-interacting single particle oscillator states with oscillator length,

$$\ell_{eff} = R'_0 \ell_0. \tag{3.34}$$

Further, Ref. [66] gives that $R'^{(3N-1)} dR' d\Omega$ is the full volume element for the $3N$ dimensional space. All of this implies that in the large N limit, the hyperangular operator expectation value $\langle Y_{\lambda\mu} | O\left(R, \Omega\right) | Y_{\lambda\mu}\rangle$ is approximated by the full expectation value of the operator for a trial wavefunction consisting of a Slater determinant of non-interacting oscillator states, i.e.

$$\tilde{O}\left(R'_0\right) = \left\langle D_{\ell_{eff}}\left(\vec{r}_1, \vec{r}_2, ..., \vec{r}_N\right) \left| O\left(R', \Omega\right) \right| D_{\ell_{eff}}\left(\vec{r}_1, \vec{r}_2, ..., \vec{r}_N\right)\right\rangle_{3N} \tag{3.35}$$

where $D_{\ell_{eff}}\left(\vec{r}_1, \vec{r}_2, ..., \vec{r}_N\right)$ is a Slater determinant of oscillator states with oscillator length ℓ_{eff} and the subscript $3N$ is to indicate that the matrix element is taken over all $3N$ spatial and N spin degrees of freedom.

3.4.2 Density dependent zero-range interactions

The results of the previous section can now be applied to the density-dependent renormalized zero-range interactions presented in Ref. [3], in which a zero-range interaction is used whose strength is dependent on the density of the gas,

$$U_{int}\left(\vec{r}_{ij}\right) = \frac{4\pi\hbar^2}{2\mu_{2B}} \frac{\zeta\left(k_f\left(\vec{r}_i\right)a\right)}{k_f\left(\vec{r}_i\right)} \delta\left(\vec{r}_{ij}\right), \tag{3.36}$$

where a is the two-body s-wave scattering length and the Fermi wave number, $k_f = k_f\left(\vec{r}\right) = \left(6\pi^2\rho^{(1)}\left(\vec{r}\right)\right)^{1/3}$, is defined [1] in terms of the single spin component density, $\rho^{(1)}\left(\vec{r}\right)$. The effect of the density dependent interaction is to impose the appropriate short-range behavior on clusters of particles in a manner similar to that of Ref. [90]. In other words, if a cluster of particles is very close together with rms radius much less than the scattering length, the effective interaction energy they experience is the same as if the scattering length was infinite. This short-range behavior is extracted in Ref. [3] by considering a two-particle system, but the general method may be extended to a larger number of particles. The dimensionless renormalized function $\zeta\left(k_f a\right)$ from Ref. [3] is approximated by

$$\begin{aligned} \zeta\left(k_f a\right) &= A + B\arctan\left(Ck_f a - D\right), \\ A &= 0.3949, \\ B &= 1.1375, \\ C &= \frac{1+\tan^2\left(\frac{A}{B}\right)}{B} = 0.9942, \\ D &= \tan\left(\frac{A}{B}\right) = 0.3618. \end{aligned} \tag{3.37}$$

[1] This interaction is appropriate when the Fermi surfaces of two components coincide. When this is not the case, for instance when there is a population imbalance, the different components have different masses or trap frequencies, or in the case of multi-component gases, the interaction must be averaged over the different components.

Two of the fitting parameters A and B are found by fitting the asymptotic behavior of $\zeta(k_f a)$ as $k_f a \to \pm\infty$, which are given in ref. [3] by

$$\lim_{k_f a \to \infty} \zeta(k_f a) = 2.1817,$$

$$\lim_{k_f a \to -\infty} \zeta(k_f a) = -1.3919.$$

The constants C and D in Eq. 3.37 are determined by matching the Fermi pseudo-potential in the $|k_f a| \ll 1$ limit [79, 82], i.e.

$$\frac{4\pi\hbar^2}{2\mu_{2B}} \frac{\zeta(k_f a)}{k_f} \to \frac{4\pi\hbar^2 a}{m}. \tag{3.38}$$

Fig. 3.14 shows the behavior of this interaction as a function of $k_f a$.

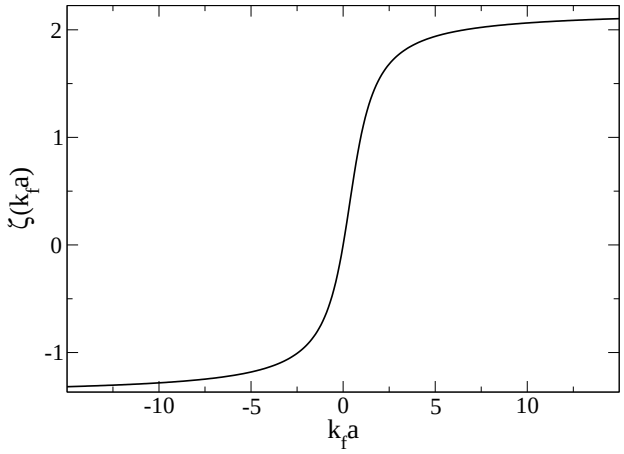

Figure 3.14: The density-dependent interaction strength function $\zeta(k_f a)$ is shown versus $k_f a$. Figure from Ref. [2].

The density of a single spin component in a Slater determinant state is given by Eq. 3.20, and in the large N limit, the Thomas-Fermi approximation can be used:

$$\rho^{(1)}_{\ell_{eff}}(\vec{r}) = \frac{1}{6\pi^2 \ell_{eff}^3} (2\mu)^{3/2} \left(1 - \frac{r^2}{2\ell_{eff}^2 \mu}\right)^{3/2}, \tag{3.39}$$

where ℓ_{eff} is given by Eq. 3.34, and $\mu = (3N)^{1/3}$ is the chemical potential at zero temperature of N non-interacting fermions divided equally between two different spin

substates. Combining this with Eq. 3.35 and some integration substitutions gives an effective interaction potential,

$$U_{eff}\left(R'\right) = \left\langle Y_{\lambda\mu} \left| \sum_{i>j} U_{int}\left(r_{ij}\right) \right| Y_{\lambda\mu} \right\rangle = \frac{64N^{4/3}}{3^{2/3}\pi^2 R'^2} f\left(\frac{k_f^0 a}{R'}\right), \tag{3.40}$$

$$f\left(\frac{k_f^0 a}{R'}\right) \equiv \int_0^1 y^6 \sqrt{1-y^2}\,\zeta\left(\frac{k_f^0 a}{R'} y\right) dy.$$

Here k_f^0 is the peak Fermi wave number for N non-interacting atoms given by Eq. 3.11b. Observe that, again, the only parameter in this expression is $k_f^0 a$ which is dimensionless. Inserting Eq. 3.40 into Eq. 3.6 now gives the final effective hyperradial potential in the $N \gg 1$ limit,

$$\frac{V_{eff}\left(R'\right)}{E_{NI}} \to \frac{1}{2R'^2} + \frac{1}{2}R'^2 + \frac{256}{9\pi^2 R'^2} f\left(\frac{k_f^0 a}{R'}\right). \tag{3.41}$$

For $\left|k_f^0 a\right| \ll R'$ the integral may be evaluated exactly giving

$$\frac{V_{eff}\left(R'\right)}{E_{NI}} \to \frac{1}{2R'^2} + \frac{1}{2}R'^2 + \frac{4096 k_f^0 a}{2835\pi^2 R'^3}$$

which is exactly the effective potential found in Eq. 3.24 for the bare zero-range pseudo-potential. It should also be noted that Eq. 3.40 holds for any density-dependent zero-range interaction in the form of Eq. 3.36, i.e. for any function ζ.

3.4.3 Finite effective interactions, $\left|k_f^0 a\right| < \infty$

Here I explore the behavior of the DFG under a repulsive effective potential where the two-body scattering length, a, is positive. The renormalized description of the interactions used here and in Ref. [3] is only accurate if the real two-body interactions are purely repulsive, meaning that the gas is somehow prevented from coalescing into molecular dimer states. In other words, with the present initial formulation, only a gas of atoms can be described, not of molecules. Figure 3.15, which shows V_{eff} for several positive two-body scattering lengths, also depicts an example of the bare non-renormalized effective potential. As with the bare pseudo-potential in Sec. 3.2, the

repulsive interactions cause the gas to push out against itself and against the trap walls, which increases the overall energy and size of the gas.

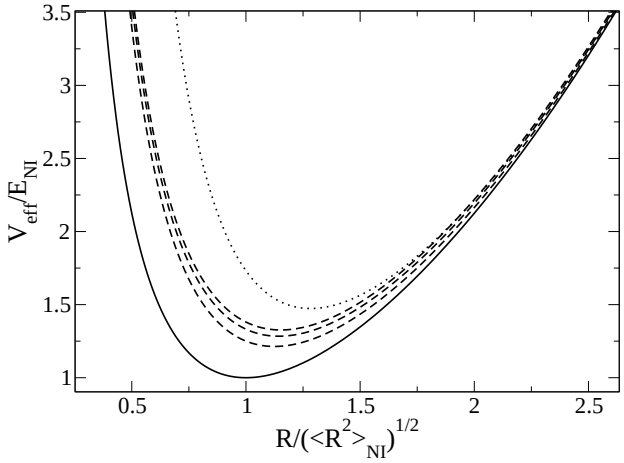

Figure 3.15: The dimensionless ratio of the effective hyperradial potential to the non-interacting total energy is plotted as a function of the dimensionless rescaled hyperradius, for several different repulsive interaction strengths. The non-interacting limit $k_f^0 a = 0$ is shown as the sold curve; the dashed curves show the renormalized effective potential for (bottom to top) $k_f^0 a = 2$, $k_f^0 a = 5$ and $k_f^0 a = 50$. Also shown is the non-renormalized effective potential with $k_f^0 a = 5$ (dotted curve). Figure from Ref. [2].

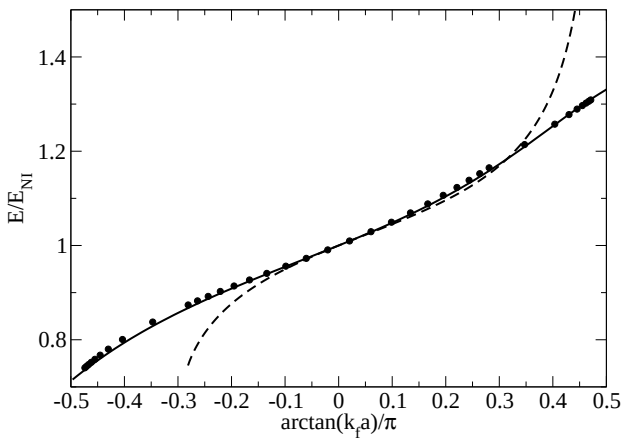

Figure 3.16: The ground state energy of the DFG in units of the non-interacting energy predicted by the K harmonic method (solid line) is plotted versus arctan $\left(k_f^0 a\right)/\pi$ and compared with that predicted by the HF method with 2280 atoms (circles) [3]. The dashed line is the ground state energy predicted by the K harmonic method using the bare Fermi pseudo-potential. Figure from Ref. [2].

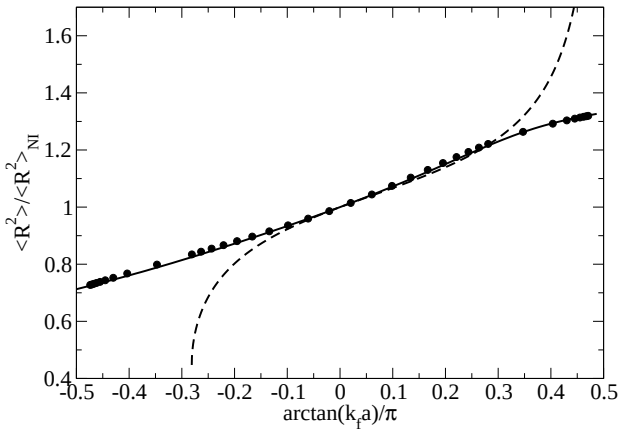

Figure 3.17: The average squared hyperradius of the two-component DFG ground state in the large-N limit, divided by the non-interacting value for this quantity, is plotted versus arctan $\left(k_f^0 a\right)/\pi$. Also shown are the values predicted by the HF method with 2280 atoms (circles) [3]. The dashed line is the ground state energy predicted by the K harmonic method using the bare Fermi pseudo-potential. Figure from Ref.. [2].

Using the large N limit, the second derivative term in Eq. 3.8 becomes negligible, and as before, the ground state energy and hyperradius can be found by simply minimizing the effective potential, $V_{eff}\left(R'\right)$. Figures 3.16 and 3.17 show the energy and average squared hyperradius of the minimum of V_{eff} as functions of $k_f^0 a$, compared to those same values calculated using the bare non-renormalized effective potential from Sec. 3.2. Also shown are the ground state energy and average squared hyperradius that are predicted by the HF method using the same density-dependent interaction. As the interaction gets stronger the renormalized energies and hyperradii flatten out and approach a constant in the unitarity limit. For $k_f^0 a \ll 1$ the Fermi pseudo-potential approximation is in good quantitative agreement with the renormalized interactions, but diverges dramatically as $k_f^0 a \to \infty$. This dramatizes the breakdown of the non-renormalized zero-range approximation, which overestimates the interaction strength as the unitarity regime is approached.

Figure 3.18 shows the behavior of the effective potential for some attractive values of the two-body scattering length, along with an example of the non-renormalized

effective potential. The decisive qualitative importance of the renormalization is now apparent. The renormalized effective potential is repulsive as $R' \to 0$, and the ground state of the gas is in a global minimum. In contrast to the bare pseudo-potential, this now has no collapse phenomenon.

Figures 3.16 and 3.17 show the ground state energy and average hyperradius squared of the system compared to the non-renormalized values. The effects of density-dependence for attractive interaction are even more striking than in the repulsive interaction case. With renormalization, as $k_f^0 a \to -\infty$ the energy and average hyperradius squared go towards a fixed value. Figures 3.16 and 3.17 also show the ground state energy and average squared hyperradius predictions from the HF method with density-dependent interactions. They show that for $\left|k_f^0 a\right| \ll 1$ the non-renormalized and renormalized values are in good agreement, but as $k_f^0 a \to k_f^0 a_c = -1.22$ the bare Fermi-pseudo-potential results diverge away from the renormalized interaction results. Just before the point of collapse the ground state energy from Eq. 3.27 is $E = \sqrt{5}E_{NI}/3 = 0.75E_{NI}$. Not only does the renormalized effective potential eliminate the collapse, it also allows the gas to reach a lower energy than would be possible without the density dependence. In other words, if the interaction coefficient in $U_{int}(\vec{r}_{ij})$ were not density-dependent, but merely involved a cut off as $k_f^0 a \to -\infty$, the gas would not be able to reach the unitarity energy before collapsing.

3.4.4 Unitarity regime

In this section, the behavior of V_{eff} for density-dependent interactions in the strong interaction regime, i.e. $a \to \pm\infty$, is explored. In contrast to the bare pseudo-potential, which had energies that diverged in the $k_f^0 a \to \infty$ limit and produced a collapse when $k_f^0 a \leq -1.22$, the effective hyperradial potential produced using density dependent interactions produces finite energies in the unitarity regimes. Examining Eq.

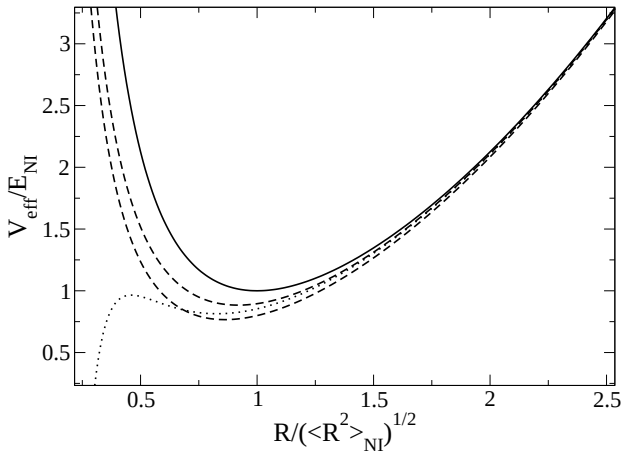

Figure 3.18: The effective potential in units of the non-interacting energy is plotted versus the hyperradius in units of $\sqrt{\langle R^2 \rangle_{NI}}$, for several interaction strengths. The non-interacting limit $k_f^0 a = 0$ is shown as the solid curve and the dashed curves show the renormalized effective potential for (top to bottom) $k_f^0 a = -1$ and $k_f^0 a = -5$. Also shown is the non-renormalized effective potential with $k_f^0 a = -1$ (dotted curve). Figure from Ref. [2].

3.40 shows that the unitarity limit appears in V_{eff} when $\left|k_f^0 a\right| \gg R'$, i.e.

$$\begin{aligned} \frac{\langle Y_{\lambda\mu} \left| V_{int}\left(R'_0, \Omega\right)\right| Y_{\lambda\mu}\rangle}{E_{NI}} &\rightarrow \frac{256\zeta_{\pm}}{9\pi^2 R'^2}\int_0^1 y^6\sqrt{1-y^2}dy \\ &= \frac{5\zeta_{\pm}}{9\pi R'^2} \end{aligned}$$

where $\zeta_{\pm}$ is the maximum $(+)$ or minimum $(-)$ value acquired by the interaction function $\zeta\left(k_f a\right)$. This gives a total effective potential of

$$\begin{aligned} \frac{V_{eff}\left(R'\right)}{E_{NI}} &\rightarrow \frac{1}{2}R'^2 + \frac{1/2 + 5\zeta_{\pm}/9\pi}{R'^2} \\ &= \begin{cases} \frac{1}{2}R'^2 + \frac{0.886}{R'^2} & \text{for} \quad k_f^0 a \gg R' \\ \\ \frac{1}{2}R'^2 + \frac{0.254}{R'^2} & \text{for} \quad -k_f^0 a \gg R' \end{cases} . \end{aligned} \tag{3.42}$$

The hyperradius is a **collective** coordinate so that, as $R \rightarrow 0$, all of the atoms in the system are forced to the center of the trap, which increases the density of the system. Thus, for small hyperradii, V_{eff} is expected to act like Eq. 3.42. In fact, the dashed

curves in Figs. 3.15 and 3.18 show that as $R' \to 0$ the renormalized effective potential curves all start to behave the same, independently of a. Alternatively if the two-body scattering length approaches $-\infty$, e.g. near a resonance, then V_{eff} can be expected to approach Eq. 3.42 for all hyperradii.

In the case where $k_f^0 a \to \pm\infty$ the effective potential takes on the form of Eq. 3.42. Minimization of V_{eff} as a function of R' gives a ground state energy:

$$\frac{E}{E_{NI}} = \sqrt{1 + 10\zeta_{\pm}/9\pi} \tag{3.43}$$
$$= \begin{cases} 1.331 \quad for \quad a \to \infty \\ 0.712 \quad for \quad a \to -\infty \end{cases} .$$

The average hyperradius of the gas is described by the value of the hyperradius at this minimum which is given by

$$R'_{\min} = (1 + 10\zeta_{\pm}/9\pi)^{1/4} \tag{3.44}$$
$$= \begin{cases} 1.154 \quad for \quad a \to \infty \\ 0.844 \quad for \quad a \to -\infty \end{cases}$$

At first glance this may seem strange, one might expect the behavior to be smooth across a resonance, and the energy to connect smoothly from the $a \to -\infty$ limit to the $a \to \infty$ limit [45]. But the density-dependent renormalization used here only applies to a gas of atoms and does not allow for the incorporation of higher order correlations, i.e. the formation of diatomic molecules. Presumably there is another branch in the renormalization that will match continuously with the $a \to -\infty$ limit (for a more complete discussion see section II of Ref. [3]).

Another quantity of interest is the chemical potential of the interacting gas at unitarity [3, 25, 91], given by

$$\mu_u = \frac{\hbar^2 k_f^2\,(0)}{2m}\,(1+\beta)\,,$$

where β is a universal parameter. From the single spin component density given in Eq.

3.39 the interacting peak Fermi wavenumber is

$$k_f(0) = \frac{k_f^0}{R'^2_{\min}}. \tag{3.45}$$

Further, from Eqs. 3.43 and 3.44, the ratio of the chemical potential of the interacting unitarity-limit gas to that of the non-interacting gas can be written in terms of the rescaled hyperradius as:

$$\frac{\mu_u}{\mu} = \frac{E}{E_{NI}} = R'^2_{\min}. \tag{3.46}$$

Solution of Eqs. 3.45 and 3.46 in the $a \to -\infty$ limit yields

$$\beta = 10\zeta_-/9\pi = -0.49. \tag{3.47}$$

This value of β coincides with the value predicted by the renormalized HF calculation of Ref. [3]. This agreement can be explained by realizing that the interaction potential in the HF approximation with the density dependent interaction in the unitarity regime takes on the form $V_{int} \propto \rho^{2/3}$ [3]. By considering the density from Eq. 3.39 this gives an interaction potential that can be approximated by an oscillator-like potential, i.e. $V_{int} \propto \left(1 - r^2/2\mu l_{eff}^2\right)$. Even though neither Ref. [3] nor the present treatment explicitly incorporates Cooper-type fermion pairing, this unitarity limit β is in fair agreement with quantum Monte Carlo estimates that have obtained $\beta = -0.58$ (Ref. [45]) and -0.56 (Ref. [24]). Also, observe that this gives a significant improvement over the value of $\beta = -0.41$ expected on the basis of BCS theory [48]. Further the value of β found here is lower than the $\beta = -0.44$ [92] found by quantum Monte-Carlo on a normal state Fermi gas. Even though the trial wavefunction used here would be more appropriate for describing a normal state Fermi gas, the lower value of β found using the density-dependent interaction indicates that a simplistic wavefunction can give surprisingly good results.

3.4.5 Breathing mode excitations

By using the effective hyperradial potential from Eq. 3.41, the lowest radial excitation frequency can be obtained from Eq. 3.29. Figure 3.19 shows the breathing mode frequency in units of the oscillator frequency compared to that calculated using non-renormalized interactions from Sec. 3.2. Of course the breathing mode frequency in the non-interacting limit is $\omega_0^B = 2\omega$, and for weak interactions, $\left|k_f^0 a\right| < 1$, the breathing mode frequency follows the same behavior for both bare the interaction and density-dependent interactions. Somewhat surprisingly, though, the frequency predicted from the density-dependent interactions turns over and returns to the non-interacting value as $k_f^0 a \to \pm\infty$. Inserting the second derivative of Eq. 3.42, the effective potential as $k_f^0 a \to \pm\infty$, gives

$$\omega_0 = \omega\sqrt{\frac{1}{E_{NI}}\left(1 + 3\frac{1 + 10\zeta_{\pm}/9\pi}{R'^4}\bigg|_{R'=R'_{\min}}\right)}. \tag{3.48}$$

When the minimum hyperradius from Eq. 3.44 is inserted, the resulting equation implies that the unitarity limits for the breathing mode frequency are both $\omega_0 = 2\omega$. This is a general property of any hyperradial potential of the form $V(R') = A/R'^2 + BR'^2$ in the large N limit where $A, B > 0$. This unitarity behavior has also been predicted in Ref. [90, 93].

3.4.6 Multiple spin components

The realization of degenerate multi-component atomic Fermi gases is now possible using present-day technology [94, 95]. Neglecting for the moment possible losses, the occupation of more than two different hyperfine states of the same species requires only moderate changes to the previous analysis. A degenerate gas consisting of the lowest three hyperfine states of ^{6}Li has already been created [94, 95], and the coexistence of three hyperfine states has already been demonstrated for ^{40}K [96]. Alternatively, a number of groups are presently pursuing the simultaneous trapping of three different atomic

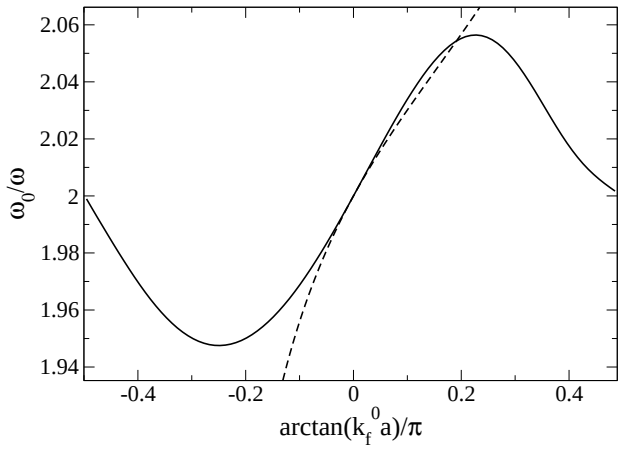

Figure 3.19: The breathing mode frequency ω_0^B is shown in units of the trap frequency ω versus arctan $\left(k_f^0 a\right)/\pi$. The solid curve shows the breathing mode predicted using the renormalized interaction while the dashed curve shows the prediction based on the bare Fermi pseudo-potential. Figure from Ref. [2].

species [97]. In the case of the same atom in different hyperfine states, the atomic masses of all components are equal, whereas in the case of different atomic species, the atomic masses of the different components differ. In either of these realizations of multi-component Fermi gases, all or some of the interspecies scattering lengths may be tunable thanks to the possible existence of magnetic or optical Fano-Feshbach resonances. With these new developments, it is of considerable interest to investigate these systems. This section provides an initial look at such a multiple component system from the K-harmonic approximation with density dependent interactions, specifically the dynamic stability of such systems.

Next consider what happens when the atoms in the gas are equally distributed among an arbitrary number χ of spin substates. In order to limit the large parameter space, that the s-wave scattering length between two atoms in any two different spin states is assumed to have the same value, a. Also, for calculational simplicity, the possibility of inelastic collisions, e.g. of the type:

$$\left|m_1 = \frac{3}{2}\right\rangle + \left|m_2 = -\frac{3}{2}\right\rangle \rightarrow \left|m_1' = \frac{1}{2}\right\rangle + \left|m_2' = -\frac{1}{2}\right\rangle$$

is neglected. To proceed, the question of what density should go into the renormalized interactions must be addressed. A particle in spin state i cannot interact with any other particle in the same spin state by the zero range approximation, but the density that determines $k_f(r)$ in the renormalization function ζ might be chosen in various alternative ways, and a unique criterion to specify the appropriate renormalization in this context has not yet been developed. As an initial exploration, I make the assumption that the appropriate interaction is merely the average of the two density dependent scattering lengths,

$$U_{int}(r_{ij}) = \frac{4\pi\hbar^2}{2m}\left(\frac{\zeta\left[k_f^{(j)}(\vec{r}_i)\,a\right]}{k_f^{(j)}(\vec{r}_i)} + \frac{\zeta\left[k_f^{(i)}(\vec{r}_j)\,a\right]}{k_f^{(i)}(\vec{r}_j)}\right)\delta(\vec{r}_i - \vec{r}_j)$$

where $k_f^{(j)}(\vec{r}) = \left[6\pi^2\rho^{(j)}(\vec{r})\right]^{1/3}$ is the Fermi wave number of the spin component that particle j belongs to.

The derivation following this assumptions is the same as that for the two-component gas, up to Eq. 3.40. The only additional pieces of information needed are the common density of each component in the effective trap with oscillator length, ℓ_{eff}, the chemical potential, the non-interacting ground state energy and the average hyperradius squared for the system with χ spin substates in the large N limit:

$$\rho^{(i)}_{\ell_{eff}}(\vec{r}) = \frac{1}{6\pi^2\ell_{eff}^3}(2\mu)^{3/2}\left(1 - \frac{r^2}{2\ell_{eff}^2\mu}\right)^{3/2}, \tag{3.49}$$

$$\mu = \left(\frac{6N}{\chi}\right)^{1/3}, \tag{3.50}$$

$$E_{NI} = \hbar\omega\frac{(6N)^{4/3}}{\chi^{1/3}8}, \tag{3.51}$$

$$\left\langle R^2\right\rangle_{NI} = \frac{\hbar}{m\omega}\frac{(6N)^{4/3}}{\chi^{1/3}8N}. \tag{3.52}$$

Evaluating the matrix element in Eq. 3.15 involves basic well known methods. With some algebra and a change of integration variables, the effective hyperradial potential

becomes

$$\frac{V_{eff}\left(R'\right)}{E_{NI}} = \frac{1}{2R'^2} + \frac{1}{2}R'^2 + \left(\chi - 1\right)\frac{256}{9\pi^2 R'^2} f\left(\frac{k_f^0 a}{R'}\right), \tag{3.53}$$
$$f\left(\frac{k_f^0 a}{R'}\right) \equiv \int_0^1 y^6\sqrt{1-y^2}\zeta\left(\frac{k_f^0 a}{R'}y\right)dy.$$

Comparison with the effective potential for the two component gas, Eq. 3.41, demonstrates that the extra spin components increase the strength of the interaction by a factor of $\chi - 1$. To analyze the stability of the gas, it is sufficient to examine the $k_f^0 a \to -\infty$ limit, i.e.

$$\frac{V_{eff}\left(R'\right)}{E_{NI}} \to \frac{1}{2}R'^2 + \frac{1 + 10\left(\chi - 1\right)\zeta_-/9\pi}{2R'^2}. \tag{3.54}$$

Taking $\chi = 3$ yields

$$\begin{aligned}\frac{V_{eff}\left(R'\right)}{E_{NI}} &\to \frac{1}{2}R'^2 + \frac{1 + 20\zeta_-/9\pi}{2R'^2}, \\ &= \frac{1}{2}R'^2 + \frac{0.00772}{R'^2}.\end{aligned} \tag{3.55}$$

In this limit the barrier preventing the gas from falling in to the center of the trap, i.e. $R' \to 0$, is **very** weak. The unitarity energy and average hyperradius are given by

$$\begin{aligned}\frac{E}{E_{NI}} &= \sqrt{1 + 20\zeta_-/9\pi} = 0.124, \\ \frac{R_{\min}}{\sqrt{\langle R^2\rangle_{NI}}} &= \left(1 + 20\zeta_-/9\pi\right)^{1/4} = 0.352.\end{aligned}$$

Since the K harmonic method is intrinsically a variational calculation, it is entirely possible that a better trial function, for example one based on the HF method, might show that the 3 component gas becomes mechanically unstable in the unitarity limit [25]. In other words the three component gas might collapse in a manner similar to that of the bosenova [67, 98, 99, 10, 100]. Further, if the asymptotic behavior of the density dependence in the two-body interaction is modified to agree with the β for the two-component gas predicted by Ref. [45] the barely repulsive unitarity potential in Eq. 3.55 becomes attractive, predicting a collapse of the three-component gas [88]. If the

asymptotic behavior of the density-dependent interaction of Eq. 3.37 are modified so that the value for β in Eq. 3.47 matches the quantum Monte-Carlo results of Ref. [45], $\beta = -0.58$, at unitarity the effective hyperradial potential for a three component gas becomes

$$\frac{V_{eff}\left(R'\right)}{E_{NI}} \rightarrow \frac{1}{2}R'^2 - \frac{0.08}{R'^2}$$

which provides no stable region, implying that the three-component Fermi gas is unstable in this regime. The critical scattering length that determines the collapse point can be calculated numerically:

$$k_f^0 a_c = -1.413. \tag{3.56}$$

Recently, degenerate gases of ^{6}Li have been created in the three lowest hyperfine states with peak densities of approximately 6×10^{11} atoms/cm^3 [94, 95]. If it is assumed that all three components interact with the same scattering length, $a = 3000$ a.u., a reasonable assumption for magnetic fields near 1000 G [4], this predicts a bosenova-like collapse at a central density of approximately

$$\rho\left(0\right) = \frac{1}{6\pi^2}\left(k_f^0\right)^3 \approx 1.4 \times 10^{13} \text{ atoms/cm}^3.$$

It is likely that the predicted instability can be achieved at a lower density by using a different magnetic field where the three scattering lengths are larger, but not approximately equal.

Setting $\chi = 4$ in Eq. 3.54, the effective potential as $k_f^0 a \rightarrow -\infty$ becomes entirely attractive, i.e.

$$\begin{aligned} \frac{V_{eff}\left(R'\right)}{E_{NI}} &\rightarrow \frac{1}{2}R'^2 + \frac{1 - 30\zeta_-/9\pi}{2R'^2} \\ &= \frac{1}{2}R'^2 - \frac{0.238}{R'^2}, \end{aligned} \tag{3.57}$$

meaning that the gas is predicted to collapse down toward $R' \rightarrow 0$. Presumably some very rich and complex dynamics (cluster formation, inelastic collisions, etc.) occur during this process, but the K-harmonic trial wave function is too simple to describe

these phenomena. When the local minimum in $V_{eff}\left(R'\right)$ becomes a saddle point the gas is no longer mechanically stable and is free to collapse. This occurs at a critical interaction strength of $k_f^0 a_c = -0.657$.

Chapter 4

The Hypervectorial Method and Anisotropic Traps

Most theoretical studies of these DFGs look either at a homogeneous gas directly, which can be related to a harmonically trapped gas through the use of the local density approximation, or at a gas in a spherically symmetric oscillator trap as in Chapter 3. While these studies can lead to interesting predictions of phenomena in such a system, experimentally the gas is often held in an anisotropic "cigar-shaped" trap [13, 15, 16, 17, 14].

The starting point for this study is akin to the hyperspherical K-harmonic method presented in the previous chapter in which the DFG was described by a set of $3N-1$ angular coordinates on the surface of a $3N$ dimensional hypersphere of radius R where N is the total number of particles in the system. To incorporate an anisotropic trap in that formulation would require a very high order in hyperspherical harmonics, and would result in a complex system of coupled 1D differential equations. To avoid these complications here I implement a hypervectorial formulation, which is based on the division of the total $3N$ dimensional space into physically meaningful subspaces in a manner similar to the hyperspherical tree depicted in Fig. 2.3. The division can be thought of as describing the gas by $3N-2$ angular coordinates on the surface of a $3N$ dimensional "hyper-cylinder" with height R_z and cylindrical radius R_ρ. These coordinates have been used previously to describe a Bose-Einstein condensate in cigar-shaped and completely anisotropic traps [68]. Their method is extended in this chapter

to describe the degenerate Fermi gas.

This chapter is arranged as follows; In Sec 4.1 I introduce the hypervectorial method. In Section 4.2 I apply this method to the case of the two-component degenerate Fermi gas with density-dependent, zero-range interactions and analyze the resulting potential surfaces. Finally, Section 4.3 uses the potential surface to extract the frequency of low-energy excitations.

4.1 The Hypervectorial Method

The use of hyperspherical coordinates is well suited to an isotropic oscillator trap because the trapping potential is easily written in terms of the hyperradius, for instance in Eq. 3.2. This is not the case in an anisotropic trap, where different Cartesian coordinates in the trap are associated with different oscillator frequencies. This section will deal with a cylindrically symmetric "cigar" shaped trap, but with minor modifications, the methods presented here carry over to a completely anisotropic trap. The Hamiltonian for this system is given by

$$H = -\frac{\hbar^2}{2m}\sum_{i=1}^{N}\nabla_i^2 + \frac{1}{2}m\sum_{i=1}^{N}\left(\omega_\perp^2\left(x_i^2+y_i^2\right)+\omega_z^2 z_i^2\right) + \sum_{i>j}U_{int}\left(r_{ij}\right), \tag{4.1}$$

where ω_z and $\omega_\perp$ are oscillator frequencies in the longitudinal and transverse directions, respectively. Here x_i, y_i, and z_i are the Cartesian coordinates of the ith atom and r_{ij} is the inter-particle distance between particles i and j. Now consider two collective coordinates, R_z and R_ρ, given by the rms longitudinal and transverse size of the gas, respectively, i.e.

$$R_z^2 = \frac{1}{N}\sum_{i=1}^{N} z_i^2, \tag{4.2}$$

$$R_\rho^2 = \frac{1}{N}\sum_{i=1}^{N}\left(x_i^2+y_i^2\right). \tag{4.3}$$

This choice of collective coordinates is equivalent to the hyperspherical tree shown pictorially in Fig. 2.3 with $R_1 = R_\rho$, and $R_2 = R_z$. Here, though, the final step of correlating

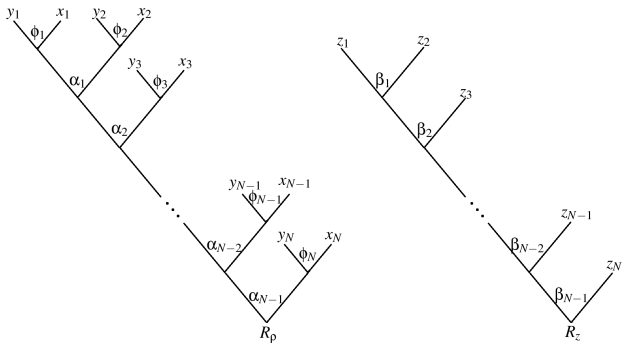

Figure 4.1: The sub-hyperspherical trees that are used to parameterize the hypervectorial coordinates R_ρ and R_z are shown.

these two collective coordinates is omitted. The remaining $3N-2$ spatial degrees of freedom in the gas are described by angles. For completeness, the Delves parameterizations shown in Fig. 4.1 can be used, i.e. N angles are merely the cylindrical polar angles for each atom $\{\phi_i\}_{i=1}^N$, while the remaining $2N-2$ angle are given by

$$\tan\beta_i = \frac{\sqrt{\sum_{j=1}^{i} z_j^2}}{z_{i+1}}, \tag{4.4}$$

$$\tan\alpha_i = \frac{\sqrt{\sum_{j=1}^{i}\left(x_j^2+y_j^2\right)}}{\rho_{i+1}}, \tag{4.5}$$

where $0 \le \beta_i, \alpha_i \le \pi/2$ and $1 \le i \le N-1$. Collectively these $3N-2$ hyperangles will be referred to as $\Omega = (\Omega_1, \Omega_2)$ where Ω_1 corresponds to the sub-hyperangles describing the transverse coordinates and Ω_2 the longitudinal sub-hyperangles. In these coordinates the sum of the Laplacians in Eq. 4.1 can be found using Eq. 2.2:

$$\sum_i^N \nabla_i^2 = \frac{1}{N}\left[\frac{1}{R_\rho^{2N-1}}\frac{\partial}{\partial R_\rho}R_\rho^{2N-1}\frac{\partial}{\partial R_\rho} - \frac{\mathbf{\Lambda}_\perp^2}{R_\rho^2} + \frac{1}{R_z^{N-1}}\frac{\partial}{\partial R_z}R_z^{N-1}\frac{\partial}{\partial R_z} - \frac{\mathbf{\Lambda}_z^2}{R_z^2}\right], \tag{4.6}$$

where $\mathbf{\Lambda}_\perp^2$ and $\mathbf{\Lambda}_z^2$ have been defined by the Eq. 2.3 in each of the two subspaces. Combining Eqs. 4.4, 4.3 and 4.6 the Hamiltonian in Eq. 4.1 can be rewritten in terms

of the hypervectorial coordinates:

$$H = -\frac{\hbar^2}{2M}\left[\frac{1}{R_\rho^{2N-1}}\frac{\partial}{\partial R_\rho}R_\rho^{2N-1}\frac{\partial}{\partial R_\rho} - \frac{\mathbf{\Lambda}_\perp^2}{R_\rho^2}\right] + \frac{1}{2}M\omega_\perp^2 R_\rho^2 + \\ -\frac{\hbar^2}{2M}\left[\frac{1}{R_z^{N-1}}\frac{\partial}{\partial R_z}R_z^{N-1}\frac{\partial}{\partial R_z} - \frac{\mathbf{\Lambda}_z^2}{R_z^2}\right] + \frac{1}{2}M\omega_z^2 R_z^2 + \sum_{i>j} U_{int}\left(r_{ij}\right), \tag{4.7}$$

where $M = Nm$.

The key to the hypervectorial method presented here is similar to the K-harmonic approximation, that of a variational ansatz wavefunction,

$$\Psi\left(R_\rho, R_z, \Omega_1, \Omega_2, \sigma_1, \sigma_2, ..., \sigma_N\right) = F\left(R_\rho, R_z\right) Y_{\lambda_\perp \lambda_z \mu}\left(\Omega_1, \Omega_2, \sigma_1, \sigma_2, ..., \sigma_N\right) \tag{4.8}$$

where $Y_{\lambda_\perp \lambda_z \mu}\left(\Omega_1, \Omega_2, \sigma_1, \sigma_2, ..., \sigma_N\right)$ is the lowest allowed harmonic for the N fermion system. Here $(\sigma_1, \sigma_2, ..., \sigma_N)$ are the spin coordinates. It would be convenient if $Y_{\lambda_\perp \lambda_z \mu}$ were merely a product of two K-harmonics, one from each subspace in the system, but this is not the case. The permutational symmetry of the system mixes sub-hyperspherical harmonics together. Fortunately, examining Eq. 4.7 with $U_{int}\left(r_{ij}\right) = 0$, it is clear that the anisotropic oscillator is separable in the hypervectorial coordinates.

A similar derivation to the one in Section 2.2.1 shows that the hyperangular behavior of the noninteracting system is given by

$$Y_{\lambda_\perp \lambda_z \mu}\left(\Omega_1, \Omega_2, \sigma_1, \sigma_2, ..., \sigma_N\right) = \frac{D\left(\vec{r}_1, \vec{r}_2, ..., \vec{r}_N, \sigma_1, \sigma_2, ..., \sigma_N\right)}{R_\rho^{(2N-1)/2} G_{0K_\perp}^{\perp}\left(R_\rho\right) R_z^{(N-1)/2} G_{0K_z}^{z}\left(R_z\right)}, \tag{4.9}$$

where $D\left(\vec{r}_1, \vec{r}_2, ..., \vec{r}_N, \sigma_1, \sigma_2, ..., \sigma_N\right)$ is a ground state Slater-determinant of independent particle states, i.e.:

$$D\left(\vec{r}_1, \vec{r}_2, ..., \vec{r}_N, \sigma_1, \sigma_2, ..., \sigma_N\right) = \sum_P (-1)^p \prod_{i=1}^{N} \psi_i\left(\vec{r}_i\right) \langle \sigma_i | m_{s_i} \rangle \tag{4.10}$$

$$\sqrt{\rho_i}\psi_i\left(\vec{r}\right) = A_{n_{\perp_i} n_{z_i} m_i} \exp\left(-\rho^2/2\ell_\perp - z^2/2\ell_z^2\right) \exp\left(im\phi\right) \\ \times \left(\frac{\rho}{\ell_\perp}\right)^{|m|+1/2} L_{n_{\perp_i}}^{|m|+1/2}\left(\frac{\rho^2}{\ell_\perp^2}\right) H_{n_{z_i}}\left(\frac{z}{\ell_z}\right)$$

where the sum runs over all permutations, P, of the N spatial and spin coordinates, $L_n^\gamma\left(x\right)$ is a Laguerre polynomial, $H_n\left(x\right)$ is a Hermite polynomial, $\ell_\perp = \sqrt{\hbar/m\omega_\perp}$, $\ell_z =$

$\sqrt{\hbar/m\omega_z}$, and $A_{n_{\perp_i} n_{z_i} m_i}$ is a normalization constant. In Eq. 4.9, $K_\perp = \lambda_\perp + N - 3/2$, $K_z = \lambda_z + N/2 - 3/2$, and the sub-hyperradial solutions to the noninteracting oscillator $G^{\perp}_{\chi K_\perp}(R_\rho)$ and $G^{z}_{\chi K_z}(R_z)$ are given by

$$R_\rho^{(2N-1)/2} G^{\perp}_{\chi K_\perp}(R_\rho) = A^{\perp}_{\chi K_\perp} \exp\left(-R_\rho^2/2\mathcal{L}_\perp\right) \left(\frac{R_\rho}{\mathcal{L}_\perp}\right)^{K_\perp+1} L_\chi^{K_\perp+1/2}\left(\frac{R_\rho^2}{\mathcal{L}_\perp^2}\right),$$

$$R_z^{(N-1)/2} G^{z}_{\chi K_z}(R_z) = A^{z}_{\chi K_z} \exp\left(-R_z^2/2\mathcal{L}_z\right) \left(\frac{R_z}{\mathcal{L}_z}\right)^{K_z+1} L_\chi^{K_\perp+1/2}\left(\frac{R_\rho^2}{\mathcal{L}_\perp^2}\right).$$

Here $\mathcal{L}_\perp = \ell_\perp/\sqrt{N}$, $\mathcal{L}_z = \ell_z/\sqrt{N}$ and $A^{\perp}_{\chi K_\perp}$ and $A^{z}_{\chi K_z}$ are normalization constants. Even though $Y_{\lambda_\perp \lambda_z \mu}(\Omega_1, \Omega_2, \sigma_1, \sigma_2, ..., \sigma_N)$ is not a product of two sub-hyperspherical harmonics, it still satisfies the relevant eigenvalue equation:

$$\Lambda_\perp^2 Y_{\lambda_\perp \lambda_z \mu}(\Omega_1, \Omega_2) = \lambda_\perp(\lambda_\perp + 2N - 2) Y_{\lambda_\perp \lambda_z \mu}(\Omega_1, \Omega_2),$$

$$\Lambda_z^2 Y_{\lambda_\perp \lambda_z \mu}(\Omega_1, \Omega_2) = \lambda_z(\lambda_z + N - 2) Y_{\lambda_\perp \lambda_z \mu}(\Omega_1, \Omega_2),$$

where the spin coordinates have been omitted for notational simplicity. The sub-hyperangular momentum eigenvalues, $\lambda_\perp$ and λ_z, are determined by the number of oscillator quanta in $D(\vec{r}_1, \vec{r}_2, ..., \vec{r}_N, \sigma_1, \sigma_2, ..., \sigma_N)$ in the longitudinal and transverse directions respectively:

$$\lambda_\perp = \sum_{i=1}^{N} (2n_{\perp_i} + |m_i|),$$

$$\lambda_z = \sum_{i=1}^{N} n_{z_i}.$$

For this treatment I will again only consider nondegenerate, filled energy shells. The nondegenerate ground state is found by filling every state in the noninteracting system up to a Fermi energy, ϵ_F. In the large N limit, which will be the focus of this chapter, the Fermi energy is given in terms of the number of atoms by

$$\epsilon_f \to \hbar\left(3N\omega_\perp^2\omega_z\right)^{1/3}, \tag{4.11}$$

where it has been assumed that there are enough atoms to occupy many longitudinal and transverse modes, i.e. the system is still three dimensional. The energy of the non-interacting system is given in terms of the hyperangular momentum quantum numbers as

$$E_{NI} = \hbar\omega_\perp \left(\lambda_\perp + 1\right) + \hbar\omega_z \left(\lambda_z + 1/2\right).$$

In the large N limit, this becomes

$$E_{NI} \to \frac{\epsilon_f^4}{4\hbar^3\omega_\perp^2\omega_z} = \frac{\hbar\left(3N\omega_\perp^2\omega_z\right)^{4/3}}{4\omega_\perp^2\omega_z}. \tag{4.12}$$

The hyperangular momentum quantum numbers, $\lambda_\perp$and λ_z, in the large N limit are given by

$$\lambda_z \to \frac{\epsilon_F^4}{12\hbar^4\omega_z^2\omega_\perp^2} = \frac{\left(3N\omega_\perp^2\omega_z\right)^{4/3}}{12\omega_\perp^2\omega_z^2}, \tag{4.13}$$

$$\lambda_\perp \to \frac{\epsilon_F^4}{6\hbar^4\omega_z\omega_\perp^3} = \frac{\left(3N\omega_\perp^2\omega_z\right)^{4/3}}{6\omega_\perp^3\omega_z}. \tag{4.14}$$

To employ the variational principle the hyperangular expectation value of the Hamiltonian given in Eq. 4.7 must be taken, leaving an effective Schrödinger equation in the collective coordinates, R_ρ and R_z:

$$\begin{aligned} ER_z^{(N-1)/2}R_\rho^{(2N-1)/2}F\left(R_\rho,R_z\right) = \Bigg[& -\frac{\hbar^2}{2M}\left(\frac{\partial^2}{\partial R_\rho^2} - \frac{K_\perp\left(K_\perp+1\right)}{2MR_\rho^2}\right) \\ & - \frac{\hbar^2}{2M}\left(\frac{\partial^2}{\partial R_z^2} - \frac{K_z\left(K_z+1\right)}{2MR_z^2}\right) \\ & + \frac{1}{2}M\omega_\perp^2R_\rho^2 + \frac{1}{2}M\omega_\perp^2R_z^2 \\ & + \sum_{i>j}\left\langle Y_{\lambda_\perp\lambda_z\mu}\left|U_{int}\left(r_{ij}\right)\right|Y_{\lambda_\perp\lambda_z\mu}\right\rangle\Bigg] R_z^{(N-1)/2}R_\rho^{(2N-1)/2}F\left(R_\rho,R_z\right). \end{aligned} \tag{4.15}$$

Here $F\left(R_\rho,R_z\right)$ has been multiplied by a factor of $R_z^{(N-1)/2}R_\rho^{(2N-1)/2}$ to remove first derivative terms. To avoid divergences in the large N limit, it is convenient to rescale

the effective Schrödinger equation by noninteracting values:

$$\begin{aligned} E &= E_{NI} E', \\ R_\rho &= \sqrt{\langle R_\rho^2 \rangle_{NI}} R'_\rho, \\ R_z &= \sqrt{\langle R_\rho^2 \rangle_{NI}} R'_z, \end{aligned}$$

where E_{NI} is the noninteracting energy, and $\langle R_\rho^2 \rangle_{NI}$ is the expectation value of the transverse collective coordinate squared given in the large N limit by

$$\begin{aligned} \langle R_\rho^2 \rangle_{NI} &= \frac{\hbar}{M\omega_\perp} \left(\lambda_\perp + N - \frac{1}{2} \right) \\ &\to \frac{(3N\gamma)^{4/3}}{6N\gamma} \ell_\perp^2, \end{aligned} \tag{4.16}$$

with $\gamma = \omega_z/\omega_\perp$. In the large N limit, with this rescaling, Eq. 4.15 becomes

$$0 = \left[-\frac{1}{2m^*} \left(\frac{\partial^2}{\partial R_\rho'^2} + \frac{\partial^2}{\partial R_z'^2} \right) + \frac{V_{eff}\left(R'_\rho, R'_z\right)}{E_{NI}} - \frac{E}{E_{NI}} \right] R_z'^{(N-1)/2} R_\rho'^{(2N-1)/2} F\left(R'_\rho, R'_z\right). \tag{4.17}$$

Here $m^* = M E_{NI} \langle R_\rho^2 \rangle_{NI} / \hbar^2$, and the effective potential, $V_{eff}\left(R'_\rho, R'_z\right)$, is given by

$$\begin{aligned} \frac{V_{eff}\left(R'_\rho, R'_z\right)}{E_{NI}} =& \frac{1}{3R_\rho'^2} + \frac{1}{3} R_\rho'^2 + \frac{1}{12\gamma^2 R_z'^2} + \frac{1}{3}\gamma^2 R_z'^2 \\ &+ \frac{\left\langle Y_{\lambda_\perp \lambda_z \mu} \left| \sum_{i>j} U_{int}\left(r_{ij}\right) \right| Y_{\lambda_\perp \lambda_z \mu} \right\rangle}{E_{NI}}. \end{aligned} \tag{4.18}$$

with $\gamma = \omega_z/\omega_\perp$. All that remains is to calculate the hyperangular expectation value of the interaction.

4.2 More density-dependent interactions

It was shown in Chapter 3 that the bare Fermi pseudo-potential in Eq. 3.9 predicted an unphysical collapse of the two component degenerate Fermi gas. With this in mind I will jump directly to using the density-dependent interaction of Eq. 3.36 in the large N limit. In the K harmonic approximation, the hyperangular expectation value in the large N limit is equivalent to a simple expectation value of a Slater-determinant,

ground state, independent particle wavefunction in an effective oscillator trap taken over all $3N$ spatial degrees and N spin degrees of freedom. A similar derivation here yields the same result, i.e.:

$$V_{int}\left(R'_{\rho},R'_{z}\right)=\left\langle Y_{\lambda_{\perp}\lambda_{z}\mu}\left|\sum_{i>j}U_{int}\left(r_{ij}\right)\right|Y_{\lambda_{\perp}\lambda_{z}\mu}\right\rangle \tag{4.19}$$
$$=\left\langle D_{\ell_{eff_{\perp}}\ell_{eff_{z}}}\left|\sum_{i>j}U_{int}\left(r_{ij}\right)\right|D_{\ell_{eff_{\perp}}\ell_{eff_{z}}}\right\rangle_{3N},$$

where $D_{\ell_{eff_{\perp}}\ell_{eff_{z}}}\left(\vec{r}_{1},\vec{r}_{2},...,\vec{r}_{N},\sigma_{1},\sigma_{2},...,\sigma_{N}\right)$ is a ground state Slater-determinant wavefunction of N independent noninteracting fermions in an anisotropic cigar-shaped trap with effective oscillator lengths,

$$\ell_{eff_{\perp}}=R'_{\rho}\ell_{\perp}, \tag{4.20}$$
$$\ell_{eff_{z}}=R'_{z}\frac{\sqrt{\left\langle R_{\rho}^{2}\right\rangle_{NI}}}{\sqrt{\left\langle R_{z}^{2}\right\rangle_{NI}}}\ell_{z}.$$

Here $\left\langle R_{z}^{2}\right\rangle_{NI}$ is the expectation value of the square of the longitudinal collective coordinate:

$$\left\langle R_{z}^{2}\right\rangle_{NI}=\frac{\hbar}{M\omega_{z}}\left(\lambda_{z}+\frac{N}{2}-\frac{1}{2}\right) \tag{4.21}$$
$$\rightarrow\frac{\left(3N\gamma\right)^{4/3}}{12N\gamma^{2}}\ell_{z}^{2}.$$

In the large N limit the density, $\rho^{(1)}_{\ell_{eff_{\perp}}\ell_{eff_{z}}}\left(\rho,z\right)$, of a single spin component in the ground state of the effective oscillator is given by [84]

$$\rho^{(1)}_{\ell_{eff_{\perp}}\ell_{eff_{z}}}\left(\vec{r}\right)=\frac{1}{6\pi^{2}\ell_{eff_{z}}\ell_{eff_{\perp}}^{2}}\left(2\mu\right)^{3/2}\left(1-\left(\ell_{eff_{z}}\ell_{eff_{\perp}}^{2}\right)^{2/3}\frac{z^{2}/\ell_{eff_{z}}^{4}+\rho^{2}/\ell_{eff_{\perp}}^{4}}{2\mu}\right)^{3/2}, \tag{4.22}$$

where $\mu=\left(3N\right)^{1/3}$ is set by $\int\rho^{(1)}_{\ell_{eff_{\perp}}\ell_{eff_{z}}}\left(\vec{r}\right)d^{3}r=N/2$.

Evaluating the expectation value in Eq. 4.19 with U_{int} given by Eq. 3.36 and

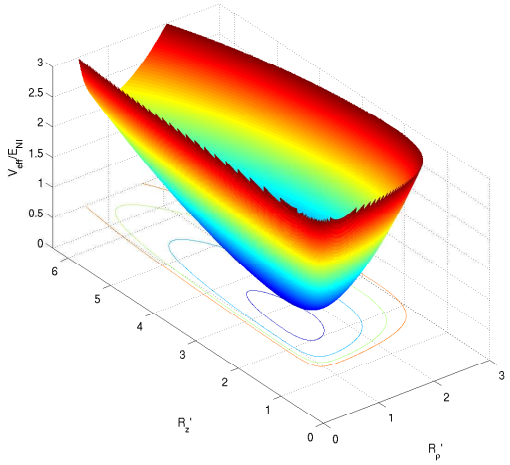

Figure 4.2: The dimensionless effective hypervectorial potential is shown plotted as a function of R'_ρ and R'_z for an interaction strength $k_f^0 a = 0$ and a trap ratio of $\gamma = 1/3$.

$k_f(r) = \left(6\pi^2 \rho^{(1)}_{\ell_{eff_\perp} \ell_{eff_z}}(\vec{r})\right)^{1/3}$ gives the effective hypervectorial interaction potential

$$\frac{V_{int}\left(R'_\rho, R'_z\right)}{E_{NI}} = \frac{256}{9\pi^2\left(\sqrt{2}\gamma R'_z R'^2_\rho\right)^{2/3}} f\left(\frac{k_f^0 a}{\left(\sqrt{2}\gamma R'_z R'^2_\rho\right)^{1/3}}\right), \tag{4.23}$$

$$f(x) = \int_0^1 y^6 \sqrt{1-y^2}\,\zeta(xy)\,dy.$$

One should note that the function $f(x)$ is the same as in the isotropic trap hyperradial effective potential, Eq. 3.40. Putting everything together yields a total effective hypervectorial potential,

$$\frac{V_{eff}\left(R'_\rho, R'_z\right)}{E_{NI}} = \frac{1}{3R'^2_\rho} + \frac{1}{3}R'^2_\rho + \frac{1}{12\gamma^2 R'^2_z} + \frac{1}{3}\gamma^2 R'^2_z + \frac{V_{int}\left(R'_\rho, R'_z\right)}{E_{NI}}. \tag{4.24}$$

An example of the effective potential is shown in Fig. 4.2 for a trap ratio $\gamma = 1/3$ and an interaction strength of $k_f^0 a = -1$.

4.2.1 Results for the hypervectorial method

Here I analyze the behavior of the effective hypervectorial potential for various values of $k_f^0 a$. Figure 4.3 shows contour plots of V_{eff} for evenly spaced values of $k_f^0 a$ from

-12 to 12 for a system with trap ratio $\gamma = 1/3$. For attractive interactions ($a < 0$), the minimum is seen to be pulled into the center as the gas pulls in on itself. For repulsive interactions ($a > 0$) the minimum is pushed out away from the center. It is also interesting to see the low lying contours behavior as it gets twisted towards the origin for attractive interactions and away for repulsive. This behavior will be studied in more detail later.

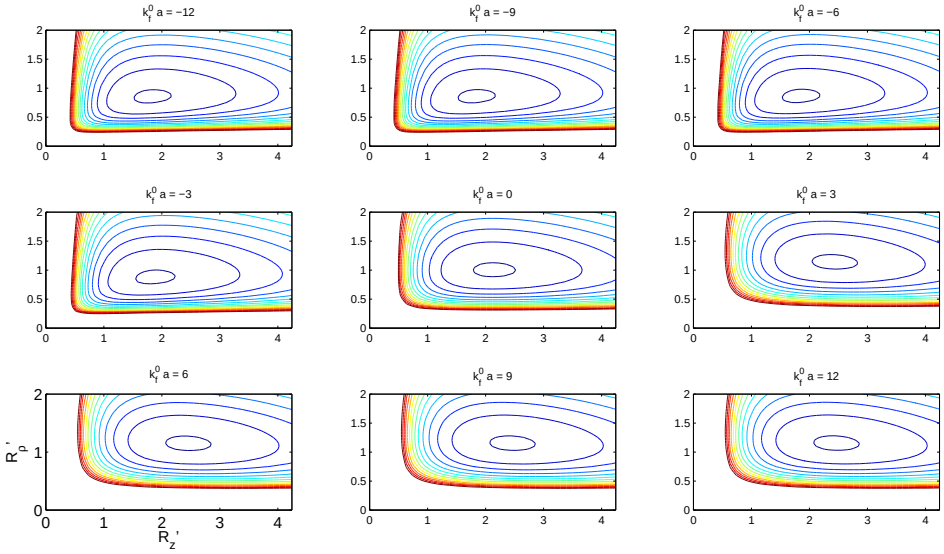

Figure 4.3: Contour plots of the dimensionless effective hypervectorial potential are shown plotted as a function of R'_ρ and R'_z for an interaction strength $k_f^0 a = -12$ to 12 and a trap ratio of $\gamma = 1/3$.

In this section the ground state energy and average squared collective coordinates for the DFG in an anisotropic trap are found, i.e. E/E_{NI}, $\langle R'^2_z \rangle$ and $\langle R'^2_\rho \rangle$. In the same way as the hyperspherical K harmonic method, these quantities can be found by minimizing V_{eff}, i.e. by solving $\dfrac{\partial V_{eff}}{\partial R'_\rho} = \dfrac{\partial V_{eff}}{\partial R'_z} = 0$. Finding the minimum of Eq. 4.24 cannot be done analytically, but because the interaction is function of $R'_z R'^2_\rho$ only, the relationship between the minimum longitudinal coordinates, $R'_{z\,\min}$, and transverse

coordinate, $R'_{\rho\,\min}$, can be found:

$$R'_{z\,\min} = \frac{R'_{\rho\,\min}}{\sqrt{2}\gamma} \tag{4.25}$$

This indicates that the DFG with density dependent interactions will always maintain the same aspect ratio. This behavior is likely due to the fact that the hyperangular behavior was frozen to the noninteracting behavior so that oscillator quanta cannot be exchanged between the longitudinal and transverse directions, i.e. λ_z and $\lambda_\perp$ are fixed. If a more complex formulation were to be used, by allowing λ_z and $\lambda_\perp$ to be function of the hypervectorial coordinates, a task beyond the scope of this study, it is likely that the aspect ratio of the gas would change with repulsive and attractive interactions. The minimum in V_{eff} must lie along the line, $R'_{z\,\min} = R'_{\rho\,\min}/\sqrt{2}\gamma$, and evauates to

$$\frac{V_{int}\left(R'_\rho, R'_z = \dfrac{R'_\rho}{\sqrt{2}\gamma}\right)}{E_{NI}} = \frac{1}{2R'^2_\rho} + \frac{1}{2}R'^2_\rho + \frac{1}{6R'^2_z} + \frac{1}{6}\gamma^2 R'^2_z + \frac{256}{9\pi^2 R'^2_\rho} f\left(\frac{k^0_f a}{R'_\rho}\right). \tag{4.26}$$

This is the exact same functional form as the effective potential found for the hyperspherical treatment in an isotropic trap, Eq. 3.41, meaning that large N expectation for E/E_{NI} and $\langle R^2_\rho\rangle / \langle R^2_\rho\rangle_{NI}$ in the ground state will be exactly the same as E/E_{NI} and $\langle R^2\rangle / \langle R^2\rangle_{NI}$ shown in Figs. 3.16 and 3.17.

4.3 Low energy excitations

One of the benefits from the hyperspherical K-harmonic was the simple extraction of the low lying radial excitations. Similarly, in the hypervectorial picture, low lying excitations can be extracted as well. The difference is that now there are two distinct types of excitation corresponding to transverse and longitudinal breathing modes. In the noninteracting limit these two modes decouple, but as interactions are turned on, excitations in the two trap axes become coupled. This behavior can be visually understood by examining the ellipses made by the low lying contours shown in Fig. 4.3.

A more quantitative view of the low lying excitations can be extracted by normal-mode type of analysis which begins by approximating the effective potential about the minimum as a harmonic oscillator potential,

$$\frac{V_{eff}\left(R'_\rho, R'_z\right)}{E_{NI}} \approx \frac{E_{GS}}{E_{NI}} + \frac{1}{2}\left[R'_\rho - R'_{\rho\,\min}, R'_z - R'_{z\,\min}\right] \begin{bmatrix} \dfrac{\partial^2 V_{eff}}{\partial R'^2_\rho} & \dfrac{\partial^2 V_{eff}}{\partial R'_\rho \partial R'_z} \\ \dfrac{\partial^2 V_{eff}}{\partial R'_\rho \partial R'_z} & \dfrac{\partial^2 V_{eff}}{\partial R'^2_z} \end{bmatrix} \begin{bmatrix} R'_\rho - R'_{\rho\,\min} \\ R'_z - R'_{z\,\min} \end{bmatrix} \tag{4.27}$$

where E_{GS} is the ground state energy found by minimizing the effective potential. The oscillator frequencies about this minimum can be extracted by finding the eigenvalues of the Hessian matrix in Eq. 4.27:

$$\omega_1 = \sqrt{\frac{1}{m^*}\nu_1},$$
$$\omega_2 = \sqrt{\frac{1}{m^*}\nu_2},$$

where ν_1 and ν_2 are the eigenvalues. These breathing modes are in units of the noninteracting energy; to get back to conventional units, the frequencies must be multiplied by $E_{NI}/\hbar$. From Eq. 4.17, $m^* = mE_{NI}N\left\langle R^2_\rho\right\rangle_{NI}/\hbar^2$, and noting that $N\left\langle R^2_\rho\right\rangle_{NI} = 2\ell^2_\perp E_{NI}/3\hbar\omega_\perp$ gives

$$\omega_1^B = \sqrt{\frac{3}{2}}\omega_\perp\sqrt{\nu_1}, \tag{4.28}$$
$$\omega_2^B = \sqrt{\frac{3}{2}}\omega_\perp\sqrt{\nu_2},$$

The eigenvectors corresponding to the eigenvalues in this equation have a direct meaning, as the directions in which the gas oscillates. Roughly, one of these frequencies corresponds to the transverse breathing mode, while the other to longitudinal. I will take ω_1 (ω_2) as the transverse (longitudinal) mode, i.e. in the noninteracting limit $\omega_1 = 2\omega_\perp$.

Figures 4.4 and 4.5 show the two breathing mode frequencies as a function of $k^0_f a$ for trap ratios $\gamma = 0.1$ to $\gamma = 1$. For $\gamma = 1$, a cusp can be seen at $k_f a = 0$ in both frequencies. This is due to the degeneracy of the two breathing modes in the isotropic trap.

Again, it should be mentioned that both the variational trial wavefunction and the density dependent interaction cannot describe a gas of bosonic dimers for positive scattering lengths. There are several worrying things that can be seen in the predicted behavior of the breathing modes. First, in the unitarity regime, $k_f^0 a \to -\infty$, both the transverse and longitudinal breathing modes are greater than the noninteracting frequencies for $\gamma < 1$, and the frequencies in this regime depend on γ. This is in disagreement with the unitarity predication from superfluid hydrodynamic models of $\omega_1^B = \sqrt{10/3}\omega_\perp$ and $\omega_2^B = \sqrt{12/5}\omega_z$ [101]. Second, and most importantly, the frequencies predicted here differ, both quantitatively and qualitatively, from those found in experiment [102]. These disagreements are likely due to the overly simplistic variational trial wavefunction, Eq. 4.8, used in the hypervectorial picture. By fixing the hyperangular behavior to that of the noninteracting Fermi gas, the wavefunction cannot take into account the higher order correlations, such as BEC-like pairing, that are present in the system.

While this study does not "hit the nail on the head", this is seen as a stepping off point for future studies that hopefully will begin to incorporate the more complex nature of this system. This chapter may also be seen as a simple example of the hypervectorial method. While the idea was applied here to a degenerate Fermi gas in an anisotropic trap, this is by no means the only possible application of the technique. For instance, in a Fermi gas of distinguishable particles, e.g. a Fermi gas where the components have unequal masses, unequal numbers, or different trapping frequencies, the hypervectorial approach can be applied with each part of the hypervector corresponds to a sub-hyperradius for each component in the gas. This might allow for higher order fluctuations, phenomena like phase separation, or a "beating" mode where two components oscillate out of phases.

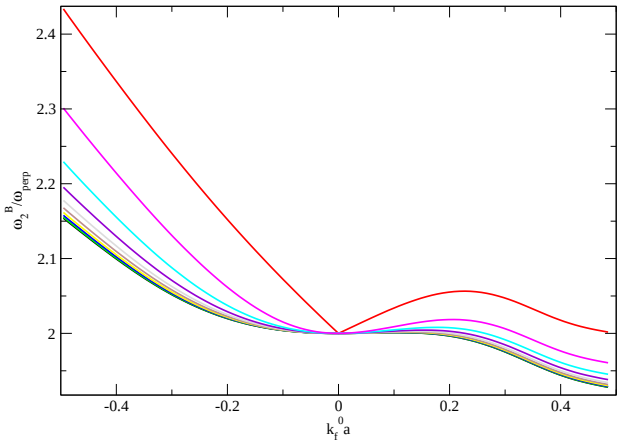

Figure 4.4: The transverse breathing mode predicted by the hypervectorial method is shown plotted versus the interaction strength $k_f^0 a$ for trap ratios $\gamma = 0.1$ to 1 in steps of 0.1 from top to bottom. The kink in the seen in the $\gamma = 1$ frequency is due to a degeneracy between the longitudinal and transverse frequencies in the non-interacting limit.

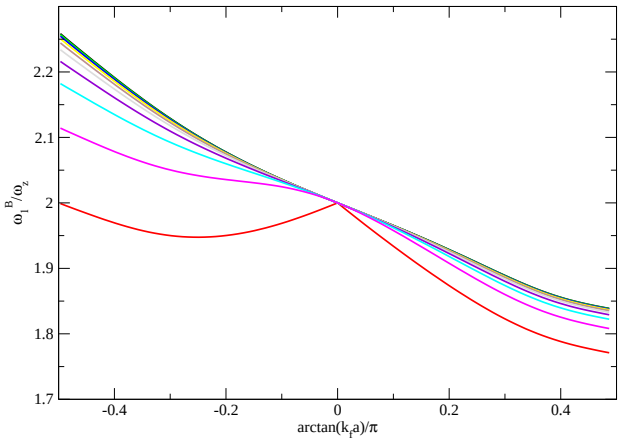

Figure 4.5: The longitudinal breathing mode predicted by the hypervectorial method is shown plotted versus the interaction strength $k_f^0 a$ for trap ratios $\gamma = 0.1$ to 1 in steps of 0.1 from top to bottom. The kink in the seen in the $\gamma = 1$ frequency is due to a degeneracy between the longitudinal and transverse frequencies in the non-interacting limit.

Chapter 5

Green's Functions and the Adiabatic Hyperspherical Method

In the previous chapters, hyperspherical coordinates were used to create simple variational trial wavefunctions that then could be used to create an effective low dimensional Schrödinger equation. In this way, complex, highly correlated systems could be analyzed using the intuition of normal Schrödinger quantum mechanics. In contrast, this chapter will deal with exact hyperspherical solutions to small systems. Rather than using a simple variational approach to approximate the hyperangular behavior of a system, I will employ a Lippmann-Schwinger (LS) equation-based method. Some of the work presented here is developed from the work of Mehta et. al. [29].

The adiabatic hyperspherical method has proven useful for analyzing many few-body systems [35, 37, 66, 103, 104, 105]. The heart of this method lies in treating the hyperradius adiabatically, and diagonalizing the remaining hyperangular behavior. The result takes a d dimensional partial differential equation to a set of coupled one-dimensional differential equations:

$$\begin{aligned} ER^{(d-1)/2}F_n(R) = &\left[-\frac{\hbar^2}{2\mu}\frac{d^2}{dR^2} + \frac{\hbar^2}{2\mu}\frac{(d-3)(d-1)}{4R^2} + U_n(R)\right] R^{(d-1)/2}F_n(R) \\ &- \frac{\hbar^2}{2\mu}\sum_m \left[2P_{nm}\frac{d}{dR} - Q_{nm}\right] R^{(d-1)/2}F_m(R), \end{aligned} \tag{5.1}$$

where d is the total number of dimensions, and $U_n(R)$ is found by solving the fixed R adiabatic Schrödinger equation,

$$\left[\frac{\hbar^2}{2\mu}\frac{\Lambda^2}{R^2} + V(R,\Omega)\right]\Phi_n(R;\Omega) = U_n(R)\,\Phi_n(R;\Omega). \tag{5.2}$$

The non-adiabatic matrices P and Q are found by inserting the expansion,

$$\Psi\left(R,\Omega\right)=\sum_{n}R^{(d-1)/2}F_{n}\left(R\right)\Phi_{n}\left(R;\Omega\right),$$

into the Schrödinger equation and are given by

$$P_{mn}=\left\langle \Phi_{m}\left(R;\Omega\right)|\frac{\partial}{\partial R}\Phi_{n}\left(R;\Omega\right)\right\rangle , \tag{5.3}$$

$$Q_{mn}=\left\langle \Phi_{m}\left(R;\Omega\right)|\frac{\partial^{2}}{\partial R^{2}}\Phi_{n}\left(R;\Omega\right)\right\rangle . \tag{5.4}$$

The integrals in Eqs. 5.3 and 5.4 are taken over the hyperangles Ω.

Approximate solutions can be found by solving the uncoupled system of equations

$$ER^{(d-1)/2}F_{n}\left(R\right)=\left[-\frac{\hbar^{2}}{2\mu}\frac{d^{2}}{dR^{2}}+\frac{\hbar^{2}}{2\mu}\frac{\left(d-3\right)\left(d-1\right)}{4R^{2}}+\frac{\hbar^{2}}{2\mu}Q_{nn}+U_{n}\left(R\right)\right]R^{(d-1)/2}F_{n}\left(R\right) \tag{5.5}$$

Ground state solutions to this give a variational minimum to the full solution to Eq. 5.1. Another method is that of the Born-Oppenheimer approximation in which the diagonal correction to the potential $\frac{\hbar^{2}}{2\mu}Q_{nn}$ is ignored. These two approximations will be the main focus of this chapter, while the non-adiabatic couplings P_{nm} will be used to describe transitions between the different hyperradial channels $U_{n}\left(R\right)$.

The sticking point of the adiabatic hyperspherical method lies in solving the adiabatic Schrödinger equation, Eq. 5.2. Often solving this equation is as hard as solving the total d dimensional Schrödinger equation in the first place. Having a variety of methods available is helpful for this reason. The benefit of using the adiabatic hyperspherical method comes from the simple final interpretation that can often be applied to the resulting coupled set of one-dimensional equations [106]. For instance, in the three-body problem, which I will discuss later in this chapter, if two particles can form a bound state, then one of the resulting scattering channels consists of an atom and a dimer colliding. In the adiabatic hyperspherical method this type of fragmentation channel arises naturally with a simple interpretation.

In Section 5.1 I derive a general form of the hyperangular Green's function for a d-dimensional system. In Section 5.2 I apply the Green's function to the problem of three particles with regularized, zero-range, s-wave interactions. Section 5.3 applies this result to the three lowest hyperfine states of ^{6}Li. Finally, Section 5.4 extends the Green's function methods to the three-body problem with multi-channel two-body interactions, and analyzes the resulting system of hyperradial potentials.

5.1 The Hyperangular Green's function

In this section I derive the free space hyperangular Green's function for an arbitrary d dimensional space, for example, $d = 3(N-1)$ for an N body system with the center of mass coordinate removed. This Green's function can then be used in a LS equation to solve Eq. 5.2. The d dimensional Laplacian written in hyperspherical coordinates is given in Eq. 2.2 as

$$\nabla^2 = \frac{1}{R^{(d-1)/2}} \frac{\partial^2}{\partial R^2} R^{(d-1)/2} - \frac{(d-1)(d-3)}{4R^2} - \frac{\mathbf{\Lambda}^2}{R^2} \tag{5.6}$$

where $R = \sqrt{\sum_{i=1}^{d} x_i^2}$. The hyperangular Green's function is given as the solution to

$$\left[\mathbf{\Lambda}^2 - \nu(\nu + d - 2)\right] G\left(\Omega, \Omega'\right) = \delta^d\left(\Omega - \Omega'\right). \tag{5.7}$$

Here Ω stands for the $d-1$ hyperangular coordinates needed to describe the surface of a d dimensional hypersphere and $\delta^d(\Omega - \Omega')$ is the Dirac δ-function in the hyperangular coordinates, i.e. $\delta(\Omega - \Omega') = 0$ if $\Omega \neq \Omega'$ and $\int \delta^d(\Omega - \Omega')\, d\Omega = 1$. The Green's function can be found in several forms, including the full hyperspherical harmonic expansion [107], and in closed form given by Szmytkowski in Ref. [108].

The simplest derivation of the Green's function relies on the completeness of hyperspherical harmonics:

$$\sum_{\lambda\mu} Y^*_{\lambda\mu}\left(\Omega'\right) Y^*_{\lambda\mu}(\Omega) = \delta^d\left(\Omega - \Omega'\right). \tag{5.8}$$

This relationship can be used in conjunction with Eq. 2.12 to find G [107]:

$$G\left(\Omega,\Omega'\right)=\sum_{\lambda\mu}\frac{Y^{*}_{\lambda\mu}\left(\Omega'\right)Y^{*}_{\lambda\mu}\left(\Omega\right)}{\lambda\left(\lambda+d-2\right)-\nu\left(\nu+d-2\right)}. \tag{5.9}$$

Unfortunately, eigenfunction expansions of Green's function often have slow convergence with respect to the number of eigenfunctions, often making them unsuitable for numeric calculations. The closed form of the Green's function from Ref. [108] is given as

$$G\left(\Omega,\Omega'\right)=\frac{-\pi}{\left(d-2\right)S_d\sin\pi\nu}C_{\nu}^{(d-2)/2}\left(-\hat{R}\cdot\hat{R}'\right), \tag{5.10}$$

where C_{ν}^{α} is a Gegenbaeur function, S_d is the surface area of the d dimensional unit hypersphere: $S_d=\int d\Omega=2\pi^{d/2}/\Gamma\left(d/2\right)$, and $\hat{R}\cdot\hat{R}'$ is the cosine of the angle between the two normalized hypervectors $\hat{R}$ and $\hat{R}'$. Here ν is defined by equation 5.7. While this does have a pleasing, compact form it is often divergent at critical points. For instance if ν is non-integer valued then $G\left(\Omega,\Omega'\right)$ diverges as $\hat{R}\cdot\hat{R}'\rightarrow 1$.

For these reasons, it is convenient to find a third form of the Green's function. The first step in this derivation relies on the division of the total d dimensional space into two subspaces in the same hyperspherical tree structure as is shown in Fig. 2.3. For the purposes of this thesis I will assume that the dimension of the two subspaces are both greater than 2: i.e. $d_1,d_2\geq 2$. The hyperangular momentum can be written in terms of the sub-hyperangular momenta using Eq. 2.11 as

$$\begin{aligned}\mathbf{\Lambda}^2=&\frac{-1}{\left(\sin\alpha\right)^{(d_1-1)/2}\left(\cos\alpha\right)^{(d_2-1)/2}}\frac{\partial^2}{\partial\alpha^2}\left(\sin\alpha\right)^{(d_1-1)/2}\left(\cos\alpha\right)^{(d_2-1)/2}\\&+\frac{\mathbf{\Lambda}_1^2+\left(d_1-1\right)\left(d_1-3\right)/4}{\sin^2\alpha}+\frac{\mathbf{\Lambda}_2^2+\left(d_2-1\right)\left(d_2-3\right)/4}{\cos^2\alpha}-\frac{\left(d-1\right)\left(d-3\right)+1}{4}.\end{aligned} \tag{5.11}$$

The Green's function can be expanded using the completeness of the sub-hyperspherical harmonics, i.e.

$$G\left(\Omega,\Omega'\right)=\sum_{\lambda_1\mu_1}\sum_{\lambda_2\mu_2}g\left(\alpha,\alpha'\right)Y^{*}_{\lambda_1\mu_1}\left(\Omega_1'\right)Y_{\lambda_1\mu_1}\left(\Omega_1\right)Y^{*}_{\lambda_2\mu_2}\left(\Omega_2'\right)Y_{\lambda_2\mu_2}\left(\Omega_2\right), \tag{5.12}$$

where

$$\mathbf{\Lambda}_1^2 Y_{\lambda_1\mu_1}(\Omega_1) = \lambda_1(\lambda_1 + d_1 - 2) Y_{\lambda_1\mu_1}(\Omega_1), \tag{5.13}$$

$$\mathbf{\Lambda}_2^2 Y_{\lambda_2\mu_2}(\Omega_2) = \lambda_2(\lambda_2 + d_2 - 2) Y_{\lambda_2\mu_2}(\Omega_2).$$

Inserting this expansion, Eq. 5.7 is satisfied if and only if

$$\begin{aligned}\frac{\delta(\alpha-\alpha')}{(\sin\alpha)^{d_1-1}(\cos\alpha)^{d_2-1}} = \Bigg[& \frac{-1}{(\sin\alpha)^{(d_1-1)/2}(\cos\alpha)^{(d_2-1)/2}} \frac{\partial^2}{\partial\alpha^2} (\sin\alpha)^{(d_1-1)/2}(\cos\alpha)^{(d_2-1)/2} \\ & + \frac{\lambda_1(\lambda_1+d_1-2) + (d_1-1)(d_1-3)/4}{\sin^2\alpha} \\ & + \frac{\lambda_2(\lambda_2+d_2-2) + (d_2-1)(d_2-3)/4}{\cos^2\alpha} \\ & - \frac{(d-1)(d-3)+1}{4} - \nu(\nu+d-2)\Bigg] g_{\lambda_1,\lambda_2}^{d_1,d_2}(\nu;\alpha,\alpha'),\end{aligned}$$

where $\delta(\alpha-\alpha')$ is a Dirac δ-function and the denominator on the left hand side arises from the hyperangular volume element associated with the angle α (See Refs. [66, 108] for details). The right hand side can be manipulated into the standard Sturm-Liouville form,

$$\begin{aligned}\frac{\delta(\alpha-\alpha')}{(\sin\alpha)^{d_1-1}(\cos\alpha)^{d_2-1}} = \Bigg[& \frac{-1}{(\sin\alpha)^{d_1-1}(\cos\alpha)^{d_2-1}} \frac{\partial}{\partial\alpha} (\sin\alpha)^{d_1-1}(\cos\alpha)^{d_2-1} \frac{\partial}{\partial\alpha} \\ & + \frac{\lambda_1(\lambda_1+d_1-2)}{\sin^2\alpha} + \frac{\lambda_2(\lambda_2+d_2-2)}{\cos^2\alpha} - \nu(\nu+d-2)\Bigg] g_{\lambda_1,\lambda_2}^{d_1,d_2}(\nu;\alpha,\alpha').\end{aligned} \tag{5.14}$$

The general solution for any differential equation of this form is given by

$$g_{\lambda_1,\lambda_2}^{d_1,d_2}(\nu;\alpha,\alpha') = \frac{f^+(\alpha_<) f^-(\alpha_>)}{(\sin\alpha)^{d_1-1}(\cos\alpha)^{d_2-1} W[f^+, f^-]}, \tag{5.15}$$

where $W[f_1, f_2] = f_1 f_2' - f_2 f_1'$ is the Wronskian (see chapter 3 of your favorite edition of Jackson [109] for details) and $\alpha_{<(>)} = \min(\alpha,\alpha')$ $(\max(\alpha,\alpha'))$. The functions $f^+(\alpha)$ and $f^-(\alpha)$ are regular at $\alpha = 0$ and $\alpha = \pi/2$ respectively and satisfy the homogeneous equation,

$$\begin{aligned}0 = \Bigg[& \frac{-1}{(\sin\alpha)^{d_1-1}(\cos\alpha)^{d_2-1}} \frac{\partial}{\partial\alpha} (\sin\alpha)^{d_1-1}(\cos\alpha)^{d_2-1} \frac{\partial}{\partial\alpha} + \frac{\lambda_1(\lambda_1+d_1-2)}{\sin^2\alpha} \\ & + \frac{\lambda_2(\lambda_2+d_2-2)}{\cos^2\alpha} - \nu(\nu+d-2)\Bigg] f^{(\pm)}(\alpha).\end{aligned} \tag{5.16}$$

The solutions to this are given in Ref. [110] as

$$f^{(\pm)}(\alpha) = (\sin\alpha)^{\lambda_1} (\cos\alpha)^{\lambda_2} {}_2F_1\left(\frac{\lambda_1+\lambda_2-\nu}{2}, \frac{\nu+\lambda_1+\lambda_2+d-2}{2}; \lambda_\pm + \frac{d_\pm}{2}; \frac{1\mp\cos 2\alpha}{2}\right), \tag{5.17}$$

$$W\left[f^+, f^-\right] = \frac{-2\Gamma\left(\lambda_1+\frac{d_1}{2}\right)\Gamma\left(\lambda_2+\frac{d_2}{2}\right)}{(\sin\alpha)^{d_1-1}(\cos\alpha)^{d_2-1}\Gamma\left(\frac{\nu+\lambda_1+\lambda_2+d-2}{2}\right)\Gamma\left(\frac{\lambda_1+\lambda_2-\nu}{2}\right)}, \tag{5.18}$$

where ${}_2F_1(a,b;c,x)$ is a hypergeometric function, $\lambda_+ = \lambda_1$, $d_+ = d_1$, $\lambda_- = \lambda_1$, and $d_- = d_2$.

5.2 The Three-Body Problem with Zero-Range Interactions

In this section I show the utility of the Green's function developed in the previous section by applying it to the three body problem with regularized, zero-range, s-wave, pseudo-potential interactions. This problem is well studied by a variety of sources [111, 26, 112, 113]. The full Hamiltonian for the untrapped system is given by

$$H_{tot} = \sum_{i=1}^{3} -\frac{\hbar^2}{2m_i}\nabla_i^2 + \sum_{i>j} V(r_{ij}), \tag{5.19}$$

where $\vec{r}_i$ is the position of the ith particle, and ∇_i^2 is the Laplacian for $\vec{r}_i$. The interaction is given by

$$V(r_{ij}) = \frac{4\pi\hbar^2 a_{ij}}{2\mu_{ij}}\delta^{(3)}(\vec{r}_{ij})\frac{\partial}{\partial r_{ij}}r_{ij}, \tag{5.20}$$

where a_{ij} is the s-wave scattering length between particles i and j and μ_{ij} is the two body reduced mass, $\mu_{ij} = m_i m_j/(m_i+m_j)$. The pseudo-potential defined in this way applies the Bethe-Peierls boundary condition to the two-body wave function as $r \to 0$, i.e. $\psi(r) \to (1 - a_{ij}/r)C$ [114]. The center of mass can be removed from this system by converting to a system of Jacobi vectors. Jacobi vectors are created for this system by

considering the separation vector between two of the three particles and then a second vector from the center of mass of that two body system to the third. The final vector is then just the center of mass coordinate. The choice of Jacobi vectors is not unique. In this study I consider three different Jacobi coordinates each of which is convenient for describing one of the three possible two-body interactions $V\left(r_{ij}\right)$. In the "odd man out" notation these are given by

$$\begin{aligned}
\vec{\rho}_1^{(k)} &= \left(\vec{r}_i - \vec{r}_j\right)/d_k, \\
\vec{\rho}_2^{(k)} &= d_k\left(\frac{m_i\vec{r}_i + m_j\vec{r}_j}{m_i + m_j} - \vec{r}_k\right), \\
\vec{r}_{CM} &= \frac{\left(m_1\vec{r}_1 + m_2\vec{r}_2 + m_3\vec{r}_3\right)}{m_1 + m_2 + m_3}, \\
d_k^2 &= \frac{\left(m_k/\mu\right)\left(m_i + m_j\right)}{m_1 + m_2 + m_3}.
\end{aligned} \tag{5.21}$$

Here μ is the three-body reduced mass given by

$$\mu = \sqrt{\frac{m_1 m_2 m_3}{m_1 + m_2 + m_3}}.$$

In these Jacobi coordinates the total Hamiltonian can be rewritten in terms of the Jacobi coordinates and the center of mass as

$$\begin{aligned}
H_{tot} &= H + H_{CM}, \\
H_{CM} &= \frac{-\hbar^2}{2M}\nabla_{CM}^2, \\
H &= -\frac{\hbar^2}{2\mu}\sum_{i=1}^{2}\nabla_{\rho_i}^2 + \sum_{i>j} V\left(r_{ij}\right).
\end{aligned} \tag{5.22}$$

Transforming the Jacobi coordinate piece of the Hamiltonian in Eq. 5.22 into hyperspherical coordinates using Eqs. 2.2 and 2.1 yields

$$H = -\frac{\hbar^2}{2\mu}\frac{1}{R^{5/2}}\frac{\partial^2}{\partial R^2}R^{5/2} + \frac{15\hbar^2}{8\mu R^2} + \frac{\hbar^2\Lambda^2}{2\mu R^2} + \sum_{i<j} V_{ij}\left(d_k\rho_1^{(k)}\right). \tag{5.23}$$

To apply the adiabatic hyperspherical formulation, the hyperangular adiabatic Schrödinger equation must be solved:

$$\left[\Lambda^2 + \frac{2\mu R^2}{\hbar^2}\sum_{i<j} V_{ij}\left(d_k\rho_1^{(k)}\right) - \nu\left(\nu + 4\right)\right]\Phi\left(R;\Omega\right) = 0.$$

This can now be accomplished with the use of the hyperangular Green's function in the Lippmann-Schwinger equation,

$$\Phi\left(R;\Omega\right)=-\frac{2\mu R^{2}}{\hbar^{2}}\int d\Omega' G\left(\Omega,\Omega'\right)\left[\sum_{i<j}V_{ij}\left(d_{k}\rho_{1}^{(k)\prime}\right)\right]\Phi\left(R;\Omega'\right), \tag{5.24}$$

where $\vec{\rho}_1^{(k)\prime}$ is the kth Jacobi vector parameterized by (R,Ω'). The hyperradial Hamiltonian from Eq. 5.1 in the absence of the non-adiabatic couplings P and Q is given in terms of the hyperangular eigenvalue ν as

$$H_{R}=\frac{-\hbar^{2}}{2\mu}\left(\frac{\partial^{2}}{\partial R^{2}}-\frac{\left(\nu+2\right)^{2}-1/4}{R^{2}}\right). \tag{5.25}$$

To evaluate the integrals in the LS equation, the Green's function from Eq. 5.12 is rotated into the appropriate Jacobi coordinate set for each interaction term in the sum with the hyperangles defined as

$$\Omega^{(k)}=\left\{\omega_{1}^{(k)},\omega_{2}^{(k)},\alpha^{(k)}\right\}, \tag{5.26}$$

where $\omega_i^{(k)}$ is the spherical polar angular coordinates for $\vec{\rho}_i^{(k)}$. The remaining hyperangle $\alpha^{(k)}$ is defined as in Eq. 2.9, i.e.

$$\begin{aligned}\rho_{1}^{(k)}&=R\sin\alpha^{(k)},\\ \rho_{2}^{(k)}&=R\cos\alpha^{(k)}.\end{aligned} \tag{5.27}$$

With this choice of hyperangles, it is clear that $d_1 = d_2 = 3$ and the hyperspherical harmonics $Y^{(i)}_{\lambda_i\mu_i}\left(\Omega_i\right)$ in Eq. 5.12 reduce to normal spherical harmonics $y_{L_iM_i}\left(\omega_i\right)$.

The δ-function implies that the two-body boundary condition for each two-body interaction can be applied and the third particle can be considered to be far away, i.e.

$$\lim_{r^{(k)}\to 0}\Phi\left(R;\Omega\right)=\left(1-\frac{a^{(k)}}{r^{(k)}}\right)y_{LM}\left(\omega_{2}^{(k)}\right)C_{LM}^{(k)} \tag{5.28}$$

where y_{LM} is a spherical harmonic describing the free space behavior in $\omega_2^{(k)}$ and carries the total angular momentum of the system, and the superscript k is indicates the odd

man out notation. Inserting Eq. 5.28 into Eq. 5.24 gives the hyperangular eigenfunction,

$$\Phi\left(R;\Omega\right)=\frac{2\mu}{R}\sum_{k}\frac{a^{(k)}}{2\mu_{ij}d_{k}^{3}}y_{LM}\left(\omega_{1}^{(k)}\right)C_{LM}^{(k)}\frac{f^{-}\left(\alpha^{(k)}\right)}{\left(\sin\alpha\right)^{2}\left(\cos\alpha\right)^{2}W\left[f^{+},f^{-}\right]}. \tag{5.29}$$

$$\left(\sin\alpha\right)^{d_{1}-1}\left(\cos\alpha\right)^{d_{2}-1}W\left[f^{+},f^{-}\right]=\frac{-\sqrt{\pi}\Gamma\left(L+\frac{3}{2}\right)}{\Gamma\left(\frac{\nu+L+4}{2}\right)\Gamma\left(\frac{L-\nu}{2}\right)}$$

where the orthonormality of spherical harmonics has been used to evaluate the $\omega_{1}^{(k)\prime}$ and $\omega_{2}^{(k)\prime}$ integrals. The δ-function in Eq. 5.20 implies that the integral in $\alpha^{(k)\prime}$ can be accomplished by evaluating at $\alpha_{<}^{(k)}=\alpha^{(k)\prime}=0$.

The analytic equation for the hyperangular eigenfunction in Eq. 5.29 is not very useful without knowing the eigenvalue ν. To obtain an equation for ν the boundary condition given in Eq. 5.28 must be applied again. Applying it to both sides of Eq. 5.29 yields

$$\begin{aligned}\lim_{\alpha^{(k')}\to0}\frac{\partial}{\partial\alpha^{(k')}}\alpha^{(k')}\Phi\left(R;\Omega^{(k')}\right)&=y_{LM}\left(\omega_{2}^{(k')}\right)C_{LM}^{(k')}\\&=\frac{2\mu}{R}\sum_{k}\frac{a^{(k)}}{2\mu_{ij}d_{k}^{3}}N_{L\nu}y_{LM}\left(\omega_{2}^{(k)}\right)C_{LM}^{(k)}\lim_{\alpha^{(k')}\to0}\frac{\partial}{\partial\alpha^{(k')}}\alpha^{(k')}f^{-}\left(\alpha^{(k)}\right),\end{aligned} \tag{5.30}$$

$$N_{L\nu}=-\frac{\Gamma\left(\frac{L-\nu}{2}\right)\Gamma\left(\frac{L+\nu+4}{2}\right)}{\sqrt{\pi}\Gamma\left(L+\frac{3}{2}\right)}.$$

To evaluate the limit on the right hand side of this the k Jacobi coordinates when $\rho_{1}^{(k')}\to0$ must be understood. Eqs. 5.21 and 5.27 give, for $k\neq k'$,

$$\lim_{\alpha^{(k')}\to0}\alpha^{(k)}=\beta_{kk'}=\arctan\left[\frac{\left(m_{1}+m_{2}+m_{3}\right)\mu}{m_{k}m_{k'}}\right];\quad\lim_{\alpha^{(k')}\to0}\rho^{(k)}\propto-\rho^{(k')}. \tag{5.31}$$

Note that if f^{+} is regular at $\beta_{kk'}$, then

$$\lim_{\alpha^{(k')}\to0}\frac{\partial}{\partial\alpha^{(k')}}\alpha^{(k')}f_{2}\left(\alpha^{(k)}\right)\to f_{2}\left(\beta_{kk'}\right).$$

Using this and evaluating limits in Eq. 5.30 yields a matrix equation for $C_{LM}^{(k)}$:

$$C_{LM}^{(k')} = \sum_k M_{k'k}^{L\nu} C_{LM}^{(k)}, \tag{5.32}$$

$$M_{k'k}^{L\nu} = \begin{cases} \dfrac{2\mu}{R} \dfrac{2\Gamma\left(\dfrac{L-\nu}{2}\right)\Gamma\left(\dfrac{\nu+L+4}{2}\right)}{\Gamma\left(\dfrac{L-\nu-1}{2}\right)\Gamma\left(\dfrac{L+\nu+3}{2}\right)} \dfrac{a^{(k')}}{2\mu_{ij} d_k^3} & \text{for} \quad k = k\prime \\ \quad + (-1)^L \dfrac{2\mu}{R} N_{L\nu} \dfrac{a^{(k)}}{2\mu_{ij} d_k^3} f^-\left(\beta_{kk'}\right) & \text{for} \quad k \neq k' \end{cases}.$$

The hyperangular eigenvalue, ν, is found by solving the closed form transcendental equation, $\det\left(\underline{\mathbf{M}} - \underline{\mathbf{1}}\right) = 0$, for any given total angular momentum L and any set of s-wave scattering lengths, $a^{(k)}$.

5.2.1 Imposing symmetry

The hyperangular eigenvalues for the general three-body problem with arbitrary exchange symmetry can be found by solving the transcendental equation implied by Eq. 5.32, but the system can be simplified by considering different permutation symmetries and imposing those symmetries on the boundary conditions $C_{LM}^{(k)}$. For example, if the particles in question are identical bosons, permutation cannot have any affect on the wave function. Thus, if a particle is exchanged in the two-body subsystem, the boundary condition must remain the same, i.e. $C_{LM}^{(1)} = C_{LM}^{(2)} = C_{LM}^{(3)} = C_{LM}$ and $a^{(1)} = a^{(2)} = a^{(3)} = a$. A complete list of the possible exchange symmetries is given in Table 5.1. To illustrate this post-symmetrization, I apply the identical boson symmetry

$X_1X_2X_3$	$C^{(1)}$	$C^{(2)}$	$C^{(3)}$
BBB	C	C	C
BBX	C_1	C_1	C_2
FFX	C	$-C$	0

Table 5.1: The possible permutation symmetries that may be imposed on the three body system with s-wave interaction are given with the appropriate boundary conditions. B stands for a boson, F for a fermion and X for a distinguishable particle with an arbitrary mass.

with $L = 0$ to Eq. 5.32 resulting in the well known transcendental equation for ν [115, 111, 26, 112, 113],

$$\frac{R}{a} = \frac{-3^{1/4}\left[\frac{8}{\sqrt{3}}\sin\left(\frac{\pi(\nu+2)}{6}\right) - (\nu+2)\cos\left(\frac{\pi(\nu+2)}{2}\right)\right]}{\sqrt{2}\sin\left(\frac{\pi(\nu+2)}{2}\right)}. \tag{5.33}$$

In the limit where $R \ll |a|$ the first solution to this transcendental equation gives a supercritical attractive $1/R^2$ effective potential,

$$U(R) = \frac{\hbar^2}{2\mu}\frac{-s_0^2 - 1/4}{R^2}, \tag{5.34}$$
$$s_0 = 1.00624.$$

This attractive potential is the source of the famous Efimov effect, where an effective dipole potential supports an infinite set of three-body bound states that accumulate at the non-interacting three-body threshold, $E = 0$.

5.2.2 Non-adiabatic couplings

As in any adiabatic treatment, the effective hyperradial potentials are coupled by non-adiabatic terms that arise from the hyperradial dependence of the hyperangular eigenfunctions. The full system described by Eq. 5.1 can be written as a coupled system of ordinary differential equations of the form,

$$\begin{aligned} 0 = &-\frac{\hbar^2}{2\mu}\sum_n\left[\left(\delta_{mn}\frac{\partial^2}{\partial R^2} + 2P_{mn}\frac{\partial}{\partial R} + Q_{mn}\right)F_n(R)\right] \\ &+\left[\frac{\hbar^2}{2\mu}\frac{(\nu_m(R)+2)^2 - 1/4}{R^2} - E\right]F_m(R) \end{aligned} \tag{5.35}$$

where

$$P_{mn} = \left\langle \Phi_m(R;\Omega)\left|\frac{\partial}{\partial R}\Phi_n(R;\Omega)\right.\right\rangle,$$
$$Q_{mn} = \left\langle \Phi_m(R;\Omega)\left|\frac{\partial^2}{\partial R^2}\Phi_n(R;\Omega)\right.\right\rangle.$$

To find the non-adiabatic coupling matrices, the methods of Ref. [116], in which derivatives of the adiabatic Schrödingier equation are considered, can be employed by considering two matrix elements,

$$\begin{aligned} \left\langle \Phi_n' \left| \left(\Lambda^2 - \varepsilon_m\right) \right| \Phi_m \right\rangle &= 0, \\ -\varepsilon_n' \left\langle \Phi_m \left| \Phi_n \right. \right\rangle + \left\langle \Phi_m \left| \left(\Lambda^2 - \varepsilon_n\right) \right| \Phi_n' \right\rangle &= 0 \end{aligned} \tag{5.36}$$

where $\varepsilon_n = \nu_n \left(\nu_n + 4\right)$ is the hyperangular eigenvalue of the nth adiabatic eigenfunction, and the prime indicates a hyperradial derivative has been taken. Taking the difference of these leads to an equation for the non-adiabatic coupling matrix element P_{mn} for $m \neq n$:

$$\left\langle \Phi_n' \left| \Lambda^2 \right| \Phi_m \right\rangle - \left\langle \Phi_m \left| \Lambda^2 \right| \Phi_n' \right\rangle - \left(\varepsilon_m - \varepsilon_n\right) P_{mn} + \delta_{mn} \varepsilon_n' = 0. \tag{5.37}$$

The difference $\left\langle \Phi_n' \left| \Lambda^2 \right| \Phi_m \right\rangle - \left\langle \Phi_m \left| \Lambda^2 \right| \Phi_n' \right\rangle$ is given by the boundary conditions of the wave functions Φ_m and Φ_n at the coalescence points:

$$\begin{aligned} \left\langle \Phi_n' \left| \Lambda^2 \right| \Phi_m \right\rangle - \left\langle \Phi_m \left| \Lambda^2 \right| \Phi_n' \right\rangle &= \sum_k \frac{a^{(k)}}{d_k R} C_m \frac{\partial}{\partial R} C_n^{(k)} - C_m^{(k)} \frac{\partial}{\partial R} \left(\frac{a^{(k)}}{d_k R} C_n^{(k)} \right) \\ &= \sum_k C_m^{(k)} C_n^{(k)} \frac{a^{(k)}}{d_k R^2}. \end{aligned} \tag{5.38}$$

Here the LM subscript in the boundary values $C_{LM}^{(k)}$ have been suppressed. Inserting this into Eq. 5.37 yields two equations,

$$\begin{aligned} P_{mn} &= \frac{\sum_k C_m^{(k)} C_n^{(k)} \dfrac{a^{(k)}}{d_k R^2}}{\left(\varepsilon_m - \varepsilon_n\right)} \text{ for } n \neq m \\ -\varepsilon_n' &= \sum_k \left(C_n^{(k)} \right)^2 \frac{a^{(k)}}{d_k R^2}. \end{aligned} \tag{5.39}$$

Because the hyperangular eigenfunctions are orthonormal, the diagonal part of the P matrix is zero, i.e. $P_{nn} = \dfrac{1}{2} \dfrac{\partial}{\partial R} \left\langle \Phi_n | \Phi_n \right\rangle = 0$. The second equation gives the normalization condition for Φ_n, with an overall phase that is free. This overall phase is chosen

here so that $\sum_k C_n^{(k)}$ is positive. A similar derivation provides the matrix elements Q_{mn}:

$$Q_{mn} = \delta_{mn}\left(\frac{\varepsilon_n' + R\varepsilon_n'' + A_n}{R^2\varepsilon_n'} + \frac{\varepsilon_n'''}{6\varepsilon_n'}\right) + 2\left(1-\delta_{mn}\right)\frac{\varepsilon_n' P_{mn} + B_{mn}}{(\varepsilon_m - \varepsilon_n)}, \tag{5.40}$$

$$A_n = \sum_k \frac{a^{(k)}}{d_k}\left[\left(C_n^{(k)}\right)'\right]^2,$$

$$B_{mn} = \sum_k \left[C_m^{(k)}\left(\frac{a^{(k)}}{d_k R^2}\right)\left(C_n^{(k)}\right)' - C_m^{(k)} C_n^{(k)}\frac{a^{(k)}}{d_k R^3}\right].$$

When the symmetries given in Table I are used, there can be a considerable simplification of the expressions for P_{mn} and Q_{mn}. For a system of identical bosons where $a^{(1)} = a^{(2)} = a^{(3)} = a$, $d_1 = d_2 = d_3 = d$ and $C_n^{(1)} = C_n^{(2)} = C_n^{(3)} = C_n$, P_{mn} and Q_{mn} are given by

$$P_{mn} = \frac{\sqrt{\varepsilon_m'\varepsilon_n'}}{(\varepsilon_m - \varepsilon_n)} \tag{5.41}$$

$$Q_{mn} = \delta_{mn}\left[-\frac{1}{4}\left(\frac{\varepsilon_n''}{\varepsilon_n'}\right)^2 + \frac{1}{6}\frac{\varepsilon_n'''}{\varepsilon_n'}\right] + \left(1-\delta_{mn}\right)\left[\frac{2\varepsilon_n'\sqrt{\varepsilon_n'\varepsilon_m'}}{(\varepsilon_m - \varepsilon_n)^2} - \frac{\varepsilon_n''}{(\varepsilon_m - \varepsilon_n)}\sqrt{\frac{\varepsilon_m'}{\varepsilon_n'}}\right],$$

which are in agreement with previously calculated nonadiabatic corrections for the three identical boson system [111].

5.3 Three distinguishable interacting particles.

In this section the results of the previous section are applied to the case of three distinguishable equal-mass particles. This system could be realized, for instance, in an ultracold three component Fermi gas of ^{6}Li atoms [94, 95]. The scattering lengths near the resonance positions used here, as a function of magnetic field, are given in Ref.

Region		
I	$r_0 \ll a^{(3)} \lesssim a^{(1)} \ll a^{(2)}$	$a^{(1)}, a^{(2)}, a^{(3)} > 0$
II	$r_0 \ll a^{(3)} \sim a^{(1)} \ll \left\|a^{(2)}\right\|$	$a^{(2)} < 0; a^{(1)}, a^{(3)} > 0$
III	$r_0 \ll \left\|a^{(2)}\right\| \ll a^{(1)}, a^{(3)}$	$a^{(2)} < 0; a^{(1)}, a^{(3)} > 0$
IV	$r_0 \ll \left\|a^{(2)}\right\| \ll \left\|a^{(1)}\right\|, a^{(3)}$	$a^{(2)}, a^{(1)} < 0; a^{(3)} > 0$
V	$r_0 \ll \left\|a^{(2)}\right\| \ll \left\|a^{(1)}\right\| \ll \left\|a^{(3)}\right\|$	$a^{(1)}, a^{(2)}, a^{(3)} < 0$

Table 5.2: The possible tunable interaction regimes near the resonances of ^{6}Li are given.

[4, 94, 95] by

$$a^{(k)} = a_b \left[1 - \frac{\Delta}{B - B_0}\right] \left[1 + \alpha \left(B - B_0\right)\right], \tag{5.42}$$

for $k = 1$:

$$a_b = -1450 a_0, \; B_0 = 834.15 \text{ G},$$

$$\Delta = 300 \text{ G and } \alpha = 4 \times 10^{-4} \text{ G}^{-1};$$

for $k = 2$:

$$a_b = -1727 a_0, \; B_0 = 690.4 \text{ G}$$

$$\Delta = 122.2 \text{ G and } \alpha = 2 \times 10^{-4} \text{ G}^{-1};$$

for $k = 3$:

$$a_b = -1490 a_0, \; B_0 = 811.22 \text{ G},$$

$$\Delta = 222.3 \text{ G and } \alpha = 3.95 \times 10^{-4} \text{ G}^{-1};$$

where a_0 is the Bohr radius. The Fano-Feshbach resonances in this system allow for a large variety of tunable interactions.

In this section I consider five different regions of magnetic field, shown in Fig. 5.1, near the three resonance positions which all have distinct behavior. In all five regions the scattering length is much larger than the effective range, allowing for the use of the zero-range interaction assumptions. Table 5.2 shows the various length scale discrepancies in these regions.

Figure 5.2(a) shows an example of the lowest four hyperangular eigenvalues $(\nu + 2)^2$

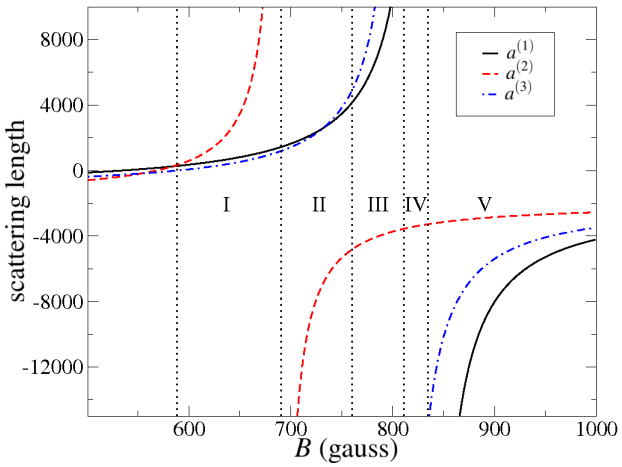

Figure 5.1: All possible s-wave scattering lengths are shown for the lowest 3 Zeeman states of Li^6 from Ref. [4]. Each marked region gives a different set of length scale discrepancies. Here $a^{(k)}$ is the scattering length between two atoms in states $|i\rangle$ and $|j\rangle$ with k as the component not involved in the interaction.

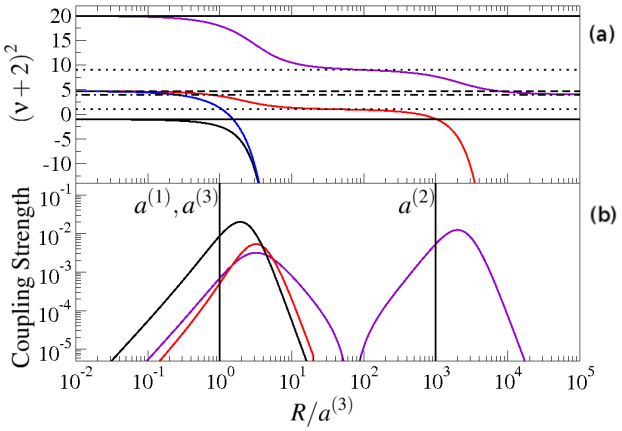

Figure 5.2: (a)The the first four hyperangular eigenvalues are shown for an example system where $a^{(1)} = a^{(3)}$ and $a^{(2)} = 1000a^{(1)}$ versus the hyperradius. The solid black horizontal lines show the expected behavior for 3 identical resonantly interaction bosons. The dashed line gives the behavior of two identical fermions interacting resonantly with a third distinguishable particle. Dotted lines give the expected universal behavior for a single resonant scattering length. Finally, the dot dashed line is the lowest expected free space behavior for three distinguishable free particles.(b)The coupling strengths between the first and second (purple), the first and fourth (red), and the second and fourth (black) adiabatic potentials are shown as a function of R.

obtained from solving Eq. 5.32 for $a^{(1)} = a^{(3)}$ and $a^{(2)} = 1000a^{(1)}$. This is provided

as an example that is qualitatively similar to the behavior of the system in region I. When the hyperradius is in a region where all other length scales are much different, the hyperangular eigenvalue $(\nu+2)^2$ becomes constant, or, in the case of 2-body bound states, becomes proportional to R^2. This behavior can be interpreted as giving a universal set of potential curves from Eq. 5.25. For example in region I where $r_0 \ll a^{(3)} \lesssim a^{(1)} \ll a^{(2)}$ there are three hyperradial regions: $r_0 \ll R \ll a^{(3)} \lesssim a^{(1)} \ll a^{(2)}$; $r_0 \ll a^{(3)} \lesssim a^{(1)} \ll R \ll a^{(2)}$; and $r_0 \ll a^{(3)} \lesssim a^{(1)} \ll a^{(2)} \ll R$. In each region the hyperangular eigenvalues take on the universal value that is expected for resonant interactions [60, 111, 112].

Figure 5.3 schematically shows the behavior of the first few hyperradial potentials

$$U_n(R) = \frac{\hbar^2}{2\mu}\frac{(\nu_n+2)^2 - 1/4}{R^2}. \tag{5.43}$$

The grey areas are the regions where potentials are transitioning from one universal behavior to the next. The zero-range pseudo-potential cannot describe the short range details of the interaction, meaning that the potentials found here are only valid for $R \gg r_0$ where r_0 is a short range parameter shown schematically in the blue region of Fig. 5.3.

Figure 5.2(b) shows the coupling strength, $P^2_{\nu\mu}/2\mu\,(E_\nu - E_\mu)$, between the different potentials. The places where this coupling peaks are the points where a transition between curves is the most probable. Figures 5.4(a-e) are examples of the hyperangular eigenvalues found in each region. The magnetic field at which each set of eigenvalues are found is shown as dotted lines in Fig. 5.4(f) from left to right for Fig. 5.4(a-e) respectively. In each figure the hyperangular eigenvalue can be seen flattening out to a universal constant in each region of length scale discrepancy. As the magnetic field is scanned through each resonance, one two body bound state becomes a virtual state. This behavior can be seen in the hyperangular eigenvalues that diverge toward $-\infty$. As each resonance is crossed, one of the hyperangular eigenvalue curves goes from diverging

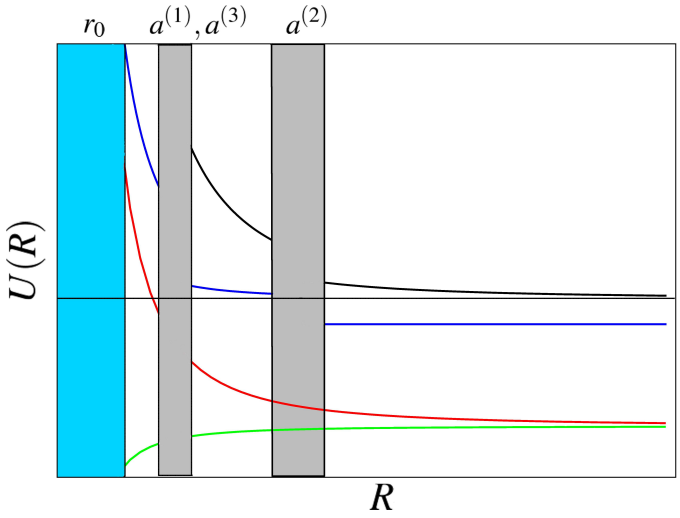

Figure 5.3: A schematic picture of the first four hyperradial potentials in region I is shown. The grey areas indicate regions where the potentials are changing from one universal behavior to another. The blue region indicates the short range region where the zero-range pseudo-potential not longer can be applied.

to $-\infty$ to converging to $(\nu+2)^2 \to 4$.

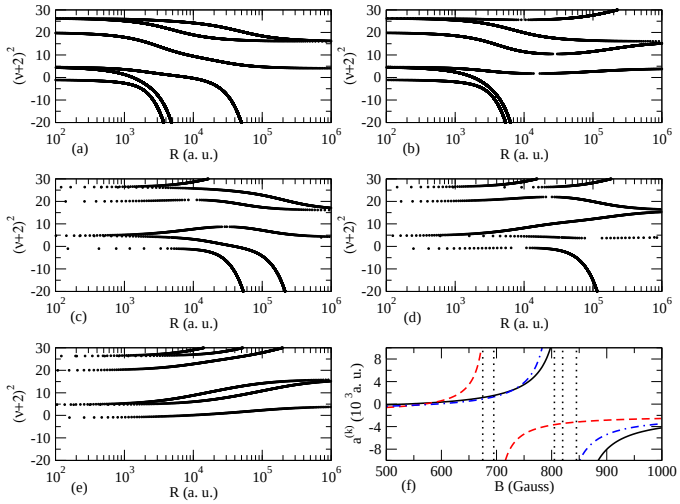

Figure 5.4: (a)-(e) Examples of the hyperangular eigenvalues from each region of magnetic field are shown as a function of the hyperradius in atomic units. (f) The three s-wave scattering lengths are shown as a reference plotted versus the magnetic field strength. The dotted lines, from right, show the magnetic field at which the hyperangular eigenvalues from (a)-(e) were found, $B = 675, 695, 805, 820$ and 845 gauss respectively.

As a final examination of this system, I extract the scaling of the low energy three body recombination rate, i.e. the rate at which three particles collide and form a dimer and a free particle. The lowest 3-body curve, the lowest potential that goes to the three-free-particle threshold, is the potential that dominates this process. Contributions from higher hyperradial potentials will be suppressed due to larger tunnelling barriers. One limitation of the zero-range pseudo-potential is that it only admits at most one dimer of each type. The process of three-body recombination releases the binding energy of the dimer state as kinetic energy between the dimer and remaining particle. For the purposes of this thesis I will concentrate on the three-body recombination processes that result in trap loss processes, where the energy released in the recombination is enough to eject the remaining fragments from a trap.

The rate coefficient for N particles transitioning from a hyperspherical potential curve with hyperangular eigenvalue λ to a lower lying final state is given by [117, 26]

$$K_N = \frac{\hbar k}{2\mu} N_S \left(\frac{2\pi}{k}\right)^{d-1} \frac{\Gamma\left(\frac{d}{2}\right)}{2\pi^{d/2}} \sum_{\lambda} (2L+1) \left|T_{f\lambda}\right|^2, \tag{5.44}$$

where d is the total dimension of the system (in the case of three-body recombination $d = 6$), $T_{f\lambda}$ is the transition matrix element between an initial channel labeled by it's free space hyperangular eigenvalue, λ, and the final channel, and $k = \sqrt{2\mu E}/\hbar$ is the wave number of the asymptotic hyperradial wavefunction. The sum in this equation runs over all the initial, asymptotic channels with total angular momentum L that contribute to the scattering process. In Eq. 5.44, N_S is the number of permutational symmetries in the system. For three distinguishable particles, which is the case studied here, $N_S = 1$, but it can be different, for instance for N bosons, $N_S = N!$. To find the T matrix element, it is sufficient to examine the Wentzel–Kramers–Brillouin (WKB) tunnelling probability to this small R region [112]:

$$P\left(R_0\right) = \exp\left(-2\int_{R_0}^{R_T} \sqrt{\frac{2\mu}{\hbar^2}\left[U\left(R\right) + \frac{\hbar^2}{2\mu}\frac{1/4}{R^2} - E\right]} dR\right), \tag{5.45}$$

where R_T is the outer classical turning point. The extra repulsive hyperradial barrier term, $\hbar^2 (1/4) /2\mu R^2$, appears due to the Langer correction [118]. The T-matrix element will be proportional to the WKB tunneling probability that the system will reach the point at which a transition is made. The total T matrix will depend on the detailed nature of the real short range interactions, but the scaling behavior with the scattering lengths will be determined by Eq. 5.45. In each region of magnetic field, there are different length scale discrepancies and different numbers of bound states. As a result, I will examine each region separately.

5.3.0.1 Region I ($a^{(1)} \sim a^{(3)} \ll a^{(2)}$)

Figure 5.4(a) shows the behavior of the first few hyperangular eigenvalues in region I. The first three eigenvalues correspond to dimer states, while the fourth corresponds to the lowest three-body potential and is the entrance channel that will control three-body recombination. The lowest two dimer states are relatively deeply bound with binding energies, $\hbar^2/ma^2$, on the order of 10^{-12} Hartree. This is close the same energy as the trap depth of a normal magneto-optical trap for experiments with ^{6}Li [94, 95] meaning that recombination into these dimer channels releases enough energy to cause trap losses. In the limit where $R \gg a^{(3)}$, the three atoms are far enough apart to be in the noninteracting regime. This means that the hyperangular eigenfunction limits to the lowest allowed three-body hyperspherical harmonic with its corresponding eigenvalue, $(\nu + 2)^2 \to 4$. In this limit the hyperspherical potential becomes

$$U\left(R \gg a^{(3)}\right) = \frac{\hbar^2}{2\mu}\frac{4 - 1/4}{R^2}. \tag{5.46}$$

For very low energy scattering, the classical turning point in Eq. 5.45, is approximately

$$R_T = \frac{1}{2k}, \tag{5.47}$$

using this potential. In fact, this will be the turning point for all of the three-body recombination processes discussed in this chapter.

It is possible for recombination to occur directly between the lowest three-body curve and the deep dimer channels, but this direct process is strongly suppressed due to the large tunneling barrier in the three body-curve at small R. The favored path is through a transition to the weakly bound dimer channel, shown schematically in Fig. 5.5. The coupling between the lowest three-body channel and the weakly bound dimer

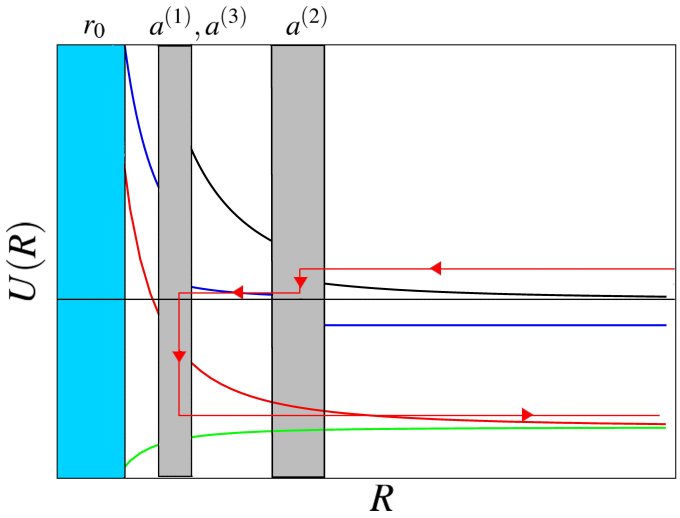

Figure 5.5: A schematic of the path for three-body recombination in region I is shown.

channel peaks at approximately $a^{(2)}$, while the coupling peak between the weakly bound dimer channel and the two deep dimer channels occurs at approximately $a^{(3)} \sim a^{(1)}$. In the regime where $a^{(1)} \sim a^{(3)} \ll R \ll a^{(2)}$ the three particles are so far apart that they cannot see the smaller scattering lengths $a^{(1)}$ and $a^{(3)}$, but the third scattering length is so large compared to the hyperradius that it might as well be infinite. This leads to a universal potential whose hyperangular eigenvalue can be found by solving Eq. 5.32 with $a^{(1)} = a^{(3)} = 0$ and $a^{(2)} \to \infty$, i.e

$$U(R) = \frac{\hbar^2}{2\mu} \frac{p_1^2 - 1/4}{R^2}, \tag{5.48}$$

$$p_1 = (\nu + 2) = 1.$$

The behavior of each channel can be approximated by the universal behavior of

the hyperradial potential in each region. Under this assumption, using Eq. 5.45, the transition probability is given by

$$P\left(a^{(3)}\right) \propto \exp\left[-2\left(\int_{a^{(3)}}^{a^{(2)}} dR\sqrt{\frac{p_1^2}{R^2}-E}+\int_{a^{(2)}}^{R_T} dR\sqrt{\frac{4}{R^2}-E}\right)\right]. \tag{5.49}$$

If the scattering energy is very small, $E \ll \hbar^2/m\left[a^{(2)}\right]^2$, then the energy dependence in these integrals becomes negligible leaving,

$$P\left(a^{(3)}\right) \propto k^4\left(a^{(2)}a^{(3)}\right)^2. \tag{5.50}$$

Inserting this in for the T-matrix element in Eq. 5.44 gives the scaling behavior of the recombination rate with the scattering lengths [112]:

$$K_3 \propto \left(a^{(2)}a^{(3)}\right)^2. \tag{5.51}$$

It was assumed here the final transition occurs at $R \sim a^{(3)}$ leading to the scaling behavior with $a^{(3)}$, but the transition could just as easily have occurred at $R \sim a^{(1)}$. $a^{(1)}$ and $a^{(3)}$ are approximately equal here, and which one dominates the transition depends on the short range behavior of the real two-body interaction. To extract the scaling behavior with respect to $a^{(1)}$, one can simply replace $a^{(3)}$ with $a^{(1)}$ in Eq. 5.51 as long as $a^{(1)}$ and $a^{(3)}$ are close.

5.3.0.2 Region II ($a^{(1)} \sim a^{(3)} \ll \left|a^{(2)}\right|$)

The recombination in region II is simpler as there is no weakly bound state. Again, I assume that the trap loss recombination is dominated by transitions to the two remaining dimer states seen in Fig. 5.4(b). The lowest three-body potential has coupling to these channels that peaks at $R \sim a^{(1)}$ and $R \sim a^{(3)}$. For $R \gg \left|a^{(2)}\right|$ the hyperangular eigenvalue takes on the non-interacting value $(\nu+2) \to 2$. For $a^{(1)}, a^{(3)} \ll R \ll \left|a^{(2)}\right|$ the universal hyperangular eigenvalue $(\nu+2) = p_1 = 1$ is seen again [111, 112, 113]. Ignoring the transitional region between these two regimes the transition probability is

given by

$$P\left(a^{(3)}\right) \propto \exp\left[-2\left(\int_{a^{(3)}}^{\left|a^{(2)}\right|} dR\sqrt{\frac{p_1^2}{R^2}} + \int_{\left|a^{(2)}\right|}^{R_T} dR\sqrt{\frac{4}{R^2}}\right)\right]. \tag{5.52}$$

Inserting this into Eq. 5.44 gives a recombination rate that has the same scaling behavior as in region I [112]:

$$K_3 \propto \left(a^{(2)}a^{(3)}\right)^2. \tag{5.53}$$

Again it is assumed that the final transition occurs at $R \sim a^{(3)}$, but it could occur at $a^{(1)}$ as well. As in Region I, the scaling behavior with respect to $a^{(1)}$ can be found by simply replacing $a^{(3)}$ with $a^{(1)}$ in Eq. 5.51 as long as $a^{(1)}$ and $a^{(3)}$ are close.

5.3.0.3 Region III ($\left|a^{(2)}\right| \ll a^{(1)} \sim a^{(3)}$) and Region IV ($\left|a^{(2)}\right| \ll \left|a^{(1)}\right| \sim a^{(3)}$)

In Region III, none of the dimers predicted by the zero-range model have enough binding energy to cause trap loss. While recombination can occur into these channels, I will focus on the process of recombination to deeply bound states here. In reality, the deep interaction potential between two Li atom in different spin states admits many deeply bound dimer states, and a true hyperspherical description of the system would have channels going to each possible dimer-atom threshold. The energy released in recombining into these deep states is enough to kick the atoms out of any normal trap. Because the deeply bound states are of the size of the range of the interaction, coupling to the deeply bound hyperradial channels will peak at small hyperradius, $R \sim r_0$, and the rate can be found by studying the tunneling probability of reaching these states.

As with the recombination process in Region I, the most favorable pathway involves multiple steps. Starting from the lowest three-body channel, a transition is made to either the first or second weakly bound dimer channel. Because $a^{(1)}$ and $a^{(3)}$ are similar in magnitude, the coupling to these channels peaks in the same region. If the transition is made to the highest dimer channel, then another transition is made directly to the second.

This pathway is shown schematically in Fig. 5.6. An interesting thing occurs

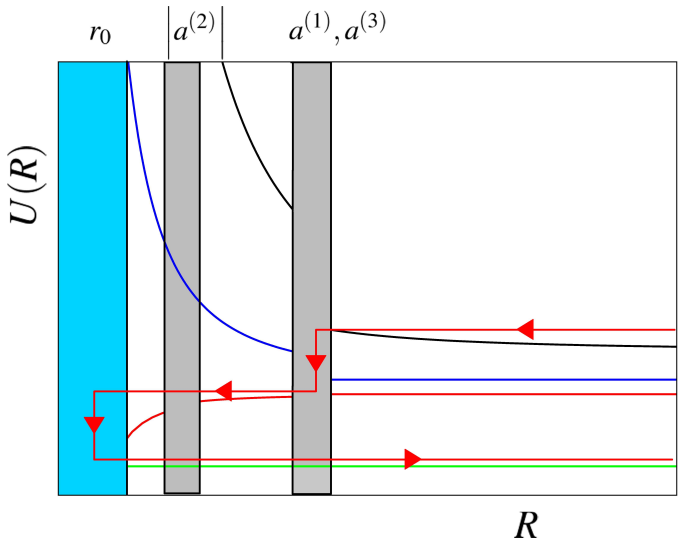

Figure 5.6: A schematic of the potentials and the path for three-body recombination in region III is shown. Again the grey regions indicate a transition from one universal potential behavior to another. The green line represents the hyperradial potential for a deeply bound dimer state. The blue area is the short range region not described by zero-range interactions.

in the lowest weakly bound potential when $\left|a^{(2)}\right| \ll R \ll a^{(1)} \sim a^{(3)}$: the universal potential becomes attractive. This region of attractive potential gives rise to a number of phenomena. For instance, in the limit $a^{(1)}, a^{(3)} \to \infty$, the universal attractive potential supports an infinite number of geometrically spaced three-body bound states, giving rise to the Efimov effect. In the process of three-body recombination to deeply-bound dimmer states, though, there is no tunnelling suppression in this channel, and the hyperradial wavefunction merely accumulates phase in this region. As a result the WKB tunnelling probability is controlled by the transition at $R \sim a^{(1)}, a^{(3)}$:

$$P\left(a^{(1)}\right) \propto \exp\left[-2\int_{a^{(1)}}^{R_T} dR\sqrt{\frac{4}{R^2}}\right].$$

Inserting this into Eq. 5.44 gives the scaling of three-body recombination to deep dimer states as

$$K_3 \propto \left[a^{(1)}\right]^4. \tag{5.54}$$

Again, it is assumed here that $a^{(1)}$ and $a^{(3)}$ are similar in magnitude. If this is not the case, for instance if $a^{(1)} \gg a^{(3)}$, then a scaling behavior similar to that of Eq. 5.51 is recovered:

$$K_3 \propto \left[a^{(1)} a^{(3)}\right]^2. \tag{5.55}$$

In Region IV there is only a single weekly bound dimer state available, and trap loss will occur through recombination to deeply bound dimers. The path here is similar to that of Region III, where a transition happens from the lowest three-body channel to the weakly bound dimer channel. From there the hyperradial wavefunction can go to the small R region without further suppression. This process then yields the same three-body recombination scaling behavior as Eq. 5.54 when $a^{(1)} \sim \left|a^{(3)}\right|$. When $a^{(3)} \gg \left|a^{(1)}\right|$, the scaling predicted by Eq. 5.55 is recovered.

5.3.0.4 Region V ($\left|a^{(2)}\right| \ll \left|a^{(3)}\right| \ll \left|a^{(1)}\right|$)

In this regime the recombination process is entirely controlled by the lowest three-body channel, shown schematically in Fig. 5.7. The hyperradial potential has three universal regimes. The first, when $r_0 \ll R \ll \left|a^{(2)}\right| \ll \left|a^{(3)}\right| \ll \left|a^{(1)}\right|$, is identical to that of three strongly interacting bosons. The hyperangular eigenvalue, $(\nu+2)^2$, is the first solution to Eq. 5.33 in the limit where $R/a \to 0$, yielding the hyperradial potential,

$$U(R) = \frac{\hbar^2}{2\mu} \frac{-(s_0)^2 - 1/4}{R^2}, \tag{5.56}$$

$$s_0 = 1.0062.$$

In the next regime, when $r_0 \ll \left|a^{(2)}\right| \ll R \ll \left|a^{(3)}\right| \ll \left|a^{(1)}\right|$, the three particles are far enough apart so as not to see the smallest scattering length. As a result the hyperangular eigenvalue is governed by Eq. 5.32 with the BBX symmetry of Table 5.1 imposed:

$$U(R) = \frac{\hbar^2}{2\mu} \frac{-(s_1)^2 - 1/4}{R^2}, \tag{5.57}$$

$$s_1 = 0.4137.$$

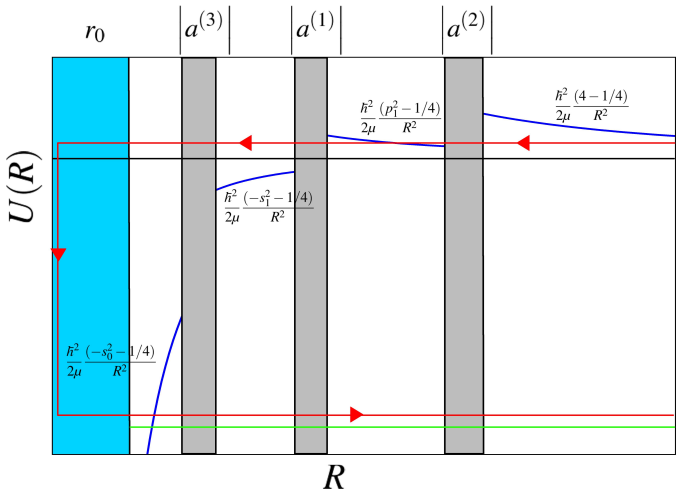

Figure 5.7: A schematic of the lowest hyperradial potential is shown with the path for three-body recombination to deeply bound states. The green line represents the hyperradial potential for a deeply bound dimer state. Grey areas indicate transition regions from one universal behavior to another, and the blue region indicates the short range regime.

In the regime where $r_0 \ll |a^{(2)}| \ll |a^{(3)}| \ll R \ll |a^{(1)}|$, there is only one scattering length that is seen by the system, and the universal potential becomes that of Eq. 5.48. In the final regime, where the hyperradius is much larger than all of the scattering lengths, the potential goes to the non-interacting behavior of a hyperspherical harmonic.

The transition to a deeply bound dimer state occurs at $R \sim r_0$ following the path shown in Fig. 5.7. To get to this region, the wavefunction must first tunnel through a barrier, leading to suppression of the recombination rate. Once through the barrier, the wavefunction accumulates phase in the attractive potential regime. If enough phase can be accumulated in this regime, then a three-body bound state (a so called Efimov state) can be present leading to a resonance in the recombination rate. The final recombination rate for this process is [26, 111, 112, 61]

$$K_3 \propto A \frac{\sinh 2\eta}{\sin^2(\phi_{WKB}) + \sinh^2 \eta}, \tag{5.58}$$

where η is controlled by the short range properties of the system, ϕ_{WKB} is the WKB phase accumulated in the attractive regime from r_0 to $|a^{(3)}|$, and A is proportional to

the tunneling suppression through the barrier:

$$A \propto \left[a^{(3)}a^{(1)}\right]^2, \tag{5.59}$$

$$\phi_{WKB} = s_1 \ln\left(\frac{a^{(1)}}{a^{(2)}}\right) + s_0 \ln\left(\frac{\left|a^{(2)}\right|}{r_0}\right). \tag{5.60}$$

Figures 5.8 (a-c) show a log-log plots of the recombination rate as a function of $\left|a^{(1)}\right|$, $\left|a^{(2)}\right|$ and $\left|a^{(3)}\right|$ respectively for magnetic fields from 834.15 to1000 gauss with $\eta = 0.01$. The short range length scale here is chosen to be approximately the van der Waals length of ^{6}Li, $r_0 = r_d \approx 60$ atomic units. In Fig. 5.8(a), for smaller $\left|a^{(1)}\right|$,

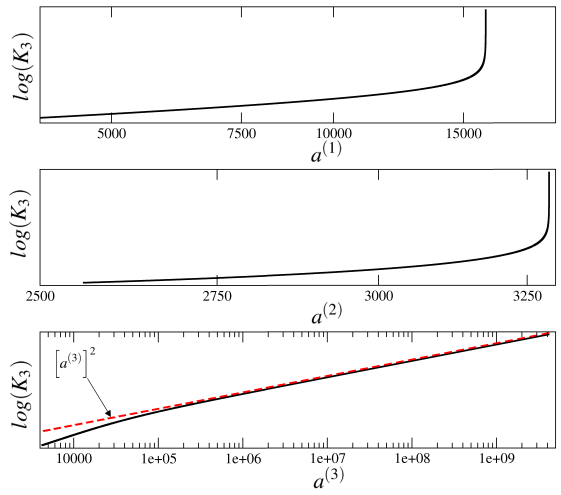

Figure 5.8: (a-c) The log of the three-body recombination rate from Eq. 5.58 for ^{6}Li is shown for magnetic fields ranging from 834.15 to 1000 gauss is shown plotted versus $\left|a^{(1)}\right|$, $\left|a^{(2)}\right|$ and $\left|a^{(3)}\right|$ respectively with $\eta = 0.01$ and the short range length scale chosen to be approximately the van der Waals length, $r_0 = r_d \approx 30$ a.u. The beginning of an Efimov resonance can be seen in (a) and (b) while the scaling law $K_3 \propto \left[a^{(3)}\right]^2$ can be seen in (c).

the scaling predicted in Eq. 5.59 cannot clearly be seen because of deviations due to an Efimov state beginning to appear. Though the Efimov state has not quite become bound, its effects on the recombination rate can clearly be seen. In Fig. 5.8(b), there is no scaling behavior with $\left|a^{(2)}\right|$, though the effects of the Efimov state are present. Figure 5.8(c) shows only slight deviations from the predicted scaling behavior in Eq.

5.59 as a function of $\left|a^{(3)}\right|$, this is because $a^{(3)}$ takes on a large range of values in this range of magnetic fields, from -4000 a.u. to $-\infty$, but does not play a role in the size of the phase accumulation regime.

With three overlapping resonances, ^{6}Li provides a rich hunting ground for the study of three-body physics. Further, because it is a fermionic atom, three-body interactions involving only two of the three lowest components are strongly suppressed meaning that the majority of the three-body physics is controlled by a system of three distinguishable particles. While only the processes of three-body recombination that lead to trap losses were studied in this section, there is still a rich and complex array of behaviors not discussed that can be described using the model presented here.

5.4 Multi-channel interactions

In this section I develop a multi-channel generalization of the Green's function methods, in which each particle in the three-body system can be in one of two different internal states. While the exact nature of the internal states is not required, for reference one can think of them as Zeeman states of atoms in an ultracold gas. Allowing the atoms to be in different internal states leads to an interaction that is intrinsically multi-channel in nature, where each channel corresponds to a different two-body combination of internal states. The benefits of having a true multi-channel interaction are many fold. For instance, instead of tuning a single channel interaction's scattering length to model a broad s-wave Fano-Feshbach resonance, using a multi-channel interaction allows for the real resonance to be mimicked. In the previous section a deeply bound two body state had to be put in by hand with assumptions about the coupling behavior to this state. With a multi-channel interaction a deeply bound state can be included directly in the two body interaction. Another benefit is that the three-body system can be studied at excited scattering thresholds with coupling to lower thresholds. This topic will be the main focus of this section.

To begin, I will assume that each atom in the three-body system can be in one of two internal states, $|1\rangle$ and $|2\rangle$, and that these internal states have energy 0 and ε respectively. To reduce the large parameter space involved here, I will assume that the particles are identical bosons. Two atoms can interact in different symmetric internal state channels labeled by $\{|\sigma\rangle\} = \left\{|11\rangle, (|12\rangle + |21\rangle)/\sqrt{2}, |22\rangle\right\}$ with asymptotic threshold energies, $E_\sigma = 0, \varepsilon, 2\varepsilon$, respectively. The interaction between the two particles is assumed to be a zero-range multi-channel extension of the pseudo-potential,

$$\bar{v}(r) = \frac{4\pi\hbar^2}{2\mu_{2B}} \bar{A} \delta^{(3)}(\vec{r}) \frac{\partial}{\partial r} r, \tag{5.61}$$

where $\mu_{2B} = m/2$ is the two body reduced mass. The symmetric matrix,

$$\bar{A} = \begin{bmatrix} A_{11} & A_{12} & A_{12} \\ A_{12} & A_{22} & A_{23} \\ A_{13} & A_{23} & A_{33} \end{bmatrix}, \tag{5.62}$$

is expressed in the $|\sigma\rangle$ basis and can be considered as a multi-channel generalization of the scattering length in Eq. 5.20. Figure 5.9 gives a schematic picture of this interaction. When the channels are weakly coupled, the diagonal elements of $\bar{A}$ can be thought of as

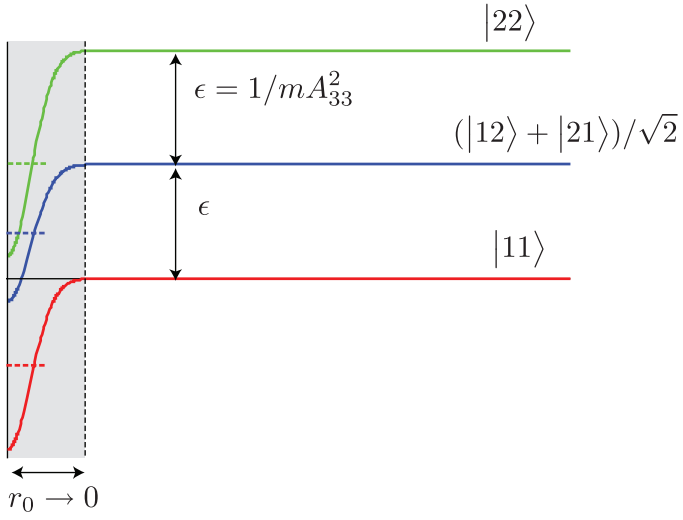

Figure 5.9: A schematic picture of the multi-channel two body interaction is shown.

the scattering length in each channel while the off diagonal elements are the coupling. In a more rigorous treatment, $\bar{A}$ is simply minus the scaled reactance matrix $\bar{K}_0$ from multi-channel quantum defect theory [114, 119, 120]. The regularization factor serves to impose the generalization of the Bethe-Peierls boundary condition. This multi-channel interaction has been used in previous three-body studies as well [121].

To extend this interaction to a three-body system, I first use the Jacobi coordinates described in Eq. 5.21 and the hyperspherical coordinates described by Eqs. 5.26 and 5.27. The possible three-body internal states are given by $\{|\Sigma\rangle\} = \{|111\rangle, |112\rangle, |121\rangle, |211\rangle, |122\rangle, |212\rangle, |221\rangle, |222\rangle\}$ with threshold energies $E_\Sigma = 0, \varepsilon, \varepsilon, \varepsilon, 2\varepsilon, 2\varepsilon, 2\varepsilon$, and 3ε. The hyperangular piece of the three-body Hamiltonian with the center of mass motion removed is given by

$$H_{ad} = \frac{\hbar^2}{2\mu}\frac{\Lambda^2}{R^2}\bar{I} + \bar{V}(R,\Omega) + \bar{E}_{Th}, \tag{5.63}$$

where $\bar{I}$ is the identity matrix, $\bar{V}(R,\Omega)$ is a matrix representing the sum of all possible two-body interactions, and $\bar{E}_{th}$ is the threshold energies of each internal state. The resulting Schrödinger equation is then solved by the Lippmann-Schwinger equation,

$$\vec{\Phi}(\Omega) = \int \sum_k \bar{G}\left(\Omega^{(k)}, \Omega^{(k)\prime}\right) \frac{2\mu R^2}{\hbar^2} \bar{v}^{(k)}\left(d\rho_1^{(k)\prime}\right) \vec{\Phi}\left(\Omega^{(k)\prime}\right) d\Omega^{(k)\prime}, \tag{5.64}$$

where $d = \sqrt{\mu/\mu_{2B}} = \sqrt{2/3^{1/2}}$. The two-body interaction, $\bar{v}^{(k)}$, is the zero-range pseudo-potential from Eq. 5.61 written in the $|\Sigma\rangle$ basis by considering the third particle

as a spectator. For example when $k = 1$ the two body interaction is given by,

$$\bar{v}^{(1)}\left(d\rho_1^{(1)}\right) = \frac{4\pi\hbar^2}{2\mu_{2B}}\bar{A}^{(1)}\frac{\partial}{\partial\rho_1^{(1)}}\rho_1^{(1)}, \tag{5.65}$$

$$\bar{A}^{(1)} = \begin{bmatrix} A_{11} & \frac{A_{12}}{\sqrt{2}} & \frac{A_{12}}{\sqrt{2}} & 0 & A_{13} & 0 & 0 & 0 \\ \frac{A_{12}}{\sqrt{2}} & A_{22} & 0 & 0 & \frac{A_{23}}{\sqrt{2}} & 0 & 0 & 0 \\ \frac{A_{12}}{\sqrt{2}} & 0 & A_{22} & 0 & \frac{A_{23}}{\sqrt{2}} & 0 & 0 & 0 \\ 0 & 0 & 0 & A_{11} & 0 & \frac{A_{12}}{\sqrt{2}} & \frac{A_{12}}{\sqrt{2}} & A_{13} \\ A_{13} & \frac{A_{23}}{\sqrt{2}} & \frac{A_{23}}{\sqrt{2}} & 0 & A_{33} & 0 & 0 & 0 \\ 0 & 0 & 0 & \frac{A_{12}}{\sqrt{2}} & 0 & A_{22} & 0 & \frac{A_{23}}{\sqrt{2}} \\ 0 & 0 & 0 & \frac{A_{12}}{\sqrt{2}} & 0 & 0 & A_{22} & \frac{A_{23}}{\sqrt{2}} \\ 0 & 0 & 0 & A_{13} & 0 & \frac{A_{23}}{\sqrt{2}} & \frac{A_{23}}{\sqrt{2}} & A_{33} \end{bmatrix},$$

where A_{ij} is defined in terms of the two-body interaction given by Eq. 5.62. The somewhat odd form of this scattering length matrix has been chosen so that the two internal states, $|12\rangle$ and $|21\rangle$, have the same interactions. Extra factors of $1/\sqrt{2}$ in some matrix elements are included for symmetrization purposes.

In Eq. 5.64 $\bar{G}\left(\Omega,\Omega'\right)$ is the multi-channel generalization of the hyperangular Greens function whose matrix elements are given by

$$\left[G\left(\Omega,\Omega'\right)\right]_{\Sigma\Sigma'} = \delta_{\Sigma\Sigma'}G_{\nu_\Sigma}\left(\Omega,\Omega'\right), \tag{5.66}$$

where $G_{\nu_\Sigma}\left(\Omega,\Omega'\right)$ is the single channel Green's function from Eq. 5.12 with the hyperangular eigenvalue modified to include the threshold energy offsets, i.e.

$$v_\Sigma\left(\nu_\Sigma+4\right) = \nu\left(\nu+2\right) - \frac{2\mu R^2}{\hbar^2}\left[E_{Th}\right]_{\Sigma\Sigma}.$$

It is clear from this definition that $\bar{G}\left(\Omega,\Omega'\right)$ is the solution to the multi-channel Green's equation,

$$\Lambda^2\bar{I} - \left[\nu\left(\nu+2\right)\bar{I} - \frac{2\mu R^2}{\hbar^2}\bar{E}_{Th}\bar{I}\right]\bar{G}\left(\Omega,\Omega'\right) = \delta\left(\Omega-\Omega'\right)\bar{I},$$

where ν_Σ can be interpreted as the hyperangular eigenvalue with respect to the Σth three-body threshold. Hyperangular solutions to the multi-channel three-body problem give the hyperradial Schrödinger equation

$$\left[-\frac{\hbar^2}{2\mu}\frac{d^2}{dR^2}+\frac{\hbar^2}{2\mu}\frac{(\nu+2)^2-1/4}{R^2}\right]R^{5/2}F(R)=ER^{5/2}F(R),$$

where the nonadiabatic matrices $\bar{P}$ and $\bar{Q}$ have been omitted.

As in Sec. 5.2, each integral in Eq. 5.64 is performed in the Jacobi coordinates where $\vec{\rho}_1^{(k)}=d(\vec{r}_i-\vec{r}_j)$. The regularization factor, $\frac{\partial}{\partial\rho_1^{(k)}}\rho_1^{(k)}$, acting on the wavefunction $\vec{\Phi}\left(\Omega^{(k)}\right)$ at $\alpha^{(k)}\to 0$ gives a boundary condition vector,

$$\lim_{\alpha^{(k)}\to 0}\frac{\partial}{\partial\rho_1^{(k)}}\rho_1^{(k)}\vec{\Phi}\left(\Omega^{(k)}\right)=\vec{C}^{(k)}y_{LM}\left(\omega_2^{(k)}\right). \tag{5.67}$$

where $y_{LM}(\omega)$ is a normal spherical harmonic. The three boundary condition vectors are related by assuming that any two particles in the same internal state are identical:

$$\vec{C}^{(1)}=\begin{pmatrix}C_1\\C_2\\C_3\\C_4\\C_5\\C_6\\C_7\\C_8\end{pmatrix},$$

$$\vec{C}^{(2)}=\bar{P}_-\vec{C}_1,$$

$$\vec{C}^{(3)}=\bar{P}_+\vec{C}_1,$$

where the matrices P_+ and $\bar{P}_-$ correspond to cyclic and anti-cyclic permutations of the

internal states:

$$\bar{P}_+ = \begin{pmatrix} 1 & 0 & 0 & 0 & 0 & 0 & 0 & 0 \\ 0 & 0 & 0 & 1 & 0 & 0 & 0 & 0 \\ 0 & 1 & 0 & 0 & 0 & 0 & 0 & 0 \\ 0 & 0 & 1 & 0 & 0 & 0 & 0 & 0 \\ 0 & 0 & 0 & 0 & 0 & 1 & 0 & 0 \\ 0 & 0 & 0 & 0 & 0 & 0 & 1 & 0 \\ 0 & 0 & 0 & 0 & 1 & 0 & 0 & 0 \\ 0 & 0 & 0 & 0 & 0 & 0 & 0 & 1 \end{pmatrix} \tag{5.68}$$

$$\bar{P}_- = \bar{P}_+^T. \tag{5.69}$$

Evaluating the integral in the LS equation for each component of $\vec{\Phi}$ proceeds in the same way as in Sec. 5.2:

$$\begin{aligned} \Phi_\Sigma(\Omega) = & \frac{1}{dR} \sum_{\Sigma'} N_{\nu_\Sigma L} \frac{f_\Sigma^-\left(\alpha^{(k)}\right)}{(\sin\alpha)^2 (\cos\alpha)^2 W[f^+, f^-]} \bar{A}^{(1)}_{\Sigma\Sigma'} y_{LM}\left(\omega_2^{(1)}\right) \vec{C}^{(1)}_{\Sigma'} \\ & + \frac{1}{dR} \sum_{\Sigma'\Sigma''} N_{\nu_\Sigma L} \frac{f_\Sigma^-\left(\alpha^{(3)}\right)}{(\sin\alpha)^2 (\cos\alpha)^2 W[f^+, f^-]} \bar{A}^{(2)}_{\Sigma\Sigma'} y_{LM}\left(\omega_2^{(3)}\right) \left[\bar{P}_+\right]_{\Sigma'\Sigma''} \vec{C}^{(1)}_{\Sigma''} \\ & + \frac{1}{dR} \sum_{\Sigma'\Sigma''} N_{\nu_\Sigma L} \frac{f_\Sigma^-\left(\alpha^{(3)}\right)}{(\sin\alpha)^2 (\cos\alpha)^2 W[f^+, f^-]} \bar{A}^{(3)}_{\Sigma\Sigma'} y_{LM}\left(\omega_2^{(3)}\right) \left[\bar{P}_-\right]_{\Sigma'\Sigma''} \vec{C}^{(1)}_{\Sigma''}, \end{aligned} \tag{5.70}$$

where $f_\Sigma^-(\alpha)$ and $(\sin\alpha)^2 (\cos\alpha)^2 W[f^+, f^-]$ are given by Eqs. 5.17 and 5.18 respectively with ν taken to ν_Σ, $l_1 = 0$, $l_2 = L$, and $d_1 = d_2 = 3$. The pseudo-potential treatment is that of enforces s-wave boundary conditions on each interacting pair of particles, meaning that in Eq. 5.70 the spherical harmonics, $y_{LM}\left(\omega_2^{(k)}\right)$, in each term hold the entire three-body spatial angular momentum.

For the purposes of this thesis I consider only zero total angular momentum states, $L = 0$, but it is clear how this can be generalized to arbitrary total angular momentum. To find the hyperangular eigenvalue, ν, the boundary condition in Eq. 5.67 is applied

to both sides of Eq. 5.70 for $k = 1$. Using the behavior of the Jacobi vectors described by Eq. 5.31 and a bit of algebra, the matrix equation becomes

$$\left[\frac{1}{dR}\bar{M}^{(1)} + \frac{1}{dR}\bar{M}^{(2)}\bar{P}_{+} + \frac{1}{dR}M^{(3)}\bar{P}_{-} - \bar{I}\right]\vec{C}^{(1)} = 0 \tag{5.71}$$

where the 8×8 matrices $\bar{M}^{(k)}$ are given by

$$M^{(k)}_{\Sigma\Sigma'} = \begin{cases} A^{(k)}_{\Sigma\Sigma'}\left(\nu_{\Sigma}+2\right)\cot\left[\left(\nu_{\Sigma}+2\right)\pi/2\right], & k = 1 \\ -\dfrac{4}{\sqrt{3}}A^{(k)}_{\Sigma\Sigma'}\dfrac{\sin\left[\left(\nu_{\Sigma}+2\right)\pi/6\right]}{\cos\left[\left(\nu_{\Sigma}+2\right)\pi/2\right]}, & k = 2,3 \end{cases} . \tag{5.72}$$

Solving this matrix equation will give both the hyperangular eigenvalue, ν, and the boundary condition vector $\vec{C}^{(1)}$ up to an arbitrary constant.

There is one last issue that must be dealt with. In the description of the internal states it was assumed that two interacting particles could have unsymmetrized internal states. Correcting this is a simple matter of projecting out the antisymmetric linear combination of internal states in each two particle interaction. Following this procedure gives the final matrix equation describing the hyperangular eigenvalue for three bosons with multi-channel two-body interactions,

$$\bar{S}\left[\frac{1}{dR}\bar{M}^{(1)} + \frac{1}{dR}\bar{M}^{(2)}\bar{P}_{+} + \frac{1}{dR}M^{(3)}\bar{P}_{-} - \bar{I}\right]\bar{S}^{T}\vec{C}^{(1)}_{S} = 0, \tag{5.73}$$

where $\vec{C}^{(1)}_{S}$ is a 6 dimensional vector of boundary conditions in the set of symmetrized states given by $\left\{\left|\Sigma^{S}\right\rangle\right\} = \left\{|111\rangle, \left(|112\rangle + |121\rangle\right)/\sqrt{2}, |211\rangle, |122\rangle, \left(|212\rangle + |221\rangle\right)/\sqrt{2}, |222\rangle\right\}$ with each interacting pair in one of the symmetrized internal states shown in Fig. 5.9. Here $\bar{S}$ is the matrix that projects the original $|\Sigma\rangle$ basis onto this subset of three-body internal states

$$\bar{S} = \begin{bmatrix} 1 & 0 & 0 & 0 & 0 & 0 & 0 & 0 \\ 0 & \frac{1}{\sqrt{2}} & \frac{1}{\sqrt{2}} & 0 & 0 & 0 & 0 & 0 \\ 0 & 0 & 0 & 1 & 0 & 0 & 0 & 0 \\ 0 & 0 & 0 & 0 & 1 & 0 & 0 & 0 \\ 0 & 0 & 0 & 0 & 0 & \frac{1}{\sqrt{2}} & \frac{1}{\sqrt{2}} & 0 \\ 0 & 0 & 0 & 0 & 0 & 0 & 0 & 1 \end{bmatrix}. \tag{5.74}$$

Solving the transcendental equation implied by Eq. 5.71 is by no means simple, as the determinant of the resulting 6×6 determinantal equation has many roots with a very complex structure. Further, the complex system of coupled hyperradial differential equations can have many very narrow avoided crossings and sharp features. As a result I will limit the implementation in what follows to the prediction of qualitative features of the system.

5.4.1 Efimov States embedded in the continuum

The adiabatic hyperspherical method has proven especially useful in the description of Efimov physics. In Sec 5.3, it was seen that when three particles are interacting resonantly, they can form a series of bound states called Efimov states. In the case of three bosons, in the limit where $a \to \pm\infty$, the lowest adiabatic hyperradial potential takes on a universal $1/R^2$ attractive potential when the hyperradius is much greater than a short range length scale, r_0,

$$U(R) = \frac{\hbar^2}{2\mu} \frac{-s_0^2 - 1/4}{R^2},$$

where $s_0 = \sqrt{-(\nu+2)^2} = 1.00624$ is the first solution to Eq. 5.33 in the limit $R/a \to 0$. This attractive dipole–like potential supports an infinite number of geometrically spaced bound states that accumulate at the zero-energy threshold [32, 60]. The position of the first bound state will depend on the short range length scale r_0, and each trimer after

that has energy

$$E_n = E_{n-1}e^{-2\pi/s_0} \approx \frac{E_{n-1}}{(22.7)^2}. \tag{5.75}$$

The first strong experimental evidence of Efimov states has recently been seen experimentally in the work of Kramer et. al. [62] in observations of trap losses caused by three-body recombination. Unfortunately, this experiment has only seen one resonant feature. To really show that the observation corresponds to an Efimov state, two resonances must be observed with the characteristic geometric scaling factor between scattering lengths, $a_2 \approx e^{-2\pi/s_0}a_1 = 22.7a_1$. Of course, increasing the scattering length by more than an order of magnitude poses its own problems. For instance the three-body recombination rate scales with a^4 [26, 111, 61], a fact that can easily be confirmed using the WKB tunneling methods described in Sec. 5.3, severely limiting the lifetime of the gas in the large scattering length limit. In this section I propose a method of observing Efimov states utilizing the multi-channel nature of the two-body interactions.

To limit the 6 dimensional parameter space of the interaction scattering length matrix $\bar{A}$, in this study I investigate only a parameter regime where $A_{11} = A_{33}$, $A_{22} = 2A_{33}$ and $A_{12} = A_{23} = A_{33}/4$. The qualitative results found here are not changed by this particular choice of parameters. The only requirement is that A_{33} must be positive. For the initial study I will assume that the first and third two body channel in Fig. 5.9 are not directly coupled, i.e. $A_{13} = 0$. Effects of weak coupling between these two channels will be discussed later. The main idea here is to tune the interactions to a resonance in an *excited* two-body threshold. This occurs when a quasistable two-body bound state attached to the third two-body scattering threshold is degenerate with the second two-body threshold. This is achieved by tuning the asymptotic two-body energy to $\varepsilon = \hbar^2/mA_{33}^2$. By choosing these parameters, I have also chosen a rough short range length scale of $r_0 \sim A_{33}$.

Inserting these parameters into Eq. 5.73 and solving gives a somewhat intimidat-

ing set of potentials. Figure 5.10(a) shows the first 300 adiabatic hyperradial potentials for these parameters in units of ε plotted as a function of R/A_{33}.In this figure the

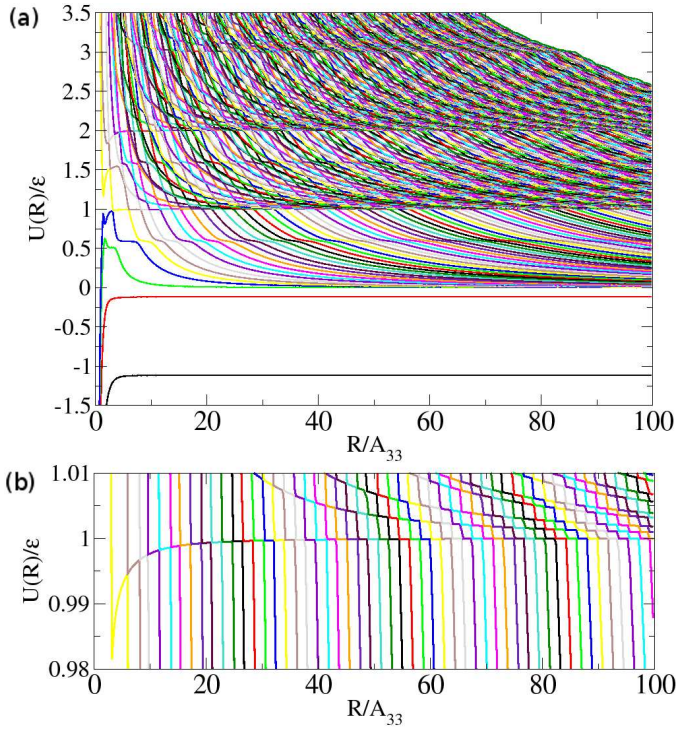

Figure 5.10: (a) The first 300 adiabatic hyperradial potentials are shown for the multichannel three-boson problem in units of ε as a function of R/A_{33}. (b) The adiabatic three-body potentials near the second three-body scattering threshold are shown. The attractive Efimov diabat can be clearly seen approaching the second scattering threshold.

various possible asymptotic three-body threshold energies and the corresponding internal states in the $\left|\Sigma^S\right\rangle$ internal state basis where particle 1 is treated as a spectator particle can clearly be seen. At first glance, it seems likely impossible to extract any useful information from this figure, but upon close examination several features become apparent.

First, there is a clear three-body scattering threshold at $E = 0$ with three body potential curves converging to this value. In fact there is a series of diabatic curves going through a series of very sharp avoided crossing limiting to each three-body internal state

threshold, $E_\Sigma = 0, \varepsilon, 2\varepsilon$, and 3ε. Looking below the zero energy threshold, two potentials corresponding to states consisting of a dimer and a free particle can be seen. This is a clear difference between the multi-channel model for three identical bosons and the single channel model. In the single channel model of three identical bosons, there is only a single length scale, the scattering length, allowing only at most a single two-body bound state. In the multi-channel model there are multiple length scales, and multiple bound states are allowed attached to different thresholds. In this case the deepest two-body state is attached to the $|111\rangle$ scattering threshold and corresponds to a $|11\rangle$ dimer with binding energy $E_b = (1.11)\,\varepsilon$. This binding energy is about what one would expect from the scattering length in this channel:

$$a_{11} = \frac{\left(180 - \sqrt{2}\right)}{194} A_{33} = 0.92 A_{33}.$$

With this scattering length, the zero range single channel model predicts a binding energy of $E_b \approx \hbar^2/m a_{11}^2 = (1.18)\,\varepsilon$. The difference in these two energies is due to the extra short range physics added in the multi-channel interaction. The second, weakly bound hyperradial potential has an asymptotic energy $E_b = 0.11\varepsilon$. This state comes from a $|11\rangle$ bound state attached to the *second* three body scattering threshold and is not present in the zero-range single channel predictions.

Examining Fig. 5.10(a) further reveals a series of avoided crossings at $E \approx 0.6\varepsilon$, these correspond to a quasi-bound two-body state with an internal state $\left(|12\rangle + |21\rangle\right)/\sqrt{2}$ attached to the second three body channel. Another series of avoided crossings is seen in Fig. 5.10(a) at $E \approx 1.6\varepsilon$ corresponding to the same type of two-body quasi-bound state attached to the third three-body threshold. Further discussion characterizing the features and potentials seen in this figure would take more time and space than is available, and as such I will limit myself to one more interesting region.

The original purpose stated in this section was to analyze the three-body hyperradial potentials when a quasi-bound two-body state was made resonant with an excited

two-body scattering threshold. By tuning the threshold spacing, ε to $\varepsilon = \hbar^2/mA_{33}^2$, this is exactly the case. With the chosen parameters, $A_{11} = A_{33}$, $A_{22} = 2A_{33}$ and $A_{12} = A_{23} = A_{33}/4$, the $|\sigma = 2\rangle = (|12\rangle + |21\rangle)/\sqrt{2}$ threshold scattering length can be found:

$$a_{22} = a_{22}^{\mathrm{Re}} + a_{22}^{\mathrm{Im}}, \tag{5.76}$$

$$a_{22}^{\mathrm{Re}} = \frac{1}{16} A_{33} \left(30 + \frac{1}{1 - A_{33}\sqrt{\frac{m\varepsilon}{\hbar^2}}} + \frac{1}{1 + A_{33}^2 \frac{m\varepsilon}{\hbar^2}} \right),$$

$$a_{22}^{\mathrm{Im}} = -\frac{1}{16} \frac{A_{33}^2 \sqrt{\frac{m\varepsilon}{\hbar^2}}}{1 + A_{33}^2 \frac{m\varepsilon}{\hbar^2}}.$$

With a resonance at the second two-body scattering threshold, it might be a good idea to consider the behavior of the three-body potentials at the second three-body threshold. Figure 5.10(b) shows an enlarged view of the adiabatic hyperradial potential in the region near this threshold. It becomes obvious that the adiabatic potentials here go through a series of very narrow avoided crossings here forming a set of diabatic hyperradial potentials asymptotically approaching the $|\Sigma^{symm} = 2\rangle = (|112\rangle + |121\rangle)/\sqrt{2}$ threshold including an attractive potential. The attractive diabatic potential of interest is given by

$$U_{diab}(R) = \frac{\hbar^2}{2\mu} \frac{(\nu_{\Sigma=2} + 2)^2 - 1/4}{R^2} + \varepsilon \tag{5.77}$$

$$\rightarrow \frac{\hbar^2}{2\mu} \frac{-s_1^2 - 1/4}{R^2} + \varepsilon \tag{5.78}$$

where $\nu_{\Sigma=2}$ is the hyperangular eigenvalue with respect to the second threshold. Figure 5.11 shows $(\nu_{\Sigma=2} + 2)^2$ as a function of the hyperradius. In the limit $R \gg A_{33}$ this hyperangular eigenvalue approaches a constant, $(\nu_{\Sigma=2} + 2)^2 \rightarrow -s_1^2 = -(0.4137)^2$ where s_1 is the universal constant given in Eq.5.57 that describes three equal mass particles with two resonant interactions [32, 122], the exact behavior one might would predict for a resonance in the $|\sigma = 2\rangle$ two body channel. With this universal attractive potential,

the Efimov diabat can support an infinite number of geometrically spaced states that are bound with respect to the second three-body threshold:

$$E_n = \varepsilon - E_0 e^{-2\pi/s_1} \approx \varepsilon - 2.5 \times 10^{-7} E_0. \tag{5.79}$$

Because the diabat goes through some avoided crossings with finite width, it is coupled to the three-body $|111\rangle$ continuum, making the Efimov states quasi-stable. Because of the multi-channel nature of the three-body interaction, these states are interpreted as fully three-body Fano-Feshbach resonances in a three-body continuum [18, 123, 19]. Similar resonances have been predicted due to Efimov states in the context of particle dimer scattering in nuclear halo systems [124].

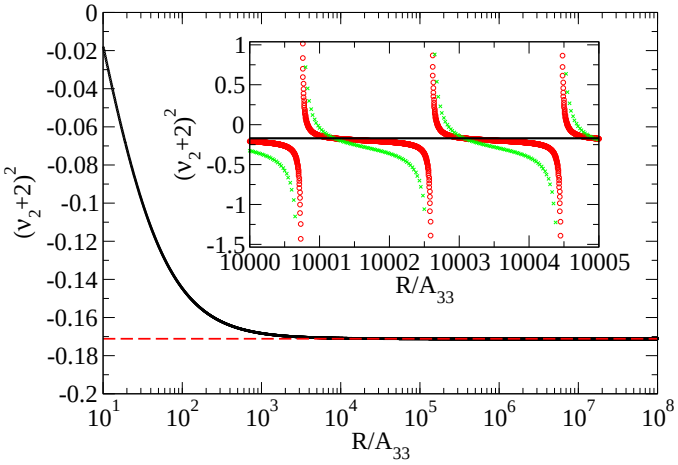

Figure 5.11: The hyperangular eigenvalue corresponding to the Efimov diabat is shown as a function of R/A_{33}. (inset) The hyperangular eigenvalue is shown for $A_{13} = 0$, $0.005A_{33}$ and $0.01A_{33}$ (black, red and green respectively). As A_{13} increases the width of the avoided crossings that create the Efimov diabat can be seen to increase.

5.4.2 Non-adiabatic matrices for the multi-channel problem

The states predicted in this section can only exist if the nonadiabatic diagonal correction falls off fast enough. Specifically, if $Q_{nn}^{diab}(R)$ for the diabatic Efimov potential dies off more slowly than s_1^2/R^2, the long range $1/R^2$ behavior that allows for the infinite

number of states will be cut off. If the diagonal correction dies of as $1/R^2$ then it can change the spacing of the states.

The derivation of the non-adiabatic matrix elements P_{mn} is shown in Appendix B the result of which is:

$$P_{mn} = -\frac{12\mu R\left(4\pi\right)^2}{dR\left(\varepsilon_n-\varepsilon_m\right)^2}\left[\vec{C}_m^{(1)}\cdot\left[\bar{E}_{th}\bar{A}^{(1)}\vec{C}_n^{(1)}\right]-\vec{C}_n^{(1)}\cdot\left[\bar{E}_{Th}\bar{A}^{(1)}\vec{C}_m^{(1)}\right]\right] \tag{5.80}$$
$$+\frac{3\left(4\pi\right)^2}{\left(\varepsilon_n-\varepsilon_m\right)}\left[-\frac{1}{dR}\vec{C}_n^{(1)\prime}\cdot\left(\bar{A}^{(1)}\vec{C}^{(1)}\right)-\frac{1}{dR^2}\vec{C}_m^{(1)}\cdot\left(\bar{A}^{(1)}\vec{C}_{n'}^{(1)}\right)+\frac{1}{dR}\vec{C}_m^{(1)}\cdot\left(\vec{A}^{(1)}\vec{C}_{n'}^{(1)\prime}\right)\right]$$

where $\varepsilon_n=\left(\nu_n+2\right)^2-4$ and the prime indicates a derivative with respect to the hyperradius. This equation holds if the hyperangular channel function, $\vec{\Phi}_n\left(\Omega\right)$, is normalized correctly. The normalization condition can be found through the boundary value vector, $\vec{C}_n^{(1)}$, by first "pre-normalizing" with $\vec{C}_n^{(1)}=N\vec{C}_{0n}^{(1)}$ where $\left[\vec{C}_{0n}^{(1)}\cdot\bar{C}_{0n}^{(1)}\right]=1$, and the constant N is defined by

$$1=N^2\frac{3\left(4\pi\right)^2}{dR}\left[\vec{C}_{0n}^{(1)}\cdot\left(\varepsilon_n'-4\mu R\bar{E}_{Th}\right)^{-1}\bar{A}\vec{C}_n^{1\prime}\right. \tag{5.81}$$
$$\left.-\vec{C}_{0n}^{(1)\prime}\cdot\left(\varepsilon_n'-4\mu R\bar{E}_{Th}\right)^{-1}\bar{A}\vec{C}_{0n}^{(1)}-\frac{1}{R}\vec{C}_{0n}^{(1)}\cdot\left(\varepsilon_n'-4\mu R\bar{E}_{Th}\right)^{-1}\bar{A}\vec{C}_{0n}^{(1)}\right].$$

The second derivative non-adiabatic diagonal matrix elements, Q_{nn}, are somewhat more complex, and are given in Appendix B. The resulting diagonal correction matrix element for the diabatic Efimov potential is shown in Fig. 5.12. It is clear that for large R, the diagonal correction, Q_{nn}, falls as $1/R^3$, and that including this non-adiabatic correction does not destroy the Efimov states.

The lifetime of the quasi-stable Efimov states will be partly controlled by the short range coupling to the continuum and to deeply bound states. A WKB velocity can be used to find the time it takes for the Efimov state to travel out to the far classical turning point and back to the short range region,

$$T=\int_{r_0}^{R_t}\frac{\mu}{\sqrt{2\mu\left[-E_n-U\left(R\right)\right]+1/4R^2}}dR, \tag{5.82}$$

where R_T is the classical turning point at large R, r_0 is the inner turning point controlled by the short-range details of the interaction, E_n is the binding energy of the nth Efimov

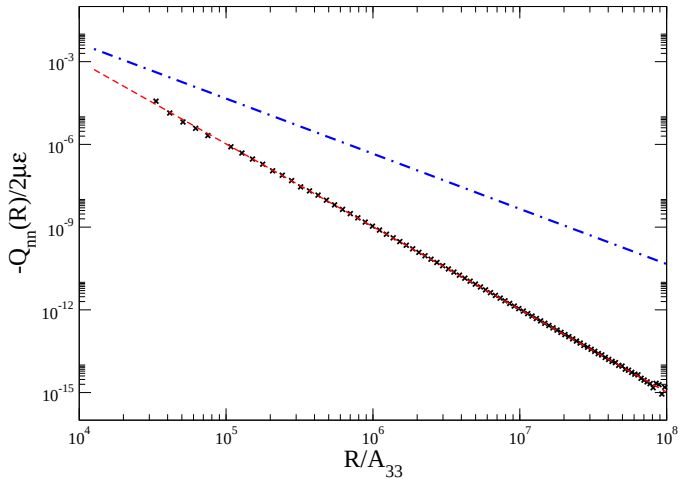

Figure 5.12: The diagonal correction, $-Q_{nn}/2\mu$ is shown in dimensions of the two-body threshold separation ε plotted as a function of R. The red dashed line shows $1/R^3$ scaling while the blue dot-dashed line shows $1/R^2$ scaling.

state with respect to the second three-body threshold, and $U(R)$ is the diabatic Efimov potential from Eq. 5.78. If it is assumed that every time the Efimov state oscillates through the short range region there is a fixed probability of transitioning to a deep state, the lifetime of the state is found to be

$$\Gamma_n = \frac{P_{SR}}{2T} \approx \Gamma_{n-1} e^{-2\pi/s_1}, \tag{5.83}$$

where P_{SR} is the short-range transition probability, T is given by Eq.5.82, and Γ_n is the width of the nth Efimov state. This means that if the width of the first Efimov state is narrow enough, then each of these resonances will be isolated from the others.

The final mechanism that can limit the lifetime of the quasistable Efimov states is the width of the avoided crossings at large R. Direct calculation of the P matrix elements is numerically difficult as it requires a large number of adiabatic potentials, calculated to high accuracy, to construct the diabatic Efimov potential and find the $\bar{P}$ matrix coupling at large R. A good estimate of the widths of these couplings is the lifetime of the two-body resonant state. This means that the Efimov state can remain as long as two-body interactions keep the system in the resonant two-body channel.

The parameter that controls the width of the large R avoided crossings is the coupling A_{13}. The inset of Fig. 5.11 shows $(\nu_{\Sigma=2}+2)^2$ for large R for of $A_{13}=0$ (black line), $0.005A_{33}$ (red circles), and $0.01A_{33}$ (green crosses).As A_{13} grows, the width of each crossing increases. The $|\sigma=2\rangle=(|12\rangle+|21\rangle)/\sqrt{2}$ two-body scattering length can be determined as a function of A_{13}:

$$\begin{aligned} a_{22} &= a_{\mathrm{Re}} + i a_{\mathrm{Im}}, \\ a_{\mathrm{Re}} &= \frac{A_{33}^3}{16A_{13}^2}, \\ a_{\mathrm{Im}} &= \frac{A_{33}\left(32A_{13}^2+2A_{13}A_{33}+A_{33}^2\right)}{16A_{13}^2}. \end{aligned} \tag{5.84}$$

The lifetime of the quasi-bound resonant state can be approximated by one over the imaginary part of the energy $E_{res}\approx\hbar^2/ma_{22}^2$. For $A_{13}\ll A_{33}$ this yields

$$T\approx\frac{\hbar}{\mathrm{Im}\left(E_{res}\right)}\approx\frac{mA_{33}^6}{\hbar 128A_{13}^4}. \tag{5.85}$$

This clearly demonstrates that for $A_{13}\to 0$ the the large R avoided crossings in the diabatic Efimov potential become level crossings, and for $A_{13}\ll A_{33}$ the crossings will be very narrow, and the lifetime of the Efimov states will be mostly controlled by the short range couplings.

The prediction of the Efimov state induced Fano-Feshbach resonances leads me to suggest a new method of experimentally probing these states with the use of radio frequency (RF) spectroscopy. In a cold atomic gas, the different internal states are Zeeman states which are weakly coupled by an RF field. By probing an ultracold gas of bosons in the lowest internal state using an RF field, resonances in the loss rate from the gas should appear when the frequency of the field is at the energy of one of the quasistable Efimov states. Further, the atoms in the gas will spend the majority of their time near the $E=0$ threshold and in the $|1\rangle$ state. Because the scattering length between atoms in the $|1\rangle$ state is not necessarily large, the gas will be stable with respect to the a^4 scaling of three-body recombination, allowing for long probing times. If it is

assumed that the first Efimov state appears at $E_1 \approx \hbar \times 2\pi\,(40\text{ MHz})$ below the second threshold, an energy that is not unreasonable for a three-body state of ^{85}RB atoms that is approximately the van der Waals length $r_d \approx 200$ a.u. in size, Eq. 5.79 shows that the second state will appear at approximately $E_2 = \hbar \times 2\pi\,(40\text{ MHz})\,e^{-2\pi/s_1} \approx \hbar \times 2\pi\,(10\text{ Hz})$. This binding energy is very small compared to the 2 GHz spacing of the hyperfine levels of ^{85}Rb, but still possibly within experimental resolution. The geometric scaling factor in the spacing of the Efimov states, $e^{-2\pi/s_1}$, can be made considerably better by creating a resonance at the $|22\rangle$ two-body scattering threshold and considering Efimov states attached to the $|222\rangle$ identical boson threshold. Another tactic to improve the geometric spacing is that of using more favorable mass ratios [111, 112, 113]. The multi-channel treatment of these scenarios is a task beyond the scope of this thesis, but should be accessible using the methods shown here.

Chapter 6

Four Fermions and Dimer-Dimer Scattering

The physics of strongly interacting fermions is of fundamental importance to many areas of physics, including condensed matter physics, nuclear and particle physics, and astrophysics. Specifically the last few years have seen explosive growth, both experimentally [12, 13, 14, 15, 16, 17] and theoretically [46, 47, 48, 49], in the area of degenerate Fermi gases of atoms. Combined with a Fano-Feshbach resonance that allows for tuning of the s-wave interactions, these systems exhibit a variety of interesting phenomena including the Bose-Einstein condensate (BEC) and the Bardeen-Cooper-Schreiffer (BCS) crossover that smoothly links two fundamentally different types of superfluidity, BEC ($a > 0$) to BCS ($a < 0$), through a resonance. In these systems, few-body correlations play a fundamental role in understanding the many-body behavior [23]. For instance, a full solution of the four-fermion problem is required to understand the energy and dynamics of a BEC of bosonic molecules composed of two fermions each.

The Hamiltonian for the four-fermion problem is given by

$$H = \sum_{i=1}^{4} -\frac{\hbar^2}{2m}\nabla_i^2 + \sum_{i>j} V\left(r_{ij}\right). \tag{6.1}$$

Generally speaking the resulting 12 dimensional Schrödinger equation is unmanageable. In this chapter I incorporate a variety of existing theoretical methods together to first reduce the dimensionality of this partial differential equation, and then to develop a basis set that allows for manageable variational calculations of the scattering potentials. This

chapter is organized as follows: in Section 6.1, the various coordinate systems used in solving the four-fermion problem are discussed as well as various properties of each system; in Section 6.2 the variational basis set used to describe the system is developed; in Section 6.3 the resulting dimer-dimer wave function is analyzed; in Section 6.4 the energy dimer-dimer scattering length is examined; and finally in Section 6.5 the process of dimer-dimer relaxation is discussed.

6.1 Coordinate systems

The use of different coordinate systems plays a significant role in the treatment of few-body scattering problems. Depending on the symmetries, interactions, and fragmentation channels inherent in the problem, different coordinates may significantly affect the ease with which the problem can be described. For example, in the four fermion problem, the fermionic symmetry of the system can be used to significantly reduce the size of the basis needed to describe the possible scattering processes. Describing this symmetry in the wrong coordinate system, as I will show in this section, can create a considerable amount of difficulty. Here I detail the variety of coordinate systems that are used to describe the four-fermion problem in the adiabatic hyperspherical framework and the necessary transformations to describe one set in terms of another. The coordinate systems used here are not only needed to describe correlations between particles, they also allow the system to be reduced in dimensionality by removing the center of mass motion and moving into a body fixed frame.

6.1.1 Jacobi coordinates

The first and most obvious symmetry in the Hamiltonian described by Eq. 6.1 is that of translational symmetry. By describing the system in the center of mass frame, the dimensionality of the system can be reduced from $d = 12$ to $d = 9$. This is done with the use of Jacobi coordinates. In the interest of brevity, I constrain myself here

to only those coordinates directly concerned with the problem at hand. The Jacobi coordinates relevant to the four-body problem may be broken into two sets, H-type and K-type, shown schematically in Fig. 6.1.

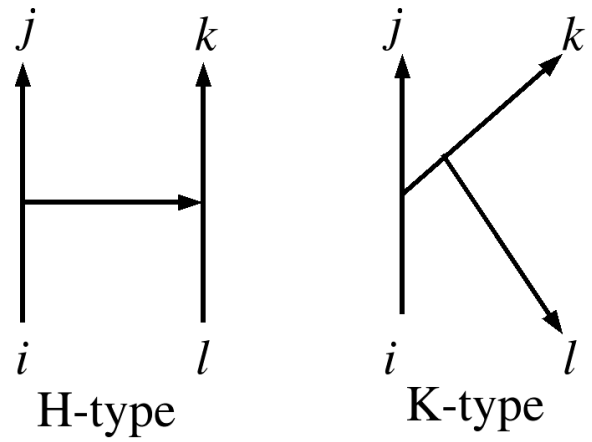

Figure 6.1: The two Jacobi coordinates configurations possible in the four body problem are shown schematically.

H-type Jacobi coordinates are constructed by considering the separation vector for two two-body subsystems, and the separation vector between the centers of mass of those two subsystems, i.e.

$$\begin{aligned}
\vec{\rho}_1^{H\sigma} &= \sqrt{\frac{\mu_{ij}}{\mu}}\left(\vec{r}_i - \vec{r}_j\right), \\
\vec{\rho}_2^{H\sigma} &= \sqrt{\frac{\mu_{kl}}{\mu}}\left(\vec{r}_k - \vec{r}_l\right), \\
\vec{\rho}_3^{H\sigma} &= \sqrt{\frac{\mu_{ij,kl}}{\mu}}\left(\frac{m_i\vec{r}_i + m_j\vec{r}_j}{m_i + m_j} - \frac{m_k\vec{r}_k + m_l\vec{r}_l}{m_k + m_l}\right), \\
\vec{\rho}_{cm} &= \frac{(m_1\vec{r}_1 + m_2\vec{r}_2 + m_3\vec{r}_3 + m_4\vec{r}_4)}{m_1 + m_2 + m_3 + m_4}, \\
\mu_{ij} &= \frac{m_i m_j}{m_i + m_j}, \mu_{ij,kl} = \frac{(m_i + m_j)(m_l + m_k)}{m_1 + m_2 + m_3 + m_4}.
\end{aligned} \tag{6.2}$$

Here the superscript σ enumerates the 24 different H-type coordinates that may be obtained through particle permutation, $\vec{\rho}_{cm}$ is the position of center of mass of the four-body system, and μ is an arbitrary reduced mass for the four-body system. The prefactors in each Jacobi vector, which are given in terms of the various reduced masses

in the problem, are chosen to give the so-called mass scaled Jacobi vectors. The kinetic energy in these coordinates can be written as

$$-\sum_{i=1}^{4}\frac{\hbar^2}{2m_i}\nabla^2_{r_i} = -\frac{\hbar^2}{2M}\nabla^2_{\rho_{cm}} - \frac{\hbar^2}{2\mu}\sum_{j=1}^{3}\nabla^2_{\rho_j},$$

where M is the total mass of the four particles. The reduced mass, μ, can be chosen to preserve the differential volume element for the full 3D problem, ensuring that $d^3\rho_1^\sigma d^3\rho_2^\sigma d^3\rho_3^\sigma d^3\rho_{cm} = d^3r_1 d^3r_2 d^3r_3 d^3r_4$:

$$\mu = \left(\frac{m_1 m_2 m_3 m_4}{m_1+m_2+m_3+m_4}\right)^{1/3}.$$

Physically, the H-type coordinates are useful for describing correlations between two particles, for example a two body bound state or a symmetry between two particles, or two separate two-body correlations. It is interesting to note that when two particles are on top of each other, for instance in a bound dimer, the H-type coordinate system reduces to a three body system, i.e. when $\vec{r}_i = \vec{r}_j$ in Eq. 6.2:

$$\begin{aligned}
\vec{\rho}_1^{H\sigma} &= 0,\\
\vec{\rho}_2^{H\sigma} &= \sqrt{\frac{\mu_{kl}}{\mu}}\left(\vec{r}_k - \vec{r}_l\right),\\
\vec{\rho}_3^{H\sigma} &= \sqrt{\frac{\mu_{ij,kl}}{\mu}}\left(\vec{r}_i - \frac{m_k\vec{r}_k + m_l\vec{r}_l}{m_k+m_l}\right).
\end{aligned}$$

This observation will be useful later when constructing a basis to examine the four fermion problem. This point is called a coalescence point and finding a way of accurately describing these point is crucial for describing interactions between particles.

K-type Jacobi coordinates are constructed in an iterative way by first constructing a three body coordinate set as in Eq. 5.21, and then taking the separation vector between

the fourth particle and the center of mass of the three particle sub-system, yielding

$$\begin{aligned}
\vec{\rho}_1^{K\sigma} &= \sqrt{\frac{\mu_{ij}}{\mu}}\left(\vec{r}_i - \vec{r}_j\right), \\
\vec{\rho}_2^{K\sigma} &= \sqrt{\frac{\mu_{ij,k}}{\mu}}\left(\frac{m_i\vec{r}_i + m_j\vec{r}_j}{m_i + m_j} - m_k\vec{r}_k\right), \\
\vec{\rho}_3^{K\sigma} &= \sqrt{\frac{\mu_{ijk,l}}{\mu}}\left(\frac{m_i\vec{r}_i + m_j\vec{r}_j + m_k\vec{r}_k}{m_i + m_j + m_k} - m_l\vec{r}_l\right), \\
\vec{\rho}_{cm} &= \frac{(m_1\vec{r}_1 + m_2\vec{r}_2 + m_3\vec{r}_3 + m_4\vec{r}_4)}{m_1 + m_2 + m_3 + m_4}, \\
\mu_{ij} &= \frac{m_i m_j}{m_i + m_j}, \mu_{ij,k} = \frac{(m_i + m_j)\, m_k}{m_i + m_j + m_k}, \\
\mu_{ijk,l} &= \frac{(m_i + m_j + m_k)\, m_l}{m_1 + m_2 + m_3 + m_4}.
\end{aligned} \tag{6.3}$$

Again σ enumerates the 24 different K-type coordinates that result from particle permutations. Examining Fig. 6.1 shows that K-type Jacobi coordinate systems are useful for describing correlations between three particles within the four particle system. In the four fermion system, there are no weakly bound trimer states meaning that K-type Jacobi coordinates will not be used here, but the methods described in this report can be easily generalized to include these type of states. Unless explicitly stated all Jacobi coordinates from here on will be of the H-type, and for notational simplicity, I will drop the H superscripts.

6.1.2 Coalescence points and symmetry

The proper description of coalescence points is crucial for describing two-body interactions, but they are also important for describing points of symmetry. For instance if two identical fermions are on top of one another it is known that the wave function must vanish at this point owing to the anti-symmetry of fermionic wave functions. In this thesis I will be concerned with four fermions in two different "spin" states. Away from a p-wave resonance, the interactions between identical fermions can be neglected for low energy collisions. This means that there are two types of coalescence points that must be described; two "symmetry" points, when two fermions of the same type are

on top of each other, and four "interaction" points, places where two distinguishable fermions interact via an s-wave potential.

It might be tempting at this point to choose a single Jacobi coordinate system and then try to describe the interactions and symmetries in the same coordinates, but this leads to problems. For instance if it is assumed that particles 1 and 3 are spin up and particles 2 and 4 are spin down one might start with coordinates that are simple to anti-symmetrize the system in:

$$\begin{aligned}
\vec{\rho}_1^{\,s} &= \sqrt{\frac{4^{1/3}}{2}}\left(\vec{r}_1 - \vec{r}_3\right), \\
\vec{\rho}_2^{\,s} &= \sqrt{\frac{4^{1/3}}{2}}\left(\vec{r}_2 - \vec{r}_4\right), \\
\vec{\rho}_3^{\,s} &= \sqrt{4^{1/3}}\left(\frac{\vec{r}_1 + \vec{r}_3}{2} - \frac{\vec{r}_2 + \vec{r}_4}{2}\right),
\end{aligned} \tag{6.4}$$

where it has been assumed that all of the particle masses are equal, $m_1 = m_2 = m_3 = m_4 = m$ leaving $\mu = m/4^{1/3}$. The generalization to distinguishable fermions of different masses is clear. I will refer to this Jacobi coordinate system as the symmetry coordinates for fairly obvious reasons. If a permutation of two identical fermions is considered, for instance 1 and 3, the transformation is simple:

$$P_{13}\vec{\rho}_1^{\,s} = -\vec{\rho}_1^{\,s}, \tag{6.5}$$

$$P_{13}\vec{\rho}_2^{\,s} = \vec{\rho}_2^{\,s}, \tag{6.6}$$

$$P_{13}\vec{\rho}_3^{\,s} = \vec{\rho}_3^{\,s}. \tag{6.7}$$

Similarly for the exchange of particle 2 and 4,

$$P_{24}\vec{\rho}_1^{\,s} = \vec{\rho}_1^{\,s}, \tag{6.8}$$

$$P_{24}\vec{\rho}_2^{\,s} = -\vec{\rho}_2^{\,s}, \tag{6.9}$$

$$P_{24}\vec{\rho}_3^{\,s} = \vec{\rho}_3^{\,s}. \tag{6.10}$$

The points where two identical fermions are on top of each other are also simply described by taking either $\vec{\rho}_1^{\,s} \to 0$ or $\vec{\rho}_2^{\,s} \to 0$. Everything seems to be progressing

nicely until an interaction between two distinguishable fermions, for instance 1 and 2, is considered. This interaction occurs around the point $\vec{r}_1 = \vec{r}_2$. In the symmetry coordinates this means that

$$\vec{\rho}_1^{\,s} = \vec{\rho}_2^{\,s} - \sqrt{2}\vec{\rho}_3^{\,s}.$$

This equation describes a 6 dimensional sheet in the 9 dimensional space, something that is not easy to describe directly in any basis set. To get around this problem I introduce two more Jacobi coordinate systems that are useful for describing interactions,

$$\begin{aligned}
\vec{\rho}_1^{\,i1} &= \sqrt{\frac{4^{1/3}}{2}}\left(\vec{r}_1 - \vec{r}_2\right), \\
\vec{\rho}_2^{\,i1} &= \sqrt{\frac{4^{1/3}}{2}}\left(\vec{r}_3 - \vec{r}_4\right), \\
\vec{\rho}_3^{\,i1} &= \sqrt{4^{1/3}}\left(\frac{\vec{r}_1 + \vec{r}_2}{2} - \frac{\vec{r}_3 + \vec{r}_4}{2}\right),
\end{aligned} \tag{6.11}$$

and

$$\begin{aligned}
\vec{\rho}_1^{\,i2} &= \sqrt{\frac{4^{1/3}}{2}}\left(\vec{r}_1 - \vec{r}_4\right), \\
\vec{\rho}_2^{\,i2} &= \sqrt{\frac{4^{1/3}}{2}}\left(\vec{r}_3 - \vec{r}_2\right), \\
\vec{\rho}_3^{\,i2} &= \sqrt{4^{1/3}}\left(\frac{\vec{r}_1 + \vec{r}_4}{2} - \frac{\vec{r}_2 + \vec{r}_3}{2}\right).
\end{aligned} \tag{6.12}$$

The superscript $i1$ and $i2$ in Eqs. 6.11 and 6.12 indicate that these Jacobi coordinates are appropriate for interactions between distinguishable fermions. For instance, a coalescence point between particles 1 and 2 is described by $\vec{\rho}_1^{\,i1} \to 0$. Another benefit of these coordinates is that they are well suited to describing a dimer wavefunction. If particles 2 and 3 are in a weakly bound molecule then the wavefunction for that molecule is only a function of $\vec{\rho}_2^{\,i2}$.

Using combinations of these three coordinate systems, $\vec{\rho}_j^{\,s}$, $\vec{\rho}_j^{\,i1}$ and $\vec{\rho}_j^{\,i2}$, can describe all of the possible two-body correlations of the fermionic system. This assumes that the system in question is that of four equal mass fermions in two internal states with s-wave interactions only. However, the method used is quite general. Coordinates can be

chosen to describe the possible three-body correlations that can arise due to things like the Efimov effect [59, 60, 113]. The only requirement in constructing the appropriate Jacobi coordinates for a given problem is a bit of physical intuition.

6.1.3 Kinematic rotations

Since I am going to be using different Jacobi systems to describe different types of correlations, a method of transforming between different sets of coordinates is needed. In the above section, equal mass particles are considered. This is because extension to arbitrary masses was fairly obvious. To describe the kinematic rotations I will keep the masses arbitrary and specify for equal masses later. It is convenient here to deal with transforming all of the Jacobi coordinates at once. Thus the matrices whose columns are made of the Jacobi vectors are used:

$$\begin{aligned} \bar{\varrho}^{s} &= \{\vec{\rho}_1^{s}, \vec{\rho}_2^{s}, \vec{\rho}_3^{s}\} \\ \bar{\varrho}^{i1} &= \left\{\vec{\rho}_1^{i1}, \vec{\rho}_2^{i1}, \vec{\rho}_3^{i1}\right\} \\ \bar{\varrho}^{i2} &= \left\{\vec{\rho}_1^{i2}, \vec{\rho}_2^{i2}, \vec{\rho}_3^{i2}\right\}. \end{aligned} \tag{6.13}$$

The transformation that takes one coordinate system to another cannot stretch or shrink the differential volume element, and thus it must be a unitary transformation. Further, the transformation cannot mix the Cartesian components of the Jacobi vector, i.e. ρ_x^{i1} has no part of ρ_y^s in it. This means that the transformation will be a unitary matrix that acts from the right, e.g.

$$\bar{\varrho}^{i1} = \bar{\varrho}^{s}\bar{U}_{s\to i1}. \tag{6.14}$$

The matrices that perform these operations are called kinematic rotations [125, 126, 127], and they will be put to extensive use in the calculations that follow. In truth, transformations between coordinates systems that do not require an inversion should be considered, but the general principle still holds if improper rotations are included.

Note that all of the matrix elements must be real, so that the inverse transformation is given merely by the transpose.

I employ a direct "brute force" method of finding these matrices where the system of equations given in Eq. 6.2 are solved for $\vec{r}_1$, $\vec{r}_2$, $\vec{r}_3$ and $\vec{r}_4$ in a given Jacobi system. These normal lab-fixed coordinates can then be inserted into the definition of the Jacobi coordinates that I wish to describe. The kinematic rotation can then be extracted from the resulting relations. Following this procedure gives

$$\bar{U}_{s\to i1} = \begin{bmatrix} \frac{m_3}{m_1+m_3}\sqrt{\frac{\mu_{12}}{\mu_{13}}} & -\frac{m_1}{m_1+m_3}\sqrt{\frac{\mu_{34}}{\mu_{13}}} & \sqrt{\frac{\mu_{13}}{\mu_{12,34}}} \\ -\frac{m_4}{m_2+m_4}\sqrt{\frac{\mu_{12}}{\mu_{24}}} & \frac{m_2}{m_2+m_4}\sqrt{\frac{\mu_{34}}{\mu_{24}}} & \sqrt{\frac{\mu_{24}}{\mu_{12,34}}} \\ \sqrt{\frac{\mu_{12}}{\mu_{13,24}}} & \sqrt{\frac{\mu_{34}}{\mu_{13,24}}} & \frac{m_1m_4-m_2m_3}{\sqrt{(m_1+m_2)(m_3+m_4)}}\sqrt{\frac{\mu_{12,34}}{\mu_{13,24}}} \end{bmatrix}, \tag{6.15a}$$

$$\bar{U}_{s\to i2} = \begin{bmatrix} \frac{m_3}{m_1+m_3}\sqrt{\frac{\mu_{14}}{\mu_{13}}} & -\frac{m_1}{m_1+m_3}\sqrt{\frac{\mu_{23}}{\mu_{13}}} & \sqrt{\frac{\mu_{13}}{\mu_{12,34}}} \\ \frac{m_4}{m_2+m_4}\sqrt{\frac{\mu_{14}}{\mu_{24}}} & -\frac{m_2}{m_2+m_4}\sqrt{\frac{\mu_{23}}{\mu_{24}}} & -\sqrt{\frac{\mu_{24}}{\mu_{14,23}}} \\ \sqrt{\frac{\mu_{14}}{\mu_{13,24}}} & \sqrt{\frac{\mu_{23}}{\mu_{13,24}}} & \frac{m_1m_2-m_3m_4}{\sqrt{(m_2+m_3)(m_1+m_4)}}\sqrt{\frac{\mu_{14,24}}{\mu_{13,24}}} \end{bmatrix}, \tag{6.15b}$$

$$\bar{U}_{i1\to s} = \left[\bar{U}_{s\to i1}\right]^T;\ \bar{U}_{i2\to s} = \left[\bar{U}_{s\to i2}\right]^T, \tag{6.15c}$$

$$\bar{U}_{i1\to i2} = \bar{U}_{i1\to s}\bar{U}_{s\to i2} = \left[\bar{U}_{s\to i1}\right]^T\bar{U}_{s\to i2};\ \bar{U}_{i2\to i1} = \left[\bar{U}_{i1\to i2}\right]^T. \tag{6.15d}$$

The same method can be used to find the kinematic rotations to other Jacobi systems, for instance to K-type coordinates.

6.1.4 Hyperangular coordinates

As with Jacobi coordinates, there is no unique way to construct the hyperangles of a system. In this section I construct the hyperangular coordinates used in the four-fermion problem. The choice of hyperangular parameterization has physical meaning. Different parameterizations can be used to describe different correlations within the system. Also, in the case of body-fixed coordinates, hyperspherical coordinates can be

used to remove the Euler angles of solid rotation, reducing the dimensionality of the system.

The first hyperangular parameterization used here is in the form of Eq. 2.10 for three 3D vectors. The hyperradius is defined in the same way as in Eq. 2.1,

$$R^2 = \sum_{i=1}^{d} x_i^2, \tag{6.16}$$

where each x_i is a Cartesian component of one of the Jacobi vectors. The hyperspherical trees that will be used for the four fermion problem will of the type in Fig. 2.4 in which N vectors are described by the spherical polar angles of each vector and a set of hyperangles correlating the lengths of each vector. Specifically, the hyperangles are defined by the tree shown in Fig. 6.2 combined with the spherical polar angles of each Jacobi vector. Following the rules described in Chapter 2 gives the hyperangles,

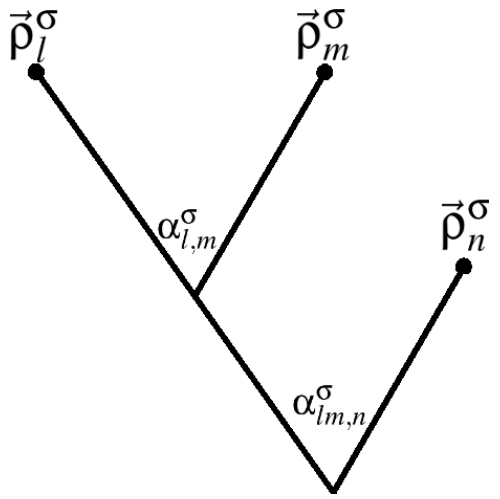

Figure 6.2: The hyperspherical tree used to parameterize the hyperangular coordinates in the four-fermion problem is shown. See Chapter 2 or Ref. [5] for details.

$$\alpha_{l,m}^{\sigma} = \tan^{-1} \frac{|\vec{\rho}_l^{\sigma}|}{|\vec{\rho}_m^{\sigma}|}, \tag{6.17}$$
$$\alpha_{lm,n}^{\sigma} = \tan^{-1} \frac{\sqrt{|\vec{\rho}_l^{\sigma}|^2 + |\vec{\rho}_m^{\sigma}|^2}}{|\vec{\rho}_n^{\sigma}|}.$$

Here the superscript $\sigma = s, i1, i2$ indicates which Jacobi system is being used, while l, m, n indicate the three Jacobi vectors from that system. In principle there are six of these hyperangular coordinate systems that can be constructed from each set of Jacobi vectors giving a total of 18 different hyperangular systems. Fortunately I will not need all of these to tackle the four fermion problem. If one considers two particles, say 1 and 2, the tree defined by Fig. 6.2 with $\sigma = i1$, $l = 2, m = 3$ and $n = 1$ can be decomposed into two subtrees. The right branch describes the hyperangular behavior of the dimer alone, while the left branch describes the behavior of the remaining three body system composed of a dimer and two free particles. This type of decomposition will be important for evaluating kinetic energy matrix elements and defining basis functions.

6.1.4.1 Hyperspherical harmonics

Using the recursive definition of the hyperangular momentum operator in Eq. 2.11 the total hyperangular momentum operator can be written in terms of the hyperangular coordinates as

$$\begin{aligned}\Lambda^2 =& \Delta_1\left(\alpha^\sigma_{lm,n}\right) - \frac{1}{\sin^2\alpha^\sigma_{lm,n}\sin\alpha^\sigma_{l,m}\cos\alpha^\sigma_{l,m}}\left[\frac{\partial}{\partial\alpha^\sigma_{l,m}}\right]^2\sin\alpha^\sigma_{l,m}\cos\alpha^\sigma_{l,m} \\ &+ \frac{\hat{l}_l^2}{\sin^2\alpha^\sigma_{lm,n}\sin^2\alpha^\sigma_{m,n}} + \frac{\hat{l}_m^2}{\sin^2\alpha^\sigma_{lm,n}\cos^2\alpha^\sigma_{m,n}} + \frac{\hat{l}_n^2}{\cos^2\alpha^\sigma_{lm,n}}, \\ \Delta_1\left(\alpha^\sigma_{lm,n}\right) =& \frac{-1}{\sin^2\alpha^\sigma_{lm,n}\cos\alpha^\sigma_{lm,n}}\frac{1}{\sin\alpha^\sigma_{lm,n}}\frac{\partial}{\partial\alpha^\sigma_{lm,n}}\sin\alpha^\sigma_{lm,n}\frac{\partial}{\partial\alpha^\sigma_{lm,n}}\sin^2\alpha^\sigma_{lm,n}\cos\alpha^\sigma_{lm,n},\end{aligned} \tag{6.18}$$

where $\hat{l}_l, \hat{l}_m$ and $\hat{l}_n$ are the normal spatial angular momentum operators for each Jacobi vector. This can also be written directly from Eq. 2.11 as

$$\begin{aligned}\Lambda^2 &= \Delta_1\left(\alpha^\sigma_{lm,n}\right) + \frac{\Lambda^2_{l,m}}{\sin^2\alpha_{lm,n}} + \frac{\hat{l}_n^2}{\cos^2\alpha^\sigma_{lm,n}}, \\ \Lambda^2_{l,m} &= -\frac{1}{\sin\alpha^\sigma_{l,m}\cos\alpha^\sigma_{l,m}}\left[\frac{\partial}{\partial\alpha^\sigma_{l,m}}\right]^2\sin\alpha^\sigma_{l,m}\cos\alpha^\sigma_{l,m} + \frac{\hat{l}_l^2}{\sin^2\alpha^\sigma_{m,n}} + \frac{\hat{l}_m^2}{\cos^2\alpha^\sigma_{m,n}},\end{aligned} \tag{6.19}$$

where all of the hyperangular behavior above the second node in Fig.6.2 is described by a sub-hyperangular momentum, $\Lambda^2_{lm,n}$.

Constructing the hyperspherical harmonics for the four-body system is accomplished following the procedure in Appendix A giving

$$Y^{(4b)}_{\left[\lambda\lambda_{l,m}l_l,l_m,l_n\right]}(\Omega) = N^{33}_{l_l l_m \lambda_{l,m}} N^{63}_{\lambda_{l,m} l_n, \lambda} \sin^{\lambda_{l,m}}(\alpha_{lm,n}) \cos^{l_n}(\alpha_{lm,n}) P^{\lambda_{l,m}+5/2, l_n+1}_{(\lambda-\lambda_{l,m}-l_n)/2}(\cos 2\alpha_{lm,n}) \tag{6.20}$$

$$\times N^{\lambda_{l,m}}_{l_l,l_m} \sin^{l_l}(\alpha_{l,m}) \cos^{l_m}(\alpha_{l,m}) P^{l_l+1, l_m+1}_{(\lambda_{l,m}-l_l-l_m)/2}(\cos 2\alpha_{l,m})$$

$$\times y_{l_l m_l}(\omega_l)\, y_{l_m m_m}(\omega_m)\, y_{l_n m_n}(\omega_n),$$

where $P^{\alpha,\beta}_{\gamma}(x)$ is a Jacobi polynomial of order γ, $y_{lm}(\omega)$ is a normal spherical harmonic with spherical polar solid angle ω, and N^{de}_{abc} is a normalization constant [5, 66]:

$$N^{de}_{abc} = \left[\frac{(2c+d+e-2)\,\Gamma\left(\frac{a+b+c+d+e-2}{2}\right)\left(\frac{c-a-b}{2}\right)!}{\Gamma\left(\frac{c+a-b+d}{2}\right)\Gamma\left(\frac{c+b-a+e}{2}\right)}\right]^{1/2}.$$

In Eq. 6.20 the degeneracy quantum number μ has been replaced with an explicit tabulation of the hyperangular momentum quantum numbers, i.e. $\lambda\mu \rightarrow [\lambda\lambda_{l,m}l_l, l_m, l_n]$. The total four-body hyperspherical harmonics satisfy the eigenvalue equation $\Lambda^2 Y^{(4b)}_{\left[\lambda\lambda_{l,m}l_l,l_m,l_n\right]}(\Omega) = \lambda(\lambda+7)\, Y^{(4b)}_{\left[\lambda\lambda_{l,m}l_l,l_m,l_n\right]}(\Omega)$. The sub-harmonics that are eigenfunctions of $\Lambda^2_{l,m}$ can be found as well:

$$Y^{(3b)}_{\left[\lambda_{l,m}l_l,l_m\right]}(\Omega_{l,m}) = N^{33}_{l_l,l_m\lambda_{l,m}} \sin^{l_l}(\alpha_{l,m}) \cos^{l_m}(\alpha_{l,m}) P^{l_l+1,l_m+1}_{(\lambda_{l,m}-l_l-l_m)/2}(\cos 2\alpha_{l,m}) \tag{6.21}$$

$$\times y_{l_l m_l}(\omega_l)\, y_{l_m m_m}(\omega_m).$$

Here the superscript, (3b), indicates that this eigenfunction behaves as a 3-body hyperspherical harmonic. For instance if a hyperspherical tree is used with Jacobi vectors defined in the $i1$ interaction coordinate system and $l = 1$, $m = 3$, and $n = 2$, this three-body harmonic describes the free-space behavior of a dimer with two free particles. The three body harmonics obey the eigenvalue equation, $\Lambda^2_{l,m} Y^{(3b)}_{\left[\lambda_{l,m}l_l,l_m\right]}(\Omega_{l,m}) =$

$\lambda_{l,m}\left(\lambda_{l,m}+4\right) Y^{(3b)}_{\left[\lambda_{l,m} l_l, l_m\right]}\left(\Omega_{l,m}\right)$. The restrictions on the values of λ and $\lambda_{l,m}$ are

$$\begin{aligned} \lambda_{l,m} &= l_l + l_m + 2j, \\ \lambda &= \lambda_{l,m} + l_n + 2k \\ &= l_l + l_m + l_n + 2j + 2k, \end{aligned} \tag{6.22}$$

where $j, k = 0, 1, 2, ...$ The quantum numbers l_l, l_m and l_n are the spatial angular momentum quantum numbers associated with each Jacobi vector, and each has a z-projection quantum number associated with it which I have suppressed in Eqs. 6.20 and 6.21.

6.1.4.2 Democratic coordinates

Using Delve's coordinates greatly simplifies evaluating hyperangular momentum matrix elements, but it still leaves the 8 dimensional space of hyperangles. I will only be considering systems with total angular momentum $L = 0$. Therefore it is convenient to move into a body-fixed coordinate system, as the final wavefunction for the four-body problem will not depend on the Euler angles that produce a solid rotation of the system. Removing the Euler angle dependence is accomplished by transforming into the so-called democratic, or body-fixed coordinates. Four-body democratic coordinates are developed in several references (see Refs. [125, 126, 127]). In this work I use the parameterization of Aquilanti and Cavalli. For a detailed derivation of the coordinate system see their work in Ref. [125].

At the heart of democratic coordinates is a rotation from a space fixed frame to a body fixed frame:

$$\bar{\varrho} = \tilde{D}\left(\alpha, \beta, \gamma\right) \bar{\varrho}_{bf} \tag{6.23}$$

where $\bar{\varrho}$ is the matrix of Jacobi vectors defined in Eq. 6.13, $\bar{\varrho}_{bf}$ is the set of body fixed Jacobi coordinates, and $D\left(\alpha, \beta, \gamma\right)$ is an Euler rotation matrix defined in the standard

way as

$$\bar{D} = \begin{bmatrix} \cos\alpha & -\sin\alpha & 0 \\ \sin\alpha & \cos\alpha & 0 \\ 0 & 0 & 1 \end{bmatrix} \begin{bmatrix} \cos\beta & 0 & \sin\beta \\ 0 & 1 & 0 \\ -\sin\beta & 0 & \cos\beta \end{bmatrix} \begin{bmatrix} \cos\gamma & -\sin\gamma & 0 \\ \sin\gamma & \cos\gamma & 0 \\ 0 & 0 & 1 \end{bmatrix}. \tag{6.24}$$

The "˜" in Eq. 6.23 indicates a transpose has been taken.

The body-fixed coordinates are defined in a system whose axes are defined by the principle moments of inertia, I_1, I_2 and I_3. In this coordinate system the body-fixed Jacobi coordinates are given by

$$\bar{\varrho}_{bf} = \Pi \bar{D}\left(\phi_1, \phi_2, \phi_3\right), \tag{6.25}$$

where $\bar{D}$ is defined in the same way as in Eq. 6.24 with ϕ_1, ϕ_2 and ϕ_3 replacing α, β, and γ. Π is a 3×3 diagonal matrix whose diagonals are given by ξ_1, ξ_2 and ξ_3 which are parameterized by the hyperradius and two hyperangles Θ_1 and Θ_2:

$$\begin{aligned} \xi_1 &= \frac{R}{\sqrt{3}} \cos\Theta_1, \\ \xi_2 &= \frac{R}{\sqrt{3}} \sqrt{3\sin^2\Theta_1 \sin^2\Theta_2 + \cos^2\Theta_1}, \\ \xi_3 &= \frac{R}{\sqrt{3}} \sqrt{3\sin^2\Theta_1 \cos^2\Theta_2 + \cos^2\Theta_1}. \end{aligned} \tag{6.26}$$

To avoid double counting and to allow for different chiralities, Θ_1 and Θ_2 are restricted to $0 \leq \Theta_1 \leq \pi$ and $0 \leq \Theta_2 \leq \pi/4$. With this parameterization the moments of inertia are given by

$$\begin{aligned} \frac{I_1}{\mu} &= \xi_2^2 + \xi_3^2 = \frac{R^2}{3}\left(2 + \sin^2\Theta_1\right), \\ \frac{I_2}{\mu} &= \xi_1^2 + \xi_3^2 = \frac{R^2}{3}\left(3\sin^2\Theta_1 \cos^2\Theta_2 + 2\cos^2\Theta_1\right), \\ \frac{I_3}{\mu} &= \xi_1^2 + \xi_2^2 = \frac{R^2}{3}\left(3\sin^2\Theta_1 \sin^2\Theta_2 + 2\cos^2\Theta_1\right). \end{aligned} \tag{6.27}$$

The hyperradius in terms of the principle moments of inertia can be then written as $R^2 = \xi_1^2 + \xi_2^2 + \xi_3^2 = \left(I_1 + I_2 + I_3\right)/2\mu$.

With this parameterization, all 8 hyperangles have been defined. The first three are the Euler angles $\{\alpha, \beta, \gamma\}$, which are external degrees of freedom describing solid rotations of the four body system. The two angles, Θ_1 and Θ_2, defined in Eq. 6.26, describe the overall x, y and z extent of the four-body system in the body fixed frame. From Eq. 6.27, if $\Theta_1 = 0, \pi$, then the principle moments of inertia are all equal, i.e. $I_1 = I_2 = I_3$, meaning that the four particles are arranged at the vertices of a regular tetrahedron. When $\Theta_1 = \pi/2$, Eq. 6.26 shows that the particles are in a planar configuration. The remaining angles, $\{\phi_1, \phi_2, \phi_3\}$, are kinematic rotations within the system, and coalescence points and operations like particle exchange are described in these angles. Broadly speaking, the democratic angles Θ_1 and Θ_2 can be thought of as correlating the overall x, y, and z spatial extent of the four-body system in the body-fixed frame, while the kinematic angles ϕ_1, ϕ_2, and ϕ_3 parameterize the internal configuration of the particles.

Since transformations from one Jacobi set to another are merely rotation matrices (sometimes combined with an inversion), the democratic parameterization can always be written in the same form for any given Jacobi coordinate system. For example, the symmetry coordinates (Eq. 6.4) can be transformed into the second set interaction coordinates (Eq. 6.12) using the kinematic rotation defined by Eq. 6.15b. If the democratic parameterization defined in Eqs. 6.23 and 6.25 is used, this transformation reads

$$\begin{aligned} \bar{\varrho}^{i2} &= \bar{D}\left(\alpha, \beta, \gamma\right) \bar{\Pi} \tilde{D}\left(\phi_1, \phi_2, \phi_3\right) \bar{U}_{s \to i2}, \\ &= \bar{D}\left(\alpha, \beta, \gamma\right) \bar{\Pi} \tilde{D}\left(\phi_1', \phi_2', \phi_3'\right) \end{aligned}$$

where I have used the fact that the product of two rotations in 3D is itself a rotation. From this it is clear that within a given type of Jacobi coordinate (H-type or K-type), all coalescence points are equally well described. This is an important feature as it does not appear in Delve's type coordinates, which are strongly dependent on which Jacobi

tree is used to define them. For the purposes of this paper, to make symmetrization of the wave function easier, we will always define the body fixed coordinates in terms of the symmetry Jacobi system $\bar{\varrho}^s$.

Putting this all together, the body-fixed Jacobi vectors in terms of the internal hyperangles can be defined:

$$
\begin{aligned}
\rho^s_{1x} &= \frac{R}{\sqrt{3}} \cos\Theta_1 \left(\cos\phi_1 \cos\phi_2 \cos\phi_3 - \sin\phi_1 \sin\phi_3\right), \\
\rho^s_{1y} &= \frac{R}{\sqrt{3}} \sqrt{\sin^2\Theta_1 \sin^2\Theta_2 + \cos^2\Theta_1} \left(\sin\phi_1 \cos\phi_2 \cos\phi_3 + \cos\phi_1 \sin\phi_3\right), \\
\rho^s_{1z} &= \frac{-R}{\sqrt{3}} \sqrt{\sin^2\Theta_1 \cos^2\Theta_2 + \cos^2\Theta_1} \sin\phi_2 \cos\phi_3, \\
\rho^s_{2x} &= \frac{-R}{\sqrt{3}} \cos\Theta_1 \left(\cos\phi_1 \cos\phi_2 \sin\phi_3 + \sin\phi_1 \cos\phi_3\right), \\
\rho^s_{2y} &= \frac{-R}{\sqrt{3}} \sqrt{\sin^2\Theta_1 \sin^2\Theta_2 + \cos^2\Theta_1} \left(\sin\phi_1 \cos\phi_2 \sin\phi_3 - \cos\phi_1 \cos\phi_3\right), \\
\rho^s_{2z} &= \frac{R}{\sqrt{3}} \sqrt{\sin^2\Theta_1 \cos^2\Theta_2 + \cos^2\Theta_1} \sin\phi_2 \sin\phi_3, \\
\rho^s_{3x} &= \frac{R}{\sqrt{3}} \cos\Theta_1 \cos\phi_1 \sin\phi_2, \\
\rho^s_{3y} &= \frac{R}{\sqrt{3}} \sqrt{\sin^2\Theta_1 \sin^2\Theta_2 + \cos^2\Theta_1} \sin\phi_1 \sin\phi_2, \\
\rho^s_{3z} &= \frac{R}{\sqrt{3}} \sqrt{\sin^2\Theta_1 \cos^2\Theta_2 + \cos^2\Theta_1} \cos\phi_2, \\
&0 \leq \Theta_1 \leq \pi; 0 \leq \Theta_2 \leq \frac{\pi}{4}, \\
&0 \leq \phi_1, \phi_2, \phi_3 \leq \pi.
\end{aligned}
\tag{6.28}
$$

The restriction on the range of the internal hyperangles is to avoid double counting configurations and allows for configurations of different chirality .

By moving into democratic coordinates, the dimensionality of the four-body problem can be decreased from 9 to 6, but, as with many simplifications, there is a cost.

This cost comes in the form of the differential volume element $d\Omega$ [125]:

$$d\Omega = (d\alpha \sin\beta d\beta d\gamma)\, \frac{\sqrt{3}\cos^3\Theta_2 \sin^3\Theta_2 \cos 2\Theta_2 \sin^9\Theta_1}{\left[\left(\cos^2\Theta_2 + 3\sin^2\Theta_1\cos^2\Theta_2\right)\left(\cos^2\Theta_2 + 3\sin^2\Theta_1\sin^2\Theta_2\right)\right]^{1/2}} \tag{6.29}$$

$$\times\, d\Theta_1 d\Theta_2 d\phi_1 \sin\phi_2 d\phi_2 d\phi_3.$$

The first factor is purely from the Euler angle rotation and will always yield a factor of $8\pi^2$ for functions that are independent of α, β and γ.

Another price that is paid using democratic coordinates comes in the form of the hyperangular momentum operator, Λ^2. In terms of the democratic hyperangles, Λ^2 is quite complex and can be found in Ref. [125]:

$$\begin{aligned}
\Lambda^2 = &-\Delta\left(\Theta_1,\Theta_2\right) + 2\mu R^2 \left\{ \frac{I_1}{2\left(I_2 - I_3\right)^2}\left(L_1^2 + J_1^2\right)\right. \\
&+ \frac{I_2}{2\left(I_1 - I_3\right)^2}\left(L_2^2 + J_2^2\right) + \frac{I_3}{2\left(I_1 - I_2\right)^2}\left(L_3^2 + J_3^2\right) \\
&+ \frac{2\left[I_1^2 - \left(I_2 - I_3\right)^2\right]^{1/2}}{\left(I_2 - I_3\right)^2} L_1 J_1 \\
&+ \frac{2\left[I_2^2 - \left(I_1 - I_3\right)^2\right]^{1/2}}{\left(I_1 - I_3\right)^2} L_2 J_2 \\
&\left. + \frac{2\left[I_3^2 - \left(I_1 - I_2\right)^2\right]^{1/2}}{\left(I_1 - I_2\right)^2} L_3 J_3 \right\},
\end{aligned}$$

where $\vec{J}$ is the total angular momentum operator, and

$$\begin{aligned}
\Delta\left(\Theta_1,\Theta_2\right) = &\frac{1}{\sin^7\Theta_1}\frac{\partial}{\partial\Theta_1}\sin^7\Theta_1\frac{\partial}{\partial\Theta_1} + \frac{2}{\sin^2\Theta_1}\left[\frac{\partial^2}{\partial\Theta_2^2} + \cot\Theta_1\left(\frac{4}{\sin^2 2\Theta_2} - 1\right)\frac{\partial}{\partial\Theta_1}\right] \\
&+ \frac{4}{\sin^2\Theta_1}\left\{\frac{1}{4\sin 4\Theta_2}\frac{\partial}{\partial\Theta_2}\sin 4\Theta_2\frac{\partial}{\partial\Theta_2} + \frac{2}{3}\cot^2\Theta_1\left[\frac{1 + 3\cos^2 2\Theta_2}{\sin^2 2\Theta_2}\right.\right. \\
&\left.\left. \times \left(\frac{1}{4}\frac{\partial^2}{\partial\Theta_2^2} + \frac{\cot 2\Theta_2}{2}\frac{\partial}{\partial\Theta_2}\right) - \frac{1}{\sin 4\theta_2}\frac{\partial}{\partial\Theta_2}\right] + \cot\Theta_1\cot 2\Theta_2\frac{\partial}{\partial\Theta_2}\frac{\partial}{\partial\Theta_2}\right\}.
\end{aligned}$$

Terms in J_i^2 are centrifugal contributions, terms in $L_i J_i$ are Coriolis contributions and

terms in L_i^2 are contributions from internal kinematic angular momentum with

$$\vec{L} = i\hbar \begin{bmatrix} \sin\phi_1 \cot\phi_2 & \cos\phi_1 & -\dfrac{\sin\phi_1}{\cos\phi_2} \\ \cos\phi_1 \cot\phi_2 & -\sin\phi_1 & -\dfrac{\sin\phi_1}{\sin\phi_2} \\ 1 & 0 & 0 \end{bmatrix} \begin{bmatrix} \dfrac{\partial}{\partial\phi_1} \\ \dfrac{\partial}{\partial\phi_2} \\ \dfrac{\partial}{\partial\phi_3} \end{bmatrix}.$$

Fortunately, the methods for evaluating matrix elements in what follows will not directly require this form of the hyperangular momentum, but it is included here for completeness.

The final element needed from the democratic coordinates is the inter-particle spacing. The ability to define these will be necessary to describe pairwise interactions and correlations. Using Eqs. 6.2, 6.14 and 6.25,

$$|\vec{r}_{12}|^2 = \sqrt{\frac{\mu}{\mu_{12}}} \left[\left(\bar{\varrho}^s_{bf} \bar{U}_{s\to i1} \right)^\dagger \left(\bar{\varrho}^s_{bf} \bar{U}_{s\to i1} \right) \right]_{11}, \tag{6.30}$$

$$|\vec{r}_{13}|^2 = \sqrt{\frac{\mu}{\mu_{13}}} \left[\bar{\varrho}^{s\dagger}_{bf} \bar{\varrho}^s_{bf} \right]_{11}, \tag{6.31}$$

$$|\vec{r}_{14}|^2 = \sqrt{\frac{\mu}{\mu_{14}}} \left[\left(\bar{\varrho}^s_{bf} \bar{U}_{s\to i2} \right)^\dagger \left(\bar{\varrho}^s_{bf} \bar{U}_{s\to i2} \right) \right]_{11}, \tag{6.32}$$

$$|\vec{r}_{23}|^2 = \sqrt{\frac{\mu}{\mu_{23}}} \left[\left(\bar{\varrho}^s_{bf} \bar{U}_{s\to i2} \right)^\dagger \left(\bar{\varrho}^s_{bf} \bar{U}_{s\to i2} \right) \right]_{22}, \tag{6.33}$$

$$|\vec{r}_{24}|^2 = \sqrt{\frac{\mu}{\mu_{24}}} \left[\bar{\varrho}^{s\dagger}_{bf} \bar{\varrho}^s_{bf} \right]_{22}, \tag{6.34}$$

$$|\vec{r}_{34}|^2 = \sqrt{\frac{\mu}{\mu_{23}}} \left[\left(\bar{\varrho}^s_{bf} \bar{U}_{s\to i1} \right)^\dagger \left(\bar{\varrho}^s_{bf} \bar{U}_{s\to i1} \right) \right]_{22}, \tag{6.35}$$

where $[\,]_{ij}$ indicates the ijth element of a matrix. In this equation, only the body fixed Jacobi coordinates from Eq. 6.25 are used. This is because the unitary Euler rotation used to rotate into the body fixed frame is the same for all Jacobi coordinates canceling out the $\{\alpha, \beta, \gamma\}$ dependence in the inter-particle spacings.

Figure 6.3 shows the surfaces in $\{\phi_1, \phi_2, \phi_3\}$ for constant r_{ij} in a planar configuration for $\Theta_2 = \pi/4, \pi/6$, and $\pi/12$ for equal mass particles. The ϕ_1 coordinate axis has been transformed to $\phi_1 - \pi\Theta(\phi_1 - \pi/2)$, where $\Theta(x)$ is the unit step function, to emphasize the symmetry of the surfaces. The red surfaces correspond to the interact-

ing particles in the four-fermion system (r_{12}, r_{14}, r_{23} and r_{34}) while the blue surfaces correspond to the identical fermions (r_{13} and r_{24}). The identical particle surfaces surround a coalescence point that must be a Pauli exclusion node in the final four-body wave function. The simple nature of these coalescence points makes clear the reason for choosing to base the democratic coordinates on the symmetry Jacobi vectors. The red surfaces will play an important role in the pairwise interaction as these surfaces outline the valleys of the potential. As the system becomes more linear (Θ_2 becomes smaller) it can be seen that the surfaces become broader in the ϕ_1 direction. In fact, when $\Theta_2 = 0$ (in perfectly linear configurations) these surfaces become independent of ϕ_1.

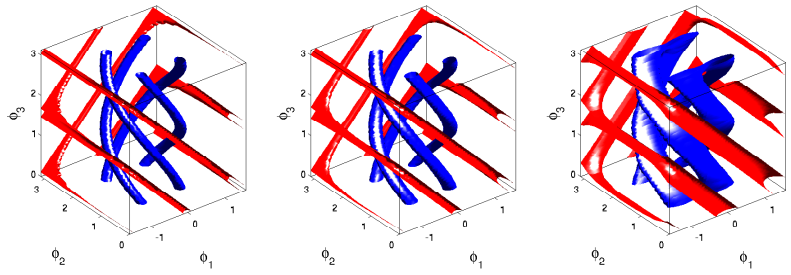

Figure 6.3: Surfaces surrounding the coalescence points in the body-fixed democratic coordinates are shown for $\theta_1 = \pi/2$ and $\theta_2 = \frac{\pi}{4}$ (a), $\frac{\pi}{6}$ (b), and $\frac{\pi}{12}$ (c) respectively. Blue surfaces surround interaction coalescence points while red surfaces surround Pauli exclusion nodes.

6.2 Variational Basis Elements

In the previous section, the 12 dimensional four-body problem was reduced to a 6 dimensional problem for total spatial angular momentum $J = 0$, by removing the center of mass coordinate and rotating into a body-fixed frame. By treating the hyperradius

adiabatically, the remaining 5 dimensional hyperangular partial differential equation,

$$\left[\frac{\Lambda^2}{2\mu R^2} + \sum_{i,j} V\left(r_{ij}\right)\right] \Psi\left(R;\Omega\right) = U\left(R\right)\Psi\left(R;\Omega\right), \tag{6.36}$$

must be solved to obtain the adiabatic channel functions and potentials used in the adiabatic hyperspherical formulation, Eq. 5.1. Here $V\left(r\right)$ is a short-range s-wave pairwise interaction between distinguishable fermions, and the sum runs over all possible pairs of distinguishable fermions. This thesis will only consider a potential whose zero energy s-wave scattering length a is positive and large compared with the range r_0 of the interaction. Further, unless otherwise stated, I assume that the potential can support only a single weakly bound dimer.

The 5 dimensional PDE given by Eq. 6.36 is still too much for most numerical methods, such as B-splines and finite elements. In fact if $40 - 100$ B-splines were used (a common number in three body calculations [26, 128, 112]) in each dimension, there would be $10^8 - 10^9$ basis functions resulting in $10^{11} - 10^{13}$ non-zero matrix elements in a banded matrix. The computational power required for such a calculation is currently beyond reach. Therefore, to proceed a different strategy must be developed.

The strategy used here is not unknown [129]. It involves using a variational basis that diagonalizes the adiabatic Hamiltonian (Eq. 6.36) asymptotically ($R \gg a$) and at small distances ($R \ll r_0$). It is thought that linear combinations of these basis elements will provide a variationally accurate description of the wavefunction in the intermediate regime. In the asymptotic regime, there are three scattering thresholds to consider; a threshold corresponding to weakly bound dimers at twice the dimer binding energy, a threshold consisting of a single weakly bound dimer and two free particles, and finally a threshold consisting of four free particles. In general, it would be necessary to consider another set of thresholds with trimer states (for instance a set of Efimov states for bosons). In the case of fermions though, such considerations are not needed as there are no weakly bound dimers in the $a \gg r_0$ regime. I will proceed by developing the

variational basis based on these threshold behaviors.

6.2.0.3 Dimer-dimer threshold

The asymptotic behavior of the four-body system must include a description of two s-wave dimers separated by a large distance. To incorporate this behavior the variational basis must include a basis function of the form,

$$\Psi_{2+2}(R,\Omega) = \phi_d(r_{12})\,\phi_d(r_{34}), \tag{6.37}$$

where the subscript 2+2 indicates the dimer-dimer nature of this function, and the dimer wavefunction, ϕ_d, is given by the two-body Schrödinger equation

$$\left[-\frac{\hbar^2}{2\mu_{2b}}\frac{\partial^2}{\partial r^2} + V(r)\right] r\phi_d(r) = -E_b r\phi_d(r). \tag{6.38}$$

Here μ_{2b} is the reduced mass of the two distinguishable fermions, and $E_b \approx \hbar^2/2\mu_{2b}a^2$ is the binding energy of the weakly bound dimer. At first glance the right hand side of Eq. 6.37 depends only implicitly on the hyperradius and hyperangles. To make this dependence explicit, Eqs. 6.30 and 6.35 are employed to extract $r_{12}(R,\Omega)$ and $r_{34}(R,\Omega)$. It can also be noted that the basis function, Eq. 6.37, does not respect the symmetry of the identical fermions, i.e. $P_{13}\Phi_{2+2} \neq -\Phi_{2+2}$. The anti-symmetrization of the variational basis will be discussed later in this thesis.

6.2.0.4 Dimer-atom-atom threshold

Another fragmentation possibility that must be incorporated into the asymptotic behavior of the four fermion system is that of an s-wave dimer with two free particles. The description of this configuration at fixed hyperradius is somewhat more difficult than the dimer-dimer configuration. Fortunately, the hyperspherical tree described by Eq. 6.17 can be used with interaction Jacobi coordinates, e.g. $\sigma = i1$, with $l = 2, m = 3$ and $n = 1$. If we assume that particles 1 and 2 are bound in a dimer, then the system

may be thought of as three distinguishable particles consisting of two distinguishable fermions and a dimer. The hyperangles, Ω_{3B}, of this three-body sub-system are then described by the three-body sub-tree seen in Fig. 6.2. Furthermore, the three free particle behavior is merely given by a three-body hyperspherical harmonic, Eq. 6.21. Assembling all of this together, a set of basis functions can be constructed of the form,

$$\Psi^{\lambda_{3B}\mu_{3B}}(R,\Omega) = \phi_d(r_{12})\,\Phi_{\lambda_{3B}\mu_{3B}}\left(\Omega_{3B}^{12}\right), \tag{6.39}$$

where λ_{3B} is the three body hyperangular momentum of the system and ϕ_d is, again, defined by Eq. 6.38. Here the superscript 12 in Ω_{3B}^{12} indicates that the third particle in the three body subsystem is a dimer made from particles 1 and 2. Further, for notational simplicity, μ_{3B} has been used to denote the set of quantum numbers, $\{l_2, l_3, m_2, m_3\}$, which enumerate the degenerate states for each λ_{3B}.

So far the basis function defined by Eq. 6.39 can easily be written in Delve's coordinates. Unfortunately, this function is not written in a way that uses the total angular momentum L of the system as a good quantum number. To get around this we must couple the angular momenta corresponding to the interaction Jacobi coordinates $i1$ to total angular momentum $L = 0$. The angular momentum of the dimer is by definition zero and all that remains is to restrict the angular momentum of the three-body subsystem to zero. This can be achieved by recognizing that the angular momentum of the individual Jacobi vectors are good quantum numbers in the hyperspherical harmonics defined by Eq. 6.21, meaning that we may proceed by normal Clebsch-Gordan angular momentum coupling, i.e.

$$\Psi_{2+1+1}^{\lambda_{3B}l_1l_2}(R,\Omega) = \phi_d(r_{12}) \sum_{m_2=-l_2}^{l_2} \sum_{m_3=-l_3}^{l_3} \langle l_2 m_2 l_3 m_3 | 00\rangle\, \Phi_{\lambda_{3B}\mu_{3B}}\left(\Omega_{3B}^{12}\right), \tag{6.40}$$

where $\langle l_2 m_2 l_3 m_3 | LM\rangle$ is a Clebsch-Gordan coefficient, and l_2 (l_3) is the angular momentum quantum number associated with $\vec{\rho}_2^{\,i1}$ ($\vec{\rho}_3^{\,i1}$) from the interaction Jacobi coordinates defined in Eqs. 6.11. Now with the total angular momentum set to $L = 0$, there can be

no Euler angle dependence in the total wavefunction. The Delve's coordinates may then be defined for this system using Eq. 6.17. The Delve's hyperangles can then be written in terms of the democratic coordinates without including the Euler angle dependence.

6.2.0.5 Four free particles

The final asymptotic threshold that must be considered is that of four free particles. Using Delve's coordinates, this behavior is already described by the four-body hyperspherical harmonics given by Eq. 6.20, i.e.

$$\begin{aligned}\Phi^{(4b)}_{\lambda\mu}(\Omega) =& N^{33}_{l_l l_m \lambda_{l,m}} N^{63}_{\lambda_{l,m} l_n} \sin^{\lambda_{l,m}}(\alpha_{lm,n}) \cos^{l_n}(\alpha_{lm,n}) P^{\lambda_{l,m}+5/2, l_n+1}_{(\lambda-\lambda_{l,m}-l_n)/2}(\cos 2\alpha_{lm,n}) \\ & \times N^{\lambda_{l,m}}_{l_l,l_m} \sin^{l_l}(\alpha_{l,m}) \cos^{l_m}(\alpha_{l,m}) P^{l_l+1, l_m+1}_{(\lambda_{l,m}-l_l-l_m)/2}(\cos 2\alpha_{l,m}) \\ & \times Y_{l_l m_l}(\omega_l) Y_{l_m m_m}(\omega_m) Y_{l_n m_n}(\omega_n),\end{aligned}$$

where μ has again been used to denote the set of quantum numbers $\{\lambda_{12}, l_1, l_2, l_3, m_1, m_2, m_3\}$ that enumerate the degenerate states for each λ. Here l_i is the spatial angular momentum quantum number associated with the Jacobi vector $\vec{\rho}^{\sigma}_i$ with z-projection m_i, and λ_{12} is the sub-hyperangular momentum quantum number associated with the sub-hyperangular tree in Fig. 6.2.

The choice of quantum numbers here does not give the total angular momentum of the four particle system as a good quantum number. To accomplish this, the three angular momenta of the Jacobi vectors must be coupled to a total momentum $L = 0$. This gives a variational basis element of the form

$$\begin{aligned}\Psi^{\lambda\lambda_{12} l_1 l_2 l_3}_{1+1+1+1}(\Omega) = & \sum_{M_{12}=-L_{12}}^{L_{12}} \sum_{m_3=-l_3}^{l_3} \sum_{m_2=-l_2}^{l_2} \sum_{m_1=-l_1}^{l_1} \langle L_{12} M_{12} l_3 m_3 | 00 \rangle \\ & \times \langle l_1 m_1 l_2 m_2 | L_{12} M_{12} \rangle \Phi^{(4b)}_{\lambda\mu}(\Omega).\end{aligned} \tag{6.41}$$

Now that the total angular momentum is set to $L = 0$ the same procedure used for the $\Psi^{\lambda_{3B} l_1 l_2}_{2+1+1}$ basis functions may be employed. However, this time the hyperangular

parameterization is defined using the symmetry Jacobi coordinates in Eqs. 6.4. As there is no dependence on the Euler angles, the Jacobi coordinates may then be defined in the body fixed frame given by Eqs. 6.28.

6.2.1 Symmetrization

The definition of the basis functions developed in the previous subsection do not include the fermionic symmetry of the four particle system in question. Until this point, only the symmetry and the first interaction coordinate systems have been employed. Imposing the $S_2 \times S_2$ symmetry of two sets of two identical fermions will now require us to incorporate the extra interaction coordinate Jacobi set given in Eq. 6.12. First we define the projection operator,

$$\bar{P} = \frac{1}{4}\left(\bar{I} - \bar{P}_{13}\right)\left(\bar{I} - \bar{P}_{24}\right), \tag{6.42}$$

where $\bar{I}$ is the identity operator, and $\bar{P}_{ij}$ is the operator that permutes the coordinates of particles i and j. This operator will project any wavefunctions onto the space of wavefunction that are antisymmetric under exchange of identical fermions. Since I am treating the fermion species as distinguishable, permutations of members of different species is ignored. Using this projection operator on the dimer-dimer basis wave function yields

$$\Psi_{2+2}^{(symm)}\left(R,\Omega\right) = \bar{P}\Psi_{2+2}\left(R,\Omega\right) = \frac{1}{2}\left(\phi_d\left(r_{12}\right)\phi_d\left(r_{34}\right) - \phi_d\left(r_{14}\right)\phi_d\left(r_{23}\right)\right), \tag{6.43}$$

where the inter-particle spacings r_{14} and r_{23} given by Eqs. 6.32 and 6.33.

Imposing the antisymmetric constraints on the dimer plus two free particle basis

functions in Eq. 6.40 yields

$$\begin{aligned}\Psi_{2+1+1}^{(symm)\lambda_{3b}l_2l_3}(R,\Omega) &= \bar{P}\Psi_{2+1+1}^{\lambda_{3b}l_2l_3}(R,\Omega) \\ &= \frac{1}{4}\phi_d(r_{12})\sum_{m_2=-l_2}^{l_2}\sum_{m_3=-l_3}^{l_3}\langle l_2m_2l_3m_3|00\rangle\, Y_{\lambda_{3B}\mu_{3B}}\left(\Omega_{3B}^{12}\right) \\ &\quad - \frac{1}{4}\phi_d(r_{23})\sum_{m_2=-l_2}^{l_2}\sum_{m_3=-l_3}^{l_3}\langle l_2m_2l_3m_3|00\rangle\, Y_{\lambda_{3B}\mu_{3B}}\left(\Omega_{3B}^{23}\right) \\ &\quad - \frac{1}{4}\phi_d(r_{14})\sum_{m_2=-l_2}^{l_2}\sum_{m_3=-l_3}^{l_3}\langle l_2m_2l_3m_3|00\rangle\, Y_{\lambda_{3B}\mu_{3B}}\left(\Omega_{3B}^{14}\right) \\ &\quad + \frac{1}{4}\phi_d(r_{34})\sum_{m_2=-l_2}^{l_2}\sum_{m_3=-l_3}^{l_3}\langle l_2m_2l_3m_3|00\rangle\, Y_{\lambda_{3B}\mu_{3B}}\left(\Omega_{3B}^{34}\right),\end{aligned} \tag{6.44}$$

where Ω_{3B}^{ij} is the set of three-body hyperangles associated with particles i and j in a dimer and the remaining two particles free. The democratic parameterizations for the inter-particle distances from Eqs. 6.30-6.35 can be used in the dimer wavefunction directly. By using the symmetry coordinates, the hyperangles of the four-body system can be divided into a dimer subsystem and a three body subsystem where the third particle is the dimer itself. Using the three-body hyperangles in the three-body harmonic in each term in Eq. 6.44 combined with the kinematic rotations from Eqs. 6.15a and 6.15b, the three body harmonics are then fully described in the hyperangles from symmetry Jacobi coordinates. Since $\Psi_{2+1+1}^{(symm)\lambda_{3b}l_2l_3}$ has been constrained to zero total spatial angular momentum, $L = 0$, the body-fixed parameterization of the Jacobi vectors can be inserted directly without worrying about the Euler angles α, β and γ.

The final set of basis functions that must be symmetrized with respect to identical fermion exchange are the four-body hyperspherical harmonics. Permutation of the identical fermions is accomplished in the symmetry coordinates using Eqs. 6.5-6.10. Using these permutations gives

$$\begin{aligned}P_{13}\Psi_{1+1+1+1}^{\lambda\lambda_{12}l_1l_2l_3}(\Omega) &= (-1)^{l_1}\,\Psi_{1+1+1+1}^{\lambda\lambda_{12}l_1l_2l_3}(\Omega), \\ P_{12}\Psi_{1+1+1+1}^{\lambda\lambda_{12}l_1l_2l_3}(\Omega) &= (-1)^{l_2},\end{aligned}$$

which clearly indicates that the four free particle basis functions are anti-symmetrized by choosing l_1 and l_2 to be odd.

Another symmetry in this system is that of inversion where all Jacobi coordinates are sent to their negatives,

$$\vec{\rho}_j^{\sigma} \rightarrow -\vec{\rho}_j^{\sigma},$$

where $\sigma = s, i1, i2$ and $j = 1, 2, 3$. Following the definitions of the Jacobi coordinates positive inversion symmetry in the 1+1+1+1 basis functions, $\Psi_{1+1+1+1}^{\lambda\lambda_{12}l_1l_2l_3}(\Omega)$, is imposed by choosing λ to be even. The $2+1+1$ basis functions,$\Psi_{2+1+1}^{(symm)\lambda_{3b}l_2l_3}(R,\Omega)$, must already have positive inversion symmetry since $\phi_d(r)$ is an s-wave dimer wavefunction and $l_2 = l_3$ for zero total spatial angular momentum, $L = 0$. The dimer-dimer basis function, $\Psi_{2+2}^{(symm)}(R,\Omega)$, is already symmetric under inversion and does not need further restrictions placed on it.

The final symmetry to be imposed is not quite as obvious as the symmetries discussed so far. By performing a "spin-flip" operation in which the distinguishable species of fermions are exchanged, i.e. $\bar{P}_{12}\bar{P}_{34}$, the Hamiltonian in Eq. 6.1 remains the same. This operation is identical to inverting the two dimers in the dimer-dimer basis function. One can see that $\Psi_{2+2}^{(symm)}$ is unchanged under this operation. Because I will limit myself to dimer-dimer collisions in this chapter, I will only be concerned with basis functions that have this symmetry. This symmetry is imposed on both the $2+1+1$ ($\Psi_{2+1+1}^{(symm)\lambda_{3b}l_2l_3}$) and the $1+1+1+1$ ($\Psi_{1+1+1+1}^{\lambda\lambda_{12}l_1l_2l_3}$) basis functions by the condition

$$l_3 = \text{even}$$

for the $\Psi_{1+1+1+1}^{\lambda\lambda_{12}l_1l_2l_3}$ basis functions.

6.3 Four-fermion potentials and the dimer-dimer wavefunction

Calculating the hyperradial potentials and channel functions using the variational basis is conceptually simple. All that is required are matrix elements of the hyperangular

part of the full Hamiltonian,

$$H_{ad} = \frac{\hbar^2}{2\mu}\frac{\Lambda^2}{R^2} + \sum_{i,j} V\left(r_{ij}\right),$$

where the sum runs over all interacting pairs of distinguishable fermions. In the previous sections, the specific two-body interaction was kept general. All that was required was a weakly bound dimer state and a positive scattering length much larger than the range of the interaction. At this point I choose the so called Posch-Teller potential,

$$V\left(r\right) = -\frac{U_0}{\cosh^2\left(r/r_0\right)}, \tag{6.45}$$

where r_0 is the range of the interaction. Unless otherwise stated U_0 is tuned so that $V\left(r\right)$ gives the appropriate scattering length with only a single bound state. This potential is chosen because the bound state wavefunctions and binding energies are known analytically [130], but any two-body interaction can be used with interpolated bound state wavefunctions and numerically obtained energies.

Using the variational basis results in a generalized eigenvalue problem,

$$\bar{H}\left(R\right)\vec{x}_\nu\left(R\right) = U_\nu\left(R\right)\bar{S}\left(R\right)\vec{x}_\nu\left(R\right) \tag{6.46}$$

where $U_\nu\left(R\right)$ is the νth adiabatic hyperradial potential, and $\vec{x}_\nu$ is the channel function expansion in the variational basis. The matrix elements of $\bar{H}$ are given by matrix elements of the adiabatic Hamiltonian at fixed hyperradius,

$$\bar{H}_{nm} = \left\langle \Psi_n \left| H_{ad} \right| \Psi_m \right\rangle.$$

Because the variational basis is not orthogonal, an overlap matrix, $\bar{S}$, appears in this matrix equation. While the method employed here is conceptually simple, the actual calculation of the matrix elements is numerically difficult. For instance the valleys in the hyperangular potential surface, $\sum_{i,j} V\left(r_{ij}\right)$, become localized in the hyperangular space for large hyperradius. Further, examination of Fig. 6.3 shows that these coalescence points have a complex structure in the five dimensional body-fixed hyperangular space.

To accurately calculate the matrix elements in Eq. 6.46 numerically, a large number of integration points must be placed within these valleys. Calculation of these matrix elements is in fact the time limiting step in this treatment with each interaction matrix element taking approximately 0.5 cpu hours on a modern computer.

Calculation of the non-adiabatic matrices, $\bar{P}$ and $\bar{Q}$, is done directly through numerical differentiation of the channel functions,

$$P_{\nu\nu'} = \left\langle \Phi_\nu\left(R;\Omega\right) | \frac{\partial}{\partial R} \Phi_{\nu'}\left(R;\Omega\right) \right\rangle$$
$$Q_{\nu\nu'} = \left\langle \Phi_\nu\left(R;\Omega\right) | \frac{\partial^2}{\partial R^2} \Phi_{\nu'}\left(R;\Omega\right) \right\rangle$$

where $\Phi_\nu\left(R;\Omega\right)$ is the νth hyperangular channel function that results from solving Eq. 6.46.

With all of these complications in mind the adiabatic potential can be found approximately. Figure 6.4 shows the full set of hyperradial potentials including the diagonal non-adiabatic correction (solid curves) calculated using 8 variational basis elements, one $2+2$ element, four $2+1+1$ elements, and three $1+1+1+1$ elements. Also shown are the expectation values of the basis elements themselves (dashed curves). All calculations here are for $a = 100$. It is clear that the lowest potential converges very quickly with respect to the number of variational basis elements used. The lowest potentials converge well when only a few variational basis elements are included, while the higher potentials are somewhat suspect. The adiabatic potentials become universal for large scattering lengths. In other words, the potentials look the same when scaled by the scattering length and the binding energy. Comparison with a correlated Gaussian method of calculating these potentials shows excellent agreement in the lowest dimer-dimer potential with reasonable agreement in the lowest few dimer-atom-atom potentials [8].

In Fig. 6.4 the lowest hyperradial adiabatic potential approaches twice the binding energy of a single dimer indicating that this channel corresponds to the dimer-dimer

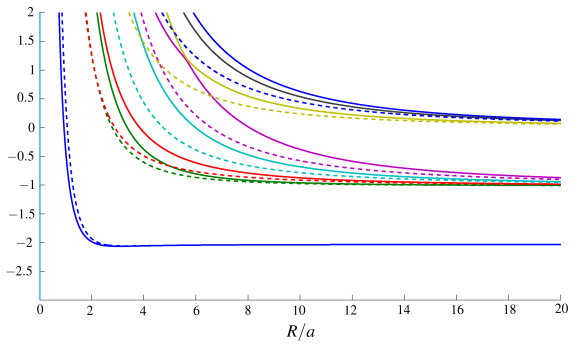

Figure 6.4: The hyperradial potentials are shown (solid lines) calculated for $a = 100$ as a function of R/a. Also shown are the expectation values of the variational basis elements used (dashed curves).

potential. Examining this potential further, one can see that at hyperradii less than the scattering length, $R < a$, the dimer-dimer potential becomes strongly repulsive. This can almost be thought of as hard wall scattering giving a dimer-dimer scattering length, a_{dd}, similar in magnitude to the two-body scattering length,

$$a_{dd} \sim 3.5a. \tag{6.47}$$

Higher potential curves are seen to approach the dimer binding energy, indicating that these potentials correspond to a dimer with two free particles in the large R limit. As the scattering length becomes much larger than the range of potentials, the potential becomes universal in the range of $r_0 \ll R \ll a$:

$$U(R) \to \frac{\hbar^2}{2\mu}\frac{p_0^2 - 1/4}{R^2}, \tag{6.48}$$

where $p_0 = 2.55$. This universal potential was extracted by von Stecher, Greene, and Blume [131, 58] by examining the behavior of the ground state energy of four fermions in a trap in the unitarity limit.

Figure 6.5 shows the coupling strengths, $\hbar^2 P_{nm}^2 / \{2\mu [(U_m(R) - U_n(R))]\}$, between the dimer-dimer potential and the lowest three dimer-atom-atom adiabatic potentials for a two-body scattering length of $a = 100r_0$. In each case the coupling

strength peaks strongly near the short range region, $R \sim r_0$, and near the scattering length, $R \sim a$, and then falls off quickly in the large R limit. This behavior indicates that recombination from a state consisting of a deeply bound dimer and two free particles to the dimer-dimer state occurs mainly at hyperradii near a. Looking at Fig. 6.5 one might think that a recombination path that occurs at small R, $R \sim r_0$, will also contribute, but the strong repulsion between $R \sim r_0$ and $R \sim a$ in the dimer-atom-atom potentials, shown in Fig. 6.4, suppresses this pathway.

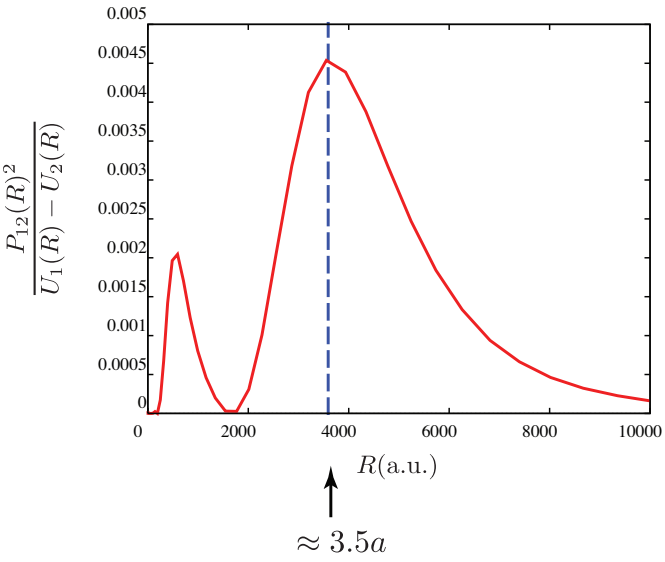

Figure 6.5: The coupling strength between the dimer-dimer potential and the lowest dimer-atom-atom potential is shown as a function of R/a. The blue dashed line shows the position of the coupling peak at $R/a \approx 3.5$.

Figure 6.6 shows an isosurface of the hyperangular probability density in the configurational angles $\{\phi_1, \phi_2, \phi_3\}$ after integrating out Θ_1 and Θ_2 at a fixed hyperradius of $R = 0.41a$. The ϕ_1 axis has been modified here by shifting the region $\pi/2 \leq \phi_1 \leq \pi$ to emphasize the symmetry of the system. Each cobra-like surface corresponds to a peak in the four-body probability density. By examining Fig. 6.3, it is clear that the spine of each cobra corresponds to an interaction coalescence point. For each choice of $\{\phi_1, \phi_2, \phi_3\}$, the maximum of the probability density in Θ_1 and Θ_2 is given in a planar

geometry, $\Theta_1 = \pi/2$. The coloring of each cobra indicates the value of Θ_2 at which the maximum occurs. Darker colors indicate a more linear geometry, i.e. Θ_2 is closer to 0. Figure 6.7 shows the same plot for the $2 + 2$ basis function only. Comparing Figs. 6.6 and 6.7 it is clear that the added variational basis elements are critical for describing the full dimer-dimer channel function for hyperradii less than the scattering length. Figure 6.8 shows the cobra isosurface of Fig 6.6 in a slightly more picturesque setting. No extra physical insight is gained from showing this, but it does look very nice, though some have suggested a palm tree would be a good addition [132].

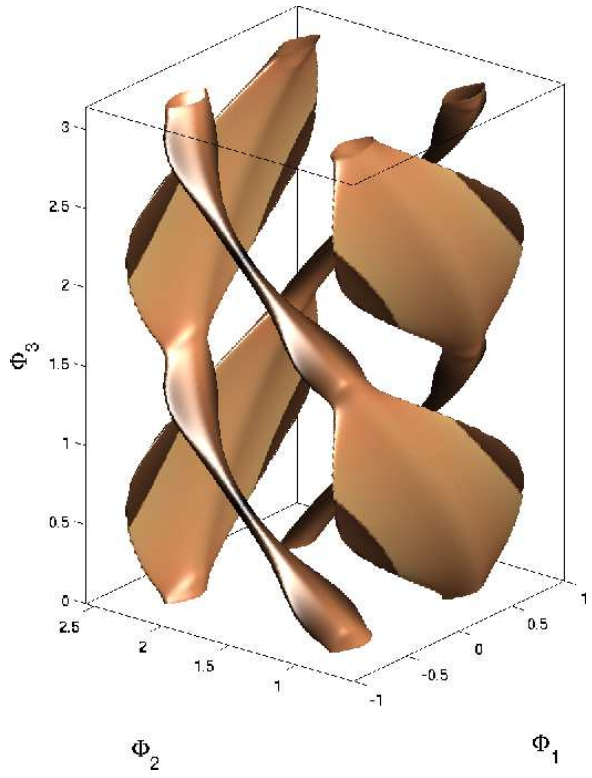

Figure 6.6: An isosurface of the dimer-dimer probability density is shown. The surfaces are found by integrating the total probability over θ_1 and θ_2 and plotting with respect to the remaining democratic angles (ϕ_1, ϕ_2, ϕ_3). The peak probability always occurs in planar symmetry, $\theta_1 = \pi/2$. The coloring (light to dark) indicate the value of θ_2 at the peak.

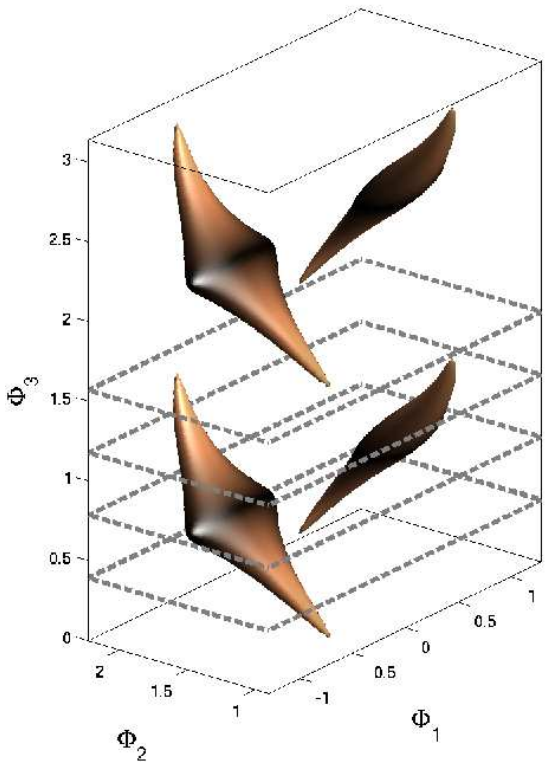

Figure 6.7: The same as Fig. 6.6, but only using the $2+2$ basis function. The dashed gray lines are purely for perspective.

6.4 Dimer-Dimer Scattering

With the hyperradial potentials and non-adiabatic couplings in hand, low energy dimer-dimer scattering properties can be examined. The zero-energy dimer-dimer scattering length in the large two-body scattering length limit was first calculated by Petrov et. al [23] and found to be

$$a_{dd}\,(0) = 0.60\,(2)\,a, \tag{6.49}$$

where the number in the parentheses indicates ± 0.02, the 4% error stated in this work. This prediction has been confirmed using several different theoretical approaches [133, 131, 58].

Using the adiabatic potentials shown in Fig. 6.4 and the resulting non-adiabatic

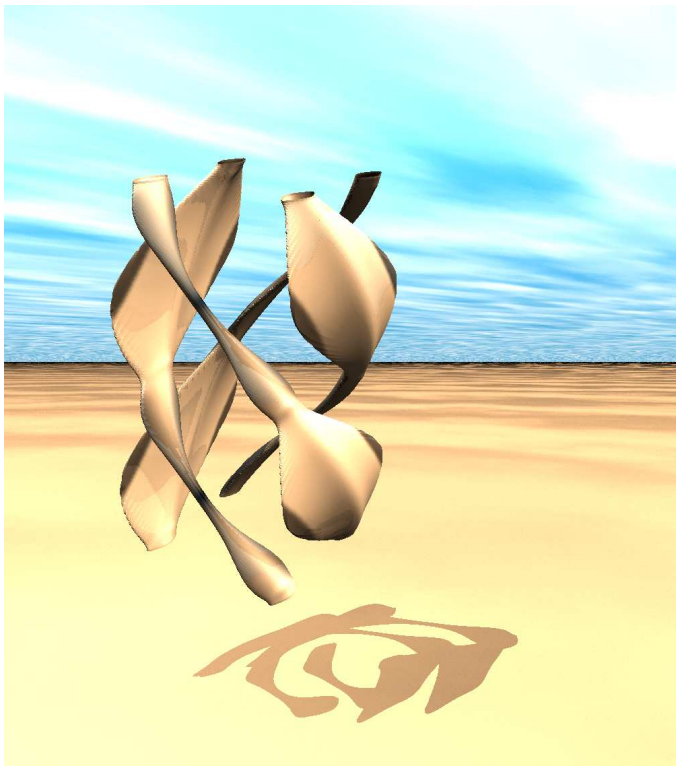

Figure 6.8: The isosurfaces shown here are the same as in Fig. 6.6, but in a pleasing environment.

couplings, the energy dependent dimer-dimer scattering length defined by

$$a_{dd}\left(E_{\mathrm{col}}\right) = \frac{-\tan\delta_{dd}}{k_{dd}} \tag{6.50}$$

can be calculated. Here E_{col} is the collision energy of the two dimers with respect to the dimer-dimer threshold, and δ_{dd} is the s-wave dimer-dimer phase shift. An interesting thing occurs when the collision energy becomes greater than the dimer binding energy. At this point the two dimers collide with enough energy to dissociate one of them. When this happens, the four fermion system leaves in an excited channel causing a loss of flux from the dimer-dimer channel. This process is parameterized by the imaginary part of the dimer-dimer scattering length which will become non-zero when $E_{\mathrm{col}} > E_b$.

Figures 6.9 and 6.10 respectively show the real and imaginary parts of the dimer-dimer scattering length calculated with different numbers of adiabatic channels plotted

as a function of $E_{\rm col}$ in units of the dimer binding energy. Also shown in Fig. 6.9 is the dimer-dimer scattering length calculated from the variational potential that results from using a single variational basis element. It is important to note that the single adiabatic channel calculation and the single basis element calculation are not the same. In the former, the single potential used is the lowest potential resulting from a calculation using multiple basis elements while the latter is the result of using only the $2+2$ variational basis element. Not surprisingly, the scattering length at collision energies found near the binding energy depends strongly on the number of channels used. With just a single channel in use, there is no decay pathway available for the system. As more channels are included the system has more pathways available to fragment into, modifying the high energy behavior.

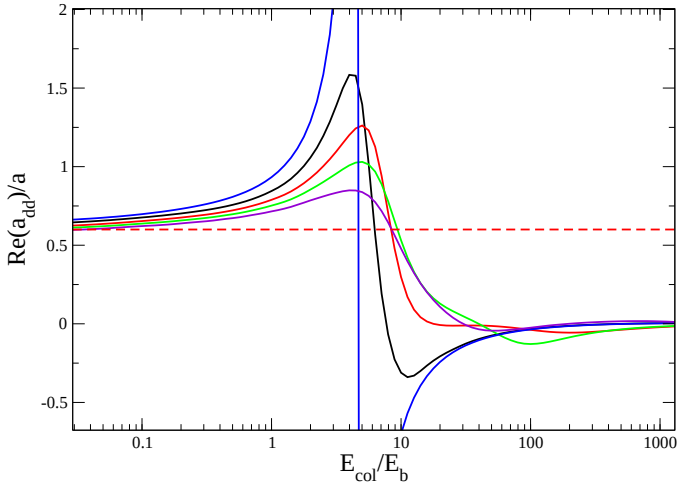

Figure 6.9: The real part of the energy dependent dimer-dimer scattering length is shown in dimensions of a plotted versus the collision energy in units of the binding energy. The calculation if done with one, two, three, four, and five adiabatic channels (blue, black, red, green, and purple curves respectively) from the 8 basis element calculation. The red dashed line shows $a_{dd} = 0.6a$, the prediction of Ref. [6].

What is more surprising is the low energy behavior seen in Fig. 6.9. For a single variational basis element, the dimer-dimer zero energy scattering length is found to be $a_{dd} = 0.72a$, which is already fairly close to the result of Ref. [23], $a_{dd}(0) = 0.6a$. A

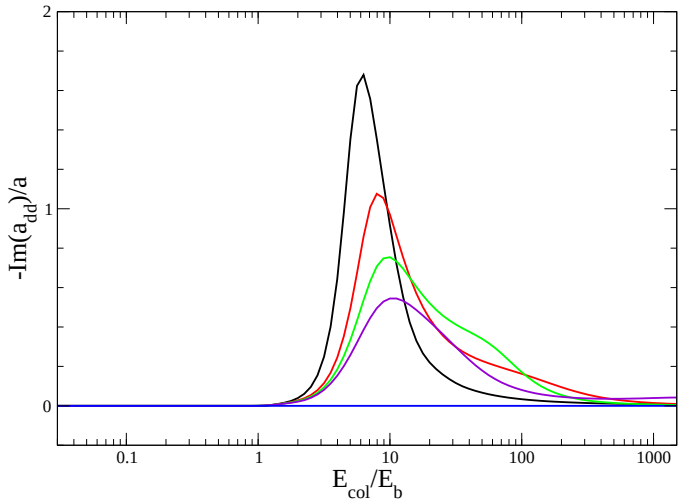

Figure 6.10: The imaginary part of the energy dependent dimer-dimer scattering length is shown in dimensions of a plotted versus the collision energy in units of the binding energy. The calculation if done with one, two, three, four, and five adiabatic channels (blue, black, red, green, and purple curves respectively) from the 8 basis element calculation.

single channel calculation using the dimer-dimer potential and channel function that results from using 5 basis elements improves considerably on this yielding $a_{dd}(0) = 0.64a$, indicating that including correlations describing two free particles at hyperradii less than a gives a significant contribution to the physics of dimer-dimer scattering. It is somewhat unexpected that the single channel calculation is only 8% off of the predicted value. As the scattering energy approaches zero, the higher fragmentation channels become strongly closed but still apparently play a small role in the dimer-dimer scattering process. By including progressively more channels in the scattering calculation the zero-energy dimer-dimer scattering can be extracted for large two body scattering length:

$$a_{dd}(0) = 0.605(5)\,a. \tag{6.51}$$

This result is in agreement with the results of Ref. [131, 58] which found the zero-energy dimer-dimer scattering length to similar accuracy using different methods.

6.4.1 Energy dependence

By examining the low energy behavior of the energy dependent dimer-dimer scattering length, the effective range can be extracted. The two dimers "see" each other when their wavefunctions are overlapping, i.e. when the hyperradius is approximately equal to the scattering length, $R \sim a$. If one thinks of the effective range of an interaction as proportional to the size of the interaction region, then one would expect the effective range for dimer-dimer scattering to be proportional to the scattering length. By fitting the low energy scattering phase shift to the effective range expansion,

$$k \cot \delta_{dd} = -\frac{1}{a_{dd}(0)} + \frac{1}{2} r_{dd} k^2, \tag{6.52}$$

this intuitive behavior is born out giving an effective range,

$$r_{dd} = 0.13a, \tag{6.53}$$

where a is the two-body scattering length. Figure 6.11 shows both the real and imaginary parts of the energy dependent dimer-dimer scattering length as a function of collision energy in units of the binding energy compared to the effective range expansion, Eq. 6.52. This clearly shows that, while the low energy behavior of dimer-dimer scattering is well described by the effective range expansion, it is only accurate over a small range of collision energies. In fact, for collision energies larger than the binding energy, $a_{dd}(E_{\rm col})$ actually turns over and decreases as dimer breakup channels become open. Further, when the collision energy is equal to the dimer binding energy, $E_{\rm col} = E_b$, the dimer-dimer scattering length becomes complex, with an imaginary part that parameterizes inelastic processes. These results indicate that both the real and imaginary dimer-dimer scattering lengths are universal functions of the collision energy, i.e. insensitive to the short range nature of the two-body interaction, for scattering lengths much larger than the two-body interaction length scale, r_0. Because very few basis functions were used in these calculations, the results at higher energies, $E_b \ll E_{\rm col} \ll \hbar^2/mr_0^2$, are

not well converged, though their qualitative nature is expected to persist. Well above the dissociation threshold, oscillations in the real part of the dimer-dimer scattering length can be seen. These oscillations are caused by interference between different scattering paths. As more basis functions are included and the high energy results converge, the large number of available pathways will generally cancel the oscillatory behavior, but the decrease in the real part of the dimer-dimer scattering length should persist.

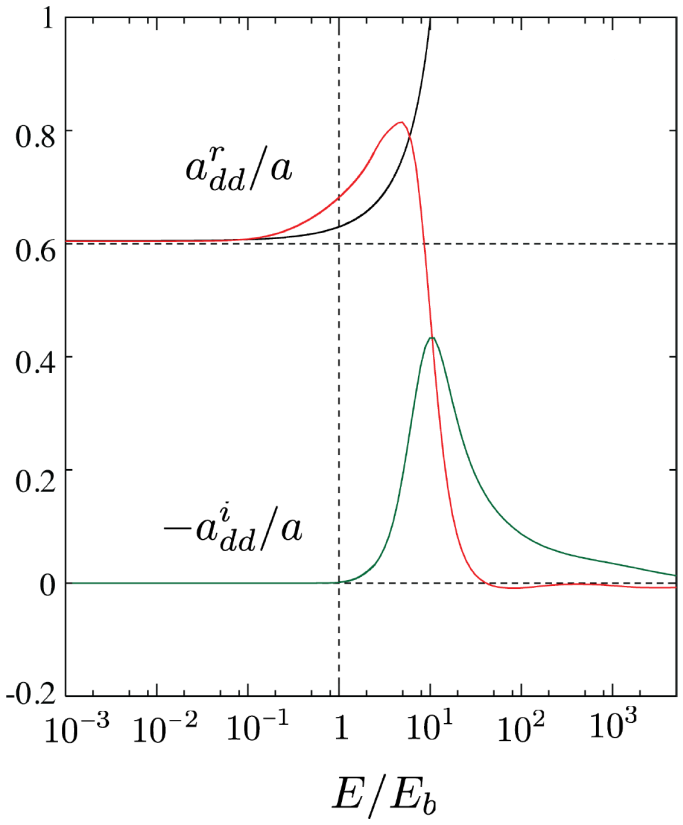

Figure 6.11: The real (red) and imaginary (green) parts of the energy dependent dimer-dimer scattering length is shown in dimensions of a plotted versus the collision energy in units of the binding energy. Also shown is the energy dependent scattering length using the effective range expansion. Figure from Ref. [7].

An interesting aspect of these results is in the two-body scattering length dependence of the dimer-dimer scattering length at finite collision energy. In the large scattering length limit, the dimer binding energy becomes $E_b \approx \hbar^2/ma^2$, so that as

the scattering length increases the binding energy decreases. At the critical scattering length,

$$a_c = \frac{\hbar}{\sqrt{mE_{\rm col}}},$$

the collision energy is the same as the binding energy. As a result, Fig. 6.11 shows that one expects the real part of the dimer-dimer scattering length to turn over and remain finite for all two-body scattering lengths. This behavior is demonstrated in Fig. 6.12 which shows the real part of the dimer-dimer scattering length at several fixed collision energies compared to the zero-energy result, $a_{dd}\,(0) = 0.6a$. The scattering length were fixed by setting the range of the interaction to be approximately the Van der Waals length of ^{40}K, $r_0 \approx 100$ a.u. Another aspect of the finite collision energy behavior is that at large scattering length, the dimer-atom-atom channels become open, and dimer dissociation is allowed. This leads to the idea that near unitarity the Fermi gas might be thought of as a coherent mixture of atoms and weakly bound dimers.

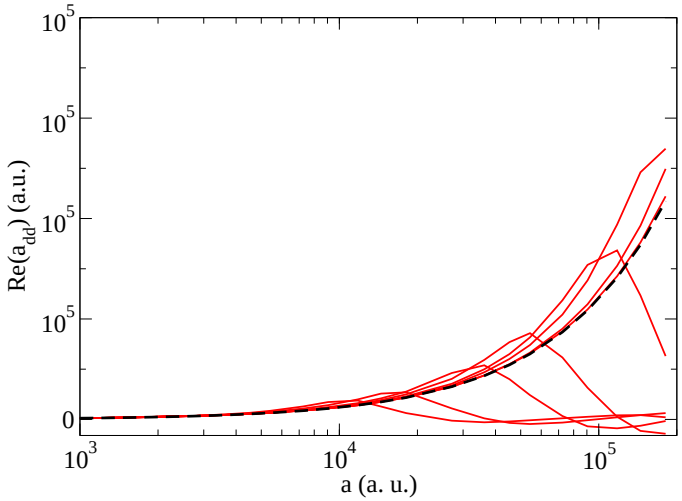

Figure 6.12: The real part of the energy dependent dimer-dimer scattering length is shown plotted as a function of the two-body scattering length in atomic units is shown calculated for several collision energies; $E_{\rm col}/k_b$ =250nK,100nK, 25nK, 10nK, 2.5nK, 1nK, 10^{-1}nK, and 10^{-2}nK. Also shown is the zero energy prediction (black dashed curve). Figure from Ref. [7].

6.5 Dimer-dimer relaxation

A significant loss process in an ultracold gas of bosonic dimers is that of dimer-dimer relaxation in which two dimers collide, and in the process one of the dimers relaxes to a deeply bound two-body state. The excess energy is released as kinetic energy and is then enough to eject the remaining fragments from the trap. This process was studied by Petrov, Salomon and Shlyapnikov [23, 6] by assuming that this process is controlled by the probability of three particles being in proximity to one another. With this assumption and the further assumption that the fourth particle is far away and plays no role in the scattering process, they predict that the relaxation rate is suppressed at large two-body scattering lengths with a scaling law, $V_{rel}^{dd} \propto a^{-2.55}$.

In this section I introduce a new method for finding the dimer-dimer relaxation rate based directly on Fermi's golden rule. The key observation in this section is that the final allowed states in the hyperspherical appear as an infinite set of hyperspherical potentials corresponding to a deeply bound dimer with two free atoms. The transition rate to a single one of these states can be described by Fermi's golden rule, i.e.

$$T_p^{\lambda} \propto \left|\left\langle \Psi_{dd}\left(R;\Omega\right)\left|V\left(R,\Omega\right)\right|\Psi_{\lambda}\left(R,\Omega\right)\right\rangle\right|^2. \tag{6.54}$$

Here Ψ_{λ} is the final outgoing state, Ψ_{dd} is the dimer-dimer wavefunction, and $V\left(R,\Omega\right)$ is the sum of the two-body interactions. The evaluation of this matrix element and the sum over the final states is shown in Appendix D. The final result of this analysis is given as an integral over the hyperradius,

$$V_{rel}^{dd} \propto \int \frac{P_{WKB}\left(R\right)\mathcal{F}\left(R\right)}{R\kappa\left(R\right)}\rho\left(R\right)dR \tag{6.55}$$

where $P_{WKB}\left(R\right)$ is the WKB probability of the dimer-dimer wavefunction at hyperradius R, $\kappa\left(R\right)$ is the WKB wavenumber given by

$$\kappa\left(R\right) = \sqrt{\frac{2\mu}{\hbar^2}\left(V_{dd}\left(R\right) + \frac{\hbar^2}{2\mu}\frac{1/4}{R^2} - E_{\mathrm{col}}\right)}. \tag{6.56}$$

In Eq. 6.55 $\rho(R)$ is the nearly constant density of final states, and $\mathcal{F}(R)$ is the probability of finding three particles in near proximity to one another in the dimer-dimer wavefunction at hyperradius R, given by,

$$\mathcal{F}(R) = \langle \Phi_{dd}(R;\Omega) \left| f(R,\Omega) \right| \Phi_{dd}(R;\Omega) \rangle . \tag{6.57}$$

Here Φ_{dd} is the hyperangular dimer-dimer channel function, and $f(R,\Omega)$ is a proximity function that only peaks when three particles are within approximately the range of the two-body interaction of one another.

Equation 6.55 makes physical sense upon closer examination. It says that the rate at which a dimer relaxes to a deeper state is determined, with some extra factors, by the probability that three particles are close enough together that two of them can fall into a deeply bound state and release the extra binding energy to the third particle. Figure 6.13 shows the integrand from Eq. 6.55 for several scattering lengths as a function of the hyperradius in units of the scattering length. This quantity can be interpreted as being proportional to the transition rate per unit hyperradius, i.e. the probability that the transition will occur between R and $R + dR$. The overall transition rate is determined by the nature of the interaction at short range and is not predictable using this method. By examining the relaxation rate as a function of scattering length, a scaling law can be extracted at each fixed hyperradius.

Figure 6.14 shows the relaxation rate per unit hyperradius for several fixed values of R/a as a function of the scattering length, a. The large a behavior in each case appears to follow a scaling law, but the scaling law changes with R/a. This behavior indicates that, contrary to the prediction of Ref. [6], when the integral in Eq. 6.55 is evaluated, the relaxation rate will not be determined by a mere scaling law. By integrating over different hyperradial regions, contribution to the transition rate from different processes can be extracted. For instance, if integral in Eq. 6.55 is performed only over small hyperradii, $R \lesssim 5r_0$, the result is the transition rate due to processes

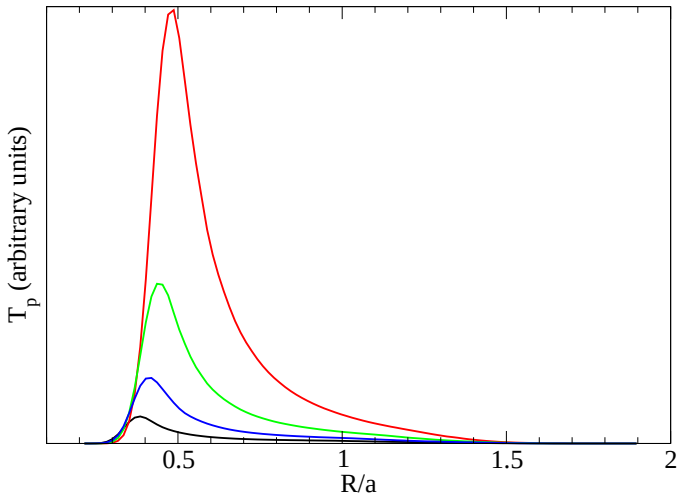

Figure 6.13: The integrand from Eq. 6.55 is shown for $a = 50r_0, 64r_0, 80r_0$, and $100r_0$ as a function of R in units of a.

in which all four particles are in close proximity. If the integral is evaluated over larger hyperradii, $R > 10r_0$, the result is the rate due to three-body processes only.

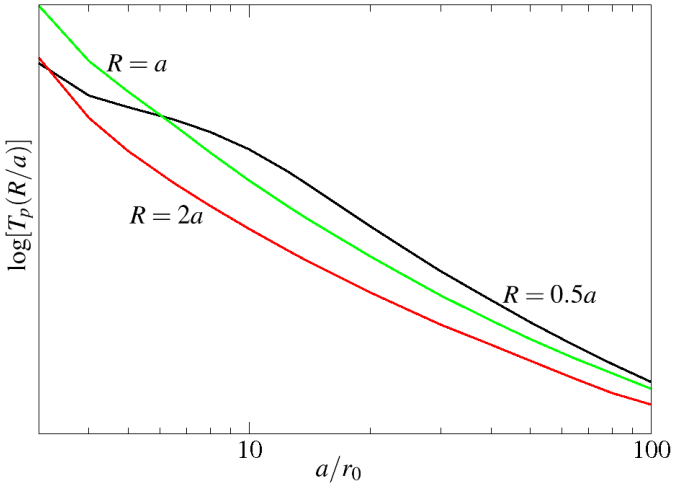

Figure 6.14: The integrand from Eq. 6.55 is shown for various values of R/a as a function of a in units of r_0.

Figure 6.15 shows the the relaxation rate as a function of the scattering length in atomic units as a red solid line. In this result the range of the interaction is set to the van der Walls length of ^{40}K, $r_0 \approx 100$ a.u. Also shown in Fig 6.15 are the

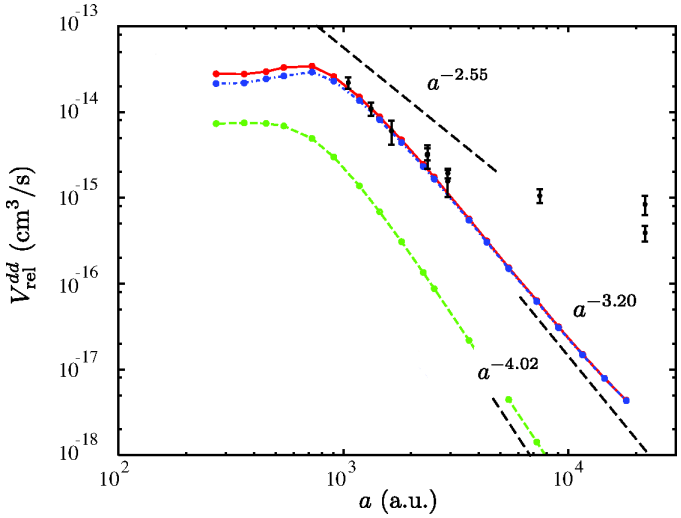

Figure 6.15: The relaxation rate is shown as a function of scattering length (see text). The red curve represents all possible relaxation pathways. The blue dot-dashed curve represents only the contribution to relaxation for processes occurring at $R > 10r_0$. The green dashed line shows the contributions for prosses occurring at $R < 5r_0$. Figure from Ref. [7]

contribution to this relaxation rate due to four-body processes (dashed blue curve), and the contribution to this rate due to three-body processes (dotted green curve). Also shown is the expected scaling law, $V_{rel}^{dd} \propto a^{-4.02}$, for transitions that occur at small hyperradius, $R = 5r_0$. Figure 6.15 also shows the predicted scaling law, $V_{rel}^{dd} \propto a^{-2.55}$, from Ref. [6], and an intermediate scaling law that can be extracted. In this regime, because the hyperradius is small, the probability of three particles being in proximity is near unity, meaning that the transition probability per unit hyperradius is determined by the probability that the system can tunnel through the repulsive potential seen in Fig. 6.4 at $R \lesssim a$. The universal repulsive potential in this regime [8, 7],

$$U(R) = \frac{\hbar^2}{2\mu}\frac{p_0^2 - 1/4}{R^2}, \tag{6.58}$$

$$p_0 = 2.55, \tag{6.59}$$

leads to a scaling law for transitions in the small R regime that behaves as

$$V_{rel}^{dd} \propto a^{1-2p_0} = a^{-4.20}. \tag{6.60}$$

Figure 6.15 also shows the experimentally determined relaxation rates from Ref. [134]. Both the scaling law predicted in Ref. [6] of $a^{-2.55}$ and the prediction using Eq. 6.55 fit the experimental data in the regime for 1000 a.u.$\lesssim a \lesssim$ 4000 a.u.. The experimental data for $a >$ 3000 a.u. are in the regime where the average dimer separation distance is less than the dimer size where the dimer-dimer scattering picture discussed here no longer applies.

Chapter 7

Summary

In this dissertation I have analyzed the effects of few-body physics on many-body systems, and the dynamics that result from fundamental few-body systems. Within the framework of hyperspherical coordinates, complex many dimensional systems can be described by a set of effective coupled 1D Schrödinger equations, allowing all of the intuition and understanding of standard 1D Schrödinger quantum mechanics to be brought to bear on the problem. While obtaining the effective hyperradial potentials is often a significant challenge, once these potentials have been obtained, a variety of complex dynamics can be analyzed such as low energy excitation frequencies in trapped many-body systems and inelastic scattering in few-body systems.

In the first chapters of this thesis I generalized known few-body methods to a many-body system through the use of a variational ansatz wavefunction. While the variational wavefunction used does not allow for complex correlations, it does provide an intuitive picture for the many-fermion system in the form of an effective potential. This approach also provides an initial link between standard methods in few-body systems and the complex world of many-body physics. By tuning the few-body parameters through a Fano-Feshbach resonance the behavior of the degenerate Fermi gas was explored throughout the resonance.

By applying the K-harmonic approximation in Chapter 3, a simple effective potential was extracted which gave the ground state energy and rms size of the gas in good

agreement with those predicted from the Hartree-Fock method. In the case of the bare zero-range Fermi pseudo-potential, the effective potential predicted an unphysical collapse on the negative side of a resonance in the strongly interacting regime. This collapse can be avoided by incorporating a density dependent interaction. Using this interaction the ground state energy is predicted with excellent agreement with the Hartree-Fock prediction, both of which yield the universal constant $\beta = -0.49$. This value of β is larger than the variational prediction from quantum Mote Carlo studies, $\beta = -0.58$, but lower than the β value predicted from a normal degenerate Fermi gas, $\beta = -0.44$. This method does not describe the behavior of the gas on the positive side of the resonance, as neither the interaction or the variational wave function are capable of describing a BEC of dimers. By further extending the K-harmonic method to incorporate multiple internal states, a dynamic instability is predicted in a degenerate Fermi gas with four components. The three-component gas was predicted to be barely stable at unitarity using a density dependent interaction, and by modifying the interaction to fit the two-component gas, the three-component system is predicted to be unstable. These results do not include the possibility of a ground state consisting of trimer states. Further examination, both theoretically and experimentally, is needed to clarify whether the three-component gas will collapse in a manner similar to the Bosenova first, or boil off through inelastic three-body recombination. This question is increasingly pertinent as recent experiments with the three lowest hyperfine states of ^{6}Li are near the predicted density required for collapse.

In the case of an anisotropic trap, the K-harmonic method is difficult to apply. By generalizing the hyperspherical picture to that of the hyper-vectorial method in Chapter 4, the anisotropic nature of the trap is easily incorporated. The ground state energy and rms longitudinal and transverse size of the gas are in perfect agreement with the K-harmonic prediction in an anisotropic trap. However, the low energy excitation frequencies disagree strongly with both previous theoretical predications and with ex-

perimental observations. This is possibly due to the somewhat unphysical assumption of the distribution of oscillator quanta in the variational wavefunction used. It is hoped that this work can provide a starting point for later studies in this system.

In the second half of this dissertation, several fundamental few-body systems were explored in the context of the adiabatic hyperspherical method. This method lends itself well to scattering dynamics by incorporating the various fragmentation channels that can result in few-body systems. By including the non-adiabatic coupling, the qualitative behavior of inelastic scattering was easily found. In Chapter 5 I introduced a novel form of the free-space hyperangular Green's function. When used in a Lippmann-Schwinger equation based approach, this Green's function was shown to yield the same results for the three-body hyperradial potential curves that are found using conceptually different theoretical approaches, such as Faddeev decompositions. The results of this study were then used to predict the scaling behavior of trap-loss recombination events across the three resonances in the three lowest hyperfine states of ^{6}Li. The resulting scaling at higher magnetic fields (834 to1000 gauss) are in agreement with other theoretical predictions, but further experimental investigation is required to explore this system.

The Green's function method was then applied to the complex systems of three bosons with multi-channel two-body interactions leading to the prediction of a new class of Efimov states. While other theoretical treatments have examined this multi-channel system, this is the first prediction of three-body Fano-Feshbach resonances embedded in the three-body continuum due to the presence of a quasistable Efimov state. There are no current experiments looking for these states, but current radio frequency spectroscopy techniques could possibly be used to probe them. Using this method, multiple Efimov states might be seen experimentally for the first time.

Finally, in Chapter 6 I explored the four-fermion problem with large positive scattering lengths. While no specific new method was developed to describe this complex

system, a variety of existing ideas were incorporated in new ways to extract a set of variationally accurate hyperradial potentials. This method gives the zero-energy dimer-dimer scattering length to high precision in good agreement with previous predictions. At higher energies, the energy dependent dimer-dimer scattering length is in agreement with previous effective range expansions but deviates from this prediction at collision energies well below the dimer binding energy. Further, it was shown that at any finite collision energy, the dimer-dimer scattering length will never diverge.

By incorporating the full multi-threshold behavior of the system, inelastic dimer breakup scattering was also incorporated in the form of a complex energy dependent dimer-dimer scattering length. By developing a new Fermi's golden rule based method, the dimer-dimer relaxation rate was also predicted, disagreeing the previous predictions, $V_{rel}^{dd} \propto a^{-2.55}$, that ignored the effects of the presence of a fourth particle in the relaxation process. The predictions given here agree with the experimentally measured behavior in the relevant regime, and explain the agreement of experiment with the previously predicted scaling law through the effects of short-range corrections.

Bibliography

[1] S. T. Rittenhouse, M. J. Cavagnero, J. von Stecher, and C. H. Greene, Phys. Rev. A **74**, 053624 (2006).

[2] S. T. Rittenhouse and C. H. Greene, J. Phys. B **41**, 205302 (2008).

[3] J. von Stecher and C. H. Greene, Phys. Rev. A **75**, 022716 (2007).

[4] M. Bartenstein, A. Altmeyer, S. Riedl, R. Geursen, S. Jochim, C. Chin, J. H. Denschlag, R. Grimm, A. Simoni, E. Tiesinga, et al., Phys. Rev. Lett. **94**, 103201 (2005).

[5] Y. F. Smirnov and K. V. Shitikova, Sov. J. Part. Nucl. **8**, 44 (1977).

[6] D. S. Petrov, C. Salomon, and G. V. Shlyapnikov, Phys. Rev. A **71**, 012708 (2005).

[7] J. P. D'Incao, S. T. Rittenhouse, N. P. Mehta, and C. H. Greene, Phys. Rev. A **79**, 030501 (2009).

[8] J. V. Stecher, Trapped Ultracold Atoms with Tunable Interactions, PhD thesis, University of Colorado, 2008.

[9] M. H. Anderson, J. R. Ensher, M. R. Matthews, C. E. Wieman, and E. A. Cornell, Science **269**, 198 (1995).

[10] C. Bradley, C. Sackett, J. Tollett, and R. Hulet, Phys. Rev. Lett. **75**, 1687 (1995).

[11] K. B. Davis, M. O. Mewes, M. R. Andrews, N. J. Van Druten, D. S. Durfee, D. M. Kurn, and W. Ketterle, Phys. Rev. Lett. **75**, 3969 (1995).

[12] B. DeMarco and D. S. Jin, Science **285**, 1703 (1999).

[13] C. Regal, M. Greiner, and D. Jin, Phys. Rev. Lett. **92**, 40403 (2004).

[14] J. Kinast, S. Hemmer, M. Gehm, A. Turlapov, and J. Thomas, Phys. Rev. Lett. **92**, 150402 (2004).

[15] M. Zwierlein, C. Stan, C. Schunck, S. Raupach, A. Kerman, and W. Ketterle, Phys. Rev. Lett. **92**, 120403 (2004).

[16] M. Bartenstein, A. Altmeyer, S. Riedl, S. Jochim, C. Chin, J. Denschlag, and R. Grimm, Phys. Rev. Lett. **92**, 120401 (2004).

[17] T. Bourdel, L. Khaykovich, J. Cubizolles, J. Zhang, F. Chevy, M. Teichmann, L. Tarruell, S. Kokkelmans, and C. Salomon, Phys. Rev. Lett. **93**, 50401 (2004).

[18] U. Fano, Nuovo Cimento **12**, 154 (1935).

[19] H. Feshbach, Ann. of Phys. **5**, 357 (1958).

[20] A. J. Leggett, J. Phys. C (Paris) **41**, 7 (1980).

[21] M. Drechsler and W. Zwerger, Ann. Phys. (Germany) **504** (1992).

[22] M. Holland, S. Kokkelmans, M. L. Chiofalo, and R. Walser, Phys. Rev. Lett. **87**, 120406 (2001).

[23] D. S. Petrov, C. Salomon, and G. V. Shlyapnikov, Phys. Rev. Lett. **93**, 90404 (2004).

[24] S. Y. Chang, V. R. Pandharipande, J. Carlson, and K. E. Schmidt, Phys. Rev. A **70**, 43602 (2004).

[25] H. Heiselberg, Phys. Rev. A **63**, 43606 (2001).

[26] B. D. Esry, C. H. Greene, and J. P. Burke, Phys. Rev. Lett. **83**, 1751 (1999).

[27] E. Nielsen and J. H. Macek, Phys. Rev. Lett. **83**, 1566 (1999).

[28] P. F. Bedaque, E. Braaten, and H. W. Hammer, Phys. Rev. Lett. **85**, 908 (2000).

[29] N. P. Mehta, S. T. Rittenhouse, J. P. D'Incao, and C. H. Greene, Phys. Rev. A **78**, 020701 (2008).

[30] L. M. Delves, Nucl. Phys **9**, 391 (1958).

[31] L. M. Delves, Nuc. Phys. **20**, 275 (1960).

[32] V. Efimov, Sov. J. Nucl. Phys **12**, 589 (1971).

[33] M. Fabre de la Ripelle and J. Navarro, Ann. Phys. **123**, 185 (1978).

[34] J. Macek, J. Phys. B **1**, 831 (1968).

[35] U. Fano, Phys. Today **29**, 32 (1976).

[36] U. Fano, Rep. Prog. Phys **46**, 97 (1983).

[37] C. W. Clark and C. H. Greene, Physical Review A **21**, 1786 (1980).

[38] M. Cavagnero, Phys. Rev. A **33**, 2877 (1986).

[39] M. Cavagnero, Phys. Rev. A **36**, 523 (1987).

[40] V. Kokoouline and C. H. Greene, Phys. Rev. A **68**, 012703 (2003).

[41] A. Igarashi and N. Toshima, Phys. Rev. A **50**, 232 (1994).

[42] J. Macek, M. Cavagnero, K. Jerjian, and U. Fano, Phys. Rev. A **35**, 3940 (1987).

[43] J. L. Bohn and U. Fano, Phys. Rev. A **53**, 4014 (1996).

[44] P. Nozieres and S. Schmitt-Rink, J. Low-Temp. Phys. **59**, 195 (1985).

[45] G. E. Astrakharchik, J. Boronat, J. Casulleras, and S. Giorgini, Phys. Rev. Lett. **93**, 200404 (2004).

[46] A. Bulgac, J. E. Drut, and P. Magierski, Phys. Rev. Lett. **96**, 090404 (2006).

[47] A. Perali, P. Pieri, and G. C. Strinati, Phys. Rev. Lett. **93**, 100404 (2004).

[48] A. Perali, P. Pieri, and G. C. Strinati, Phys. Rev. Lett. **93**, 100404 (2004).

[49] S. Tan and K. Levin, Phys. Rev. A **74**, 43606 (2006).

[50] S. Tan, Annals of Physics **323**, 2952 (2008).

[51] S. Tan, Annals of Physics **323**, 2971 (2008).

[52] S. Tan, Annals of Physics **323**, 2987 (2008).

[53] S. Zhang and A. J. Leggett, Phys. Rev. A **79**, 023601 (2009).

[54] G. Baym, C. J. Pethick, Z. Yu, and M. W. Zwierlein, Phys. Rev. Lett. **99**, 190407 (2007).

[55] E. Braaten and L. Platter, Phys. Rev. Lett. **100**, 205301 (2008).

[56] C. De Melo, M. Randeria, and J. R. Engelbrecht, Phys. Rev. Lett. **71**, 3202 (1985).

[57] P. Pieri and G. C. Strinati, Phys. Rev. B **61**, 15370 (2000).

[58] J. Von Stecher, C. H. Greene, and D. Blume, Phys. Rev. A **77**, 43619 (2008).

[59] V. N. Efimov, Sov. J Nucl. Phys. **12**, 589 (1970).

[60] V. N. Efimov, Nucl. Phys. A **210**, 157 (1973).

[61] E. Braaten and H. W. Hammer, Phys. Rev. A **70** (2004).

[62] T. Kraemer, M. Mark, P. Waldburger, J. G. Danzl, C. Chin, B. Engeser, A. D. Lange, K. Pilch, A. Jaakkola, H. Naegerl, et al., Nature **440**, 315 (2006).

[63] J. P. D'Incao, C. H. Greene, and B. D. Esry, J. Phys. B **42**, 044016 (2009).

[64] S. Knoop, F. Ferlaino, M. Mark, M. Berninger, H. Schöbel, H. Nägerl, and R. Grimm, Nature Physics **5**, 227 (2009).

[65] J. V. Stecher, J. P. D'incao, and C. H. Greene, eprint arXiv:0810.3876 (2009).

[66] J. Avery, Hyperspherical Harmonics: Applications in Quantum Theory, Kluwer Academic Publishers, Norwell, MA, 1989.

[67] J. L. Bohn, B. D. Esry, and C. H. Greene, Phys. Rev. A **58**, 584 (1998).

[68] Y. E. Kim and A. Zubarev, J. Phys. B **33**, 55 (2000).

[69] R. Zhang and C. Deng, Phys. Rev. A **47**, 71 (1993).

[70] N. K. Timofeyuk, Phys. Rev. C **65**, 0406306 (2002).

[71] N. K. Timofeyuk, Phys. Rev. C **69**, 034336 (2004).

[72] M. De La Ripelle and J. Navarro, Ann. Phys. **123**, 185 (1979).

[73] M. Fabre de la Ripelle, S. Sofianos, and R. Adam, Ann. of Phys. **316**, 107 (2005).

[74] P. Pieri, L. Pisani, and G. Strinati, Phys. Rev. B **72**, 12506 (2005).

[75] D. Kushibe, M. Mutou, T. Morishita, S. Watanabe, and M. Matsuzawa, Phys. Rev. A **70**, 63617 (2004).

[76] D. Z. Goodson, M. López-Cabrera, D. R. Herschbach, and J. D. Morgan III, J. Chem. Phys. **97**, 8481 (1992).

[77] J. G. Loeser, J. H. Summerfield, A. L. Tan, and Z. Zheng, J. of Chem. Phys. **100**, 5036 (1994).

[78] M. Dunn and D. K. Watson, Ann. Phys. **251**, 266 (1996).

[79] E. Fermi, Ric. Sci. **7**, 13 (1936).

[80] M. Houbiers, R. Ferwerda, H. Stoof, W. McAlexander, C. Sackett, and R. Hulet, Phys. Rev. A **56**, 4864 (1997).

[81] G. Bruun and K. Burnett, Phys. Rev. A **58**, 2427 (1998).

[82] R. Roth and H. Feldmeier, Phys. Rev. A **64**, 43603 (2001).

[83] R. D. Cowan, The Theory of Atomic Structure and Spectra, University of California Press, Los Angeles, CA, 1981.

[84] M. Brack and R. K. Bhaduri, Semiclassical Physics, Addison-Wesley, Reading, MA, 1997.

[85] B. D. Esry and C. H. Greene, Phys. Rev. A **60**, 1451 (1999).

[86] L. Vichi and S. Stringari, Phys. Rev. A **60**, 4734 (1999).

[87] B. M. Fregoso and G. Baym, Phys. Rev. A **73**, 043616 (2006).

[88] D. Blume, S. T. Rittenhouse, J. V. Stecher, and C. H. Greene, Phys. Rev. A **77**, 033627 (2008).

[89] T. C. Germann, D. R. Herschbach, M. Dunn, and D. K. Watson, Phys. Rev. Lett. **74**, 658 (1995).

[90] S. Tan, eprint cond-mat/0412764 (2004).

[91] K. O'Hara, S. Hemmer, M. Gehm, S. Granade, and J. Thomas, Science **298**, 2179 (2002).

[92] S. Giorgini, L. P. Pitaevskii, and S. Stringari, preprint arXiv:0706.3360 (2007).

[93] F. Werner and Y. Castin, Phys. Rev. A **74**, 53604 (2006).

[94] T. B. Ottenstein, T. Lompe, M. Kohnen, A. N. Wenz, and S. Jochim, Phys. Rev. Lett. **101**, 203202 (2008).

[95] J. Huckans, J. Williams, E. Hazlett, R. Stites, and K. O'Hara, Arxiv preprint arXiv:0810.3288 (2008).

[96] C. A. Regal and D. S. Jin, Phys. Rev. Lett. **90**, 230404 (2003).

[97] M. Taglieber, A. C. Voigt, F. Henkel, S. Fray, T. W. Hänsch, and K. Dieckmann, Phys. Rev. A **73**, 11402 (2006).

[98] E. Shuryak, Phys. Rev. A **54**, 3151 (1996).

[99] H. Stoof, J. Stat. Phys. **87**, 1353 (1997).

[100] E. Donley, N. Claussen, S. Cornish, J. Roberts, E. Cornell, and C. Wieman, Nature **412**, 295 (2001).

[101] S. Stringari, Europhys. Lett. **65**, 749 (2004).

[102] M. Bartenstein, A. Altmeyer, S. Riedl, S. Jochim, C. Chin, J. H. Denschlag, and R. Grimm, Phys. Rev. Lett. **92**, 203201 (2004).

[103] Y. Zhou, C. D. Lin, and J. Shertzer, J. Phys. B **26**, 3937 (1993).

[104] C. D. Lin, Phys. Rep. **257**, 1 (1995).

[105] V. Kokoouline and C. H. Greene, Phys. Rev. A **68**, 012703 (2003).

[106] U. Fano, Phys. Rev. A **24**, 2402 (1981).

[107] M. Fabre de la Ripelle, Few-Body Systems **14**, 1 (1993).

[108] R. Szmytkowski, J. Math. Phys. **47**, 063506 (2006).

[109] J. Jackson and R. Fox, Am. J. Phys. **67**, 841 (1999).

[110] M. Abramowitz and I. Stegun, Handbook of Mathematical Functions, With Formulas, Graphs, and Mathematical Tables, Dover Publications, New York, NY, 1965.

[111] E. Nielsen, D. V. Fedorov, A. S. Jensen, and E. Garrido, Phys. Rep. **347**, 373 (2001).

[112] J. P. DIncao and B. D. Esry, Phys. Rev. Lett. **94**, 213201 (2005).

[113] E. Braaten and H.-W. Hammer, Phes. Rep. **428**, 259 (2006).

[114] M. Ross and G. Shaw, Ann. Phys. **13**, 147 (1961).

[115] V. Efimov, Physics Letters B **33**, 563 (1970).

[116] O. I. Kartavtsev and A. V. Malykh, J. Phys. B **40**, 1429 (2007).

[117] N. P. Mehta, S. T. Rittenhouse, J. von Stecher, J. P. D'Incao, and C. H. Greene, eprint arXiv:0903.4145 (2009).

[118] R. Langer, Phys. Rev. **51**, 669 (1937).

[119] C. H. Greene, A. R. P. Rau, and U. Fano, Phys. Rev. A **26**, 2441 (1982).

[120] J. P. Burke, C. H. Greene, and J. L. Bohn, Phys. Rev. Lett. **81**, 3355 (1998).

[121] J. H. Macek, Few-Body Systems **31**, 241 (2002).

[122] A. Bulgac and V. Efimov, Sov. J. Nucl. Phys. **22**, 153 (1976).

[123] U. Fano, Phys. Rev. **124**, 1866 (1961).

[124] I. Mazumdar, A. R. P. Rau, and V. S. Bhasin, Phys. Rev. Lett. **97**, 062503 (2006).

[125] V. Aquilanti and S. Cavalli, Journal of the Chemical Society, Faraday Transactions **93**, 801 (1997).

[126] A. Kuppermann, J. Phys. Chem. A **101**, 6368 (1997).

[127] R. Littlejohn, K. Mitchell, and V. Aquilanti, Phys. Chem. Chem. Phys. **1**, 1259 (1999).

[128] H. Suno, B. D. Esry, C. H. Greene, and J. P. Burke Jr, Phys. Rev. A **65**, 42725 (2002).

[129] H. Sadeghpour, Very Highly-Excited States of Two-Electron Systems, PhD thesis, Louisiana State University., 1990.

[130] L. Landau and E. Lifshitz, Quantum Mechanics: Non-Relativistic Theory, Butterworth-Heinemann, 1981.

[131] J. Von Stecher, C. H. Greene, and D. Blume, Phys. Rev. A **76**, 53613 (2007).

[132] Private communication with J. L. Bohn.

[133] J. Levinsen and V. Gurarie, Phys. Rev. A **73**, 53607 (2006).

[134] C. A. Regal, M. Greiner, and D. S. Jin, Phys. Rev. Lett. **92**, 083201 (2004).

[135] O. I. Kartavtsev and A. V. Malykh, Phys. Rev. A **74**, 042506 (2006).

[136] M. V. Berry and K. E. Mount, Rep. Prog. Phys. **35**, 315 (1972).

Appendix A

Consructing Hyperspherical Harmonics

In this appendix I describe the construction of hyperspherical harmonics. The construction method is taken from the work of Smirnov and Shitikova [5], but it is detailed here for completeness. In Sec. 2.2 the it was shown that each nod in a hyperspherical tree has an associated hyperangular momentum quantum number. In the hyperspherical trees there are four types of node; a node with two free branches, two types of nod with one free branch, and a nod with no free branches. Theses nodes are illustrated in Fig. A.1. The construction of hyperspherical harmonics follows from each of these types.

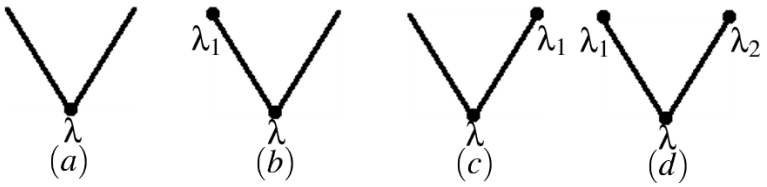

Figure A.1: The four possible hyperangular node types are shown.

A.0.0.1 Two free branches

A node with two free branches is fairly straight forward as there are no sub-hyperangular momenta that need to be worried about. In fat a nod with two free branches represents a normal polar coordinate parametrization. The hyperangular vol-

ume element for a tree with this node pick up a factor of $d\phi$. A hyperspherical harmonic for a tree with this node pick up a factor of

$$Y_m(\phi) = \frac{1}{\sqrt{2\pi}} e^{im\phi}, \tag{A.1}$$

with hyperangular momentum quantum number $m = 0, \pm 1, \pm 2, ...$

A.0.0.2 One free branch

To simplify the description I will begin by discussing a node of the type shown in Fig. A.1(b) where the right hand branch is free. A node of this type has a sub-hyperangular momentum quantum number, λ_1, associated with it. The hyperangular volume element picks up a factor of $\sin^{d_1-1}\beta d\beta$. A hyperspherical harmonic for a tree with this node pick up a factor of

$$Y_{\lambda\lambda_1}(\beta) = N^{d_1}_{\lambda|\lambda_1|} \sin^{|\lambda_1|}\beta P^{|\lambda_1|+(d_1-3)/2,|\lambda_1|+(d_1-3)/2}_{\lambda-|\lambda_1|}(\cos\beta), \tag{A.2}$$

$$N^{d_1}_{\lambda|\lambda_1|} = \left[\frac{\Gamma(\lambda+|\lambda_1|+d_1-2)(2\lambda+d_1-2)(\lambda-|\lambda_1|)!}{2^{2|\lambda_1|+d_1-2}\pi\Gamma\left(\lambda+\frac{(d_1-1)}{2}\right)\Gamma\left(\lambda+\frac{(d_1-1)}{2}\right)}\right]^{1/2},$$

where $\lambda_1 = \lambda, \lambda-1, \lambda-2, ...1, 0$, and $P^{\gamma,\delta}_n$ is a Jacobi polynomial.

To find the hyperspherical harmonic for a node of type Fig A.1(c) all that must be done is to make the transformation $\beta \to \pi/2 - \beta$.

A.0.0.3 No free branches

A node of the type shown in Fig. A.1(d) has two sub-hyperangular momentum quantum numbers associated with it, λ_1 and λ_2 associated with sub-spaces of dimension d_1 and d_2 respectively. The hyperangular momentum volume element picks up a factor of $\sin^{d_1-1}\alpha\cos^{d_2-1}\alpha d\alpha$. A hyperspherical harmonic for a tree with this node pick up a

factor of

$$Y_{\lambda\lambda_1\lambda_2} = N^{d_1 d_2}_{\lambda\lambda_1\lambda_2} \sin^{\lambda_1}\alpha \cos^{\lambda_2}\alpha P^{\lambda_1+d_1/2-1,\lambda_2+d_2/2-1}_{(\lambda-\lambda_1-\lambda_2)/2}(\cos 2\alpha)\,, \tag{A.3}$$

$$N^{d_1 d_2}_{\lambda\lambda_1\lambda_2} = \left[\frac{(2\lambda+d_1+d_2-1)\,\Gamma\left(\frac{\lambda_1+\lambda_2+\lambda+d_1+d_2-2}{2}\right)\left(\frac{\lambda-\lambda_1-\lambda_2}{2}\right)!}{\Gamma\left(\frac{\lambda+\lambda_1-\lambda_2+d_1}{2}\right)\Gamma\left(\frac{\lambda+\lambda_2-\lambda_1+d_2}{2}\right)}\right]^{1/2},$$

with the restriction

$$\lambda - \lambda_1 - \lambda_2 = \text{even number.}$$

Appendix B

Non-Adiabatic Corrections for the Three-Body Problem

In this Appendix, I give the $\bar{P}$ matrix and the diagonal correction Q_{nn} matrices discussed in Chapter 5 for the multi-channel three-boson problem. The derivation is similar to that of Kartatsev and Malykh [135, 116].I begin by considering the free space Schrödinger equation the hyperangular channel function,

$$\left(\Lambda^2 - \lambda_n^2 + 2\mu R^2 \bar{\varepsilon}\right) \vec{\Phi}_n = 0, \tag{B.1}$$

where $\vec{\Phi}_n$ is the nth channel function whose components are the hyperangular behavior in each internal three-body state, $\bar{\varepsilon}$ is the internal state energy offset matrix, and for notational simplicity I have written the hyperangular eigenvalue as $(\nu_n + 2)^2 = \lambda_n^2$. Next consider the matrix element between the same components of the mth and nth channel functions.

$$\langle \phi_{m\Sigma} | \left(\Lambda^2 - \lambda_n^2 + 2\mu R^2 \varepsilon_\Sigma\right) | \phi_{n\Sigma} \rangle = 0.$$

To find the P matrix I begin by taking a hyperradial derivative of the hyperangular Schrödinger equation away from the interaction points. Reversing the indices yields two equations that can be combined giving

$$\langle \phi_{m\Sigma} | \phi_{n\Sigma} \rangle = \frac{\left\langle \phi_{m\Sigma} \left| \Lambda^2 \right| \phi_{n\Sigma} \right\rangle - \left\langle \phi_{n\Sigma} \left| \Lambda^2 \right| \phi_{m\Sigma} \right\rangle}{(\lambda_n^2 - \lambda_m^2)}$$

Using the definition of Λ^2 and applying the generalized Bethe-Peirles boundary condition,

$$\lim_{r^{(k)} \to 0} \vec{\Phi}_n(\Omega) = \left(1 - \frac{\bar{A}^{(k)}}{r^{(k)}}\right) \vec{C}_n^k, \tag{B.2}$$

gives a normalization equation

$$\langle\phi_{m\Sigma}|\phi_{n\Sigma}\rangle = -\frac{(4\pi)^2}{dR}\frac{1}{\sum_k \sum_{\Sigma'}\left[C^k_{m\Sigma}A^{(k)}_{\Sigma'\Sigma}C^k_{n\Sigma'} - C^{\sigma k}_n A^{(k)}_{\Sigma'\Sigma}C^k_{m\Sigma}\right]}{(\lambda_n^2-\lambda_m^2)}. \tag{B.3}$$

To find the $\bar{P}$ matrix, I consider the derivative of Eq. B.1,

$$\frac{\partial}{\partial R}\left[\left(\Lambda^2-\lambda_n^2+2\mu R^2\varepsilon_\Sigma\right)|\phi_{n\Sigma}\rangle\right]=0, \tag{B.4}$$

Considering the matrix elements yields two equations,

$$\left(-\lambda_n^{2\prime}+4\mu R\varepsilon_\Sigma\right)\langle\phi_{m\Sigma}|\phi_{n\Sigma}\rangle+\left\langle\phi'_{m\Sigma}\right|\left(\Lambda^2-\lambda_n^2+2\mu R^2\varepsilon_\Sigma\right)\left|\phi'_{n\Sigma}\right\rangle=0,$$
$$\left\langle\phi'_{n\Sigma}\right|\left(\Lambda^2-\lambda_m^2+2\mu R^2\varepsilon_\Sigma\right)|\phi_{m\Sigma}\rangle=0.$$

Here the primes indicate an R derivative. Combining these two equations and solving for $\langle\phi_{m\Sigma}|\phi'_{n\Sigma}\rangle$ yields

$$\left\langle\phi_{m\Sigma}|\phi'_{n\Sigma}\right\rangle=\frac{\left(-\lambda_n^{2\prime}+4\mu R\varepsilon_\Sigma\right)\langle\phi_{m\Sigma}|\phi_{n\Sigma}\rangle+\langle\phi_{m\Sigma}|\Lambda^2|\phi'_{n\Sigma}\rangle-\langle\phi'_{n\Sigma}|\Lambda^2|\phi_{m\Sigma}\rangle}{(\lambda_n^2-\lambda_m^2)}.$$

The $\langle\phi_{m\sigma}|\Lambda^2|\phi'_{n\sigma}\rangle-\langle\phi'_{n\sigma}|\Lambda^2|\phi_{m\sigma}\rangle$ term can be solved for by considering the boundary condition again. Summing over the internal states yields the equation for the $\bar{P}$ matrix elements

$$\begin{aligned}\left\langle\vec{\Phi}_m|\vec{\Phi}'_n\right\rangle = &-\frac{12\mu R\,(4\pi)^2}{dR\,(\lambda_n^2-\lambda_m^2)^2}\left[\vec{C}^k_m\cdot\left[\bar{\varepsilon}\bar{A}^{(k)}\vec{C}^k_n\right]-\vec{C}^k_n\cdot\left[\bar{\varepsilon}\bar{A}^{(k)}\vec{C}^k_m\right]\right]\\ &-\frac{(4\pi)}{dR\,(\lambda_n^2-\lambda_m^2)}\sum_{\Sigma,\Sigma',k}C^{k\prime}_{n\Sigma}A^{(k)}_{\Sigma'\Sigma'}C^k_{m\Sigma'}\\ &-\frac{(4\pi)^2}{dR^2\,(\lambda_n^2-\lambda_m^2)}\sum_{\Sigma,\Sigma',k}C^k_{m\sigma}A^{(k)}_{\Sigma'\Sigma'}C^k_{n\sigma'}\\ &+\frac{(4\pi)^2}{dR\,(\lambda_n^2-\lambda_m^2)}\sum_{\Sigma,\Sigma',k}C^k_{m\sigma}A^{(k)}_{\Sigma'\Sigma'}C^{k\prime}_{n\sigma'}\end{aligned} \tag{B.5}$$

The diagonal part of the $\bar{Q}$ matrix can be found through a similar, but much uglier

derivation which yields

$$\left\langle \vec{\Phi}_n | \vec{\Phi}''_n \right\rangle = 3\,(4\pi)^2 \left\{ \frac{2}{3dR^2}\vec{C}'_n \cdot \left[\frac{1}{(-\lambda_n^{2\prime} + 4\mu R\bar{\varepsilon})} \bar{A}\vec{C}'_n \right] + \frac{1}{3dR}\vec{C}_n^{1\prime\prime} \cdot \left[\frac{1}{(-\lambda_n^{2\prime} + 4\mu R\bar{\varepsilon})} \bar{A}\vec{C}'_n \right] \right. \tag{B.6}$$

$$- \frac{1}{3dR}\vec{C}_n^{1\prime} \cdot \left[\frac{1}{(-\lambda_n^{2\prime} + 4\mu R\bar{\varepsilon})} \bar{A}\vec{C}''_n \right] + \frac{7}{6dR}\vec{C}_n \cdot \left[\frac{\left(-\lambda_n^{2\prime\prime} + 4\mu\bar{\varepsilon}\right)}{(-\lambda_n^{2\prime} + 4\mu R\bar{\varepsilon})^2} \bar{A}\vec{C}''_n \right]$$

$$- \frac{1}{3dR^2}\vec{C}''_n \cdot \left[\frac{1}{(-\lambda_n^{2\prime} + 4\mu R\bar{\varepsilon})} \bar{A}\vec{C}_n \right] - \frac{7}{6dR}\vec{C}''_n \cdot \left[\frac{\left(-\lambda_n^{2\prime\prime} + 4\mu\bar{\varepsilon}\right)}{(-\lambda_n^{2\prime} + 4\mu R\bar{\varepsilon})^2} \bar{A}\vec{C}_n \right]$$

$$+ \frac{7}{3dR^3}\vec{C}_n \cdot \left[\frac{\left(-\lambda_n^{2\prime\prime} + 4\mu\bar{\varepsilon}\right)}{(-\lambda_n^{2\prime} + 4\mu R\bar{\varepsilon})^2} \bar{A}\vec{C}_n \right] + \frac{2}{3dR^2}\vec{C}_n \cdot \left[\frac{\lambda_n^{2\prime\prime\prime}}{(-\lambda_n^{2\prime} + 4\mu R\bar{\varepsilon})^2} \bar{A}\vec{C}_n \right]$$

$$+ \frac{7}{6dR^2}\vec{C}_n \cdot \left[\frac{\left(-\lambda_n^{2\prime\prime} + 4\mu\bar{\varepsilon}\right)^2}{(-\lambda_n^{2\prime} + 4\mu R\bar{\varepsilon})^3} \bar{A}\vec{C}_n \right] - \frac{2}{3dR}\vec{C}_n \cdot \left[\frac{\lambda_n^{2\prime\prime\prime}}{(-\lambda_n^{2\prime} + 4\mu R\bar{\varepsilon})^2} \bar{A}\vec{C}'_n \right]$$

$$- \frac{7}{3dR^2}\vec{C}_n \cdot \left[\frac{\left(-\lambda_n^{2\prime\prime} + 4\mu\bar{\varepsilon}\right)}{(-\lambda_n^{2\prime} + 4\mu R\bar{\varepsilon})^2} \bar{A}\vec{C}'_n \right] - \frac{7}{6dR}\vec{C}_n \cdot \left[\frac{\left(-\lambda_n^{2\prime\prime} + 4\mu\bar{\varepsilon}\right)^2}{(-\lambda_n^{2\prime} + 4\mu R\bar{\varepsilon})^3} \bar{A}\vec{C}'_n \right]$$

$$- \frac{2}{3dR^3}\vec{C}'_n \cdot \left[\frac{1}{(-\lambda_n^{2\prime} + 4\mu R\bar{\varepsilon})} \bar{A}\vec{C}_n \right] + \frac{2}{3dR}\vec{C}'_n \cdot \left[\frac{\lambda_n^{2\prime\prime\prime}}{(-\lambda_n^{2\prime} + 4\mu R\bar{\varepsilon})^2} \bar{A}\vec{C}_n \right]$$

$$\left. + \frac{7}{6dR}\vec{C}'_n \cdot \left[\frac{\left(-\lambda_n^{2\prime\prime} + 4\mu\bar{\varepsilon}\right)^2}{(-\lambda_n^{2\prime} + 4\mu R\bar{\varepsilon})^3} \bar{A}\vec{C}_n \right] \right\}$$

Appendix C

N-Body Recombination Rate

In this appendix, I derive the N-body recombination rate given in Eq. 5.44 [117]. In Chapter 5 this formula was applied to three-body recombination, but it is applicable to any loss process involving N free initial particles in a gas phase. The starting point of the derivation is to assume a hyperspherically symmetric potential in d dimensions. This can be thought of in terms of uncoupled λ-wave channels in direct analogy to spherically symmetric potentials in three dimensions. At very large hyperradius the solutions to the Schrödinger equation can be written as

$$\Psi^I = e^{i\vec{k}\cdot\vec{R}} + f\left(\hat{k},\hat{k}'\right)\frac{e^{ikR}}{R^{(d-1)/2}}, \tag{C.1}$$

where $\vec{R}$ is a position vector in d dimensions. Alternatively the large R solution can be written in terms of a hyperspherical harmonic expansion with a phase shift,

$$\Psi^{II} = \sum_{\lambda\mu} A_{\lambda\mu} Y_{\lambda\mu}\left(\hat{R}\right)\left[j_\lambda^d\left(kR\right)\cos\delta_\lambda - n_\lambda^d\left(kR\right)\sin\delta_\lambda\right], \tag{C.2}$$

where j_λ^d and n_λ^d are hyperspherical Bessel functions of the first and second kind [66],

$$j_\lambda^d\left(kR\right) = \frac{\Gamma\left(\alpha\right)}{(d-4)!!}\frac{J_{\alpha+\lambda}\left(kR\right)}{\left(kR\right)^\alpha},$$
$$\alpha = \frac{d}{2} - 1,$$

where J_γ is a normal Bessel function. Here $\hat{R}$ is used to denote the hyperangles of the vector $\vec{R}$. It will be useful to have this written in the large kR limit,

$$j_\lambda^d(kR) \overset{kR\to\infty}{\longrightarrow} \frac{\Gamma(\alpha)\,2^{\alpha-1}}{(d-4)!!}\sqrt{\frac{2}{\pi}}\frac{\cos\left(kR-\frac{2\alpha+2\lambda-1}{2}\pi\right)}{(kR)^{\alpha+1/2}}. \tag{C.3}$$

The d-dimensional plane wave can also be expanded in terms of hyperspherical Bessel functions and harmonics [66] as

$$e^{i\vec{k}\cdot\vec{R}} = (d-2)!!\frac{2\pi^{d/2}}{\Gamma(d/2)}\sum_\lambda i^\lambda j_\lambda^d(kR)\,Y_{\lambda\mu}^*\left(\hat{k}\right)Y_{\lambda\mu}\left(\hat{R}\right). \tag{C.4}$$

Comparing Eqs. C.3 and C.4, the incoming planewave part of Ψ^{II} can be extracted and the expansion coefficients $A_{\lambda\mu}$ can be found. This can then be inserted into Eq. C.2 to find the scattering amplitude:

$$f\left(\hat{k},\hat{k}'\right) = \left(\frac{2\pi}{k}\right)^{(d-1)/2}\sum_{\lambda\mu} i^\lambda e^{-i(2\alpha+2\lambda+1)/4}Y_{\lambda\mu}^*\left(\hat{k}\right)Y_{\lambda\mu}\left(\hat{k}'\right)\left(e^{2i\delta_\lambda}-1\right). \tag{C.5}$$

At this point, the scattering amplitude $f\left(\hat{k},\hat{k}'\right)$ can be immediately generalized to include coupling between hyperradial channels, i.e.

$$f\left(\hat{k},\hat{k}'\right) = \left(\frac{2\pi}{k}\right)^{(d-1)/2}\sum_{\lambda\mu,\lambda'\mu'} i^\lambda e^{-i(2\alpha+2\lambda+1)/4}Y_{\lambda\mu}^*\left(\hat{k}\right)Y_{\lambda'\mu'}\left(\hat{k}'\right)\left(S_{\lambda\mu,\lambda'\mu'}-\delta_{\lambda\lambda'}\delta_{\mu\mu'}\right). \tag{C.6}$$

From this the total elastic cross section can be extracted, given by

$$\sigma = \int\left|f\left(\hat{k},\hat{k}'\right)\right|^2 d\hat{k}. \tag{C.7}$$

This cross section is the for the incoming states with hyperspherical momentum direction $\hat{k}'$ summed over all outgoing hyperspherical momentum directions $\hat{k}$. For the cross section in a gas phase, all of the initial momenta must be **averaged** over. Using the orthonormality of hyperspherical harmonics, this procedure yields

$$\sigma^{dist} = \frac{1}{\Omega_d}\left(\frac{2\pi}{k}\right)^{d-1}\sum_{\lambda\mu,\lambda'\mu/}\left|S_{\lambda\mu,\lambda'\mu'}-\delta_{\lambda\lambda'}\delta_{\mu\mu'}\right|^2, \tag{C.8}$$

$$\Omega_d = \int d\Omega = \frac{2\pi^{d/2}}{\Gamma(d/2)}.$$

This can immediately be interpreted as the generalized average cross section that takes an initial state $i \equiv \lambda\mu$ to a final state $f \equiv \lambda'\mu'$, i.e.

$$\sigma_{i\to f}^{dist} = \left(\frac{2\pi}{k}\right)^{d-1} \frac{\Gamma\left(d/2\right)}{2\pi^{d/2}} \left|S_{fi} - \delta_{fi}\right|^2 . \tag{C.9}$$

This expression must only be summed over the initial and final states of interest. For example, when the scattering potential is purely hyperradial all μ substates are degenerate and the sum over initial states yields a factor of

$$M\left(d,\lambda\right) = \frac{\left(2\lambda + d - 2\right)\Gamma\left(\lambda + d - 2\right)}{\Gamma\left(\lambda + 1\right)\Gamma\left(d - 1\right)},$$

which is exactly the degeneracy of hyperspherical harmonics for fixed λ [66]. The hyperspherically symmetric version of Eq. C.9 has been found using the Born approximation by Fabre de la Ripelle [107]. Equation C.9 describes the behavior of distinguishable particles in the initial state.

To specify indistinguishable particles, all possible identical configurations must be summed over in the scattering amplitude and only unique states included in the sum over final states,

$$\sigma^{indist} = \int \frac{d\hat{k}}{N_p} \int \frac{d\hat{k}'}{\Omega_d} \left|N_p f\left(\hat{k},\hat{k}'\right)\right|^2 = N_p \sigma^{dist}, \tag{C.10}$$

where N_p is the number of permutation symmetries in the system. For instance, for N identical particles, $N_p = N!$, or for two species of identicle particles, $N_p = N_\uparrow! N_\downarrow!$. Using this gives the final scattering cross section for total angular momentum J and parity Π ,

$$\sigma_{fi}^{J^\Pi} = N_p \left(\frac{2\pi}{k}\right)^{(d-1)} \frac{\Gamma\left(d/2\right)}{2\pi^{d/2}} \sum_i \left(2J+1\right) \left|S_{fi}^{J^\Pi} - \delta_{fi}\right|^2 , \tag{C.11}$$

where I have explicitly included the angular momentum degeneracy. To turn this into a rate coefficient, the cross section must be multiplied by the "velocity", $v = \hbar k/\mu_d$, resulting in

$$K_d = \frac{\hbar k}{\mu_d} \sigma_{fi}^{J^\Pi} \tag{C.12}$$

where μ_d is the d dimensional reduced mass of the system, and $k = \sqrt{2\mu_d E}/\hbar$. For N particles in three dimensions with the center of mass motion removed, $d = 3\,(N-1)$ and $\mu_d = \left(\prod_{i=1}^{N} m_i / \sum_{i=1}^{N} m_i\right)^{1/(N-1)}$ yielding Eq.5.44.

C.1 Scaling laws for N identical bosons

In this section, I apply the result of Eq. C.12 to a system of N identical bosons at ultracold temperatures. Ultracold here means that only the lowest channel in the sum in Eq. C.11 contributes to the inelastic rate coefficient. In general the lowest asymptotic channel for N bosons has $\lambda = 0$ and $J^{\Pi} = 0^+$. I assume that the process in question is an inelastic rate to a deeply bound channel yielding

$$K_N = \frac{\hbar k}{2\mu_N} N! \left(\frac{2\pi}{k}\right)^{(3N-4)} \frac{\Gamma\left(3\,(N-1)\,/2\right)}{2\pi^{3(N-1)/2}} \left|S_{0f}^{0^+}\right|^2. \tag{C.13}$$

For a thermal gas of identical bosons, the density, n, of the gas follows the equation,

$$\frac{\partial n}{\partial t} = -\sum_{N=2}^{N_{\max}} L_N n^N, \tag{C.14}$$

where $N_{\max}$ is the highest order recombination process that is allowed, and L_N is the N-body recombination rate scaled by the number of particles lost in the process and including symmetry factors.

From Eq. 2.19, the large R behavior of the lowest hyperradial potential has the form of an effective centrifugal barrier,

$$U(R) = \frac{\hbar^2}{2\mu} \frac{l_{eff}\,(l_{eff}+1)}{R^2},$$
$$l_{eff} = \lambda + \frac{d}{2} - \frac{3}{2}.$$

The energy normalized hyperradial wavefunction for this entrance channel at large R for low energy behaves as $F(R) \propto k^{l_{eff}+1/2}$. If it is assumed that this entrance channel dominates the behavior of the S matrix and that the only relevant length scale in the problem is the s-wave scattering length, a, i.e. $S_{0f}^{0^+} \propto (ka)^{l_{eff}+1/2}$, the recombination

rate from Eq. C.13 is

$$K_N \propto \frac{\hbar k}{2\mu_N} N! \left(\frac{2\pi}{k}\right)^{(3N-4)} (ka)^{3N-5} \frac{\Gamma\left(3\left(N-1\right)/2\right)}{2\pi^{3(N-3)/2}},$$
$$= \frac{\hbar}{2\mu_N} N! \left(2\pi\right)^{(3N-4)} a^{3N-5} \frac{\Gamma\left(3\left(N-3\right)/2\right)}{2\pi^{3(N-1)/2}}. \tag{C.15}$$

It is interesting to note that this indicates that the inelastic N-body recombination rate for bosons is always a constant at threshold. For $N = 3$, this gives

$$K_3 \propto \frac{192\pi^2\hbar}{2\mu_3} a^4, \tag{C.16}$$

which is the well know a^4 scaling law for three boson recombination [111]. For $N = 4$ this gives

$$K_4 \propto \frac{20160\pi^4}{2\mu_4} a^7. \tag{C.17}$$

C.2 Four-bosons: beyond scaling laws

In this section I examine the four boson problem using the work of von Stecher [8, 65]. Specifically I will be concerned with the process of four-body recombination to an Efimov state at negative scattering lengths, i.e. $K_4^{B+B+B+B\rightarrow B_3+B}$. This process can be important in identifying Efimov states [65], creating Efimov states, or in the high density regime of an ultracold gas of bosons.

Several examples of the four-boson potentials at negative scattering length are shown schematically in Figs. C.1(a-d) [8, 65]. These potentials are from the region where at least one Efimov states is bound. For a full analysis of the properties of these potentials the reader is pointed towards Ref. [8]. The important aspect here is that each potential corresponding to an Efimov state and a free particle supports two four-body bound states. Further, as the scattering length becomes more negative, eventually another Efimov state is formed. The potential corresponding to the new Efimov state is the same as the previous potential scaled by the characteristic Efimov scaling, i.e. the

length scale is multiplied by a factor of 22.7 and the energy scale is divided by a factor of $(22.7)^2 \approx 515$.

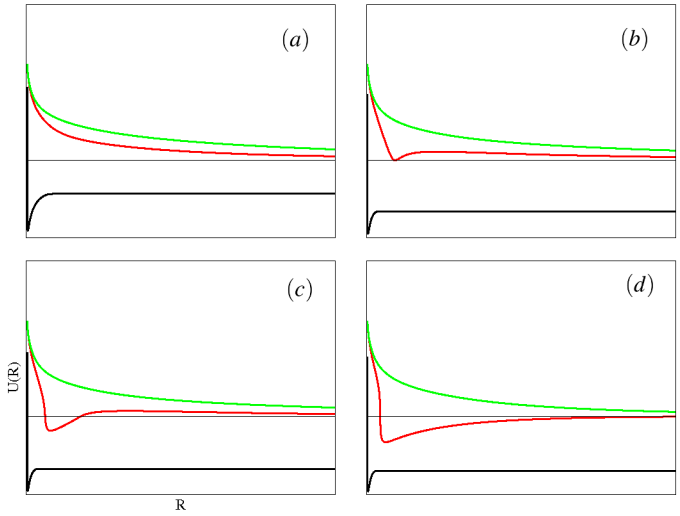

Figure C.1: (a)-(d) Schematic of the four-boson potentials from Ref. [8] are shown, As the scattering length becomes more negative (a-d inorder) an inner well appears and is pulled further down until a second Efimov state is bound.

I will model this process as a single channel scattering problem with a complex scattering phase shift to simulate loss from the lowest four-free-boson potential. With this assumption the S matrix element corresponding to the transition to the Efimov state is given in the low energy limit by

$$\begin{aligned} |S_{B+B+B+B\to B_3+B}|^2 &= 1 - |S_{B+B+B+B\to B+B+B+B}|^2 , \\ &= 4\,\mathrm{Im}\,\delta, \end{aligned} \tag{C.18}$$

where δ is the single channel complex phase shift. Figure C.2 shows a schematic path of this process where the transition is assumed to occur at the peak in the coupling strength between the two potentials. It is important to note that when a new Efimov state is formed, I assume that all recombination proceeds out the new channel, and the recombination out of the old channel is turned off. Assuming a WKB wavefunction and

using the WKB connection formulas [136] the imaginary part of the phase shift is

$$4\,\mathrm{Im}\,\delta = \frac{\sinh 2\eta}{\sin^2(\phi - \pi/2) + \sinh^2\eta} e^{-2\gamma},$$

where ϕ is the WKB phase accumulated in an inner well such as the one seen in Fig C.2, γ is the WKB tunnelling for the entire process, and η parameterizes the transition probability to the Efimov channel. In this treatment η is kept as a free parameter, but in truth it is fixed by the exact nature of the four-boson system. This connection will not be discussed further here.

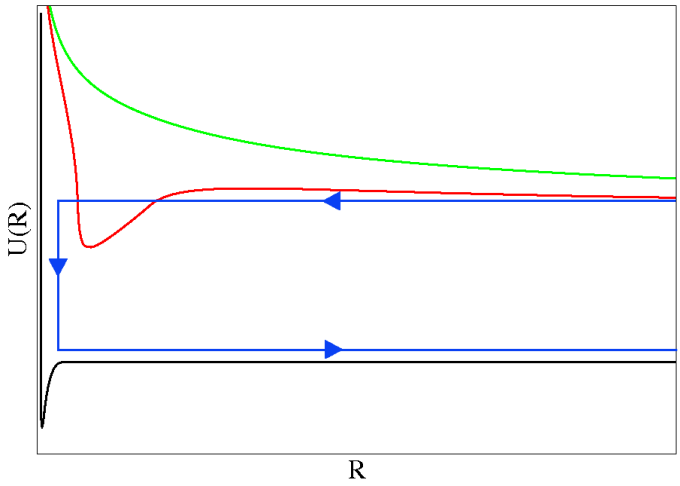

Figure C.2: A schematic of the four-body recombination process into an Efimov state plus a free particle.

Inserting this into Eq. C.13 gives

$$K_4 = A\frac{20160\pi^4}{2\mu_4}\frac{\sinh 2\eta}{\sin^2(\phi - \pi/2) + \sinh^2\eta}\frac{e^{-2\gamma}}{k^4}, \tag{C.19}$$

where A is an overall scaling that is not determined by this model. This rate coefficient assumes that the recombination process is entirely controlled by the incoming channel. Including the behavior due to the outgoing channel is a subject for later work. The apparent k^4 behavior of this rate coefficient will be cancelled by the strong tunnelling suppression in the asymptotic regime from the effective centrifugal barrier. Figure C.3

shows the resulting four-body recombination rate coefficient. Here it is assumed that the transition occurs at the point where the coupling strength peaks. Several things are readily apparent in this result. First the rate has an overall scaling of a^7 predicted by the simple dimensional argument in Eq. C.17. Second, there is a cusp in the rate at exactly the point where a new Efimov state becomes bound, $a = a_{Efi} \approx -104r_0$. It is unclear if this cusp behavior is physical, due to the approximations used in this treatment. Finally, two strong resonances can be seen. These correspond to four-body states appearing at the scattering threshold at $a = 0.43a_{Efi}$ and $a = 0.9a_{Efi}$ exactly as predicted in Ref. [8]. This gives another handle on identifying Efimov states, a task that can be quite difficult. If such four-body resonances can be associated with a three-body resonance it gives strong evidence that the three-body resonance is in fact due to an Efimov state [65].

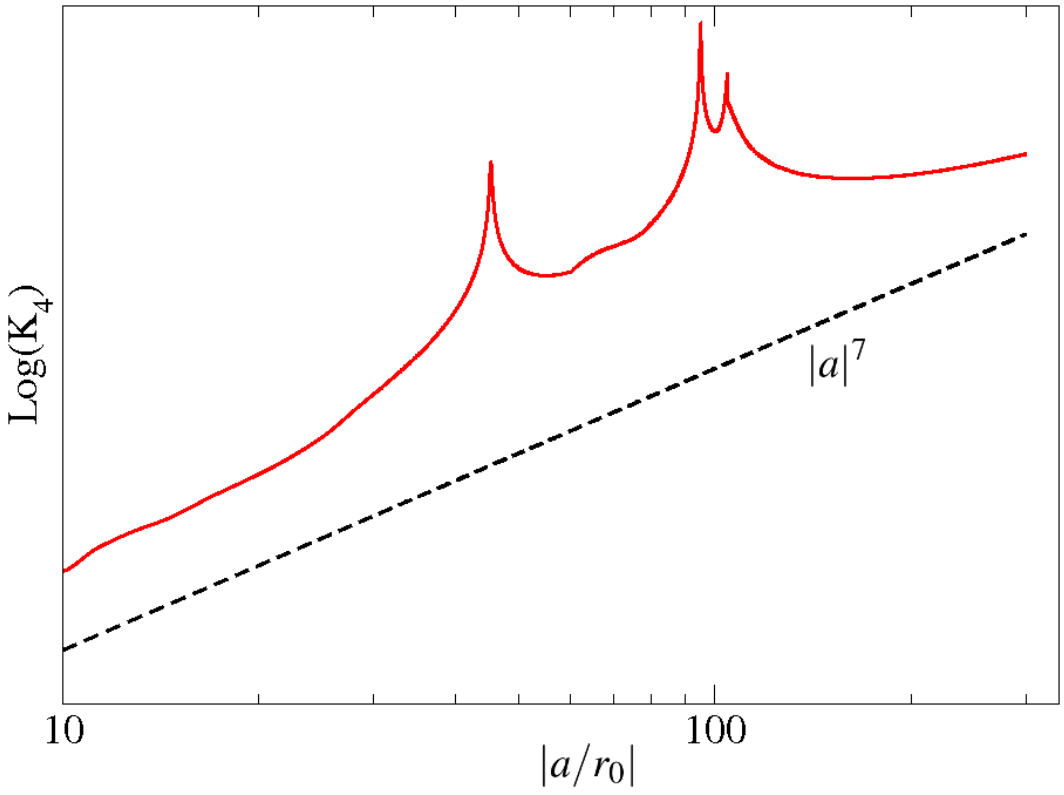

Figure C.3: The four-body recombination rate is shown plotted as a function of $|a|$ in units of the range of the two-body interaction.

Appendix D

Dimer-Dimer Relaxation Rates

In this appendix I present the derivation of the dimer-dimer relaxation rate used in Section 6.5. This process occurs when the two dimers collide causing at least one of the dimers to relax to a deeply bound state. The difference of the binding energies is then releases as kinetic energy. This process can be pictured in the hyperspherical picture as an infinite series of very closely spaced crossings between the dimer-dimer channel and channels consisting of a deeply bound dimer and two free particles. This near continuum of crossings is shown schematically in Fig. D.1(a).

Using Fermi's golden rule between the initial dimer-dimer state and the final states gives

$$V_{rel}^{dd} \propto \sum_{\lambda} \left| \left\langle \Psi_{dd}\left(R;\Omega\right) \left| V\left(R,\Omega\right) \right| \Psi_{\lambda}\left(R,\Omega\right) \right\rangle \right|^2, \tag{D.1}$$

where $\Psi_{dd}\left(R;\Omega\right)$ is the dimer-dimer wavefunction, $V\left(R,\Omega\right)$ is the interaction potential and Ψ_k is the λth deeply bound dimer state. I now will assume that the dimer-dimer wavefunction is approximated by

$$\Psi_{dd}\left(R;\Omega\right) \approx F_{dd}\left(R\right) \Phi_{dd}\left(R;\Omega\right), \tag{D.2}$$

where $\Phi_{dd}\left(R;\Omega\right)$ is the dimer-dimer hyperangular channel function and $F_{dd}\left(R\right)$ is the hyperradial wavefunction resulting from the single channel approximation. I further assume that the outgoing deeply bound dimer wavefunction can be written as

$$\Psi_k\left(R,\Omega\right) \approx \psi\left(r_{12}\right) \theta_{\lambda}\left(\vec{r}_{34},\vec{r}_{12,34}\right) \tag{D.3}$$

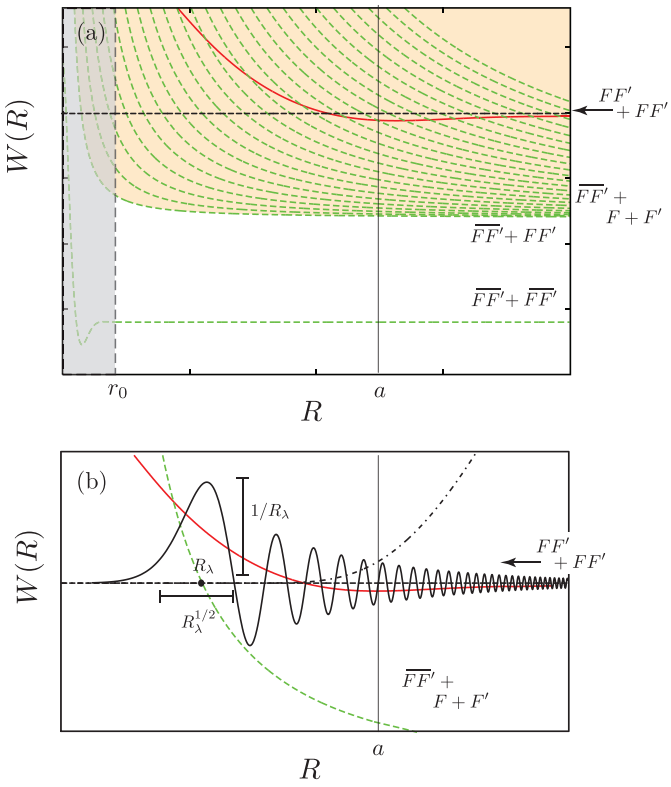

Figure D.1: (a) A schematic of the channels involved involved inthe dimer-dimer relaza-xtion process is shown. The dimer-dimer potential (red curve) goes through an inifinite number of crossing with deeply bound states (green dashed curves). (b) The hyperradial behavior of the outgoing wavefunction is shown.

where $\psi\left(r_{12}\right)$ is the wavefunction for an s-wave deeply bound dimer and $\theta_\lambda\left(\vec{r}_{34},\vec{r}_{12,34}\right)$ is the free space behavior of the resulting three particle system.

Examining one of the terms from the sum in Eq. D.1 with a single two-body interaction gives

$$V_{rel}^{dd(\lambda)} \propto \left| \int F_{dd}\left(R\right) \Phi_{dd}\left(R;\Omega\right) V_{23}\left(r_{23}\right) \psi\left(r_{12}\right) \theta_\lambda\left(\vec{r}_{34},\vec{r}_{12,34}\right) dR d\Omega \right|^2, \tag{D.4}$$

where $V_{rel}^{dd(k)}$ is the contribution to the relaxation rate by the λth term in Eq. D.1. The first thing to notice is in this is that the factor $V_{23}\left(r_{23}\right)\psi\left(r_{12}\right)$ is non-zero only when particles $1,2$, and 3 are in close proximity, and when particles $1,2$, and 3 are in close

proximity the remaining degrees of freedom are simplified as well,

$$\vec{r}_{34} \approx C\vec{r}_{12,34}. \tag{D.5}$$

This means that the wavefunction $\theta\left(\vec{r}_{34}, \vec{r}_{12,34}\right)$ can be rewritten as

$$\theta_\lambda\left(\vec{r}_{34}, \vec{r}_{12,34}\right) \approx G_\lambda\left(R\right) f_\lambda\left(\Omega\right), \tag{D.6}$$

where G_λ and f_λ are the hyperradial and hyperangular behavior associated with the λth outgoing channel. A further simplification can be made by realizing that $f_\lambda\left(\Omega\right)$ must be independent of Ω when particles $1, 2$, and 3 are in close proximity because the total wavefunction must have zero spatial angular momentum. Rewriting D.4 with these simplifications yields

$$V_{rel}^{dd(\lambda)} \propto \left| \int F_{dd}\left(R\right) G_k\left(R\right) \int \Phi_{dd}\left(R;\Omega\right) V_{23}\left(r_{23}\right) \psi\left(r_{12}\right) d\Omega dR \right|^2. \tag{D.7}$$

The hyperangular integral is approximated by the probability that three-particles are close to each other in the dimer-dimer channel function.

And example of G_λ is shown in Fig. D.1(b). Away from the classical turning point G_λ oscillates very rapidly. This fast oscillation will generally cancel out meaning the main contribution to the hyperradial integral is from the region near the classical turning point R_λ. Putting this all together yields

$$V_{rel}^{dd} \propto \sum_\lambda \frac{\left|F_{dd}\left(R_\lambda\right)\right|^2}{R_\lambda} \mathcal{F}\left(R_\lambda\right), \tag{D.8}$$

where $\mathcal{F}\left(R_\lambda\right)$ is the probability that three particles are in close proximity in the dimer-dimer channel function. The final step in this derivation is to turn the sum over λ into an integral over R_λ,

$$V_{rel}^{dd} \propto \int \rho\left(R_\lambda\right) \frac{\left|F_{dd}\left(R_\lambda\right)\right|^2}{R_\lambda} \mathcal{F}\left(R_\lambda\right) dR_\lambda \tag{D.9}$$

where $\rho\left(R_\lambda\right)$ is the, nearly constant, density of states. This is possible due to the near-continuum nature of the outgoing states. By inserting the WKB approximation

wavefunction for $F_{dd}(R)$, the result of Eq. 6.55 is obtained, i.e.

$$V_{rel}^{dd} \propto \int \rho(R) \frac{P_{WKB}(R_\lambda)}{\kappa(R) R} \mathcal{F}(R) dR. \tag{D.10}$$

Appendix E

Related Publications

- "Dimer-dimer Collisions at Finite Energies in Two-Component Fermi Gases," J. P. D'Incao, S. T. Rittenhouse, N. P. Mehta and C. H. Greene, Phys. Rev. A **79**, 030501 (2009).
- "Efimov States Embedded in the Three-Body Continuum," N. P. Mehta, S. T. Rittenhouse, J. P. D'Incao and C. H. Greene, Phys. Rev. A **72**, 020701 (2008).
- "The degenerate Ferm gas with density-dependent interactions in the large N limite under the K-Harmonic approximation," S. T. Rittenhouse and C. H. Greene, J. Phys. B **41**, 205302 (2008).
- "Stability of inhomogeneuos multicomponent Fermi gases," D. Blume, S. T. Rittenhouse, J. von Stecher and C. H. Greene, Phys. Rev A **77**, 033627 (2008).
- "Hyperspherical description of the degenerate Fermi gas: s-wave interactions," S. T. Rittenhouse, M. J. Cavagnero, J. von Stecher and C. H. Greene, Phys. Rev A **75**, 053624 (2006).
- "A hyperspherical variational approach tothe N-body problem," S. T. Rittenhouse, M. J. Cavagnero, J. von Stecher and C. H. Greene, Few Body Systems **38**, 85-90 (2005).